

Hydration of multi-component cements containing cement clinker, slag, calcareous fly ash and limestone

THÈSE N° 6834 (2016)

PRÉSENTÉE LE 19 FÉVRIER 2016

À LA FACULTÉ DES SCIENCES ET TECHNIQUES DE L'INGÉNIEUR
LABORATOIRE DES MATÉRIAUX DE CONSTRUCTION
PROGRAMME DOCTORAL EN SCIENCE ET GÉNIE DES MATÉRIAUX

ÉCOLE POLYTECHNIQUE FÉDÉRALE DE LAUSANNE

POUR L'OBTENTION DU GRADE DE DOCTEUR ÈS SCIENCES

PAR

Paweł Tadeusz DURDZIŃSKI

acceptée sur proposition du jury:

Prof. H. Hofmann, président du jury
Prof. K. Scrivener, Prof. J. Deja, directeurs de thèse
Dr M. Ben Haha, rapporteur
Prof. M. Geiker, rapporteuse
Prof. P. Bowen, rapporteur



ÉCOLE POLYTECHNIQUE
FÉDÉRALE DE LAUSANNE

Suisse
2016

Breathe, breathe in the air
Don't be afraid to care
Leave but don't leave me
Look around and choose your own ground

Long you live and high you fly
And smiles you'll give and tears you'll cry
And all you touch and all you see
Is all your life will ever be

Breathe

— Pink Floyd

Moim wspaniałym rodzicom, dziadkom i rodzeństwu

Acknowledgements

Special thanks to Prof. Karen Scrivener, the head of the Laboratory of Construction Materials, EPFL for giving me the opportunity to work in this exceptional environment. Thank you for supervising my thesis research, for your support, guidance and comments to streamline my work. Thank you for your dynamism, energy and flexibility towards new ideas. Thanks to you I understood the value of working in an international and multi-disciplinary team of scientists. Thank you for having many visiting researchers in the lab and for allowing me to attend the numerous conferences and workshops! This thesis has been an extraordinary experience. Thank you Karen!

I would like to thank HeidelbergCement for sponsoring my research. In particular I would like to thank Dr. Wolfgang Dienemann, Dr. Mohsen Ben Haha, Dr. Maciej Zajac, almost-Dr. Frank Bullerjahn and other members of the HeidelbergCement team for their help, encouragement and feedback during my thesis.

I would like to thank Prof. Jan Deja from the AGH University of Science and Technology in Cracow, who was my co-supervisor during this thesis. I met Prof. Deja during my bachelor studies in Cracow and he helped me set my first steps in research.

I would like to thank the members of the jury for reading of my thesis and for their useful comments that helped me improve the final document: Prof. Karen Scrivener, Prof. Mette Geiker, Prof. Paul Bowen, Prof. Jan Deja, Dr. Mohsen Ben Haha and Prof. Heinrich Hofmann.

I would like to give special thanks to Dr. Cyrille Dunant, who has greatly contributed to this work with his knowledge, 'outside the box' ideas and critical thinking. He had the first idea of using frequency plots, but also violin plots, bubble plots, etc. Thank you Cyrille for our every-day discussions, for teaching me statistics and coding and for the fun we had doing science.

I would like to thank my friends and colleagues from LMC and from other laboratories. However, I must first emphasize that it is mainly thanks to Karen who found, hired and encouraged us, young (and less-young) researchers, sent us to courses and conferences and let us interact with top-notch scientists, some of whom used to be her students, that this great team we were became a 'critical mass' of ideas and skills. Thanks to Bizzo, Mo, Élise, Berta, Ruben, Aslam,

Acknowledgements

Hadi (lunch!), Arnaud, John, Mathieu, Frank, Luis, François, Lily, Emmanuelle, Hui, Huang, Xuerun, Mink, Wiola, Wensheng, Keren, Hamed, Aurelie, Adrien, Adrien, Abdel, Leng, Yani, Fernando, Cyrille, Alain, Alexandre, Julien Ston, Nico, Théo, Miguel, Matt, Ted, Olga, Émilie, Amélie, Vadim, Lionel, Antonino, Joao, Paul, Shigeyoshi, and Yoshida. Special thanks to my officemates: Élise and Aslam for the great ambience of MXG 235, for the jokes and discussions. It was a great pleasure to share the office with you. Great thanks to the best secretaries: Maude, Anne-Sandra and Marie-Alix.

During my PhD I had the opportunity to supervise and co-supervise bachelor and master projects and I would like to thank those students: Clémence Dézulier, Tony Länzlinger, Théo Gaudin, Lionel Wasser, Julie Perrotton, Bastien Le Gars Santoni, Adrien Chappuis.

Special thanks for those who helped me bring my French from zero level to where it is now, who always supplied me with new expressions and did not give up on me: Lionel, Bizzo, Arnaud, Nico Henning, Rox.

I would like to thank my friends from Poland, in particular Zdębski, Troszok, Czaja, Jedynak, Ziemięć, Łatek, Piotr Kuchta. Dzięki! I would also like to thank my friends from Switzerland, especially the families Henning and Sandoz, but also Maxime, Stefano and Silvio. Thanks to MX students for the great ambience in the Materials department and integration, especially Maxime, Juliette, Vincent, Gaëtan, Lionel, Bastien, Théo, Tony.

I would like to address special thanks to a special person that greatly supported me, especially during the writing of my thesis. Merci Rox!

Finally, my deepest gratitude goes to my family for their love, support and strength they give me. Dziękuję Wam za pomoc, wsparcie, miłość i wiarę we mnie. Bez Waszego udziału to co osiągnąłem nie byłoby możliwe. Dziękuję Mamuś, Tatuś, Miki, Aga, Zodi! Dziękuję babci Janinie i Halinie oraz dziadkom Henrykowi i Tadeuszowi!

Lausanne, October 9th 2015

Paweł Tadeusz Durdziński

Abstract

Calcareous fly ashes are high-potential reactive supplementary cementitious materials, which present an interesting alternative to slowly reacting siliceous fly ashes and to slags, which availability is more and more limited. The main factor against an accurate qualification and a wide use of calcareous fly ashes in cement is their significant and inherent heterogeneity and variability. Current techniques often fail to characterize the dominant, most reactive, amorphous fraction of the ashes. As a result these fly ashes have not been researched much and many aspects of their reactivity in cement remain ill understood. These include the phase assemblages, microstructure development, strength and performance in aggressive environments.

This thesis focuses first on the characterization of the calcareous fly ashes. A new technique based on SEM-EDS full element mapping was developed to identify and characterize the different glassy components in fly ash. This technique was further developed to track the consumption of the individual anhydrous fly ash glasses in hydrating cement paste. A detailed study using synthetic glasses was carried out to investigate the factors influencing glass reaction in cement. Dissolution experiment in alkaline solution and the consumption of the glasses in paste indicated that the key factors of the glass reactivity are the fineness and the degree of depolymerisation of the glass structure. The latter was determined from the chemical composition of glass. The detailed knowledge of the fly ash reaction and the amounts of the elements supplied were linked the phase assemblage, notably the composition of the C-S-H, the amount of AFm phases and the maximum amount of limestone that can react in the given system. Matrix development in composite cements was followed and related to macroscopic aspects of strength and permeability.

There are many ways to optimize the replacement of clinker with SCMs. This thesis illustrates an approach that attempts to link the micro- and macro- structural properties not only to a particular fly ash or slag but rather to the amounts and reactivity of their constituent glasses. This way a more fundamental and general understanding is gained, which could form a base for a systematic and deliberate research of the composite cements.

Key words: characterization, composite cement, durability, fly ash, glass, limestone, microstructure, permeability, phase assemblage, reactivity, SEM-EDS, slag, supplementary cementitious materials, thermodynamic simulations.

Résumé

Les cendres volantes riches en calcium sont des matériaux cimentaires supplémentaires à haut potentiel de réaction. Elles sont une alternative intéressante aux cendres volantes siliceuses réagissant lentement et aux laitiers, dont la disponibilité est de plus en plus limitée. Les obstacles principaux à la grande utilisation de ce matériaux dans le ciment sont l'hétérogénéité et la variabilité importantes et inhérentes. Les techniques actuelles échouent souvent à caractériser la fraction amorphe, qui est pourtant la fraction dominante et la plus réactive. Par conséquent, ces cendres volantes n'ont pas beaucoup été étudié et de nombreux aspects de leur réactivité dans la pâte cimentaire restent insuffisamment compris, tel que l'assemblage des phases, le développement de la microstructure, la résistance à la compression et la performance dans les environnements agressifs.

Cette thèse se concentre d'abord sur la caractérisation des cendres volantes riches en calcium. Une nouvelle technique basée sur la cartographie complète des éléments par MEB-EDS a été mise au point pour identifier et caractériser les différents composants vitreux dans les cendres volantes. Ensuite, cette technique a été développée pour mesurer la consommation de chaque type de verre anhydre venant de cendres volantes dans la pâte de ciment. Une étude détaillée en utilisant des verres synthétiques a été réalisée pour étudier les facteurs qui influent la réaction des verres dans la pâte cimentaire. Un essai de dissolution dans une solution alcaline et de la consommation des verres dans la pâte ont indiqué que les facteurs clés de la réactivité des verres sont la finesse et le degré de dépolymérisation de la structure du verre. Ce dernier a été déterminée à partir de la composition chimique du verre. La connaissance détaillée de la réaction des cendres volantes et les montants des éléments fournis à la réaction étaient liés à l'assemblage des phases dans les pâtes, notamment la composition de la phase C-S-H, la quantité de phases AFm et le montant maximal de calcaire qui peut réagir dans chacun des systèmes. Le développement des matrices cimentaires a été étudié et lié à des aspects macroscopiques de la résistance à la compression et de la perméabilité.

Il existe de nombreuses façons d'optimiser le remplacement de clinker par des matériaux cimentaires supplémentaires. Cette thèse adopte une approche qui relie les propriétés sur une échelle micro et macro non seulement aux cendres volantes et laitiers mêmes, mais aux montants et à la réactivité de leurs verres constitutifs. De cette façon, une compréhension plus fondamentale et générale est acquise, qui pourrait constituer une base pour une recherche systématique des ciments composites.

Acknowledgements

Mots clefs : assemblage des phases, calcaire, caractérisation, cendres volantes, ciment composite, durabilité, laitier, matériaux cimentaires supplémentaires, MEB-EDS, microstructure, perméabilité, réactivité, simulations thermodynamiques, verre.

Zusammenfassung

Kalkreiche Flugaschen gelten als eine aussichtsreiche Klasse von Zementzusatzstoffen (SCM) (u.a. natürliche sowie künstliche puzzolanische und latent hydraulische Zusatzstoffe) und sie stellen eine interessante Alternative zu langsam reagierenden siliziumreichen Flugaschen aber auch Hüttensand dar. Darüber hinaus, ist die Verfügbarkeit von siliziumreichen Flugaschen und Hüttensand in zunehmendem Maße begrenzt. Der Hauptgrund der den weitreichenden Einsatz von kalkreichen Flugaschen im Zement bisher verhindert, ist die unvermeidbare, signifikante Heterogenität und Variabilität in ihrer chemischen und mineralogischen Zusammensetzung. Derzeit gebräuchliche Techniken zur Charakterisierung scheitern daran, die röntgenamorphe Hauptkomponente, welche ebenfalls auch zu großen Teilen auch den reaktivsten Bestandteil darstellt, genau zu bestimmen beziehungsweise deren genaue Zusammensetzung zu ermitteln. Als Folge dessen wurden solche Aschen bisher kaum untersucht und viele Aspekte ihrer Reaktivität im Zement sind bisher kaum erforscht beziehungsweise verstanden. Dies umfasst unter anderen die Entwicklung der (Hydrat-) Phasenzusammensetzung, des Mikrogefüges, Festigkeit und den Eigenschaften in aggressiven Umgebungen.

Diese Arbeit beschäftigt sich vorrangig mit der Charakterisierung von kalkreichen Aschen. Hierzu wurde eine neue Methode entwickelt, basierend auf der vollständigen Erfassung und Auswertung der elementaren Zusammensetzung aller Bestandteile mittels SEM-EDS Karten, um die verschiedenen glasigen Bestandteile der Flugasche qualitative und quantitativ zu beschreiben. Ferner wurde die Methode weiterentwickelt, um den Reaktionsfortschritt beziehungsweise den Verbrauch einzelner Glasphasen der Flugasche über den gesamten Zeitraum der Zementhydratation quantitativ zu verfolgen. Komplementär zu Versuchen an kalkreichen Flugaschen, wurden Studien mit synthetischen Gläsern durchgeführt. Die chemische Zusammensetzung der zu untersuchenden Gläser wurde anhand der in kalkreichen Aschen vorkommenden Glasphasen festgelegt. Das Ziel der Studie war die Untersuchung und gegebenenfalls Bestimmung von den Faktoren, die die Reaktionen während der Zementhydratation maßgeblich beeinflussen. Die Ergebnisse von Löslichkeitsexperimente in alkalischen Lösungen sowie die Umsetzung der verschiedenen Glasphasen im Zement zeigen, dass die Feinheit und die abnehmende Polymerisation der Glasstruktur maßgebend für die Reaktivität sind. Der Polymerisationsgrad der Gläser wurde auf Basis der chemischen Zusammensetzung berechnet. Die genaue quantitative Bestimmung der Flugaschereaktion sowie die damit verbundene detaillierte Erfassung der freigesetzten Elemente, wie zum Beispiel CaO , Al_2O_3 und SiO_2 , wurde mit der ermittelten Phasenzusammensetzung verbunden. Durch Massenbilanzrechnungen konnte die Zusammensetzung von C-S-H, die Gehalte an AFm-Phasen sowie

Acknowledgements

die maximal mögliche Menge an zu reagierendem Kalkstein für jedes vorgegebene System bestimmt werden. Die Entwicklung des Gefüges von Kompositzementen wurde bestimmt und mit makroskopischen Eigenschaften, wie zum Beispiel der Festigkeit und Durchlässigkeit, in Verbindung gebracht.

Es gibt verschiedene Möglichkeiten zur Optimierung bei der Substitution von Portlandzementklinker durch SCMs. Diese Arbeit beschreibt einen Ansatz, welcher die strukturellen Eigenschaften in der Größenordnung von Mikro- und Makrolevel kombiniert und dabei nicht nur den Gesamtgehalt an Flugasche und Hüttensand sondern vielmehr die Gehalte, Zusammensetzung und Umsetzung der einzelnen Glassbestandteile berücksichtigt. Auf diese Weise wird ein fundamentales aber auch allgemeines Verständnis erreicht, welches die Grundlage für systematische und zielorientierte Forschung im Forschungsfeld der Kompositzemente ermöglicht.

Stichwörter: Charakterisierung, Dauerhaftigkeit, Durchlässigkeit, Flugasche, Glas, Hüttensand, Kalkstein, Kompositzement, Mikrogefüge, Phasenzusammensetzung, Reaktivität, SEM-EDS, thermodynamische Simulation, Zementzusatzstoffe.

Riassunto

Le ceneri volanti calciche sono materiali cementizi supplementari ad alto potenziale. Queste ceneri presentano un'alternativa interessante rispetto alle ceneri volanti silicee ed alla loppa d'altoforno, le quali si trovano sempre più in quantità limitate. La variabilità e l'eterogeneità delle ceneri volanti calciche limitano l'uso di questo materiale e ne limitano anche l'accurata qualificazione. Le misure adottate oggi spesso falliscono nella caratterizzazione delle fasi dominanti, reattive ed amorfe delle ceneri volanti. Ne risulta una scarsa comprensione della loro reattività nel cemento. Ciò comprende lo sviluppo degli idrati, della microstruttura, della resistenza e delle performance in ambienti aggressivi.

Questa tesi si concentra inizialmente sulla caratterizzazione delle ceneri volanti calciche. Un nuovo metodo basato sulla mappatura completa degli elementi tramite SEM-EDS è stato sviluppato per identificare e caratterizzare i vari componenti vetrosi delle ceneri volanti. Questo metodo è stato maggiormente sviluppato per monitorare l'evoluzione di ogni singola fase anidra delle ceneri volanti durante l'idratazione del cemento. Uno studio dettagliato basato su fasi vetrose sintetizzate in laboratorio è stato effettuato per investigare i fattori influenzanti la reazione di queste fasi nel cemento. Esperimenti di dissoluzione in soluzioni alcaline e misure di reazione delle fasi vetrose in paste di cemento hanno indicato che i fattori chiave della reattività di queste fasi vetrose sono la finezza e il grado di depolimerizzazione della struttura vetrosa. Quest'ultimo è stato determinato a partire dalla composizione chimica della fase vetrosa. La conoscenza dettagliata della reazione delle ceneri volanti e le quantità di elementi forniti sono state correlate con lo sviluppo delle fasi idratate, in particolare la composizione del C-S-H, la quantità di fasi AFm e la quantità massima di calcare che può reagire in un determinato sistema. Lo sviluppo della matrice in cementi compositi è stato monitorato e correlato agli aspetti macroscopici quali la resistenza e la permeabilità.

Ci sono vari modi per ottimizzare la sostituzione del clinker con i materiali cementizi di sostituzione. Questa tesi illustra un approccio correlante le proprietà micro- e macro- strutturali non solamente alle ceneri volanti ed alla loppa d'altoforno ma bensì alla quantità e reattività dei suoi componenti vetrosi. In questo modo è stata acquisita una comprensione più fondamentale e generale, la quale potrebbe fondare una base per uno studio sistematico e conscio nella ricerca sui cementi compositi.

Acknowledgements

Parole chiave: caratterizzazione, cementi compositi, durabilità, ceneri volanti, vetro, calcare, microstruttura, permeabilità, sviluppo degli idrati, reattività, SEM-EDS, loppa d'altoforno, materiali cementizi supplementari, simulazione termodinamica.

Streszczenie

Popioły lotne wapienne należą do dodatków mineralnych do cementu o wysokim potencjale. Prezentują one interesującą alternatywę dla słabo reaktywnych popiołów krzemionkowych i żużli, których światowe zasoby znacznie maleją. Głównymi przeszkodami dla trafnej klasyfikacji i szeroko rozpowszechnionego zastosowania popiołów wapiennych są ich znaczna i nieodłączna zmienność i niejednorodność. Obecnie dostępne techniki często nie są w stanie trafnie scharakteryzować fazy amorficznej, która to faza bywa w popiołach dominującą i najbardziej reaktywną. W rezultacie, popioły wapienne nie były powszechnie badane i wiele aspektów ich reakcji w cemencie pozostaje niedostatecznie zrozumiałych. Do nich należał skład fazowy i mikrostruktura zaczynu, wytrzymałość na ściskanie oraz trwałość w agresywnych środowiskach.

Niniejsza praca doktorska skupia się w pierwszej kolejności na charakteryzacji popiołów wapiennych. Nowa technika oparta na mapach składu pierwiastkowego z mikroskopii elektronowej z EDS została opracowana mając na celu identyfikację i opis różnych faz szklistych występujących w popiołach. Technika ta została następnie dostosowana do pomiaru reakcji poszczególnych szkieł w zaczynie cementowym. Dodatkowe badania z użyciem syntetycznych szkieł zostały przeprowadzone w celu ustalenia głównych czynników wpływających na reakcję szkieł w zaczynie. Badanie rozpuszczalności owych szkieł w roztworze zasadowym oraz stopień reakcji w zaczynie wykazały że do czynników tych należa przede wszystkim wielkość ziaren oraz stopień depolimeryzacji struktury szkła. Ten ostatni został oceniony na podstawie składu chemicznego szkła. Znajomość dokładnego stopnia reakcji popiołu w zaczynie oraz ilości pierwiastków dostarczonych dla reakcji zostały powiązane ze składem fazowym zaczynu, a w szczególności ze składem chemicznym fazy C-S-H, ilością monoglinianów oraz maksymalną ilością kamienia wapiennego, która jest w stanie przereagować w danym układzie. Rozwój mikrostruktury w czasie został przebadany i powiązany z makroskopowymi cechami zapraw: wytrzymałością na ściskanie i przepuszczalnością.

Istnieje wiele sposobów na zoptymalizowanie zastąpienia klinkieru dodatkami mineralnymi. Niniejsza praca doktorska jest przykładem podejścia które łączy obserwacje w skali mikro i makro nie tylko z określonym popiołem i żużlem ale także z ilością i reaktywnością szkieł które one zawierają. Takie podejście pozwala na bardziej fundamentalne i uogólnione zrozumienie zagadnienia popiołów lotnych wapiennych w cemencie oraz może stanowić bazę dla bardziej systematycznego i celowego badania cementów wieloskładnikowych.

Acknowledgements

Słowa kluczowe: cementy wieloskładnikowe, charkateryzacja, dodatki mineralne, kamień wapienny, mikroskopia elektronowa, mikrostruktura, modelowanie termodynamiczne, popiół lotny, przepuszczalność, reaktywność, skład fazowy, trwałość, żużel wielkopiecowy.

Contents

Acknowledgements	i
Abstract (English/Français/Deutsch/Italiano/PolSKI)	iii
List of figures	xvii
List of tables	xxi
Glossary	xxiii
1 Introduction	1
2 Literature review	5
2.1 Fly ash	5
2.1.1 Characterization	6
2.1.2 Measuring the degree of reaction	8
2.2 Hydration of portland cement	9
2.3 Composite cements containing fly ash, slag and limestone	10
2.3.1 Hydration and phase assemblage	10
2.3.2 Limestone in composite cements	12
2.3.3 Microstructure, strength and permeability	14
2.3.4 Key questions	14
3 Materials and Methods	15
3.1 Materials	16
3.1.1 Overview	16
3.1.2 Principal materials	16
3.1.3 Fly ashes and synthetic glasses	18
3.2 Methods	18
3.2.1 Preparation of paste samples	18
3.2.2 Isothermal calorimetry	20
3.2.3 Particle size distribution (PSD)	21
3.2.4 Bulk chemical composition by X-ray fluorescence (XRF)	22
3.2.5 Thermo-gravimetric analysis (TGA)	22
3.2.6 X-ray powder diffraction (XRD)	23
	xiii

Contents

3.2.7	Scanning electron microscopy (SEM)	26
3.2.8	Mass-balance calculations	30
3.2.9	Thermodynamic modelling	32
3.2.10	Pore solution analysis	33
3.2.11	Mercury intrusion porosimetry (MIP)	34
3.2.12	Preparation of mortar samples	35
3.2.13	Compressive strength	36
3.2.14	Water absorption	36
3.2.15	Migration experiment	37
4	Fly ash characterization	39
4.1	Introduction	39
4.2	Bulk chemical composition	40
4.3	X-ray diffraction	41
4.3.1	Crystalline phases	41
4.3.2	Amorphous phase	44
4.4	Backscattered electron imaging	46
4.5	Energy-dispersive X-ray spectroscopy and image analysis	47
4.5.1	Point analysis and mapping	47
4.5.2	Algorithm-aided image analysis	48
4.5.3	A new approach to process the EDS full element map data	49
4.6	Detailed SEM-EDS analysis of a calcareous fly ash	50
4.7	SEM-EDS image analysis: comparison of selected fly ashes	55
4.8	Comparison of aluminosilicate glasses among the fly ashes	59
4.9	Summary of fly ash characterization	60
5	Degree of reaction of fly ash and slag in cement	63
5.1	Introduction	63
5.2	Adaptation of the SEM-EDS technique to measure fly ash reaction	64
5.3	Study on synthetic glasses	68
5.3.1	Glass synthesis and processing	68
5.3.2	Dissolution experiment	71
5.3.3	Hydration study of glass-portland composite cements	73
5.4	Quantitative analysis of glass reactivity in paste	78
5.5	The influence of chemical composition of glass	80
5.6	Summary on glass reactivity by SEM-EDS	84
5.7	Advances in XRD analysis - Practical implementation in HighScore Plus	85
5.7.1	PONKCS	86
5.7.2	Full Structure Method	88
5.7.3	Summary on PONKCS and FSM	91

6 Phase assemblage and microstructure development	93
6.1 Introduction	93
6.2 Degree of reaction of clinker	95
6.2.1 Hypothesis 1: Decreased reaction due to change in pore solution	98
6.2.2 Hypothesis 2: Decreased reaction due to refinement of the pore structure	98
6.2.3 Microstructure development	101
6.3 Phase assemblage of the composite pastes	107
6.3.1 Experimental evidence from TGA and XRD	107
6.3.2 C-S-H composition by SEM-EDS	110
6.3.3 Complete phase assemblage calculated by mass-balance and thermodynamic simulations	110
6.4 Potential for reaction with limestone	114
6.5 Microstructure property comparison	115
6.5.1 Compressive strength	115
6.5.2 Water absorption	117
6.5.3 Migration of ions through the matrix	118
6.6 Summary of hydration study and microstructure development	121
7 Conclusions and Perspectives	125
7.1 Conclusions	125
7.1.1 Fly ash characterization	125
7.1.2 Reactivity of amorphous SCMs	125
7.1.3 Impact of calcareous fly ash and slag on reaction in composite cements	126
7.1.4 Phase assemblage in composite cements	126
7.1.5 Microstructure-property comparison	127
7.2 Perspectives	127
7.2.1 Studies on multi-component cements	127
7.2.2 Use of calcareous fly ash	128
A New image analysis technique of EDS full element maps	129
A.1 Model sample	129
A.2 Microscope setup	129
A.3 Data treatment	130
A.4 Quality of the EDS data	132
A.5 Error assessment in image analysis	134
A.6 MATLAB® code used to plot the ternary frequency plot	138
B Preliminary study on a wide range of mix formulations	141
B.1 Mix formulations	141
B.2 Compressive strength of mortars	142
B.3 Hydration kinetics	145
B.4 Comparison of strength evolution and heat release	147
B.5 Selection of mix formulations for the main study of hydration	147

Contents

C Interaction CFA2 - Limestone	149
C.1 Introduction	149
C.2 Compressive strength	149
C.3 Theoretical optimal substitution	150
C.4 Real systems	151
C.5 Summary	154
D Durability	155
D.1 Introduction	155
D.2 Chloride ponding	155
D.3 Sulfate attack	158
E Thermo-gravimetric curves	163
F X-ray diffractograms	167
G SEM-EDS point analysis of C-S-H data	173
H Ion concentrations in pore solutions	177
I Mercury Intusion Porosimetry curves	179
Bibliography	193
List of publications	195
Curriculum Vitae	197

List of Figures

2.1	Residual mullite crystals from a reacted fly ash particle in a 3-year old concrete.	6
2.2	Example composition of fly ash particles measured by SEM-EDS point analysis.	7
2.3	Multispectral image analysis.	8
2.4	Grey level overlap in siliceous fly ash-cement paste.	9
2.5	Filler effect and chemical contribution shown in cumulative calorimetry curves for PC-slag blends.	11
2.6	Ternary diagrams of the chemical composition of SCMs and their hydration products.	11
2.7	Calculated phase assemblages in C ₃ A-CH system with various SO ₃ and CO ₂ contents.	13
3.1	Particle size distributions of materials used in the study.	17
3.2	SEM-BSE images of clinker and slag.	17
3.3	Effect of sample preparation on the phase assemblage measured by the XRD.	19
3.4	Isothermal calorimetry curve of hydration of portland - 45% Slag cement.	21
3.5	DTG curves of pure substances.	23
3.6	Determination of the C-S-H composition from the SEM-EDS point analysis.	28
3.7	Procedure used to segment anhydrous slag grains based on BSE grey level and EDS Mg content.	29
3.8	Threshold and critical radius in a differential and a cumulative MIP curve.	35
3.9	C-S-H and capillary porosity in a differential MIP curve of a white cement paste.	35
3.10	Experimental setup for chloride migration testing.	37
3.11	Example curve from chloride migration experiment.	38
4.1	X-ray diffractograms of - siliceous fly ashes.	42
4.2	X-ray diffractograms - calcareous fly ashes.	43
4.3	Calculated bulk chemical composition of the glass in the fly ashes studied.	45
4.4	BSE image of a polished section of an epoxy impregnated raw CFA2.	46
4.5	EDS point analysis.	47
4.6	Visual representation of the distribution of elements measured by EDS (CFA2).	48
4.7	Al-Si-Ca ternary frequency plot of CFA2 chemical composition.	51
4.8	Al-Si-Ca ternary plot showing main crystalline phases in siliceous and calcareous fly ashes.	51

List of Figures

4.9	Illustration of the segmentation thresholds of the four fly ash groups, C_3S and C_2S in the image analysis.	52
4.10	Chemistry and morphology of the fly ash populations by SEM-EDS and image analysis.	53
4.11	Al-Si-Ca ternary frequency plots of the fly ashes 1-5.	56
4.12	Al-Si-Ca ternary frequency plots of the fly ashes 6-11.	57
4.13	Quantitative comparison of the populations - siliceous fly ashes.	58
4.14	Quantitative comparison of the populations - calcareous fly ashes.	59
4.15	Comparison of the EDS chemical composition of the aluminosilicate population among the fly ashes studied.	60
4.16	Comparison of the EDS chemical composition of the Ca-rich aluminosilicate population among the calcareous fly ashes.	60
5.1	Image analysis procedure used to extract and quantify the reaction of the anhydrous fly ash components in hydrating cement paste.	65
5.2	Quantification of C_3S and C_2S by SEM-EDS and XRD in PC-CFA2.	66
5.3	Consumption of the anhydrous fly ash populations in hydrating pastes.	67
5.4	Al-Si-Ca ternary frequency plot of CFA2 with the marked compositions selected for glass synthesis.	69
5.5	Glass synthesis	70
5.6	XRD diffractograms of the synthetic glasses, slag and CFA2.	70
5.7	Particle size distributions of the synthetic glasses.	71
5.8	Results of the dissolution experiment.	72
5.9	Isothermal calorimetry curves of glass-portland pastes.	74
5.10	Illustration of the segmentation thresholds for image analysis.	75
5.11	Fitted kinetics of glass reaction in composite cements.	77
5.12	The surface to volume ratios of slag and C_3S measured by image analysis.	79
5.13	Intrinsic reactivity of fly ash populations and cement phases.	80
5.14	A comparison of the calculated intrinsic reactivity and the NBO/T.	83
5.15	The reaction of the aluminosilicate glasses from a siliceous and a calcareous fly ash in cement paste.	84
5.16	PONKCS analysis of slag cement.	87
5.17	Phase diagram showing the primary crystallization field of gehlenite and the slag composition.	87
5.18	Quantification of the degree of reaction of slag by different techniques.	88
5.19	Phase diagram showing the composition of the amorphous part of fly ash FFA8 with respect to the primary crystallization fields of anorthite and tridymite.	89
5.20	FSM analysis of a siliceous fly ash.	90
5.21	Quantification of the degree of reaction of the amorphous fraction from a siliceous fly ash by SEM and XRD.	90
5.22	PONKCS and FSM models of the amorphous part of two calcareous fly ashes.	91
5.23	Quantification of the degree of reaction of calcareous fly ash by XRD-FSM.	91

6.1 Phase composition and reaction of two selected calcareous fly ashes and the slag by SEM-EDS image analysis.	94
6.2 Degree of hydration of clinker in composite pastes.	97
6.3 Comparison of the Al concentration in pore solution and the degree of reaction of clinker silicates.	98
6.4 Total porosity: evolution in time measured by MIP.	99
6.5 Total degree of reaction of clinker and SCMs.	99
6.6 Threshold pore entry radius from MIP.	101
6.7 Capillary porosity by MIP.	101
6.8 BSE images of the development of the microstructure of hydrated pastes - 1000x.	102
6.9 BSE images of the development of the microstructure of hydrated pastes - 1000x.	103
6.10 BSE images of the microstructure of hydrated pastes - 4000x.	104
6.11 BSE images of the microstructure of hydrated pastes - 4000x.	105
6.12 Comparison of derivative MIP curves for PC-CFA1 and PC-CFA2 after 90 days of hydration.	107
6.13 Differential thermo-gravimetric curves of the pastes studied hydrated for 90 days.	108
6.14 XRD patterns of the pastes studied hydrated for 90 days.	109
6.15 Comparison of the C-S-H composition with the amounts of Al, Si, Ca available for the reaction.	111
6.16 Comparison of the phase assemblages determined by mass-balance and thermodynamic modeling with experimental data.	113
6.17 Volume of C-S-H in pastes after 90 days of hydration.	114
6.18 Calcite consumed in systems with the different SCMs studied.	115
6.19 Compressive strength of mortars vs. gel-space ratio in pastes.	116
6.20 Compressive strength of mortars vs. total porosity measured by MIP.	117
6.21 Water absorption of dried mortar cubes.	118
6.22 Water absorption vs. capillary porosity measured by MIP.	119
6.23 Current vs. time during the migration experiment.	120
6.24 Calculated formation factors.	121
A.1 Al, Si and Ca ternary plots obtained from the EDS data from the model sample.	131
A.2 Model sample: BSE image, EDS map, segmentation.	132
A.3 Bulk chemical composition quantified by XRF and EDS for CFA2.	132
A.4 SEM-EDS: The distribution of the X-ray density in the CFA2 sample modelled using Casino software.	134
A.5 The Hamming window used to smooth the EDS data.	134
A.6 The effect of the interaction volume on the SEM-EDS data presented in a ternary frequency plot.	135
A.7 An example convergence plot.	136
A.8 Particle size distributions and the range of the particle sizes assessed by the SEM-EDS technique.	137
B.1 Compressive strength of binary and ternary composite cement mortars.	143

List of Figures

B.2	Compressive strength of ternary and quaternary composite cement mortars. . .	143
B.3	The effect of substituting 10 wt.% of the clinker amount by limestone on the compressive strength of mortars	144
B.4	Derivative calorimetry curves.	145
B.5	Comparison of calorimetry curves of single and combined fly ash and slag systems.	146
B.6	Cumulative calorimetry curves showing filler effect and contribution of the reaction of the SCMs.	146
B.7	Cumulative heat vs. compressive strength.	147
C.1	Compressive strength of mortars with 45 wt.% CFA2 and increasing limestone content.	150
C.2	Thermodynamic modelling of the effect of replacing clinker with limestone in mixes with 45 wt.% CFA2.	150
C.3	Thermo-gravimetric curves showing calcite consumption and formation of significant amounts of AFm phases.	151
C.4	X-ray diffractograms.	152
C.5	Mass-balance analysis.	152
C.6	Calcite consumption quantified by XRD-Rietveld refinement.	153
C.7	BSE micrograph of PC-8L-CFA2 after 90 days of hydration.	153
D.1	Chloride ponding results.	157
D.2	Effective diffusion coefficient from ponding vs. capillary porosity from MIP. . .	158
D.3	XRD diffractograms of mortars in ponding experiment.	158
D.4	Linear expansion of mortars immersed in 3 g/L calcium sulfate solution.	160
D.5	Sulfate penetration profiles measured by SEM-EDS.	161
E.1	Differential thermo-gravimetric curves - 1/2.	164
E.2	Differential thermo-gravimetric curves - 2/2.	165
F.1	X-ray diffractograms - 1/4.	168
F.2	X-ray diffractograms - 2/4.	169
F.3	X-ray diffractograms - 3/4.	170
F.4	X-ray diffractograms - 4/4.	171
G.1	EDS point analysis data - 1/3.	174
G.2	EDS point analysis data - 2/3.	175
G.3	EDS point analysis data - 3/3.	176
H.1	Ion concentrations measured by ICP in the pore solutions obtained by high-pressure squeezing of pastes.	178
I.1	Mercury intrusion porosimetry curves - 1/3.	180
I.2	Mercury intrusion porosimetry curves - 2/3.	181
I.3	Mercury intrusion porosimetry curves - 3/3.	182

List of Tables

3.1	Oxide composition by XRF [wt.-%] and phase composition by XRD-Rietveld [wt.-%]	17
3.2	Phases and references used for quantitative Rietveld analysis.	25
3.3	Mass attenuation coefficients.	26
3.4	Polishing procedure for SEM sample preparation.	27
3.5	Composition and density of CSHQ end members for thermodynamic simulations. 33	
4.1	XRF analysis - siliceous fly ashes.	40
4.2	XRF analysis - calcareous fly ashes.	41
4.3	Composite mass attenuation coefficients - calcareous fly ashes.	41
4.4	Composite mass attenuation coefficients - siliceous fly ashes.	41
4.5	XRD-Rietveld phase analysis - siliceous fly ashes	43
4.6	XRD-Rietveld phase analysis - calcareous fly ashes.	44
4.7	Segmentation thresholds in the image analysis.	52
4.8	Mean chemical composition determined by SEM-EDS for the four populations identified in CFA2.	54
5.1	The targeted and obtained chemical composition of the model glasses.	69
5.2	Initial dissolution rates calculated from the batch dissolution experiment. . . .	73
5.3	Mix proportions of glass-portland composite cements.	74
5.4	Segmentation thresholds for image analysis.	75
5.5	NBO/T of the fly ash populations, the synthetic glasses and the slag.	82
6.1	Mix formulations of the hydration study.	95
6.2	Amounts of main oxides reacted after 90 days of hydration in the pastes studied. 112	
6.3	Equivalent conductivity λ_i^0 and coefficient G_i used for the calculation of the conductivity of the pore solutions.	120
A.1	XRF analysis of the materials used for the model sample for SEM-EDS analysis. 130	
A.2	Quantification of the volume fractions in the model sample.	131
B.1	Mix formulations of the preliminary study.	141
D.1	Effective diffusion coefficients from ponding experiment.	157

Glossary

Cement notation of oxide compounds:

C: CaO S: SiO₂ A: Al₂O₃ M: MgO F: Fe₂O₃ \$: SO₃ c: CO₂ H: H₂O

Notation of the main anhydrous and hydrated phases:

C ₃ S	3CaO·SiO ₂	Tricalcium silicate (Alite)
C ₂ S	2CaO·SiO ₂	Dicalcium silicate (Belite)
C ₃ A	3CaO·Al ₂ O ₃	Tricalcium aluminate
C ₄ AF	4CaO·Al ₂ O ₃ ·Fe ₂ O ₃	Ferrite
Cc	CaCO ₃	Calcite
CH	Ca(OH) ₂	Calcium hydroxide (Portlandite)
C-S-H	CaO-SiO ₂ -H ₂ O	Calcium silicate hydrate
C ₃ A·3C\$·H ₃₂	3CaO·Al ₂ O ₃ ·3CaSO ₄ ·32H ₂ O	Ettringite (Ett)
C ₃ A·C\$·H ₁₂	3CaO·Al ₂ O ₃ ·CaSO ₄ ·12H ₂ O	Monosulfate (Ms)
C ₃ A·Cc _{0.5} ·H ₁₂	3CaO·Al ₂ O ₃ ·0.5CaCO ₃ ·12H ₂ O	Hemicarbonate (Hc)
C ₃ A·Cc·H ₁₁	3CaO·Al ₂ O ₃ ·CaCO ₃ ·11H ₂ O	Monocarbonate (Mc)
C ₃ A·CaCl ₂ ·H ₁₁	3CaO·Al ₂ O ₃ ·CaCl ₂ ·10H ₂ O	Friedel's salt
C ₂ ASH ₈	2CaO·Al ₂ O ₃ ·SiO ₂ ·8H ₂ O	Strätlingite
C ₃ (A,F)H ₆	3CaO·(Al ₂ O ₃ , Fe ₂ O ₃)·6H ₂ O	Hydrogarnet
M ₄ A	Mg ₄ Al ₂ (OH) ₁₄	Hydrotalcite

Materials:

PC	Portland cement
SCM	Supplementary Cementitious Materials
CFA	Calcareous fly ash
FFA	Siliceous fly ash
S	Slag
L	Limestone
G	Gypsum

Glossary

Techniques:

BSE	BackScattered Electron
EDS	Energy-Dispersive x-ray Spectroscopy
GEMS / TS	Thermodynamic Simulation
IA	Image Analysis
MIP	Mercury Intrusion Porosimetry
PSD	Particle Size Distribution
SEM	Scanning Electron Microscopy
TGA	Thermo-Gravimetric Analysis
XRD	X-Ray Diffraction
XRF	X-Ray Fluorescence

Others:

w/b	Water to binder ratio
wt.%	Weight percent
vol.%	Volume percent

1 Introduction

Concrete is the only material with the potential to satisfy the growing needs of humanity for construction. It is cheap, environmentally-friendly and durable. It offers good performance, can be designed according to different requirements and above all, it is based on raw materials abundant all around the globe. Current production of concrete in the world is estimated at 20 - 37 Gt per year [1] and the demand is forecast to rise strongly in the coming decades. Because of these great quantities, a relatively low-environmental-impact material contributes up to 5% of man-made CO₂ emissions [2]. An important motivation for cement science is that a little reduction of CO₂ emissions achieved per kilogram of cement can lead to significant reductions on the industrial scale.

To make concrete, cement is needed. Most of the CO₂ emissions and cost in cement production are linked to the manufacture and handling of cement clinker. The main reaction of thermal decomposition of limestone is achieved in a cement kiln at around 1450 °C. This process itself is highly optimised but requires a lot of energy and releases around 0.9 ton of CO₂ per 1 ton of clinker due to the stoichiometry of the reaction. We have no influence on the stoichiometry but we can use less cement clinker in concrete. Indeed, replacing part of the Portland clinker is a highly efficient way to reduce the CO₂ emissions. Clinker can be replaced with less reactive mineral components, so called supplementary cementitious materials (SCMs). SCMs, which are usually industrial wastes or by-products, obviously differ in behaviour from the Portland clinker but under certain conditions can hydrate and transform into valuable binders with useful properties. The use of SCMs such as siliceous fly ashes from coal-powered power stations or ground granulated blast furnace slags has successfully become an everyday practice in cement production, with established standards and guidelines. The development of properties and microstructure in composite cements has been a subject of considerable research over the past decades.

To cater for the increasing cement demand it is desirable to raise clinker substitution levels. High clinker replacements up to 95 wt.% (CEM III/C) [3] are well established for slag cements, but due to globally decreasing raw steel production slag reserves are shortening. Slag production is less than 10% of that of clinker. In contrast, fly ashes are widely available. Around

Chapter 1. Introduction

670 Mt [4] are produced every year, but only around 30 wt.% of that [4] is used in concrete. This is because fly ashes are inherently very heterogeneous and variable. The properties of fly ash are easily affected by the coal type, combustion temperature, processing, and other factors [5, 6, 7, 8]. Fly ash is a by-product, whose quality is not specified, often low and variable. Because of that, many fly ashes are discarded out of hand. In an attempt to categorise fly ashes, standards such as EN 197-1 [3] and ASTM C618 [9] divide them by their bulk chemical composition, which is usually the only readily available data for characterization. The EN standard distinguishes siliceous ($\text{CaO}_{\text{reactive}} < 10 \text{ wt.}\%$) and calcareous ($\text{CaO}_{\text{reactive}} > 10 \text{ wt.}\%$) fly ashes, the ASTM divides them into class F ($\text{SiO}_2 + \text{Al}_2\text{O}_3 + \text{Fe}_2\text{O}_3 > 70 \text{ wt.}\%$) and C ($\text{SiO}_2 + \text{Al}_2\text{O}_3 + \text{Fe}_2\text{O}_3 > 50 \text{ wt.}\%$). Most of the fly ashes in use are the less variable and less heterogeneous but also less reactive siliceous fly ashes. Due to the slow reaction and thus retarded strength development the clinker replacement with siliceous fly ashes is stipulated to around 35 wt.% (CEM II/B) [3]. Higher levels of replacement seem unattainable without additional processing or activation. The calcareous fly ashes are typically more reactive and could be used directly at higher replacements, which is of large interest to the industry. However, these ashes can be significantly more unpredictable, uncontrollable, variable and heterogeneous. These fly ashes are less commonly used and consequently have not been researched much. Calcareous fly ashes are considerably more difficult to characterize and remain poorly understood. A contributing factor is the lack of appropriate techniques for the characterization of raw fly ashes and for the measurement of their reaction in hydrated composite cement.

If the use of fly ash in concrete could be increased by 10% this would mean that each year around 67 000 000 tonnes of fly ash would not need to be stockpiled but could rather contribute to a very significant reduction of the CO_2 emissions coming from the production of cement clinker. Development of a suitable characterization technique is essential, which could provide a tool for identification of potentially useful fly ashes and for a deliberate investigation that links properties of fly ash cements with the detailed composition of this material. Given the higher reactivity of calcareous fly ashes compared to the siliceous ones, a successful classification and selection could raise confidence in this material and lead to an increase in the substitution of cement clinker by calcareous fly ash allowed by the international and local standards.

This work presents a fundamental approach to understand the role of calcareous fly ashes in composite cements. It is organised in the following order:

Chapter 2 reviews the current state of the art.

Chapter 3 presents the materials and methods.

Chapter 4 introduces the complexity of the fly ash microstructure and composition. Different techniques are used to characterize the selected fly ashes. We present a new SEM-EDS data treatment that provides a detailed and quantitative description of the fractionated chemical composition of fly ash glass, so far very poorly known. Fly ash is an assemblage of glasses and similarities between fly ash and slag glass are shown.

In **chapter 5** the EDS technique is further developed to study the reaction of individual glasses in cement. Advanced XRD refinement was developed to track the hydration of glassy part and compare with the EDS results. As fly ash composite cements are very complex, more fundamental insights on glass dissolution and reaction are given in a study of model simplified glasses synthesised to match those in fly ash. Quantitative analysis of the reaction showed a clear trend to higher reactivity with increasing glass structure disorder.

Chapter 6 presents a hydration study of selected fly ashes using XRD Rietveld refinement, thermo-gravimetric analysis and SEM-EDS combined in a mass-balance approach. Comparison with thermodynamic simulations is made. We show that the phase assemblage is related to the fly ash initial composition and hydration kinetics. These factors affect the microstructure development, densification of the matrix and its permeability.

Chapter 7 summarizes the work, presents conclusions and gives perspectives for further research.

At the beginning of the study we chose two calcareous fly ashes of different chemical composition. We investigated the evolution of the compressive strength of binary, ternary and quaternary mixes containing portland cement, calcareous fly ash, slag and limestone. From the initial wide spectrum of mix compositions the most interesting were chosen for hydration study, microstructure investigation and durability experiments. To gain a more fundamental understanding of the systems we decided to improve our knowledge on the calcareous fly ash itself. We studied the ashes using SEM-EDS and we developed a new image analysis technique to assess the fractionated composition of the fly ash glass. This technique was further improved to track the reactivity of individual fly ash glasses in a hydrating cement paste. Later on, we decided to expand the scope of fly ashes studied to test the capacities of the new technique and to identify the most common types of glasses and their hydration.

2 Literature review

Contents

2.1 Fly ash	5
2.1.1 Characterization	6
2.1.2 Measuring the degree of reaction	8
2.2 Hydration of portland cement	9
2.3 Composite cements containing fly ash, slag and limestone	10
2.3.1 Hydration and phase assemblage	10
2.3.2 Limestone in composite cements	12
2.3.3 Microstructure, strength and permeability	14
2.3.4 Key questions	14

2.1 Fly ash

Fly ashes are a by-product of coal combustion in power plants. During the combustion of carbon, inorganic impurities contained in the coal such as clays, feldspars, shale and quartz are melted and part of this incombustible material is carried in the gas stream which moves towards the chimney. The melt droplets solidify mainly as amorphous spheres and are captured by filters. The crystalline part includes those original phases that did not melt and the phases that crystallized from the glass melt. Remnants of quartz are common in the ash in their original unaltered state, for example. Crystallization of mullite is possible inside of large spheres that do not cool rapidly and uniformly. One example of mullite crystals in a fly ash particle is shown in Figure 2.1.

The reactivity of fly ash in cement depends on its phase composition and particle morphology. However, there is no simple relationship between the chemical composition of a fly ash and the phases present in it. The combustion conditions and the proportion of minerals in the source coal are the major factors, which are subject to significant fluctuations and contribute greatly to the inherent heterogeneity and variability of fly ashes.

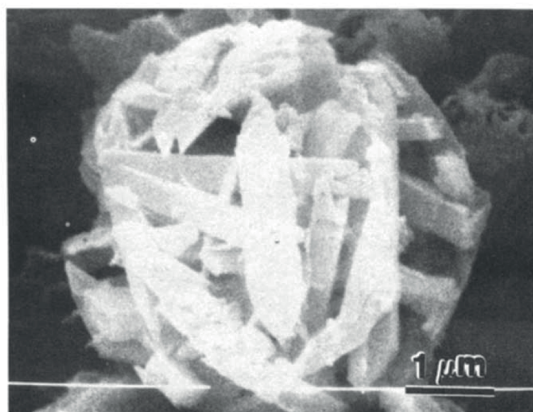


Figure 2.1: Residual mullite crystals from a reacted fly ash particle in a 3-year old concrete [15].

Among the crystalline phases present in fly ashes many are not reactive in cement. These include quartz and mullite at room temperature, hematite, magnetite and the crystalline phases present in ashes richer in Ca, such as gehlenite C_2AS , anorthite CAS_2 and akermanite C_2MS_2 . In Ca-rich ashes reactive crystalline phases are possible, which include C_3A , ye'elimite C_4A_3S , anhydrite $C\$$ and free lime.

Typically, 50 to more than 90 wt.% [10, 7] of fly ash is amorphous and this is important for the reactivity. Due to high Al and Si and low Ca, siliceous fly ashes contain principally aluminosilicate glass, of rather slow reaction. In calcareous ashes the glass is different and an analogy to slag glass was suggested based on the position of the XRD diffuse scattering 'hump' [11]. More Ca could explain the increased reactivity and the clear trend to higher strength with higher calcium content in data published by Mehta [12]. However, the glass in fly ashes is not homogeneous but a complex mixture of compositions [13, 14] and each of them could be reacting differently.

2.1.1 Characterization

The key to understand the reactivity of fly ashes lies in improved materials characterization. The main difficulty here is due to the extreme heterogeneity of fly ash particles and the huge number of possible glass compositions.

More effective tools to characterise fly ash are much needed. Nevertheless, typically the only data easily available for classification is bulk chemical composition by XRF. XRD-Rietveld refinement can quantify the crystalline phases [16], but fails to distinguish between the amorphous fly ash components. Electron microscopy WDS (wavelength-dispersive X-ray spectroscopy) or EDS (energy-dispersive X-ray spectroscopy) is the most common approach to study fly ash glass and analyse the chemical composition of different particles [14, 17, 18, 19, 20, 21, 22, 23, 24]. In manual mode the operator selects points for examination. Figure 2.2 is an example of published data showing SEM-EDS point analysis on several fly ashes carried out by

Dhole et al. [18]. Scatter in these results is primarily related to the great inherent heterogeneity of fly ash particles. It becomes clear that a significantly larger amount of data would be needed to representatively quantify the glasses in fly ashes.

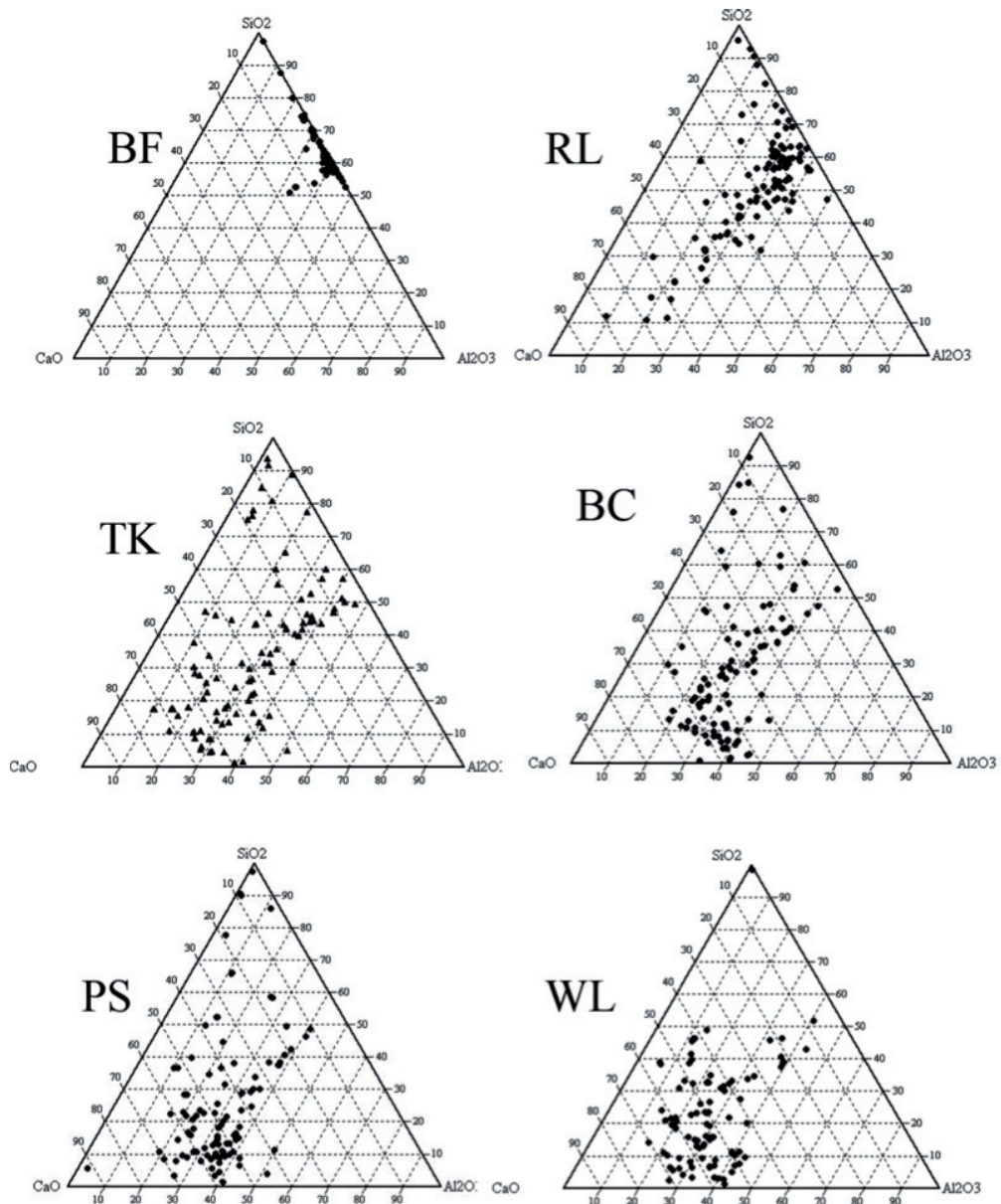


Figure 2.2: Example composition of fly ash particles measured by SEM-EDS point analysis [18].

A new approach to SEM-EDS image analysis was described by Lydon [25] for measurement of modal mineralogy of rocks and was later adapted by Chancey [26] for characterization of siliceous fly ashes. Fast, new generation EDS detectors can collect a spectrum for every pixel of the frame within an hour. The spectra are then processed into a set of element intensity maps such as in Figure 2.3a and analysed using MultiSpec® [27], a multispectral image data analysis

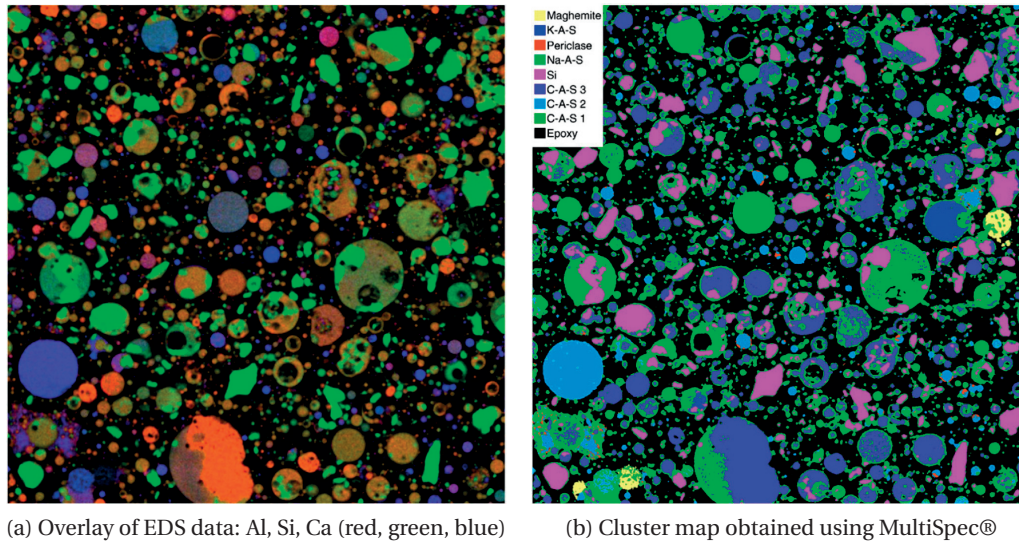


Figure 2.3: Multispectral image analysis after [26].

software, in which a clustering algorithm is used to identify and quantify groups of mutually exclusive chemical compositions. The display of a segmented image such as in Figure 2.3b allows insight into microstructure, notably location of phases and intermixing. The analysis can treat large amounts of data but is entirely based on the segmentation algorithm, which limits control over the analysis and may have unexpected influence on the results.

2.1.2 Measuring the degree of reaction

A reliable quantification of the degree of reaction of fly ash in a hydrated cement paste is difficult. The most commonly used indirect methods are the measurement of the amount of portlandite and non-evaporable water [28, 29, 30, 31, 32]. Using these methods the differentiation between the reaction of fly ash and portland clinker requires a comparison with a reference in which fly ash is replaced by an appropriate inert filler. Indeed, the anhydrous fly ash is quantified only indirectly, which means that changes in the type and amount of hydrates may greatly affect the results. Therefore, other methods were sought to measure the amount of unreacted fly ash directly. Selective dissolution [31, 32, 33, 34] is meant to eliminate the hydration products and leave the anhydrous part for quantification. However, studies show that a significant fraction of the fly ash may be dissolved, while some hydrates remain [35]. Reactivity tests in highly diluted solutions provide a more theoretical approach, but were argued not to address the fly ash reactivity in cement adequately as they are carried out outside of paste [14]. Backscattered electron image analysis (BSE-IA) can determine the degree of reaction of plain portland clinkers [36, 37, 38, 39, 40] and was further developed to tackle blended cements [35, 41, 42]. In BSE images, the grey level is a function of element composition [40] and different peaks in a grey level histogram can basically be attributed to different phases, separated and quantified. However, fly ash often contains several different glasses

with different grey levels that may overlap with those of clinker phases, slag [41], C-(A)-S-H or portlandite [35]. An example of such overlap for a siliceous fly ash is presented in Figure 2.4. To extract the fly ash particles in image analysis additional filters may be required [35, 42]. An accurate separation and quantification of fly ash is difficult and sometimes impossible, especially for the more complex, calcareous fly ashes.

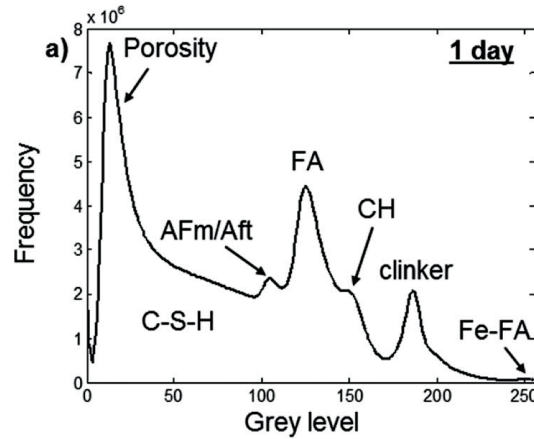


Figure 2.4: Grey level overlap in siliceous fly ash-cement paste [42].

For the time being, the most reliable estimation of fly ash reaction is obtained by combining SEM image analysis data with other techniques. However, given the limited accuracy of the aforementioned methods, fly ash can only be treated as a whole and resolution of individual glasses is the next main obstacle to be overcome.

2.2 Hydration of portland cement

Upon contact with water, cement undergoes hydration and transforms into a hardened binder. The main reactive phases of portland clinker are C_3S , C_2S , C_3A , and C_4AF . The hydration reactions are complex and dependent on system composition, which is why simplified equations are used to illustrate the processes.

Alite, impure C_3S is the dominant phase and reacts with water to give calcium silicate hydrate (C-S-H) and calcium hydroxide:



Belite, C_2S hydrates similarly to alite but slower:



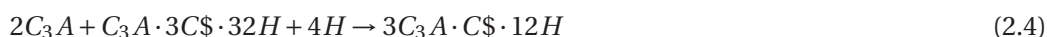
C-S-H is the principal binding phase in portland cements. The stoichiometry of C-S-H in cement paste is variable and the state of chemically and physically bound water in its structure is ill defined, which is why a hyphenated notation is used. Recent studies by Muller et al. [43]

show that the amount of water in the C-S-H can be measured by ^1H NMR relaxometry and a stoichiometry $\text{C}_{1.7}\text{SH}_4$ was found for white cement studied.

Gypsum controls the aluminate reaction by forming ettringite (AFt):



Once gypsum is depleted, the remainder of the aluminates will react with ettringite to mono-sulfate, which is one of the AFm phases:



More detailed description of cement hydration can be found in the book of Taylor [44].

2.3 Composite cements containing fly ash, slag and limestone

While the influence of slag and siliceous fly ash on the hydration, the microstructure development and the mechanical properties of blended cements has been a subject of research over the past years [45, 46, 47, 48, 49], calcareous fly ashes remain ill studied. Little is published on their characteristics, reactivity, hydration mechanisms, microstructural development, interactions with other SCMs and influence on the overall binder performance. Due to the inability to resolve the reaction of individual fly ash glasses little is known about what types of glasses constitute any fly ash and, further, how these glasses react in cement.

2.3.1 Hydration and phase assemblage

The effects of blending PC with slag or fly ash mainly concern:

- the hydration kinetics,
- the phase assemblage.

The effect of adding SCMs on clinker hydration kinetics is mainly physical. Due to the dilution of the clinker phases there is more water per unit of clinker and more space for its hydration products. These interactions also known as "filler effect" can be seen in the calorimetry curves in Figure 2.5. Due to the filler effect the reaction of clinker is enhanced, but the enhancement cannot fully compensate for the dilution.

The main effect of fly ash and slag on the phase assemblage is because they provide less Ca and more Al and Si to the reaction than the clinker. This affects the type and amount of phases formed. Figure 2.6 illustrates these dependencies. The range of chemical compositions possible in siliceous and calcareous fly ashes presented in Figure 2.6a will be compared to the findings of the characterization part of this thesis.

2.3. Composite cements containing fly ash, slag and limestone

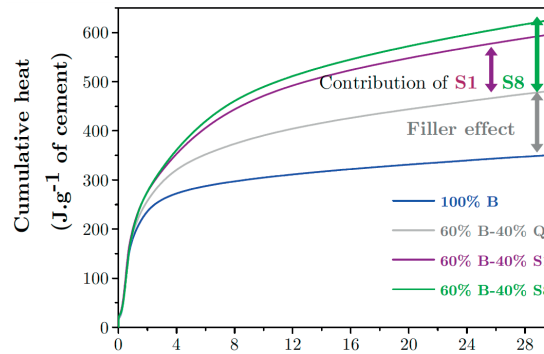


Figure 2.5: Filler effect and chemical contribution shown in cumulative calorimetry curves for PC-slag blends [50].

The pozzolanic reaction of fly ashes requires high pH to initiate and sustain the glass dissolution and a source of calcium to precipitate with the dissolved Al and Si. Clinker hydration provides both the alkalinity and the Ca. Slags and potentially some calcareous fly ashes too already contain Ca and do not require an additional supply. In composite cements less clinker is present, which is responsible for lower amounts of portlandite present and for the formation of C-S-H of lower Ca/Si ratio, about 1.5 [51]. A C-S-H of a lower Ca/Si ratio has higher capacity to incorporate Al [52]. SCM cement blends contain more alumina, which in presence of sufficient Ca increases the quantities of ettringite and AFm phases formed. Whether the dominant type of the AFm phase is monosulfate, hemicarboxylate or monocarboxylate will depend on the availability of sulfate, carbonate, Al and Ca.

It is difficult to precisely determine and quantify the phase assemblage in fly ash composite cements. The theoretical phase assemblage can be modelled thermodynamically using GEMS geochemical software (gems.web.psi.ch, accessed May 2015) [53, 54] with PSI-GEMS thermodynamic database for aqueous species and solids [55] and a cement specific CEMDATA14

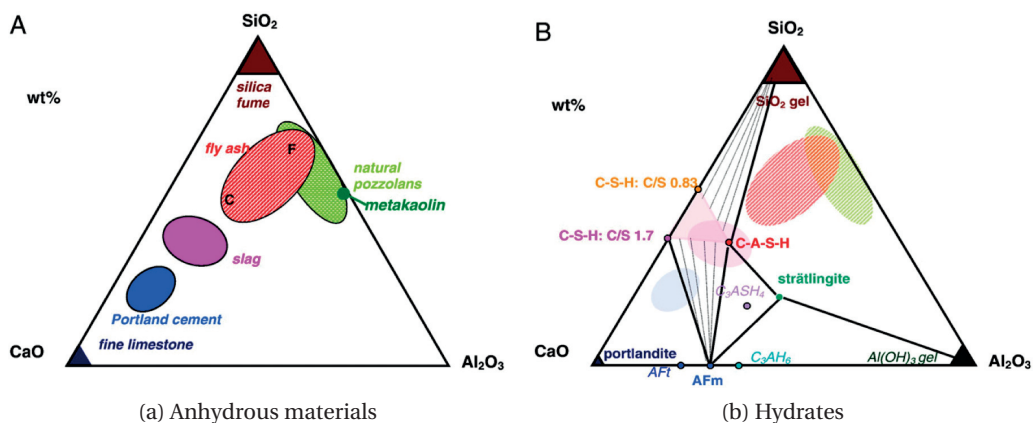


Figure 2.6: Ternary diagrams of the chemical composition of SCMs and their hydration products [51].

database from EMPA [56, 57]. The predicted phase assemblage shows the most stable phase configuration assuming ideal homogenization and complete reaction of all input components. These results differ necessarily from the phase assemblage in real systems due to kinetic and physical constraints and the discrepancies tend to increase with decreasing water/binder ratio of the modelled paste. Thermodynamic modelling of composite cements containing slag and siliceous fly ash can be found in [51, 58].

The measurement of the experimental phase assemblages requires several techniques. The anhydrous clinker phases and other crystalline components can be identified and quantified using XRD-Rietveld refinement [59]. Among the hydration products often only portlandite and ettringite are fully crystalline. The AFm phases may be poorly or non-crystalline and the C-S-H is an amorphous gel, which excludes their identification and quantification by XRD. One way to assess the phase assemblage is mass-balance analysis. In mass-balance the amounts of elements available for the reaction, which are known from the degree of reaction of clinker by XRD and its composition by XRF or EDS, are distributed among the quantified hydration products and those identified in the system but not quantifiable, such as the AFm phases. The composition of the C-S-H can be based on published data or measured by SEM-EDS point analysis.

An important input for the thermodynamic modelling and for the mass-balance is the degree of reaction of the SCMs. The reaction of slag can be measured by SEM-image analysis and assuming congruent dissolution rather reliable amounts of dissolved elements can be obtained. For fly ashes it is much more difficult to measure the degree of reaction and due to the multiple glasses possible in fly ash composition the assumption of a congruent reaction may be less justifiable. Resolution of the reaction of individual fly ash glasses is expected to improve the determinations of the phase assemblage in fly ash-cement pastes.

2.3.2 Limestone in composite cements

Limestone, if locally available for cement production, can be used as an SCM. Introducing limestone into PC dilutes the clinker and has a "filler effect" on its reaction similarly to the effect of the other SCMs. More specific alterations are observed in the paste phase assemblage. Thermodynamic modeling by Matschei *et al.* [60] in Figure 2.7 shows the effect of the increasing amounts of carbonate on the phases formed assuming excess of Ca. The carbonates react with monosulfate to hemicarbonates and then to monocarbonates, while the released sulphate is bound in ettringite. These reactions require a source of Ca and Al and if enough Ca is present the kind of products formed depends on ratios between CO_2 , Al_2O_3 and SO_3 . Carbonate-AFm phases are desirable in paste phase assemblage due to their strong stability and because their presence avoids the decomposition of ettringite after all sulfate has been consumed. Compared to sulfate- and hydroxide-AFm phases, carbonate-AFm + ettringite bind more water per unit clinker used and thus give higher compressive strength.

2.3. Composite cements containing fly ash, slag and limestone

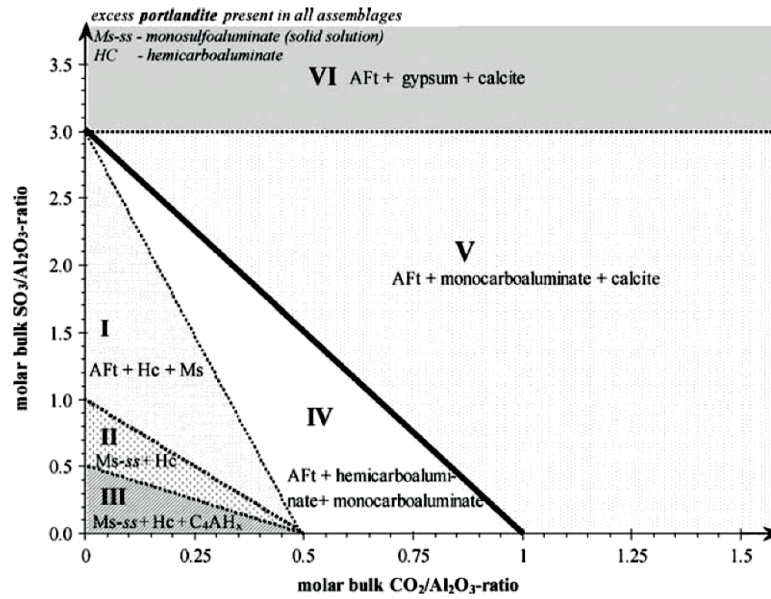


Figure 2.7: Calculated phase assemblages in C_3A -CH system with various SO_3 and CO_2 contents [60].

The optimum amount of limestone replacing portland clinker depends on the maximum amount of limestone that can react in a given system, as the rest will act as a filler. The theoretical amount of limestone consumption can be calculated by thermodynamic modeling and depends on the ratio between CO_2 , Al_2O_3 and SO_3 . In portland cements the first limiting factor is the alumina content. The maximum amount of limestone reacted in PC is quickly reached as much more Al is required than CO_2 to form the hemicarbonate and the monocarbonate. More alumina can be supplied to the system by Al-rich SCMs, in particular fly ashes, which could increase the amount of limestone reacted [61].

Thermodynamic simulations can calculate the theoretical optimum limestone addition but do not take into account the kinetic and the transport constraints of the real systems. Limestone dissolution proceeds more slowly than that of the clinker phases and high pH can further retard it [57, 62]. High initial sulfate content in the pore solution due to the rapid dissolution of sulfates may also be a retarding factor. As the cement hydration proceeds the microstructure is filled with the hydration products. With less and less water available for the dissolution and space available for the transport of ions and precipitation of products, the actual amount of limestone reacted may be lower than theoretical.

Further description of the influence of limestone on portland cement can be found in [45, 63, 64, 65, 66, 67]. Some, mainly mechanical, properties of composite cements containing limestone in combination with slag and siliceous fly ash were presented in [61, 68, 69, 70]. These published data show potential for benefits from interactions between limestone and Al-rich SCMs, but many aspects still need more investigation. In particular, the interaction between limestone and calcareous fly ashes remains largely unexplored.

2.3.3 Microstructure, strength and permeability

Partial replacement of portland clinker with slag and fly ash has an influence on the matrix development and the properties of a hardened binder. Because the reaction of slags and fly ashes is slower than that of cement, the early strength of blended cements is decreased. In the long term, if moisture is available, hydrates continue to form and densify the matrix by filling the voids. SCMs do not decrease the total porosity of a hardened cement paste but rather refine the pore size distribution [71, 72]. The refinement of the pore structure has an important impact on the permeability of composite cements and is one of the mechanisms improving the durability of these binders.

2.3.4 Key questions

The key questions in this study are therefore:

- What is the exact composition and reactivity of calcareous fly ashes?
- What is the impact of calcareous fly ash on the reaction of clinker?
- Is there an interaction between calcareous fly ash and other SCMs such as slag and limestone? What does it depend on?
- What is the phase assemblage in multi-component cements? Which phases are formed and in what quantities? Can the phase assemblage be entirely and accurately determined and how does modeling relate to experiment?
- How does the matrix densification progress in the presence of different calcareous fly ashes?
- What are the key factors affecting strength and permeability of multi-component cements?

3 Materials and Methods

Contents

3.1 Materials	16
3.1.1 Overview	16
3.1.2 Principal materials	16
3.1.3 Fly ashes and synthetic glasses	18
3.2 Methods	18
3.2.1 Preparation of paste samples	18
3.2.2 Isothermal calorimetry	20
3.2.3 Particle size distribution (PSD)	21
3.2.4 Bulk chemical composition by X-ray fluorescence (XRF)	22
3.2.5 Thermo-gravimetric analysis (TGA)	22
3.2.6 X-ray powder diffraction (XRD)	23
3.2.7 Scanning electron microscopy (SEM)	26
Measurement of the composition of C-S-H by SEM-EDS	27
Measurement of the degree of reaction of slag by image analysis	28
3.2.8 Mass-balance calculations	30
3.2.9 Thermodynamic modelling	32
3.2.10 Pore solution analysis	33
3.2.11 Mercury intrusion porosimetry (MIP)	34
3.2.12 Preparation of mortar samples	35
3.2.13 Compressive strength	36
3.2.14 Water absorption	36
3.2.15 Migration experiment	37

3.1 Materials

3.1.1 Overview

All of the materials used in this PhD thesis are presented in this section. The principal materials were:

- Portland cement (PC)
- Slag (S1)
- Two calcareous fly ashes (CFA1 and CFA2)
- Limestone (L)
- Gypsum
- Inert quartz (Q)

Because the fly ash characterization was one of the main interests of this thesis, we broadened the scope of the investigated ashes to a total of:

- seven calcareous fly ashes; CFA: 1, 2, 3, 4-1, 4-2, 5, and 6
- five siliceous fly ashes; FFA: 7, 8, 9, 10, 11

In this thesis four new glasses were synthesised to simulate a calcareous fly ash and investigate its reactivity:

- A - predominantly silicate
- B - predominantly Ca-silicate
- C - predominantly Al-silicate
- D - Ca-rich Al-silicate

3.1.2 Principal materials

The principal materials were ground to around 4200 cm²/g Blaine. Gypsum was ground finer, to around 7000 cm²/g Blaine. Particle size distributions were measured by laser diffraction using Malvern MasterSizer S; the powders were dispersed in isopropanol using an ultrasonic bath (Figure A.8). The bulk chemical composition of the raw materials was analysed by X-ray fluorescence (XRF) and their phase composition by X-ray powder diffraction with Rietveld refinement and rutile external standard. The results for PC, CFA1, CFA2 and Slag are presented in Table 3.1. Limestone contained 99 wt.% calcium carbonate and 1 wt.% quartz. The gypsum contained 6 wt.% dolomite CaMg(CO₃)₂. Quartz contained a minor impurity of 0.5 wt.% nepheline KAlSiO₄.

Scanning electron microscope backscatter electron images (SEM-BSE) of anhydrous clinker and slag are shown in Figure 3.2. Such images show atomic number contrast where high average atomic number phases appear brighter due to higher scattering of incident electrons. Clinker grains are often multi-phase. Slag is a homogeneous material.

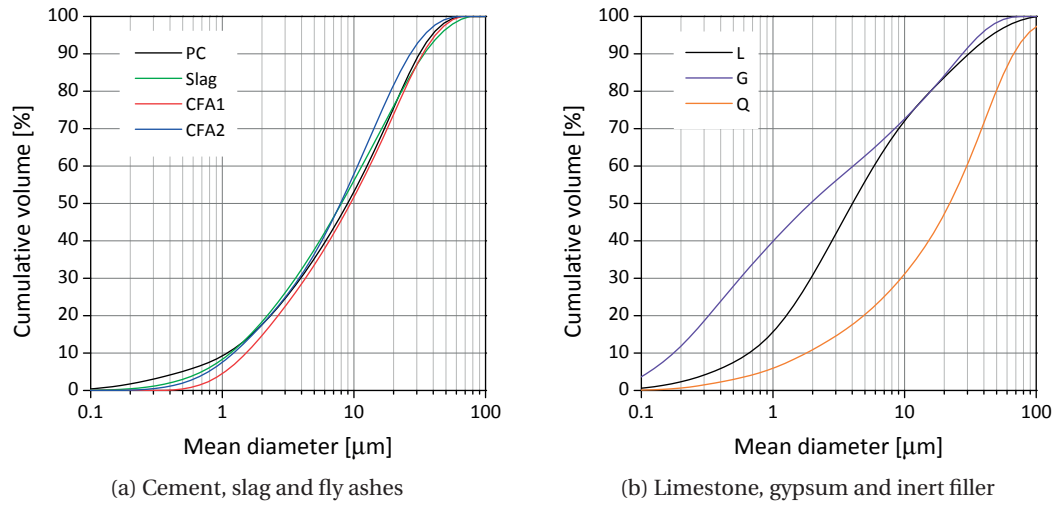


Figure 3.1: Particle size distributions of materials used in the study.

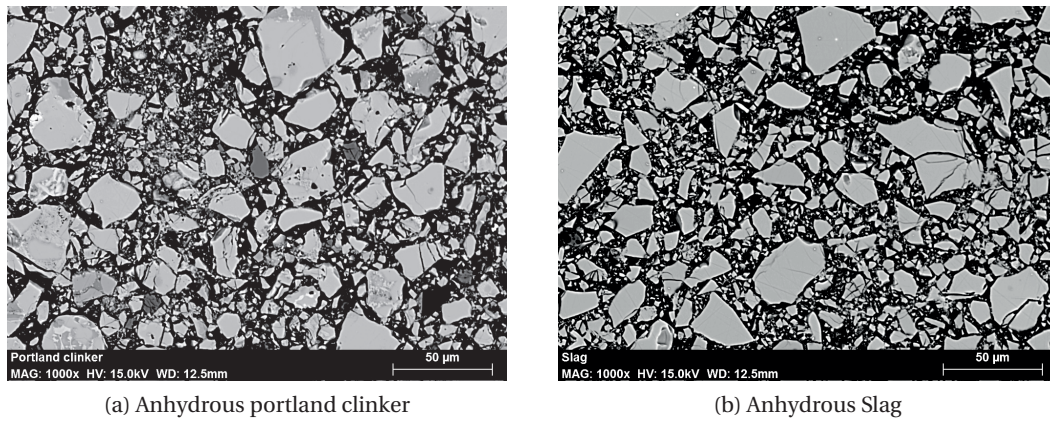


Figure 3.2: SEM-BSE images

Table 3.1: Oxide composition by XRF [wt.-%] and phase composition by XRD-Rietveld [wt.-%]

	PC	CFA1	CFA2	Slag		PC	CFA1	CFA2	Slag
Al ₂ O ₃	5.5	19.8	18.2	11.6	C ₃ S	66.3	-	-	-
SiO ₂	20.7	42.3	33.6	36.7	C ₂ S	8.3	2.5	0.5	-
CaO	65.7	20.7	26.5	38.9	C ₄ AF	8.7	2.0	1.5	-
Na ₂ O	0.2	0.3	1.9	0.2	C ₃ A	7.7	1.0	4.0	-
K ₂ O	0.4	1.5	0.4	0.7	Quartz	0.5	1.3	3.5	-
MgO	1.5	2.2	6.4	7.8	Dolomite	1.1	-	-	-
Fe ₂ O ₃	2.7	8.2	6.4	0.5	Calcite	1.8	-	-	-
SO ₃	2.6	1.4	2.2	2.8	Periclase	-	-	2.0	-
TiO ₂	0.3	0.7	1.3	0.9	Gypsum	2.6	-	-	-
P ₂ O ₅	0.2	0.3	0.9	-	Anhydrite	3.0	1.8	2.0	-
					Free lime	-	1.7	0.6	-
Sum	99.8	97.2	97.7	100.0	Amorphous	-	89.7	85.9	100.0

3.1.3 Fly ashes and synthetic glasses

Detailed characterization of fly ashes is difficult and was an object of extensive study during this thesis. The chemical and phase composition of all the fly ashes studied together with a new SEM-EDS characterization technique exceed the scope of this section and are described in detail in Chapter 4. The particle size distribution curves of the fly ashes are shown in Figure A.8a and b.

During the development of the new SEM-EDS technique it had to be validated (Appendix A.1). For this purpose we used 3 homogeneous glassy materials: Slag S1, Slag S2 and a synthetic glass G. The chemical composition of these materials is given in Table A.1 and particle size distribution is presented in Figure A.8c.

The glasses synthesised in this thesis had compositions matching those of the glasses in a real calcareous fly ash. Detailed description of the approach, the preparation, and the target and obtained chemical composition of these glasses is presented in Chapter 5. These synthetic glasses were processed in two ways to obtain:

- coarse particles (50-125 μm) for batch dissolution experiments,
- particles of size distribution similar to the fly ash for hydration study in cement paste. Details on the processing and fineness of these glasses are given in Chapter 5.

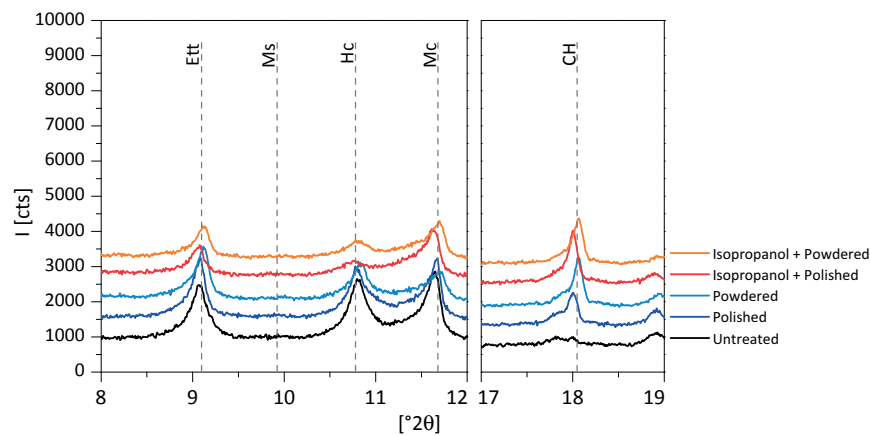
3.2 Methods

3.2.1 Preparation of paste samples

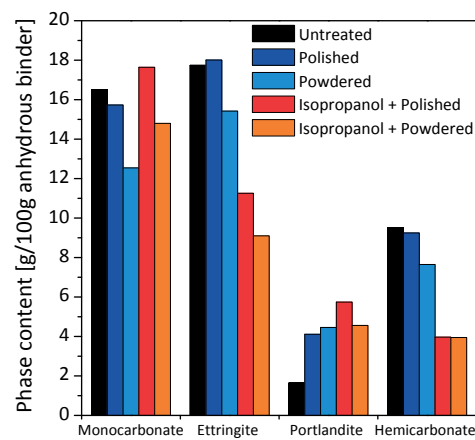
Paste samples were prepared at a water/binder ratio of 0.4. For each sample, 80 g of powder was mixed with water in a 200 mL plastic cup for 2 minutes using a laboratory mixer at 1600 rpm. The pastes were cast into cylindrical polyethylene containers, sealed and stored at 20 °C in a temperature-controlled room for curing. Testing was carried out after 1, 7, 28, 56, 90 and 365 days of hydration. At the designated times, discs were cut from the samples and immersed into isopropanol to stop hydration by solvent exchange. To ensure that hydration stoppage was effective, 1-2 discs of around 2 mm thickness were immersed in 200 mL of isopropanol. The isopropanol was replaced twice, after 1 day and after 3 days. The storage in isopropanol lasted 7 days. The disks were then dried and stored in a desiccator with silica gel beads and under vacuum for another 7 days to evaporate the isopropanol. Solvent exchange is significantly less destructive to microstructure than other methods of stopping hydration, especially oven drying or freeze drying. Nevertheless, stopping hydration with isopropanol and vacuum has an important effect on phase assemblage and pore structure. Assessment of the damage induced by isopropanol, vacuum and grinding is shown in Figure 3.3. It is based on the diffractograms and the XRD-Rietveld quantification of the hydrate phases in a sample processed in five ways:

- untreated - a disc cut from a paste cylinder and delicately dried with paper,

- polished - by hand on 1200 grade sandpaper with a drop of water until flat and smooth,
- powdered - hand ground to a fine powder,
- isopropanol + polished - polished, rinsed, immersed in isopropanol for 7 days and stored in vacuum for 7 days,
- isopropanol + powdered - immersed in isopropanol for 7 days and stored in vacuum for 7 days, then hand ground to a fine powder.



(a) Diffractograms



(b) Rietveld quantification

Figure 3.3: Effect of sample preparation on the phase assemblage measured by the XRD. Presented sample: 45 wt.% PC + 45 wt.% CFA2 + 10 wt.% limestone, w/b = 0.4, hydrated for 28 days.

The untreated sample appears to contain less portlandite, which may have been dissolved when cutting the disc from a paste cylinder under a flow of water, or is not detected correctly due to preferred orientation induced by the cutting. Polishing with only a drop of water for lubrication uncovers an intact layer of the disc. Grinding of the sample to a fine powder leads to lower quantified amounts of monocarbonate, hemicarbonate and ettringite. This may

be due to water loss from these hydrates facilitated by increased surface area of the powder compared to the disc. Isopropanol treatment decreases the measured amounts of ettringite and hemihydrate and increases those of monohydrate and portlandite. Isopropanol and vacuum may partially dehydrate C-S-H, ettringite and the AFm phases and thus decrease their total quantified mass [73]. The content of monohydrate should decrease too, but conversion of hemihydrate to monohydrate is possible [74] and could be the reason of the observed increase in the monohydrate content. The increase in portlandite content may be due to isopropanol adsorption on portlandite crystals [75]. Subsequent grinding to a fine powder could facilitate evaporation of isopropanol and the quantified portlandite content is as prior to exposure to the isopropanol. Grinding, however, further reduces the amounts of monohydrate and ettringite. The least destructive preparation should be limited to delicate polishing of the sample surface.

In this thesis, unless specified, the samples were treated with isopropanol and ground. Despite the certain bias in absolute quantification of the AFt and the AFm phases, a comparison between the systems studied should follow the same trends as in the untreated samples.

Part of the discs soaked in isopropanol and kept in vacuum were processed for electron microscopy and mercury intrusion porosimetry. Powders obtained by hand-grinding of the remaining discs were used for X-ray powder diffraction and thermo-gravimetric analysis.

3.2.2 Isothermal calorimetry

Isothermal calorimetry was used to track the heat evolution from hydration reaction, up to 140 hours. The testing was carried out using a TAM Air calorimeter from TA Instruments at 20 °C. After mixing of paste (as described in 3.2.1), 10 g of paste was placed in a glass ampoule, sealed with a cap and placed in the calorimeter. Reference sample contained an amount of water that had a similar heat capacity. This amount was calculated knowing the specific heat of cement (0.75 J/gK) and water (4.18 J/gK), water content of paste and assuming 10 g of neat cement paste.

Figure 3.4 shows an isothermal calorimetry curve of heat release during hydration of portland - 45 wt.% slag composite cement. It is composed of five main regions (times are approximate):

- up to 10 min - high early peak due to heat from initial dissolution,
- 10 min to 3 hours - slow reaction (induction),
- 3 hours to 10 hours- acceleration (setting; rapid precipitation of hydrates),
- 10 hours to 24 hours - deceleration,
- from 24 hours - slow on-going reaction.

In a properly sulfated system there is enough gypsum dissolved in early stages of reaction to provide sulfate ions that inhibit rapid aluminate reaction. The first main reaction is that of silicates followed by that of aluminates. In undersulfated systems premature sulfate depletion

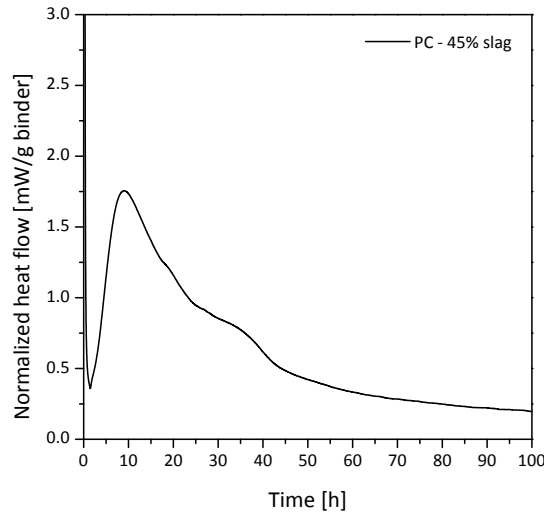


Figure 3.4: Isothermal calorimetry curve of hydration of portland - 45% Slag cement ($w/b = 0.4$).

leads to uncontrolled reaction of aluminate phases and flash setting. Also the concentration of alumina in solution inhibits the dissolution of silicates, the primary reactive components of portland clinker.

3.2.3 Particle size distribution (PSD)

The particle size distribution of powder samples was measured by laser diffraction in isopropanol suspension using Malvern MasterSizer S. The powders were dispersed in isopropanol in small plastic containers using an ultrasonic bath. The suspension is irradiated by a laser beam that diffracts on the particles and the diffracted beam is recorded by a detector. The magnitude of diffraction depends on the particle sizes. An optical model is used to deduce the particle sizes from the recorded signal and the result is presented as a fraction-diameter histogram. We used the Mie optical model, in which a complex refractive index is used to calculate the results:

$$m = n - ik \quad (3.1)$$

where n is the real component and k is the imaginary component. The n depends on the chemical composition of the sample and k on whether the sample is transparent ($k = 0.001$) or absorbing ($k = 1$). The values used in this study were $n = 1.7$ and $k = 0.01$. The refractive index of isopropanol is 1.378.

PSD data can be used to calculate the theoretical geometrical specific surface area (SSA) [44]:

$$SSA = 6 \times 10^6 \times F \times \sum \frac{f}{d \times \rho} \quad (3.2)$$

where F , typically around 1.13, is an empirical constant that takes into account assumptions on particle and surface shape, f is the mass fraction of grains whose diameter is d [μm] and density is ρ [kg/m^3]. The result is in [m^2/kg].

3.2.4 Bulk chemical composition by X-ray fluorescence (XRF)

In XRF, high energy incident X-ray radiation ionizes atoms of the studied sample by ejecting electrons from the atoms' low energy shells. To bring such ionized atom back to a stable configuration an electron from a high energy shell falls into the created space of low energy. The difference between high and low energy of the electron is characteristic of the atom and is emitted as a fluorescent X-ray. The X-rays of all the atoms of the sample are recorded by a WDS or EDS detector and provide a quantitative description of the bulk composition of the sample. In this study, the XRF analyses were carried out by external laboratories: APC solutions, Lonay, Switzerland and HeidelbergCement Technology Center, Leimen, Germany.

3.2.5 Thermo-gravimetric analysis (TGA)

In TGA the sample is heated and the mass change due to heating is recorded (TG curve). In studies of cementitious samples, the most important mass changes are the mass loss due to H_2O release (dehydration, dehydroxylation) until $550\text{ }^\circ\text{C}$ and above $550\text{ }^\circ\text{C}$ due to CO_2 release (decarbonation). In a sample which has been treated in isopropanol and vacuum to remove the free water, the mass loss until $550\text{ }^\circ\text{C}$ corresponds to the amount of bound water in the hydrate phases.

TGA allowed the identification of phases as different phases decompose within specific temperature ranges. Identification is easier using a derivative of the TG curve, called DTG, in which peaks more clearly show the ranges of decomposition of different phases. It has to be noted that TG analysis is very sensitive to measurement conditions. The peak widths in DTG curve and the temperature ranges at which the peaks appear may vary substantially depending on the experiment setup: machine type, heating program, protective gas type, amount and fineness of the sample, and whether the crucible containing the sample was covered or not. The sequence of peaks remains the same, but it may not be possible to compare results from different laboratories. A strict protocol was followed to ensure comparability of the results. DTG curves of pure substances that are common for cementitious systems are shown in Figure 3.5. These have been measured using open $70\ \mu\text{L}$ aluminum oxide crucibles filled with approx. $20\ \mu\text{g}$ solid, under $30\ \text{mL}/\text{min}$ N_2 protective gas flow. Significant overlap often hinders accurate phase identification as several phases may decompose at similar temperatures [$^\circ\text{C}$]:

- 100 - 150 Ettringite
- 150 - 180 Hemcarbonate and monocarbonate
- 180 - 200 Monosulfate and C_2ASH_8
- 250 - 280 Hemcarbonate and monocarbonate

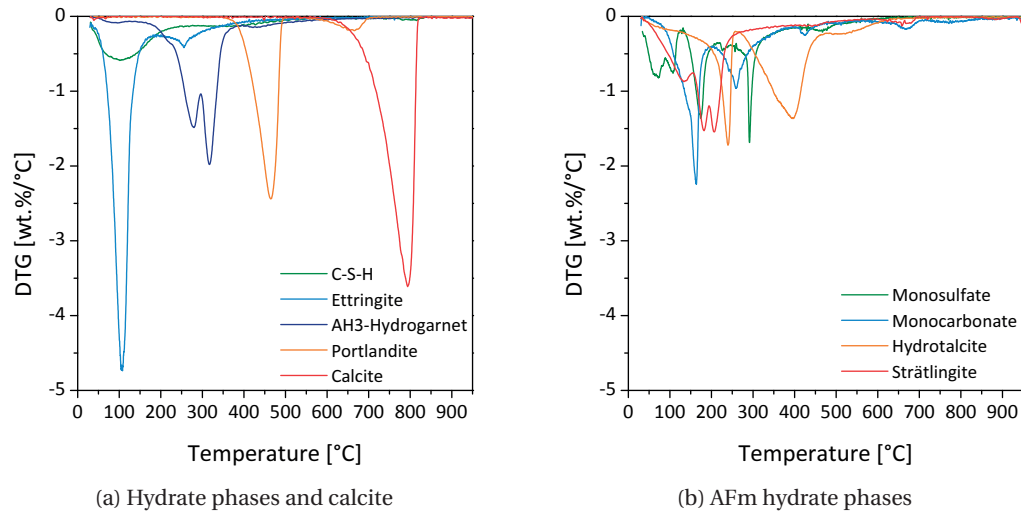


Figure 3.5: DTG curves of pure substances. Source: Personal communication with B. Lothenbach, EMPA.

- 290 - 310 Hydrogarnet
- 350 - 550 Portlandite
- 700 - 800 Calcite, hemicarbonate and monocarbonate

C-S-H decomposes over almost entire temperature range, which complicates phase identification and quantification. Quantification of phases is only possible if there is no significant overlap with other phases. To quantify the amount of a phase, the relative mass loss due to H_2O or CO_2 recorded by TGA is compared to the mass fraction of H_2O or CO_2 in the pure phase. Typically, only portlandite and calcite are quantified with satisfactory confidence. To detect and quantify most of the phases in cementitious samples TGA is coupled with X-ray powder diffraction.

In this study, thermo-gravimetric analysis was carried out using a Mettler Toledo TGA/SDTA851e. Approximately 50 mg of powdered sample was placed in 150 μ L alumina crucible without a lid. Heating from 30 °C to 950 °C at a heating rate of 10 °C/min was carried out under a protective N_2 atmosphere to minimize sample carbonation.

3.2.6 X-ray powder diffraction (XRD)

In XRD, a powder sample is irradiated with a monochromatic incident X-ray beam at an angle θ . Scattering of the X-rays on crystal planes of crystalline phases present in the sample, under certain conditions, leads to positive interference and high intensity signal recorded by a detector on the other side of the goniometer, also at an angle θ . This condition is called

Bragg's law:

$$n\lambda = 2d \sin\theta \quad (3.3)$$

where n is the order of the interference band, λ is the wavelength, d is the spacing between crystal planes and θ is the incident beam angle. Scanning over a range of angles produces a pattern characteristic for the analysed crystalline phase. Patterns of multiphase samples contain contributions of individual phases that can be identified using a pattern database. Rietveld refinement is a mathematical model that fits a calculated profile to the measured pattern and allows quantification of crystalline phases present in the sample.

An important aspect of the powder XRD is sample preparation. The powder sample is compacted into a sample holder. The key criterion of powder sample preparation is that the powder should be randomly distributed. Careless pressing, excessive displacement of the powder in the holder or unidirectional movements during preparation may all lead to preferred orientation. Preferred orientation favours reflexions related to certain orientations and reduces the others. This effect has to be corrected during analysis as it may introduce errors. Post treatment is not always successful. It is therefore important to minimize the preferred orientation in the first place. The powder should not be compacted too much neither should it contain voids. The back-loading technique can limit the distortions introduced to the irradiated sample surface and minimize preferred orientation of the grains.

The XRD measurements were carried out using PANalytical X'Pert Pro MPD diffractometer in Bragg-Brentano geometry. Cu $K\alpha$ radiation was used and an X'Celerator detector with an active length of $2.122^\circ 2\theta$. The X-ray generator was operated at 45 kV and 40 mA. Scanning was carried out from 6° to $70^\circ 2\theta$ angles using a fixed divergence slit of 0.5° , step size of 0.0167° and time per step 59.69 s. The sample was rotated during the measurement to improve statistics (one revolution in 4 seconds). One measurement lasted about 30 min.

Crystalline phases were quantified by Rietveld refinement using X'Pert High Score Plus software with rutile as an external standard, as described in [59]. A list of crystal structures used for the refinement is presented in Table 3.2.

In the external standard technique the w_k weight fraction of phase k is calculated from the following formula:

$$w_k = \frac{s_k}{s_s} \frac{\rho_k V_k^2}{\rho_s V_s^2} c_s \frac{MAC_{sample}}{MAC_s} \quad (3.4)$$

where s_k , r_k , V_k are the scale factor, density and cell volume of the phase k and s_s , r_s , V_s are the scale factor, density and cell volume of the external standard (rutile); c_s is the crystallinity of the standard. The mass attenuation coefficient (MAC) of the sample is MAC_{sample} and that of the standard is MAC_s . These MAC are needed for the absorption correction and were computed from the bulk chemical composition by XRF and using international tables of crystallography

Table 3.2: Phases and references used for quantitative Rietveld analysis.

Phase name	Chemical formula	Space group	ICSD	Reference
Alite M3	Ca ₃ SiO ₅	Cm	94742	De la Torre <i>et al.</i>
Belite β	Ca ₂ SiO ₄	P21/n	81096	Mumme <i>et al.</i>
C ₃ A cubic	Ca ₃ Al ₂ O ₆	Pa-3	1841	Mondal and Jeffery
C ₄ AF	Ca ₂ Fe _{1.40} Al _{0.60} O ₅	Ima2	2841	Colville and Geller
Gypsum	CaSO ₄ ·2(H ₂ O)	C2/c	27221	Pedersen and Semmingsen
Calcite	CaCO ₃	R-3c	73446	Maslen <i>et al.</i>
Dolomite	CaMg(CO ₃) ₂	R-3	52149	Pilati <i>et al.</i>
α-Quartz	SiO ₂	P322	174	Le Page <i>et al.</i>
Lime	CaO	Fm-3m	75786	Huang <i>et al.</i>
Periclase	MgO	Fm-3m	9863	Sasaki <i>et al.</i>
Rutile	TiO ₂	P42/mnm	93097	Ballirano and Caminiti
Corundum	Al ₂ O ₃	R-3c	77810	Riello <i>et al.</i>
Hematite	Fe ₂ O ₃	R-3c	201096	Finger and Hazen
Magnetite	Fe ₃ O ₄	Fd-3m	30860	Wechsler <i>et al.</i>
Mullite	Al _{2.34} Si _{0.66} O _{4.83}	Pbam	158098	Voll <i>et al.</i>
Gehlenite	Ca ₂ Al(AlSi)O ₇	P-421m	158171	Gemmi <i>et al.</i>
Anorthite	Ca ₂ Al ₂ Si ₂ O ₈	I-1	202710	Angel
Ye'elimite cubic	Ca ₄ Al ₆ O ₁₂ (SO ₄)	I4-3m	9560	Saalfeld and Depmeier
Albite	NaAlSi ₃ O ₈	P-1	68913	Armbruster <i>et al.</i>
Portlandite	Ca(OH) ₂	P-3m	202220	Chaix-Pluchéry <i>et al.</i>
Tobermorite 14A	Ca ₅ (Si ₆ O ₁₆)(OH) ₂ (H ₂ O) ₇	Bb	152489	Bonaccorsi <i>et al.</i>
Ettringite	Ca ₆ Al ₂ (SO ₄) ₃ (OH) ₁₂ (H ₂ O) ₂₆	P3c	155395	Goetz-Neunhoeffer and Neubauer
Monosulfate	Ca ₄ Al ₂ (OH) ₁₂ (SO ₄)(H ₂ O) ₆	R-3	100138	Allman
Hemicarbonate	Ca ₄ Al ₂ (OH) ₁₂ (OH)(CO ₃) _{0.5} (H ₂ O) ₄	R-3c	-	Runcevski <i>et al.</i>
Monocarbonate	Ca ₄ Al ₂ (OH) ₁₂ (CO ₃)(H ₂ O) ₅	P1	59327	François <i>et al.</i>
Hydrotalcite	Mg ₂ Al(OH) ₆ (CO ₃) _{0.5} (H ₂ O) _{1.5}	R-3m	81963	Bellotto <i>et al.</i>
Hydrogarnet	(CaO) ₃ (Al ₂ O ₃) _{1.425} (H ₂ O) _{4.8}	Ia-3d	158019	Schroepfer and Bartl

for Cu K α radiation [76] (Table 3.3). The water content needed for MAC calculation of hydrated samples was obtained by thermo-gravimetry as a mass loss due to heating from 20 °C to 550 °C. The difference between the total and the sum of quantified crystalline phases is due to non-refined phases and amorphous content. Direct quantification of the amorphous content and differentiation between multiple amorphous phases is extremely difficult. More details on advanced refinement techniques and quantification of amorphous phases are presented in Chapter 5.7.

The results of the external standard quantification are typically expressed per 100 g of paste or per 100 g of anhydrous binder using the equations 3.5 and 3.6 respectively:

$$w_{100gpaste} = \frac{w_k}{(1 - w_{H_2O})(1 + w/b)} \quad (3.5)$$

$$w_{100ganhydrous} = \frac{w_k}{(1 - w_{H_2O})} \quad (3.6)$$

where w_k is the quantified weight fraction of phase k , w_{H_2O} is the bound water content determined by thermo-gravimetry as a mass loss between 20 °C and 550 °C, the same which was used for MAC calculation; w/b is the water binder ratio at which the paste was mixed. The

Table 3.3: Mass attenuation coefficients [76].

MAC [cm ² /g]	
Al ₂ O ₃	31.69
SiO ₂	36.03
CaO	124.04
Na ₂ O	24.97
K ₂ O	122.3
MgO	28.6
Fe ₂ O ₃	214.9
SO ₃	44.46
TiO ₂	124.6
P ₂ O ₅	39.66
H ₂ O	10.10

degree of reaction of cement α at time t can then be expressed as:

$$\alpha(t) = \frac{w_{C_3S}(t) + w_{C_2S}(t) + w_{C_3A}(t) + w_{C_4AF}(t)}{w_{C_3S}(t=0) + w_{C_2S}(t=0) + w_{C_3A}(t=0) + w_{C_4AF}(t=0)} \quad (3.7)$$

3.2.7 Scanning electron microscopy (SEM)

SEM is a very powerful technique to study the microstructure and chemical composition of cementitious samples with resolution from micrometres to millimetres. SEM can be used to identify, quantify and measure the degree of reaction of amorphous phases, which is difficult or impossible using other techniques.

In SEM a high-energy (in the order of keV) incident electron beam is scanned over the sample surface. There is a number of possible electron-sample interactions that can be used for different analytical purposes. Backscattered electrons (BSE) are incident high-energy electrons whose path is altered by elastic Coulomb interactions with atom nuclei. For high-energy beams (>1 keV) heavier materials yield more backscatter electrons, which produces BSE contrast. BSE images can be used for phase identification based on the grey levels and for quantification by relating the area of a given grey level to the total area of the image. Energy-dispersive X-ray spectroscopy (EDS) is fundamentally similar to XRF and can provide a complete elemental analysis. The difference between EDS and XRF is that the EDS incident beam is made of electrons. Because the EDS is coupled to the microscope the chemical analysis offers spatial resolution unavailable with the XRF. The spatial resolution is limited by so called interaction volume, i.e. the volume from which X-rays are detected. The size of the interaction volume depends on the sample density and beam energy, as denser samples are less penetrated by electrons and electrons of higher energy penetrate deeper into the sample. Typical size of an interaction volume is around 1-1.5 μm^3 for cementitious samples and 15 keV beam energy. Because the number of X-rays produced and detected depends on the element and the sample, quantitative results are obtained by comparing the EDS signal with a set of standards and by

Table 3.4: Polishing procedure for SEM sample preparation.

Diamond spray	Guidelines	Approximate polishing time
9 μm	until all deep scratches are removed	15 min
3 μm	until sample surface is shiny	3 h
1 μm		2 h
1/4 μm	facultative	1 h

applying so called matrix corrections (PB-ZAF or PhiRhoZ). EDS can be operated in point or mapping mode. It can be used to identify and analyse phases according to their chemical composition and, coupled with image analysis, to quantify their amount.

A key part of SEM analysis is sample preparation. Samples for BSE and EDS analysis need to be absolutely flat, to avoid shadowing and to ensure that the X-ray escape path from the sample is equal at each analysed spot. Incorrect polishing of a cementitious sample can easily destroy its microstructure. To preserve the microstructure samples for SEM investigations were embedded in epoxy resin. Powders were first pressed into pellets using a hydraulic press. Solid samples were pre-polished by hand using sandpaper grade 1200 for pastes and 500 and 1200 for mortars. The impregnation with epoxy was carried out under vacuum with a spectrally transparent epoxy resin (EpoTek 301). The epoxy mounts were hand-polished on 1200 grade sandpaper lubricated until the entire sample surface was uncovered and edges could be seen in a grazing light. Then a polishing routine was applied. We used MD Largo Struers[®] discs lubricated with odourless petrol and diamond spray as a polishing agent. For the majority of samples 150 rpm and 20 N force gave best results. The polishing stages are summarized in Table 3.4. After each stage and after each hour of polishing the samples were washed in isopropanol in an ultrasonic bath and the polishing discs were brushed with a detergent.

After polishing the samples were stored in a vacuum desiccator for at least two days to evaporate organics and thus prevent microscope contamination. Prior to SEM investigations the samples were coated with a thin conductive layer of carbon (10 nm). The quality of polishing was verified under SEM in secondary electron mode, which is sensitive to topography. Rough or scratched areas, holes and dust particles on sample surface were avoided.

The scanning electron microscope used for this study was a FEI Quanta 200 with Bruker XFlash 4030 EDS detector with 30 mm² active surface. The microscope was operated at 15 kV accelerating voltage and 12.5 mm working distance. For the purpose of quantitative analysis the microscope was calibrated against a set of standards.

Measurement of the composition of C-S-H by SEM-EDS

The composition of C-S-H is measured by point EDS analysis of the hydration rims around cement grains (so called inner product) and of the matrix (outer product). The measurement points should be taken far from anhydrous grains, clusters of portlandite, etc. to limit the

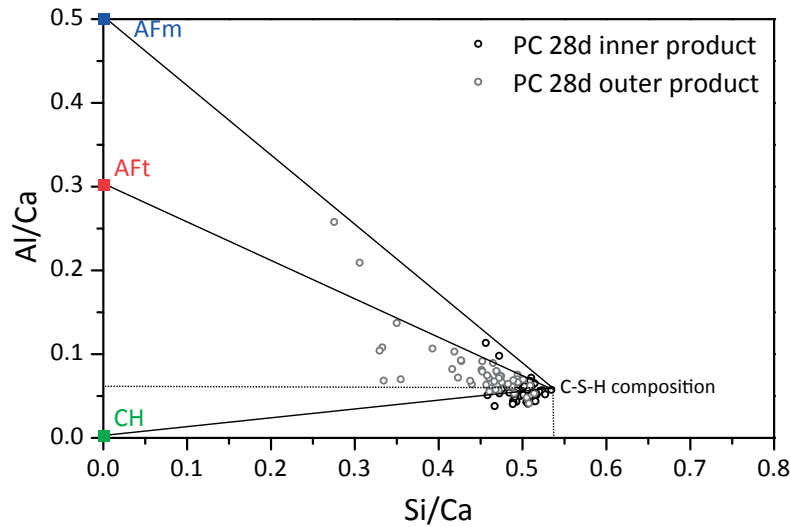


Figure 3.6: Determination of the C-S-H composition from the SEM-EDS point analysis.

signal from these phases due to the interaction volume. Around 100 points per inner product and 100 per outer product are collected. PhiRhoZ corrections of the EDS signal provide full element composition in atomic-%.

Because the influence of neighbour phases is unavoidable, the composition of C-S-H is found graphically. Ratios of Si/Ca are plotted versus Al/Ca and a cloud of points appears, which is the effect of intermixing between C-S-H, AFt, AFm and CH. The pure C-S-H composition is therefore found at the extreme right-hand side of this cloud, as demonstrated in Figure 3.6.

Measurement of the degree of reaction of slag by image analysis

The degree of reaction of slag can be measured by image analysis of a combined input from BSE grey level images and magnesium concentration maps collected by EDS. The principle of this method was described by Kocaba *et al.* [77] and a new algorithm was prepared in MATLAB by J. Bizzozero and the author. The code is presented in Appendix A.6 and the procedure is explained in Figure 3.7. Grey level segmentation of the BSE image is used to separate the slag grains, but their grey level is very similar to that of hydration products, notably portlandite, and that of some grain boundaries. Additional information is brought by Mg map collected by EDS. Mg map was chosen due to clear difference in Mg content between slag (7.8 wt.%) and portland clinker (1.5 wt.%). A grid of 15×15 frames with 252×189 μm field of view was set up. For each frame a BSE image was collected with a speed of 15 s/image and a Mg map at a speed of 60 s/map. Such quickly obtained Mg maps contain a lot of noise, and are smoothed using 25-pixel Hamming window. There is no need for very precise Mg maps as they are only used to indicate the slag grains in BSE image, whose quality influences more the quality of segmentation. The areas attributed to slag are then averaged for all the 225 frames and the resulting area fraction is equal to volume fraction of slag in the sample. The degree of reaction

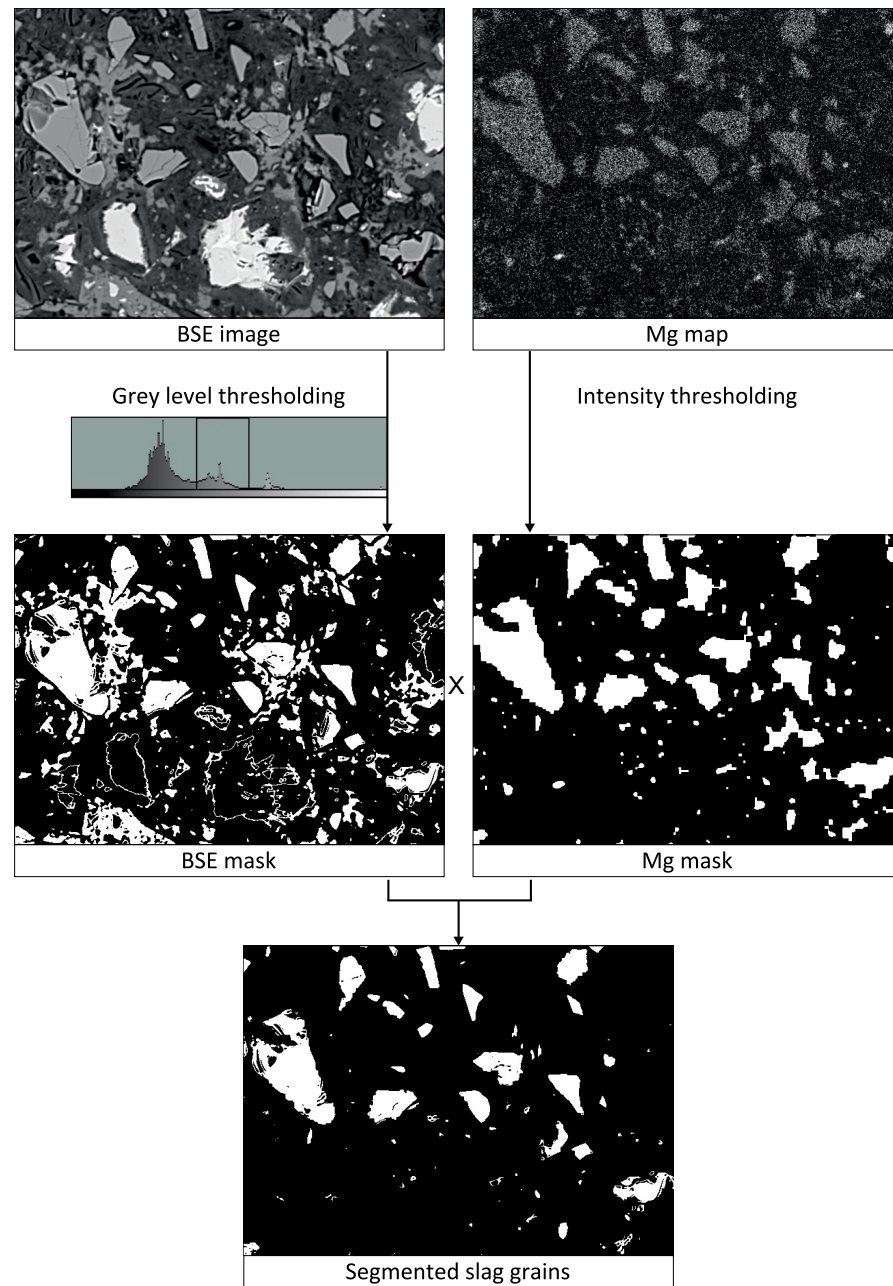


Figure 3.7: Procedure used to segment anhydrous slag grains based on BSE grey level and EDS Mg content.

of slag is calculated as:

$$DoR_{slag} = 1 - \frac{V_t}{V_0} \quad (3.8)$$

where V_t is the volume fraction at time t and V_0 is the volume fraction of slag in paste before any reaction occurred. The main limitation of this technique is limited resolution of finest particles, below $1 \mu\text{m}$, which may not be accounted for correctly. This is especially important for early hydration times, up to 7 days, when most of the finest particles are not yet consumed. As a result the calculated volume fraction is lower than in reality and the degree of reaction is overestimated. At later ages, error may be due to hydrotalcite rims around slag grains being qualified as anhydrous, which would in turn underestimate the degree of reaction of slag.

This procedure was not used to quantify fly ashes because they exhibit several grey levels. Quantification of fly ash requires a complicated algorithm linking chemical contrast with morphological filters [42], but does not guarantee good results. Instead, fly ash was quantified by image analysis of EDS full element maps, as described in detail in Chapter 4 and 5.

3.2.8 Mass-balance calculations

Mass-balance calculations were carried out to assess the amount of C-S-H and other non-crystalline or poorly-crystalline hydration products, which are very difficult or impossible to quantify by TGA, XRD-Rietveld and electron microscopy. The mass-balance procedure used in this thesis was the following:

- Measure the amount of anhydrous clinker by XRD-Rietveld and that of fly ash and slag by SEM-EDS image analysis.
- Calculate the total amount of Ca, Si, Al, Mg, S and C that reacted, knowing the chemical composition of clinker, fly ash and slag.
- Mg is included in hydrotalcite ($\text{Mg}_4\text{Al}_2\text{O}_7 \cdot 10\text{H}_2\text{O}$), subtract required Al.
- All Si is incorporated in C-S-H, subtract Ca, Al, and S required based on the Ca/Si, Al/Ca, and S/Si ratios in the C-S-H measured by SEM-EDS point analysis. The water content of the C-S-H was assumed 1.8 molecule of water per chain unit, i.e. Si and Al, as reported by Muller *et al.* for C-S-H from white cement measured by ^1H NMR relaxometry. This value excludes the gel water of the C-S-H and does not change significantly with the hydration time. Density of such C-S-H is around 2.7 g/cm^3 . The internal porosity of the C-S-H is accounted for by adding 35 wt.% of water, which is equivalent to taking a C-S-H density of 2.0 g/cm^3 .
- Take the ettringite quantified by XRD-Rietveld, subtract required Ca, Al and S.
- Remaining S is included in monosulfate, subtract required Ca and Al.
- All C is incorporated in monocarbonate, subtract required Ca and Al.
- Remaining Ca forms portlandite.

The phase masses obtained in the mass-balance calculations were converted to phase volumes by dividing by the phase density. The densities, where possible, were assumed the same as in the XRD-Rietveld refinement.

Assumptions made in the mass-balance algorithm as well as the coupling of one calculation to the result of another may affect the final result. Below is presented an assessment of how the final result is sensitive to these assumptions. It was carried out on a sample containing 49.5 wt.% PC + 45 wt.% CFA2+5.5 wt.% Limestone and hydrated for 90 days. The results are expressed in $\text{cm}^3/100 \text{ cm}^3$ of hardened paste.

- A change in the degree of reaction of clinker by 1.5 % and that of an SCM by 5 % are quite possible regarding the error of quantification by XRD and image analysis. With such variation the volume of most of the phases varied by 0.5-1.0 cm^3 and of C-S-H by 2 cm^3 .
- The Mg:Al ratio of the hydrotalcite assumed for calculations was 2.0. In reality this ratio may vary and reported values range from 1.7 [50] to 2.6 [78]. A change in Mg:Al by 0.5 has mainly an effect on hydrotalcite content by 0.2 cm^3 .
- The Ca/Si, Al/Ca and S/Si ratios of the C-S-H were measured on samples hydrated for 28 and 90 days. The values for remaining hydration times were therefore estimated from the available data. A variation in the C-S-H composition by Si/Ca 0.05, Al/Ca 0.05 and S/Si by 0.025 all affected the C-S-H volume by 0.6, 1.0, 0.4 cm^3 respectively. Portlandite content varied by no more than 1.0 cm^3 , but the most important effect had the S/Si ratio on the monosulfate content, around 3 cm^3 . Small adjustments in the sulfate content of the C-S-H were done, where necessary to avoid nonsense amounts of monosulfate to be computed and to balance the amount of Al at the end of the calculation.
- A change in the mass of ettringite in the input by 3 g, where typical values quantified by XRD ranged from 4 to 12 g, had mainly an effect on monosulfate (3 cm^3) and on portlandite (0.6 cm^3).
- A variation in the carbonate content in the input by 0.2 g results in a volume change of monocarbonate of 1.21 cm^3 .

The most sensitive result of the mass-balance is clearly monosulfate. This is because the amount of monosulfate is calculated from the amount of SO_3 which is left after assignment of sulfate to C-S-H and to ettringite, therefore with high potential to accumulate errors. Moreover, due to stoichiometry a little variation in sulfate content results to a large variation in monosulfate content. It is therefore very important to carefully measure the sulfur content of the C-S-H by SEM-EDS and to quantify ettringite on a sample that has not been treated with isopropanol, as this treatment can partially decompose ettringite (cf. 3.2.1). In this study, the majority of samples were treated in isopropanol but an additional non-treated replicate has been measured after 365 days of hydration. Consequently, to be able to use the remaining ettringite data at different ages these values were recalculated for each mix formulation based on a comparison between the treated and the non-treated analogues.

Similarly to monosulfate and sulfate, due to the stoichiometry, the calculated monocarbonate content is sensitive to variations in the carbonate amount in the input. The latter depends on the precision of quantification of calcite by XRD-Rietveld, which may be subject to variations due to preferential orientation and overlap with the amorphous background from C-S-H and many SCMs. Due to the unknown proportion between monocarbonate and hemiacarbonate the latter is not accounted for in this mass-balance and all carbonate available is attributed to monocarbonate.

The mass-balance calculation used does not include Si-bearing hydration products other than C-S-H, such as strätlingite (C_2ASH_8). Strätlingite is an AFm-type phase and may be poorly crystalline, which hinders its quantification by XRD. Without additional input, mass balance is unable to calculate the amount of this phase, but unless excess Al is present strätlingite is not expected to form anyway.

Due to a potential combination and accumulation of measurement errors from the different inputs, mass-balance calculations of AFm phases should be taken as a qualitative or at most semi-quantitative. The determination of the C-S-H content is expected to have larger precision.

3.2.9 Thermodynamic modelling

Thermodynamic modeling was used to investigate the effect of fly ash and slag on the hydrate phase assemblage and the volume of solids. GEMS geochemical software (gems.web.psi.ch, accessed may 2015) [53, 54] was used with PSI-GEMS thermodynamic database for aqueous species and solids [55] and a cement specific CEMDATA14 database from EMPA [56, 57].

The input for GEMS is the total oxide composition of the phases that are assumed to have reacted and the water content. The reacted phases are quantified by XRD-Rietveld or by SEM-image analysis and their oxide contributions summed up. GEMS calculates an equilibrium composition by minimizing Gibbs free energy ΔG of the system:

$$\Delta G = -RT \ln K \quad (3.9)$$

where $R = 8.314 \text{ J/molK}$ is the gas constant, T is the absolute temperature and K is the ion activity product of the phases present in the system. The ion activity product of a phase is a product of the activities of its component ions to the power of the stoichiometric coefficient. The activity of an i component is equal to its concentration multiplied by the activity coefficient γ_i . GEMS calculates the activity coefficients using the extended Debye-Hückel equation:

$$\log \gamma_i = \frac{-A_y z_i^2 \sqrt{I}}{1 + B_y a_i \sqrt{I}} + b_y I \quad (3.10)$$

Table 3.5: Composition and density of CSHQ end members for thermodynamic simulations [79].

End member	Bulk formula	Molar H ₂ O/Si	ρ_{sat} [g/cm ³]
TobH	(CaO) _{2/3} SiO ₂ (H ₂ O) _{3/2}	1.50	2.25
TobD	(CaO) _{5/6} (SiO ₂) _{2/3} (H ₂ O) _{11/6}	2.75	2.50
JenH	(CaO) _{4/3} SiO ₂ (H ₂ O) _{13/6}	2.17	2.30
JenD	(CaO) _{3/2} (SiO ₂) _{2/3} (H ₂ O) _{5/2}	3.75	2.10

where A_y and B_y are coefficients dependent on temperature and pressure, z_i is the ionic charge of species i , a_i depends on the ion size and is equal to 3.67 for KOH solutions, b_y is a semi-empirical parameter of 0.123 for KOH at 25 °C and I is the ionic strength. Values for KOH are taken because this is the dominant electrolyte in cement pore solution.

The output of GEMS simulations is mass, volume and composition of the modeled system. These results are reported at equilibrium conditions and no kinetic information is obtained. The effect of reaction kinetics of, for example, a fly ash can be modeled by gradually increasing the degree of reaction of the ash in the input data and modeling the equilibrium composition at each step. The phase assemblage of experimental systems may differ from the modeled ones if metastable phases are present in the real system. GEMS may predict phases that are not observed in experiments, but these phases can be excluded from simulation by the operator.

The amounts of Ca, Si and water of the C-S-H were calculated using a built-in CSHQ model by Kulik [79]. This (A,B) (C,D)X type model describes solid solutions between two tobermorite-like and two jennite-like end members and was made consistent with the Richardson-Groves model of C-S-H and with ²⁹Si NMR and solubility data. The composition and density of the end member tobermorites and jennites are given in Table 3.5 and were kept as such in the final result phase assemblage. This model allows to account for changes in Ca/Si ratio of the C-S-H, but does not calculate the other components, such as Al, S and alkalis. The content of Al and S was determined experimentally for each mix formulation by SEM-EDS point analysis of C-S-H on pastes hydrated for 28 and 90 days. This information was added manually to the model. The content of alkalis in the input data was adjusted so that the modeled concentration of Na and K in solution would match the values measured experimentally by pore solution extraction (3.2.10).

3.2.10 Pore solution analysis

Pore solutions were extracted from paste samples following a protocol similar to that of Barneyback and Diamond [80]. The pastes were mixed at water/binder ratio of 0.5 to ensure enough pore solution could be extracted at late ages, such as one year of hydration. Around 350 g of paste was cast in a plastic bottle 50 mm in diameter and 100 mm high. Sealed bottles were kept at 20 °C until testing. The top part of the bottle was cut with a saw and the paste was removed from the bottle. The extraction was carried out using a large laboratory press and

a solid metal piston similar to that in [80]. A paper filter was placed under the sample in the piston. Samples hydrated for one day were pressed at 300 kN and all other samples at 800 kN. We kept the pressure constant as much as possible for all the samples because the magnitude of the applied pressure may have an influence on measured ionic concentrations and solids may dissolve more easily at higher pressures. The pressure was applied gradually and kept at the maximum value for 5 minutes to extract around 1-5 mL of pore solution. The obtained liquid was immediately filtered through a 0.45 μm filter and 1 mL was transferred to a plastic vial containing 9 mL of cooled ultra-pure water to limit precipitation. The tightly closed vial was stored at 4 °C until testing. A Shimadzu ICP9000 spectrometer was used to measure the concentrations of Al, Si, Na, K and Ca and a Dionex ICS-3000 ion chromatograph to measure the concentration of sulfates.

3.2.11 Mercury intrusion porosimetry (MIP)

MIP was carried out on paste samples to characterize the connected pore network and the size of the pore entries. Micromeritics AutoPore IV 9500 porosimeter was used, which is capable of measuring porosity in the range from 1 mm down to 2 nm. A MIP sample contained 4-5 pieces of paste of around 1.5 g mass.

During a MIP experiment the sample is immersed in mercury and pressure is gradually applied to force the mercury into the accessible pore network of the sample. Mercury is used because it does not wet the surface of cement paste. The applied pressure is related to the pore entry radius using the Washburn equation:

$$P = \frac{2\sigma \cos\theta}{r} \quad (3.11)$$

where P is pressure, r is the pore entry radius, $\sigma = 0.485 \text{ N/m}$ is the surface tension of mercury and θ is the contact angle between mercury and cement paste, here assumed 141.3°. Published data [81] shows that for cement paste the contact angle varies between 139° and 150°. The volume of the intruded mercury corresponds to the volume of the pore network accessible through the corresponding pore entry. A common mistake is to treat a MIP curve of cumulative volume vs. pore entry diameter as a pore size distribution.

Useful information in MIP curve is related to the threshold and the critical pore entry radius. As shown in Figure 3.8 the threshold radius is defined at the pressure when significant proportion of the pore network starts to be filled with mercury (onset of percolation). The threshold radius can be identified at the take-off of the MIP curve. The critical radius corresponds to the inflection point of the MIP curve. It is the characteristic of the size at which mercury percolates the sample. This percolation threshold is expected to be related to paste permeability and transport of foreign ions through the cementitious matrix, for example the aggressive ions relevant for durability: chloride and sulfate. The threshold pore radius seems to be more representative of the size of the radius when mercury starts to intrude the sample and is used in this study. The threshold pore entry radii were determined by intersecting two tangent lines.

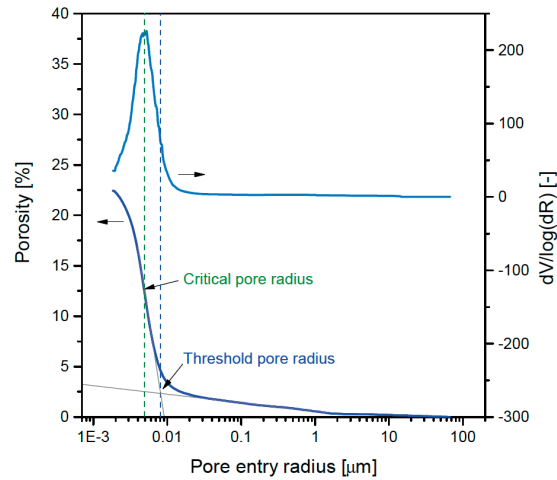


Figure 3.8: Threshold and critical radius in a differential and a cumulative MIP curve. From [82]

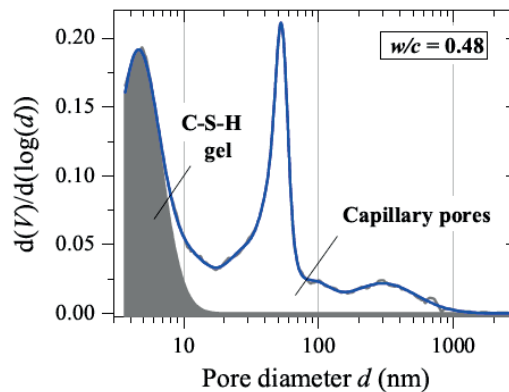


Figure 3.9: C-S-H and capillary porosity in a differential MIP curve of a white cement paste. From [83].

The total porosity refers to the maximum cumulative volume of the intruded mercury. Necessarily, this information is limited by the maximum intrusion pressure and pores with entry radii below 2 nm are not resolved. A comparison of MIP with ^1H NMR [83] has shown that the finest pores intruded by mercury, in the nm range, belong to the C-S-H. Larger pores are qualified as capillaries, as shown in Figure 3.9. The threshold between C-S-H and capillary pores used in this study was 8.5 nm (diameter 17 nm).

3.2.12 Preparation of mortar samples

Mortar samples were prepared at water/binder ratio of 0.5. Due to the interfacial transition zone with aggregates, a water/binder of 0.5 in mortar is roughly equivalent to that of 0.4 in paste. According to EN 196-1 three $4 \times 4 \times 16$ cm mortar bars are produced from 1350 g of normalized sand, 450 g of binder and 225 g of water in a standard mixer. In this study mortar

Chapter 3. Materials and Methods

bars were used not only for compressive strength testing but also for durability investigations, which required many replicas. To facilitate preparations and cast all bars from a single mix, the proportion was increased 6-fold and a bigger mixer was used. The mixing procedure was:

- 30 s - low speed - mix powders with water,
- 30 s - low speed - add sand,
- 60 s - high speed,
- 60 s - pause - use a spoon to verify homogeneity of the mix,
- 60 s - high speed.

After mixing the mortar was placed in moulds in two steps, with 60 hits on a jolting table to compact the mortar in the mould. Mortar bars for testing of sulfate-related expansion had metal pins inserted at the time of casting. Covered moulds were stored in 100% RH for one day until demoulding. The mortar bars were then kept immersed in a minimal amount of lime saturated water solution until testing. All mortar bars for durability investigations were kept in these conditions for 90 days to allow time for the fly ash and slag to react.

3.2.13 Compressive strength

Compressive strength was measured on 4×4×16 cm mortar bars following the EN 196-1 protocol. The results were obtained as an average of four compressions. Testing times were 1, 7, 28, 56, 90 and 365 days, which corresponded to the testing times of companion paste samples.

3.2.14 Water absorption

A water absorption test was carried out to assess the capillary transport of mortars. Absorption is mainly linked to the permeability and porosity of the material and the magnitude of capillary forces. It is therefore expected to provide useful information on permeability and an indication of durability against ingress of aggressive ions.

The 4×4×16 cm mortar bars were each cut into four cubes of around 3×4×4 cm. These cubes were kept for 24 hours under water in a vacuum chamber and these saturated samples were then weighed in air and under water. The cubes were then dried in a ventilated oven at 60 °C and weighed every 24 hours until the mass change between two measurements was less than 0.2 %. The dry mass was taken and the lower side of the samples were just immersed in 3 mm of water. The sample mass was recorded every 10 min for the first hour, every 20 min for the second hour, every 30 min for the next two hours, then every hour until eight hours and the last measurement was taken at 24 h.

3.2.15 Migration experiment

A migration experiment was carried out to assess the permeability of mortars. The mortars were cast in 100 mm diameter and 150 mm high cardboard cylinder moulds. These were demoulded after one day and stored immersed in lime saturated water for 28 and for 90 days prior to testing. The test samples were cut from the cylinders and ground to a thickness of 27 mm. These samples were kept for 24 h in a 0.3 M NaOH solution under vacuum for saturation. The experimental setup was provided by SIMCO@company and is shown in Figure 3.10. The cylindrical sample is fixed between two cells and sealed with a high viscosity silicone paste. The upstream cell is filled with 0.3 M NaOH + 0.5 M NaCl solution and the downstream cell is filled with 0.3 M NaOH solution. A voltage of 30 V is applied to the electrodes fixed at the cell ends and current is measured automatically or manually for around two weeks.

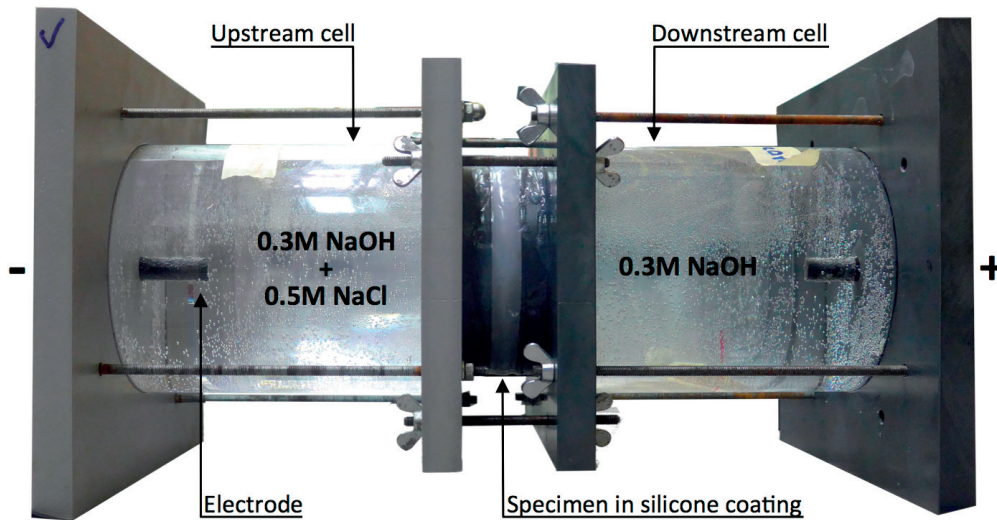


Figure 3.10: Experimental setup for chloride migration testing.

Alternative test setups are available such as those described by ASTM C1202-10 (www.astm.org) and NordTest NT BUILD 355 (www.nordtest.info). The choice of the setup for migration testing was dictated by the initial will to perform additional modeling of the service life based on the migration experiment, porosity measurements and phase assemblage, which has not been completed within the time-frame of this thesis. The ASTM setup works at 60 V, which is often considered too high as it may cause heating of the sample. At such high voltage the current is high and the system is very dynamic. As a result the test duration is only 24 hours but the result assessed is not a current vs. time curve but only the charge passed. The diffusion coefficient is thus not obtained and the permeability is not determined but assessed. The two other setups work at much lower voltages (12 V for NT and 30 V for SIMCO, but 10 V was also tested) and take significantly longer, typically between 7 and 14 days. These two setups have 0.3M NaOH in the downstream cell but differ in the upstream cell solution - NT has 1M NaCl and SIMCO has 0.5M NaCl + 0.3NaOH, which reduces the gradient of OH^- concentration. As mentioned before, the complete modeling has not been carried out, but the effect of chloride binding and

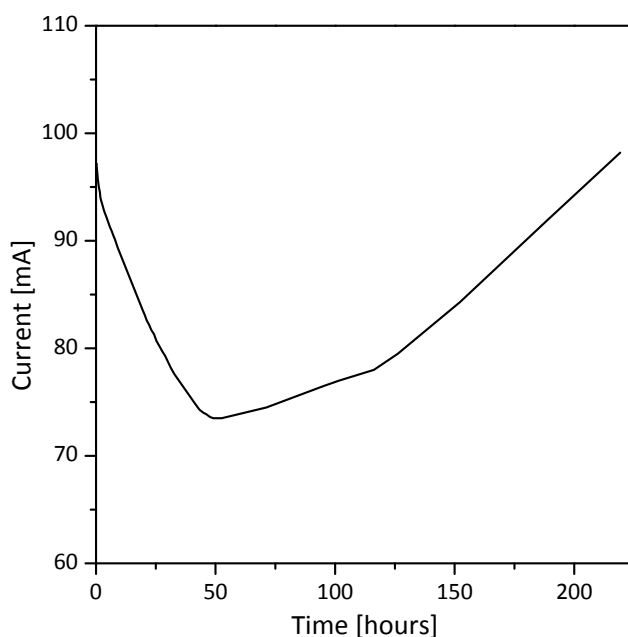


Figure 3.11: Example curve from chloride migration experiment.

the effect of matrix permeability and tortuosity were assessed from the obtained current vs. time curves.

A typical migration curve obtained in this type of experiment is shown in Figure 3.11. Three main parts can be identified in this curve:

- The first part of the curve usually shows a current drop. The drop is due to the chloride binding by hydrated phases present in the matrix, especially the AFm phases. The binding acts like a local resistance in an electric circuit.
- The low point of the curve corresponds to the moment in which chloride has reached through the sample to the downstream cell. The chloride binding reactions stop or slow down significantly.
- When no more chloride can react with the hydration products the current increases as now all the chloride coming from the upstream cell is contributing to the current.

4 Fly ash characterization

Contents

4.1 Introduction	39
4.2 Bulk chemical composition	40
4.3 X-ray diffraction	41
4.3.1 Crystalline phases	41
4.3.2 Amorphous phase	44
4.4 Backscattered electron imaging	46
4.5 Energy-dispersive X-ray spectroscopy and image analysis	47
4.5.1 Point analysis and mapping	47
4.5.2 Algorithm-aided image analysis	48
4.5.3 A new approach to process the EDS full element map data	49
4.6 Detailed SEM-EDS analysis of a calcareous fly ash	50
4.7 SEM-EDS image analysis: comparison of selected fly ashes	55
4.8 Comparison of aluminosilicate glasses among the fly ashes	59
4.9 Summary of fly ash characterization	60

Part of this work has been published in *A new quantification method based on SEM-EDS to assess fly ash composition and study the reaction of its individual components in hydrating cement paste* [84].

4.1 Introduction

This chapter looks at the characterization of a wide range of siliceous and calcareous fly ashes. X-Ray fluorescence (XRF) measures the bulk chemical composition. X-Ray powder diffraction (XRD) can identify and quantify crystalline phases but cannot resolve multiple glassy components in fly ash. For this task, electron microscopy is used. Backscatter electron images (BSE) give an insight into the complexity of fly ash microstructure and fractionated

composition. Energy-dispersive spectroscopy (EDS) is used to collect full element maps that precisely describe the local variations of chemical composition in fly ash. We introduce a ternary frequency plot of the chemical data to quickly and intuitively analyse millions of points and identify chemically distinctive populations, mostly amorphous. Image analysis is then used to quantify the relative proportions of these populations and to locate them in the fly ash microstructure.

4.2 Bulk chemical composition

X-Ray fluorescence is typically the first and most readily available data for fly ash characterization. It provides a bulk measure of elements present in the material, in their oxide form. The most frequently used fly ash classifications such as EN 197-1 and ASTM C618 are based on the bulk oxide composition. Tables 4.1 and 4.2 summarize the XRF data for the fly ashes used in this study. Fly ashes 1 - 6 can be categorized as ASTM C618 calcareous fly ashes and 7 - 11 as siliceous fly ashes. Among the selected ashes, CFA4-1 and CFA4-2 come from two different batches produced in the same power plant. Their comparison will be made to gain insight into the intra-plant variability, which is an important aspect in the use of fly ashes. Large variations between batches may be one of the principal reasons for discarding the material.

The siliceous fly ashes studied were mainly composed of Si, Al and Fe oxides. The Ca content was a few wt.%. Magnesium and alkali oxides did not exceed 2.2 wt.% each. The differences in bulk chemical composition between the siliceous ashes were generally rather small, around several wt.%.

The calcareous fly ashes in addition to Al, Si and Fe oxides contained significantly more CaO, at the expense of Al and Si. The magnesium content was higher and more sulfur oxide was present. Calcareous fly ashes are known to be much more variable than siliceous fly ashes. This large variability can already be observed on the very general level, in their bulk chemical

Table 4.1: XRF analysis of the siliceous fly ashes studied [wt.%].

	FFA7	FFA8	FFA9	FFA10	FFA11
Al ₂ O ₃	22.5	21.6	21.4	21.6	23.3
SiO ₂	57.1	56.8	53.5	56.4	59.7
CaO	3.8	4.0	4.4	4.1	1.6
Na ₂ O	0.9	0.8	1.2	0.8	0.5
K ₂ O	1.7	1.6	2.2	1.6	2.0
MgO	1.9	1.9	1.8	1.9	1.0
Fe ₂ O ₃	6.6	6.9	7.8	7.0	6.5
SO ₃	0.2	0.3	0.1	0.0	0.2
TiO ₂	1.0	1.0	0.9	1.0	1.1
P ₂ O ₅	0.4	0.4	0.0	0.4	0.2
Sum	96.1	95.2	93.3	94.7	96.1

Table 4.2: XRF analysis of the calcareous fly ashes studied [wt.%].

	CFA1	CFA2	CFA3	CFA4-1	CFA4-2	CFA5	CFA6
Al ₂ O ₃	19.8	18.2	18.0	21.8	19.5	6.2	27.8
SiO ₂	42.3	33.6	33.7	35.9	41.0	54.7	36.7
CaO	20.7	26.5	27.5	25.3	25.5	21.3	16.4
Na ₂ O	0.3	1.9	2.1	0.1	0.2	0.0	1.7
K ₂ O	1.5	0.4	0.4	0.1	0.1	0.5	1.1
MgO	2.2	6.4	6.2	1.3	1.5	3.6	2.3
Fe ₂ O ₃	8.2	6.4	5.7	6.0	4.4	4.6	3.6
SO ₃	1.4	2.2	1.9	3.8	3.4	5.4	4.0
TiO ₂	0.7	1.3	1.5	1.3	1.5	0.8	2.8
P ₂ O ₅	0.3	0.9	1.3	0.2	0.1	0.2	0.3
Sum	97.2	97.7	98.2	95.8	97.1	97.4	96.7

composition. The calcareous fly ashes studied differed widely in oxide composition, up to around 20 wt.% in SiO₂ content of CFA2 and CFA5, for example.

The important drawback of the XRF data is that it describes the bulk fly ash composition but does not take into account that fly ashes may contain multiple crystalline and amorphous phases.

4.3 X-ray diffraction

4.3.1 Crystalline phases

The crystalline phases in fly ash can be identified in X-ray diffractograms and quantified by XRD-Rietveld refinement. For the purpose of quantification, MAC absorption correction coefficients were calculated for each fly ash based on the XRF bulk chemical composition and are presented in Table 4.3 and 4.4.

Table 4.3: Composite mass attenuation coefficients of the calcareous fly ashes studied.

	CFA1	CFA2	CFA3	CFA4-1	CFA4-2	CFA5	CFA6
MAC [cm ² /g]	70.95	71.90	71.51	71.06	68.01	64.90	59.93

Table 4.4: Composite mass attenuation coefficients of the siliceous fly ashes studied.

	FFA7	FFA8	FFA9	FFA10	FFA11
MAC [cm ² /g]	53.13	53.83	56.85	54.11	51.24

The X-ray diffractograms of the siliceous fly ashes in Figure 4.1 are very similar. The crystalline phases identified were practically the same: quartz, mullite, hematite and magnetite. The amounts of these phases determined by Rietveld refinement are summarized in Table 5. The quartz content was between 10 wt.% and 20 wt.% and around the same amount for mullite.

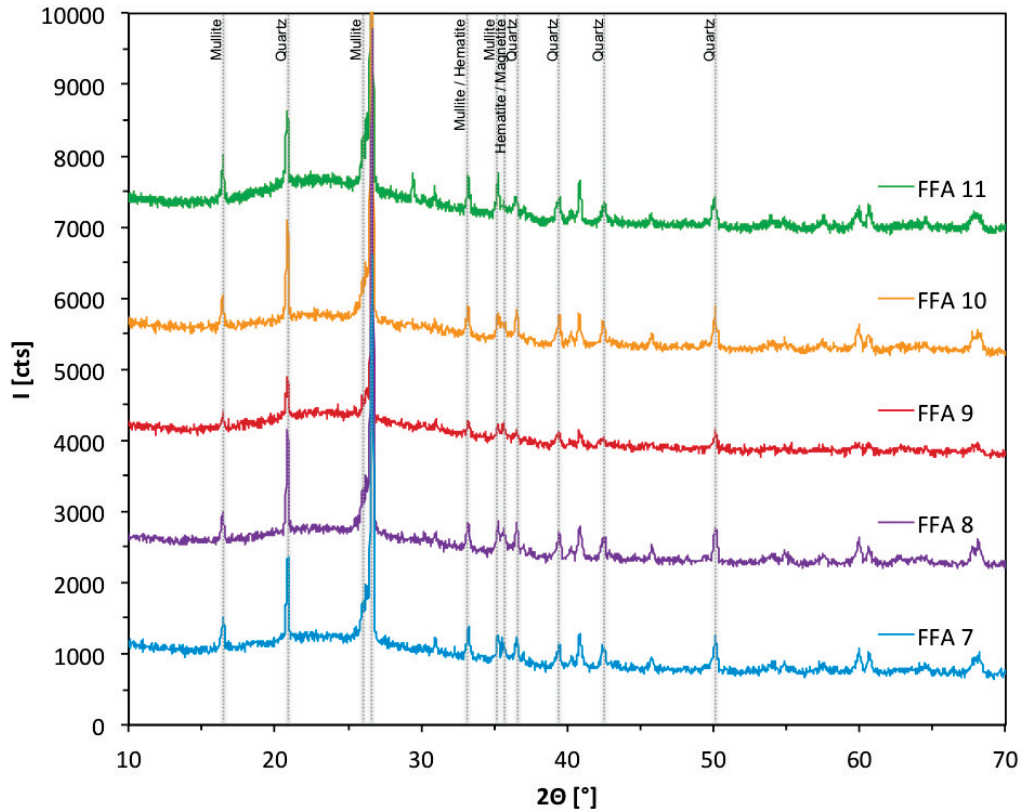


Figure 4.1: X-ray diffractograms of the siliceous fly ashes studied.

Iron oxides, hematite and magnetite, totalled around 2 wt.%. The ratio between quartz, mullite and iron oxides seems to be largely conserved, but none of these crystalline phases is reactive in cement [84]. This has an important implication on the reactivity of fly ash. The crystalline phases in these ashes account for 20 wt.% to 40 wt.%.

The X-ray diffractograms obtained for the calcareous fly ashes are presented in Figure 4.2 and the quantitative analysis of the crystalline phases in Table 6. The diffractograms contrast those of the siliceous fly ashes as different peaks are present and these diffractograms differ noticeably between themselves. This is not surprising, as calcareous fly ashes may be very variable and heterogeneous. The identified crystalline phases include quartz and may include mullite and the iron oxides, however in significantly lower quantities. The exception is CFA 5 which contains 35.8 wt.% quartz. The phase composition of calcareous fly ashes is influenced by larger quantities of calcium. Crystalline gehlenite (C_2AS) and anorthite (CAS_2), nonreactive in cement [84], reached 19 wt.% in the two CFA4 ashes, 8.5 wt.% in CFA5 and 4.5 wt.% CFA6. Reactive Ca-bearing phases present in the calcareous ashes included anhydrite, free lime, clinker phases such as C_3A , C_2S and C_4AF , as well as traces of Ye'elimite.

Table 4.5: XRD-Rietveld phase analysis of the siliceous fly ashes studied [wt.%]

	FFA 7	FFA 8	FFA 9	FFA 10	FFA11
Quartz	18.6	21.9	10.0	19.7	13.2
Mullite	16.9	17.4	7.0	17.5	13.3
Hematite	1.1	1.0	0.5	1.1	0.7
Magnetite	1.1	1.4	0.9	1.4	-
Calcite	-	-	-	-	1.1
Amorphous	62.3	58.3	81.5	60.4	71.7

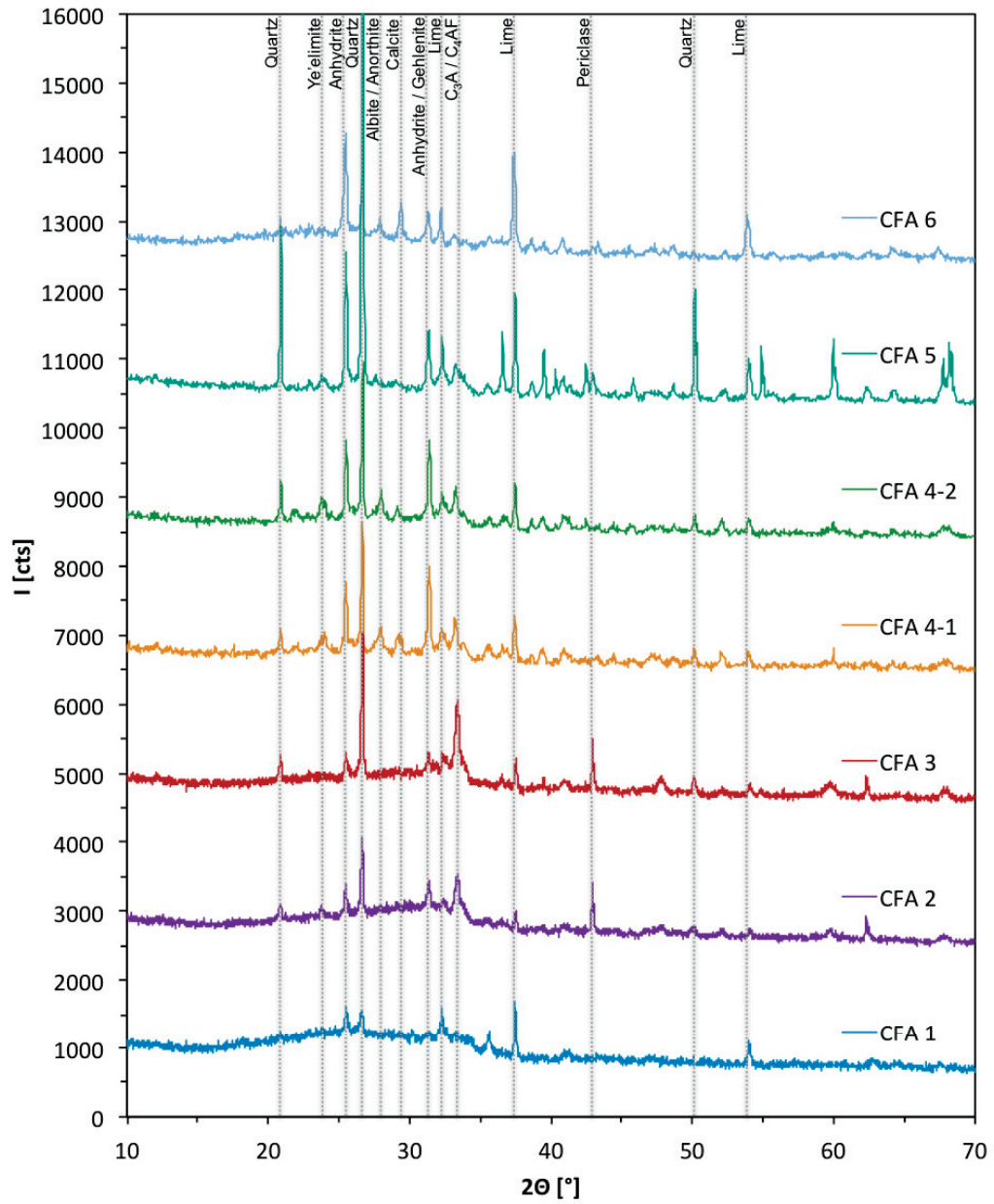


Figure 4.2: X-ray diffractograms of the calcareous fly ashes studied.

Table 4.6: XRD-Rietveld phase analysis of the calcareous fly ashes studied [wt.%].

	CFA1	CFA2	CFA3	CFA 4-1	CFA 4-2	CFA 5	CFA 6
C ₃ A	1.0	4.0	8.6	4.5	4.2	2.8	0.2
C ₂ S	2.5	0.5	2.6	3.9	7.4	5.3	-
C ₄ AF	2.0	1.5	2.7	3.1	1.8	4.0	0.7
Gehlenite	-	-	-	10.1	8.2	4.8	0.4
Albite	-	-	-	1.1	-	-	-
Anorthite	-	-	-	9.1	9.7	3.6	4.2
Ye'elimite	-	-	-	0.7	1.1	0.6	-
Anhydrite	1.8	2.0	1.7	6.4	6.5	10.5	8.6
Free lime	1.7	0.6	1.1	2.2	2.0	5.4	6.6
Calcite	-	-	-	1.8	0.1	1.2	3.6
Periclase	-	2.0	2.7	-	-	3.0	0.4
Quartz	1.3	3.5	5.5	7.3	7.9	35.0	2.6
Mullite	-	-	-	4.3	6.0	-	2.0
Hematite	-	-	-	1.1	0.4	1.2	0.7
Amorphous	89.7	85.9	75.1	44.4	44.7	22.6	70.1

The anhydrite content varied between 2 wt.% and 10 wt.% and that of free lime between 2 wt.% and 7 wt.%. Large amount of anhydrite may cause false setting when the anhydrite reacts to gypsum during mixing, which can cause rheological problems. Further, large amount of anhydrite means large amount of sulfate available for reaction. In composite cements, there exists an optimum amount of sulfate for strength which should not be exceeded. Excess sulfate will overly slow down the early aluminate reaction. In hardened concrete, excess sulfate could lead to expansion and cracking [85]. Free lime may also lead to expansion, but only if the grains are too large to react before the concrete sets.

The amount of clinker phases varied between the fly ashes from around 6 wt.% in CFA1 and CFA2 to around 14 wt.% CFA3. An exception was CFA6, which contained almost no clinker phases. The presence of clinker phases has often been pointed out as the reason for higher reactivity of calcareous fly ashes.

4.3.2 Amorphous phase

While the reactive crystalline phases may account for around 20 wt.% of fly ash it is the amorphous part that dominates the composition (50 up to even 90 wt.%). The reactivity of the amorphous fraction must be scrutinized as it may actually be of higher importance than that of the clinker phases coming from the ash. What is more, it is unlikely that the clinker phases in fly ashes form as separate grains but they rather crystallize inside of glass particles where the cooling is the slowest, as it is the case for other crystalline phases, e.g. mullite [86]. Embedded in glass, the fly ash clinker phases may not be able to react until the glass is consumed.

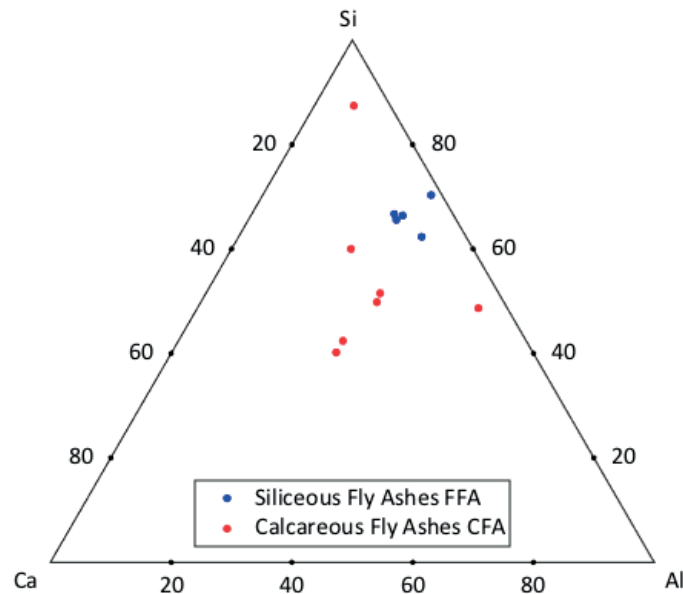


Figure 4.3: Calculated bulk chemical composition of the glass in the fly ashes studied. The data was recalculated to show the amounts of the main elements in fly ash glass: Al, Si, Ca.

A key aspect of the work in this thesis is therefore the composition and ultimately the reactivity of fly ash glasses. Unfortunately, the XRD data (Figure 4.1 and 4.2) does not provide any detailed information about the chemical composition of amorphous phases. Diamond [87] related the position of the diffuse scattering maximum to the type of glass present in fly ash. He observed that the diffuse scattering maximum usually centres near the main peak of the crystalline phase which the glass would devitrify into. He therefore suggested that glass present in fly ash may belong to one of two types. The glass of siliceous-type structure was attributed to ashes of $\text{CaO} < 20 \text{ wt.}\%$ and that of calcium aluminate-type structure to ashes of $\text{CaO} > 20 \text{ wt.}\%$. For the first type he observed a shift towards higher 2θ angles with increasing Ca content in the glass and related that to structural changes. Further work by Goto *et al.* [88] investigated this relation for fly ashes of CaO content from around 30 wt.% to 50 wt.%. The diffuse scattering maximum was found at lower 2θ angles than what could have been expected from the work of Diamond and it again shifted towards higher angles with increasing CaO content. Theoretically, XRD should be able to differentiate between amorphous phases by the position of their diffuse scattering maxima if their structures are sufficiently different. However due to the large heterogeneity and variability of fly ash glass the contributions of the individual glassy components overlap too much to be clearly identified.

With the possibility to quantify the crystalline phases in fly ash by Rietveld refinement we can combine the XRF and the XRD data and calculate the bulk chemical composition of the amorphous part. The amounts of oxides contained in the crystalline proportion are subtracted from the bulk oxide data. The result for the ashes studied is presented in Figure 4.3.

It shows a clear difference between the two fly ash types, but this representation suffers from a significant drawback; it may appear that fly ash glass is homogeneous in its composition, which is not true. Fly ash glass is known to be heterogeneous and may contain multiple phases of differing chemical composition.

4.4 Backscattered electron imaging

A significantly improved assessment of the fly ash composition can be carried out using scanning electron microscopy (SEM). Observation with the backscatter electron detector (BSE) can distinguish areas of differing mean atomic number Z . Brighter grey levels correspond to areas with higher average atomic number as these backscatter more of the incident electrons.

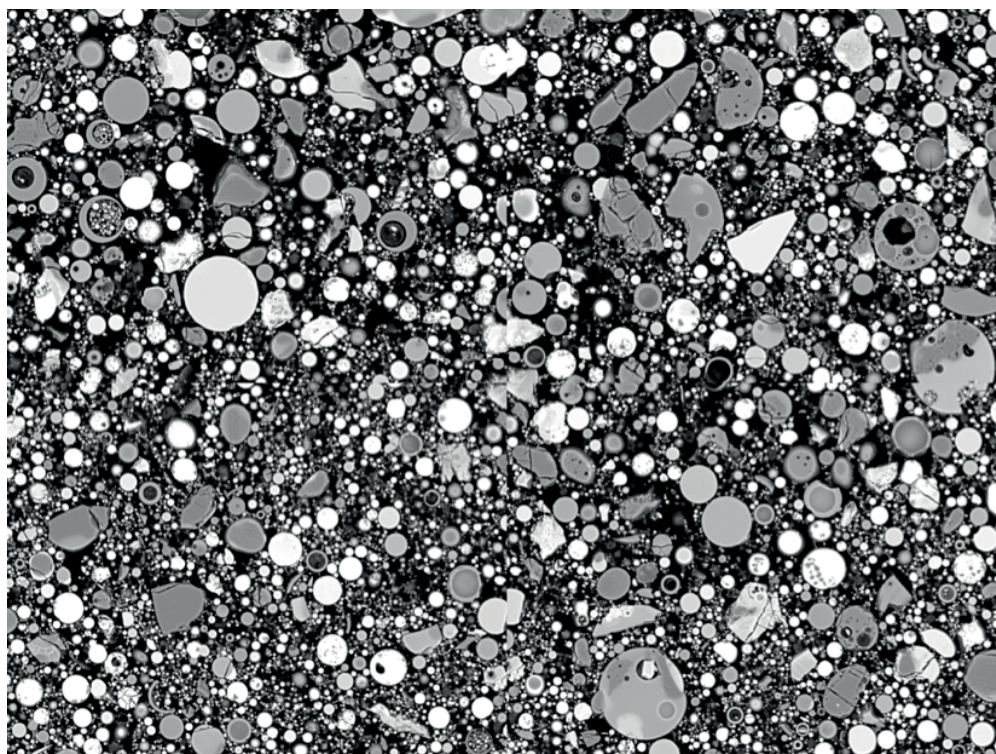


Figure 4.4: BSE image of a polished section of an epoxy impregnated raw CFA2.

A BSE image of a raw calcareous fly ash CFA2 in Figure 4.4 reveals a very complex microstructure and a multitude of phases distinguished by their grey levels. This heterogeneity is likely due to differences in composition of the source coal particles. The coal particles may contain different minerals, clays, shale, feldspars. As their combustion and cooling occurs locally the melt does not undergo homogenization. Instead, different particles would most likely contain dissimilar proportions of the above mentioned minerals that would then fuse to give glasses of different composition. Multiphase grains may form due to several particles fusing together, due to phase separation in glass melt and due to differential cooling. Phase separation is common in multi-component glass melts [14, 89, 90, 91] and glass present in fly ashes, especially

4.5. Energy-dispersive X-ray spectroscopy and image analysis

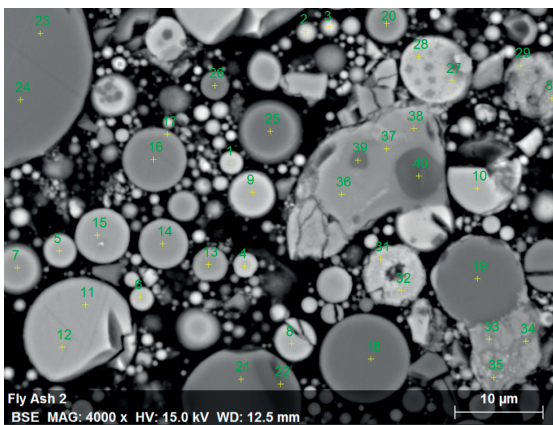
calcareous, may contain large amounts of Ca, Mg, Na and K. Differential cooling is caused by the varying rates at which heat is passed through the glass and given off at its surface.

Despite the large heterogeneity of the fly ash microstructure, we can identify at least three major glass populations: of a dark, a medium and a bright grey level. It is of high interest to study these different fly ash glass populations in detail individually. These populations cannot be separated mechanically for individual XRF or XRD analysis.

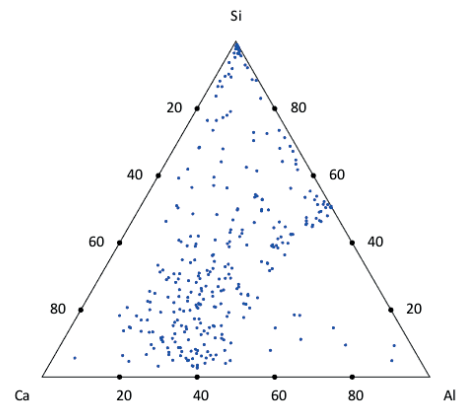
4.5 Energy-dispersive X-ray spectroscopy and image analysis

4.5.1 Point analysis and mapping

BSE images only show differences in atomic number of the analysed areas. More detailed information on chemical composition of individual glass particles can be obtained using SEM-EDS. In a manual mode the operator selects points for analysis as shown in Figure 4.5a. The analysis provides full elemental composition for each of the points. This data can be plotted in a ternary plot of key elements present in the system, here Al, Si and Ca (Figure 4.5b). Typically several hundred points need to be analysed, which makes it very tedious, especially if using older type slow EDS detector. The amount of collected data may be enough to analyse a homogeneous material such as slag or synthetic glass but clearly insufficient to assess the very heterogeneous fly ash composition.



(a) A BSE image with points selected for point EDS analysis



(b) Al-Si-Ca ternary plot containing data from around 150 EDS points shows large scatter of composition

Figure 4.5: EDS point analysis. This technique is highly insufficient against the very significant heterogeneity of fly ash, notably calcareous fly ash.

The advent of the new type of fast EDS detectors makes it possible to significantly increase the amount of data collected. In a mapping mode, a full spectrum is automatically collected for each pixel of an entire image frame and several frames one after the other. The spectra

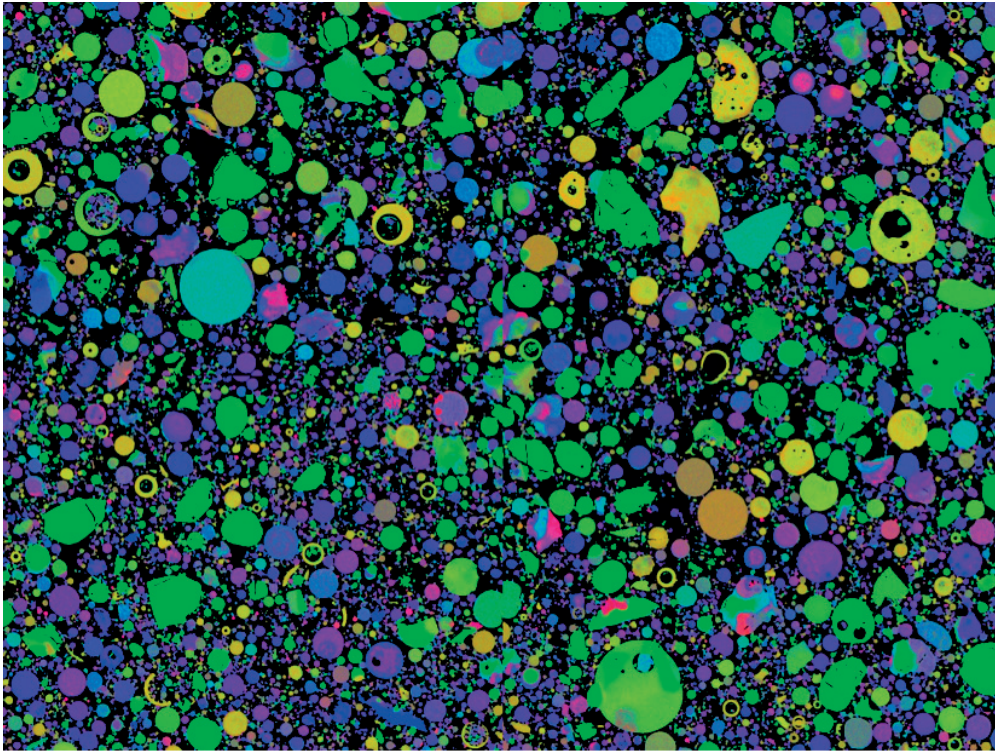


Figure 4.6: Visual representation of the distribution of elements measured by EDS (CFA2).

are processed into a set of images representing element intensity maps. Such EDS mapping data can be displayed as an overlay of the element intensity maps in which each of them is attributed a colour. In Fig. 6 the same frame as in Fig. 4 is presented with: red - Al, green - Si, blue - Ca. EDS mapping offers a significant increase in chemical resolution over the BSE images. We can now clearly identify that several populations are present in the CFA2 microstructure. Green grains likely correspond to silicate glass or quartz grains in an unchanged form as in the origin coal. Brown and orange grains are expected to be predominantly aluminosilicate while blue and violet calcium-aluminosilicate.

The colour representation as in Figure 4.6 gives some insight into the composition and microstructure of fly ash but the real potential of this technique lies in the complete elemental information acquired by the EDS. This large amount of data opens new possibilities for a more detailed and a more statistically accurate description of fly ash composition. However, robust tools are needed to treat the large datasets and accurately segment EDS maps to extract the different fly ash populations.

4.5.2 Algorithm-aided image analysis

Chancey *et al.* [26] described an approach to analyse EDS maps of a siliceous fly ash. X-ray intensity maps are analysed using MultiSpec®[27], a multispectral image analysis software

4.5. Energy-dispersive X-ray spectroscopy and image analysis

developed to treat geographic satellite data. MultiSpec® contains a clustering algorithm that identifies and quantifies populations of mutually exclusive chemical compositions. The display of a segmented image gives insight into the microstructure, notably location of phases and intermixing. This technique can treat large amounts of data but the interpretation may be complicated and may require a skilled operator.

The use of the mentioned algorithm requires the operator to specify the number of target clusters, i.e. the number of phases present in fly ash, mostly glasses. This technique was initially proposed for measurement of modal mineralogy of rocks [25]. While an approximate mineral composition of a studied rock may be known prior to the analysis, this is impossible in the case of fly ash. Therefore, the number of clusters has to be guessed or has to be determined by the algorithm purely from statistics of the dataset. This procedure may become strongly operator-dependent or might lead to inconsistent results. The number of identified clusters may fluctuate with the fluctuation of measured composition due to significant fly ash heterogeneity.

We strongly feel that the operator input can significantly contribute to the analysis and that complex, purely statistical algorithms and "black box" data processing software should be avoided, if possible.

4.5.3 A new approach to process the EDS full element map data

In this work we propose a new treatment of the SEM-EDS element maps. The X-ray intensity maps are treated with PhiRhoZ matrix corrections, which produces quantitative data of atomic-% of elements for each pixel of the analysed frame. To ensure maximum control over the segmentation and subsequent analysis the atomic-% data is extracted from the microscope's software not as images but in a numerical form. Such obtained dataset contains full elemental composition of several million points. All of this data is plotted in a single ternary diagram with the key elements: Al, Si, and Ca in the apexes. Because the number of points is so large the diagram was modified to display the number of points of particular chemical composition instead of the points themselves. This way, groups of similar chemical compositions appear as blobs in the diagram so the user can readily distinguish them and evaluate their ranges and scatter. Such defined ranges of composition are then used as input for precise image segmentation. Segmented populations:

- can be displayed back in the BSE image to facilitate the analysis of the microstructure,
- can be used as a mask to extract the complete chemical information of their constituting particles,
- can be quantified in volume fractions, which sets a baseline for quantitative comparisons of different populations.

The exact description of how a ternary frequency plot is made can be found in Appendix A.1.

4.6 Detailed SEM-EDS analysis of a calcareous fly ash

A first analysis of CFA2 with the new technique revealed that despite large overall scatter due to intrinsic heterogeneity CFA2 was composed of several populations readily distinguishable in the Al-Si-Ca ternary frequency plot (Figure 4.7). The spread of the populations in the plot varies from small spots for well defined compositions to large regions covering ranges of compositions. The Si- and aluminosilicate- dominated populations are represented by high and narrow peaks, which suggest a reduced range of chemical compositions and large abundance. The Ca-rich aluminosilicate population has a diffuse shape of nonetheless high intensity. This phase or group of phases seems the most abundant in the fly ash but its chemical composition spans a large section of the ternary graph. Intermediate phases such as calcium-silicates with moderate Al and aluminosilicates with moderate Ca are well defined but present in lower amounts. Phases appearing at the 100 % Ca corner typically include free lime (CaO), calcium sulfates and calcium carbonate (calcite). Crystalline phases often identified in fly ashes and their location in the Al-Si-Ca plot are shown in Figure 4.8 CFA2 contains around 4 wt.% C₃A by XRD-Rietveld analysis, which appears in the ternary frequency plot as a group below the calcium-rich aluminosilicate group. The blurred appearance of this group suggests that the C₃A may be finely intermixed with other phases or may have formed inside glassy particles, whose composition was close to that of the C₃A and favoured its formation.

The shadowed areas between blobs are due to EDS chemical information collected from a volume called the interaction volume. Close to particle edges and phase boundaries the EDS signal is composed of contributions of all the phases within the interaction volume. This issue is described in more detail in Appendix A.4.

Phases whose content is low, which have a broad range of composition or which have a particle size much below the size of the interaction volume (around 1 μm) may not appear or may appear displaced in a frequency plot. The quantity of non Ca-Al-Si phases such as iron oxides and magnesium oxide (periclase) is below 3 wt.%, as determined by XRD-Rietveld (Table 4.6).

To further investigate specific fly ash groups one has to define appropriate thresholds for their selection. In this study thresholding of Al, Si and Ca was sufficient to separate the groups but in different systems any of the quantified elements may be used and the selection may include more than three elements at once. The thresholds were determined as hexagons drawn around blobs of interest in the ternary frequency plot and are illustrated with white lines in Figure 4.7. The selection thresholds for the populations should be rather wide to provide the necessary margin for often broad chemical compositions. Further, wide selection thresholds reduce the measurement error due to data scatter and potentially low content of the populations. For a more universally applicable description of fly ash composition, the selection thresholds should cover most of the area of the ternary frequency plot. We propose a segmentation of the fly ash phases into four main populations, corresponding to the regions in (Figure 4.9): (1) mainly silicate, (2) calcium-silicate with low to moderate aluminium, (3) aluminosilicate with low to moderate calcium and (4) calcium-rich aluminosilicate. Al-rich phases (> 60 atomic-%

4.6. Detailed SEM-EDS analysis of a calcareous fly ash

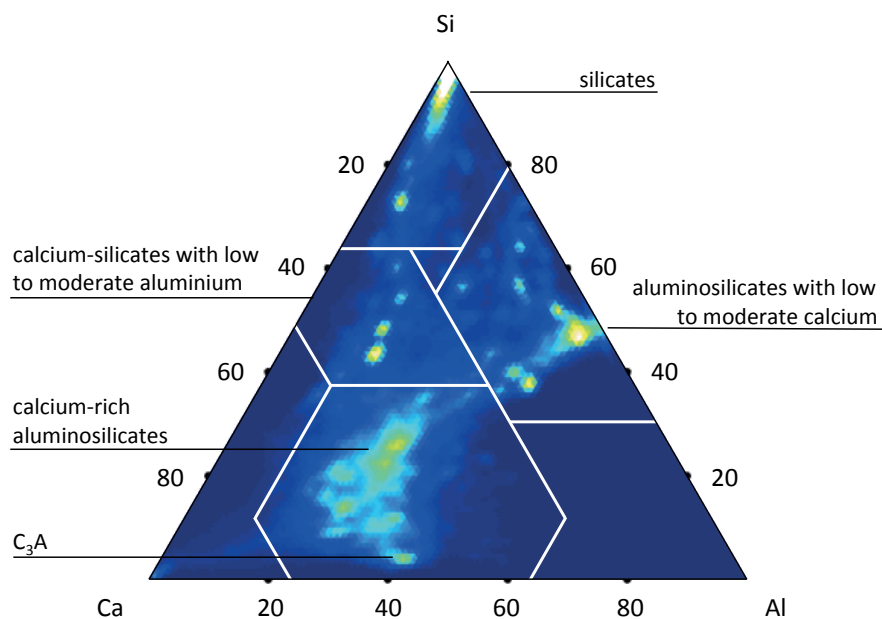


Figure 4.7: Al-Si-Ca ternary frequency plot of CFA2 chemical composition in atomic-%. White contours show the arbitrary boundaries between the groups used in this study.

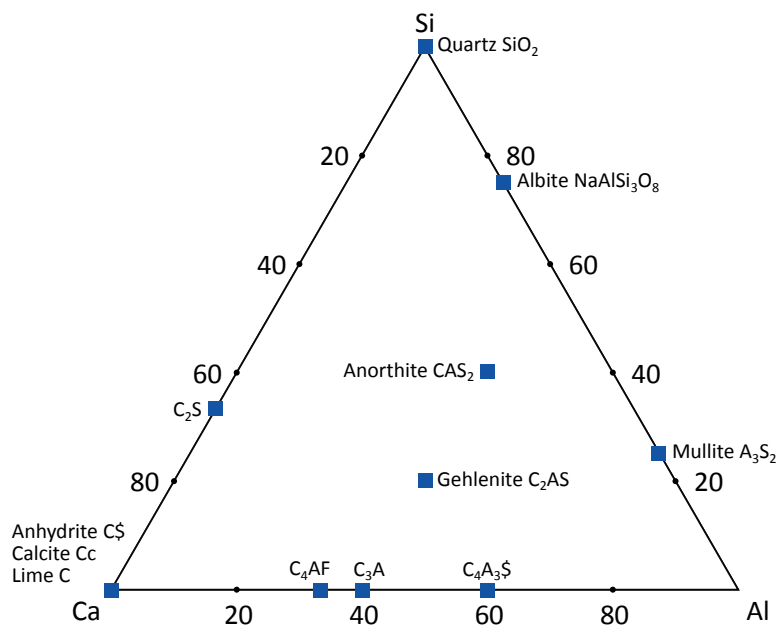


Figure 4.8: Al-Si-Ca (atomic-%) ternary plot showing main crystalline phases in siliceous and calcareous fly ashes. Anhydrite can be separated from lime and calcite in an additional plot, which has sulfur in one apex. For most formulas, cement notation is used.

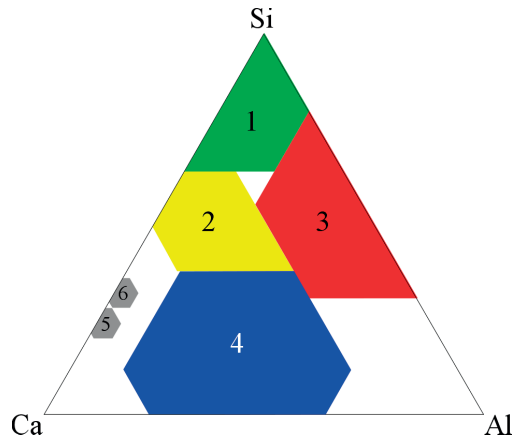


Figure 4.9: Illustration of the segmentation thresholds of the four fly ash groups, C_3S and C_2S in the image analysis. Selected areas are hexagons centred around the points of highest intensity found in the studied fly ashes. The exception is group 2, whose area was extended towards Al (+13 atomic-%). Using hexagons for selection leaves some areas unselected.

Table 4.7: Segmentation thresholds in the image analysis: coordinates of the centre points of the hexagonal areas and their spread.

	Phase	Al	Si	Ca	(+/-)
1	Silicate	-5	89	16	24
2	Ca-silicate	11	51	38	13
3	Al-silicate	44	56	0	24
4	Ca-Al-silicate	38	12	50	25
5	C_3S	1	24	75	4
6	C_2S	1	32	67	4

Al) are typically not encountered in fly ashes. Ca (> 80 atomic-% Ca) and Ca-Si (< 10 atomic-% Al) areas essentially contain crystalline phases such as free lime, calcium sulfates, calcite, C_2S and C_3S , which are assessed by XRD-Rietveld. The segmentation was carried out by applying thresholds on the content of normalized Al, Si and Ca atomic-% (Figure 4.9). The resulting segmentation was considered reasonable as the segmented areas largely correspond to entire particles or major parts of particles (Figure 4.10).

The chemical composition and microstructure of the populations that were identified in CFA2 was investigated in more detail. Figure 4.10 left shows plots of the distribution of the minor elements (Na + K) - Mg - Fe. These show that the composition of the populations 1, 3 and 4 is fairly homogeneous and they do not need to be further divided into sub-populations. There do appear to be different sub-populations in the Ca-silicate population (2), which are actually due to the two large grains visible in the associated map. Large importance of these grains is due to low overall amount of this population. For the same reason its further separation, although possible, did not seem justifiable from a practical point of view. The complete average chemical compositions of the four populations are given in Table 4.8. Mg seems to

4.6. Detailed SEM-EDS analysis of a calcareous fly ash

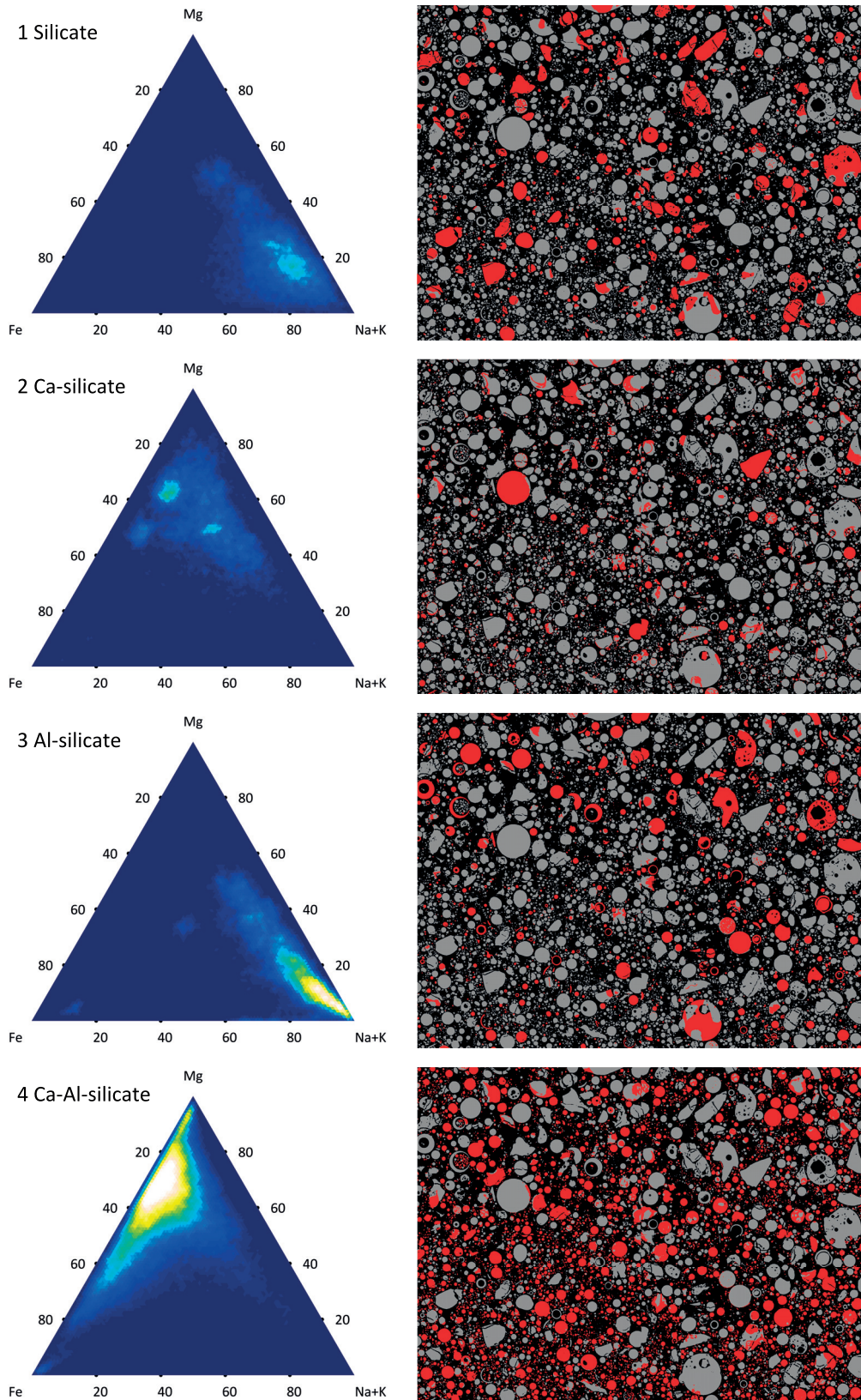


Figure 4.10: More detailed investigations provide an insight into chemistry (left) and morphology (right) of the fly ash populations.

Chapter 4. Fly ash characterization

Table 4.8: Mean chemical composition determined by SEM-EDS for the four populations identified in CFA2.

		1 Silicate		2 Ca-Silicate		3 Al-Silicate		4 Ca-Al-Silicate	
Al	$\frac{Al}{Al+Si+Ca}$	0.8	2	5.9	18	12.7	40	9.7	29
Si	$\frac{Si}{Al+Si+Ca}$	30.1	94	15.0	47	15.7	49	7.1	21
Ca	$\frac{Ca}{Al+Si+Ca}$	1.2	4	11.3	35	3.5	11	16.6	50
Al+Si+Ca		32.1	100	32.2	100	31.9	100	33.4	100
Na + K	$\frac{Na+K}{Na+K+Mg+Fe}$	1.4	65	2.0	29	5.3	72	0.7	10
Mg	$\frac{Mg}{Na+K+Mg+Fe}$	0.4	20	3.7	53	1.3	18	4.7	63
Fe	$\frac{Fe}{Na+K+Mg+Fe}$	0.3	15	1.3	18	0.7	9	2.0	27
Na+K+Mg+Fe		2.1	100	6.9	100	7.3	100	7.4	100
Oxygen and trace elements		65.8		60.8		60.8		59.1	

be more abundant in Ca-rich glasses and the content of Mg increases with Ca content, in the order of population $1 < 3 < 2 < 4$. This is probably because Mg and Ca cations have the same charge, which could facilitate their exchange or coexistence in glasses. Iron content seems to follow the same trend, $1 < 3 < 2 < 4$. Alkalis on the other hand, an opposite tendency as they are present in larger amounts in glasses poor in Ca. An exception here is the silicate population (1), which contains almost only Si and only small amounts of other elements.

Image overlays visualize the populations in the fly ash microstructure (Figure 4.10). Combining chemical and morphological information allows a qualitative correlation of the glass chemical composition and the particle sizes. Ca-rich aluminosilicate glasses tend to form smaller particles while Si-rich and aluminosilicate glasses tend to form larger ones. Further, the size of particles may affect the cooling rate of the glass and thus the spread of chemical composition observed in the frequency plot. Small Ca-rich aluminosilicate particles may cool very quickly causing the chemical compositions to "freeze" before phase separation occurs and leading to more spread ranges of chemical composition. Large particles are expected to cool down more slowly, allowing more pronounced phase separation or even devitrification and thus better defined blobs in the ternary plot.

Hollow particles, cenospheres, are present in CFA2. Although the mechanism of formation is not well understood [92], the uniform Al/Si ratio of cenospheres found in various studies suggests [93] that certain glass compositions may favour cenospheres formation, notably compositions corresponding to anauxite, or kaolinite with excess silica. Practically all of the cenospheres in CFA2 of this study belong to the aluminosilicate group, whose composition is the close to that of kaolinite.

4.7 SEM-EDS image analysis: comparison of selected fly ashes

Ternary frequency plots of all the fly ashes studied are presented in Figure 4.11. The information given by the frequency plots is much more complete than that of the average glass composition in Figure 4.3. The difference in composition between calcareous (Figure 4.11a-g) and siliceous (Figure 4.11h-l) fly ashes is striking.

The siliceous fly ashes are basically composed of silicate and aluminosilicate populations. The Al/Si ratio in the aluminosilicate population of all the studied siliceous ashes ranges from 50/50 to around 30/70 atomic-%.

The calcareous fly ashes contain much more and much more diverse populations. The presence of calcium clearly increases the spread of compositions. Beside the silicate and aluminosilicate populations that are common for the majority of these ashes, some of them may contain Ca-silicates and significant amounts of Ca-rich aluminosilicates. The aluminosilicate population in calcareous fly ashes seems to be different from that in the siliceous ashes. The Al/Si ratio is less spread and centres around 50/50 (Figure 4.11b, c, d, e, f, g) or 45/65 (Figure 4.11a, c, d, e) or 25/75 (Figure 4.11g) atomic-%. Calcium content in this population is clearly higher, up to $\text{Ca}/(\text{Al}+\text{Si}+\text{Ca})$ around 30%.

Among calcareous fly ashes CFA2 and CFA3 seem to be very similar although they come from two different power plants. At the same time, CFA4-1 and CFA4-2 come from the same plant but from different batches. Here the difference is dramatic. These two fly ashes, CFA4-1 and CFA4-2 are an excellent example of variability that has to be dealt with when using fly ash.

Ternary frequency plots allow a quick assessment of fly ash composition, but from a practical point of view it is easier to segment the ashes into similar populations and then compare the volume fractions obtained. Because most of the fly ash glasses are expected to form in the Al-Si-Ca-Mg-Fe-alkali system or its subsystems, different fly ashes should contain similar populations, although in different proportions. In this study we segmented all of the fly ashes using criteria described in Figure 4.9. The results are shown in Figures 4.11 and 4.12. These plots clearly show major differences in composition between the two types of ashes. The studied calcareous fly ashes are significantly more complex and variable than the siliceous ones.

Quantitative comparison of the composition of the ashes studied is presented in Figure 4.13 for the siliceous ashes and in Figure 4.14 for the calcareous ones. There is very little variation in phase composition between the siliceous fly ashes. They all contain around 20 wt.% silicates and around 80 wt.% aluminosilicates. In Figure 4.13 the hatched areas correspond to quartz and mullite as determined by XRD-Rietveld. The non-hatched part represents glass. As mentioned before, crystalline quartz and mullite are non-reactive. The silicate glass is most probably non-reactive as well. The only reactive part is therefore the aluminosilicate glass. Figure 4.13 shows that the studied siliceous fly ashes contained around 60 vol.% and in case of

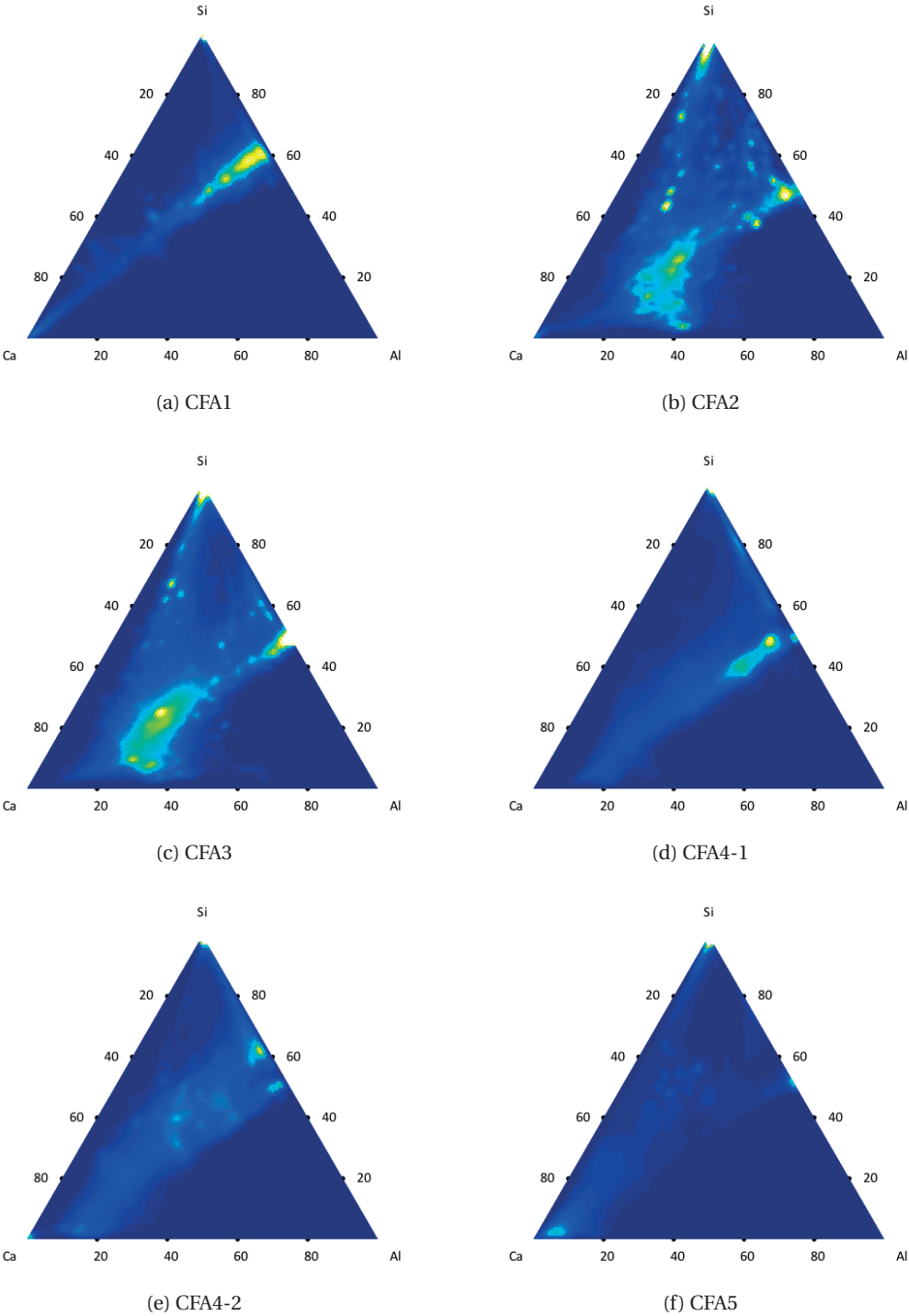


Figure 4.11: Al-Si-Ca atomic-% ternary frequency plots of the fly ashes 1-5.

4.7. SEM-EDS image analysis: comparison of selected fly ashes

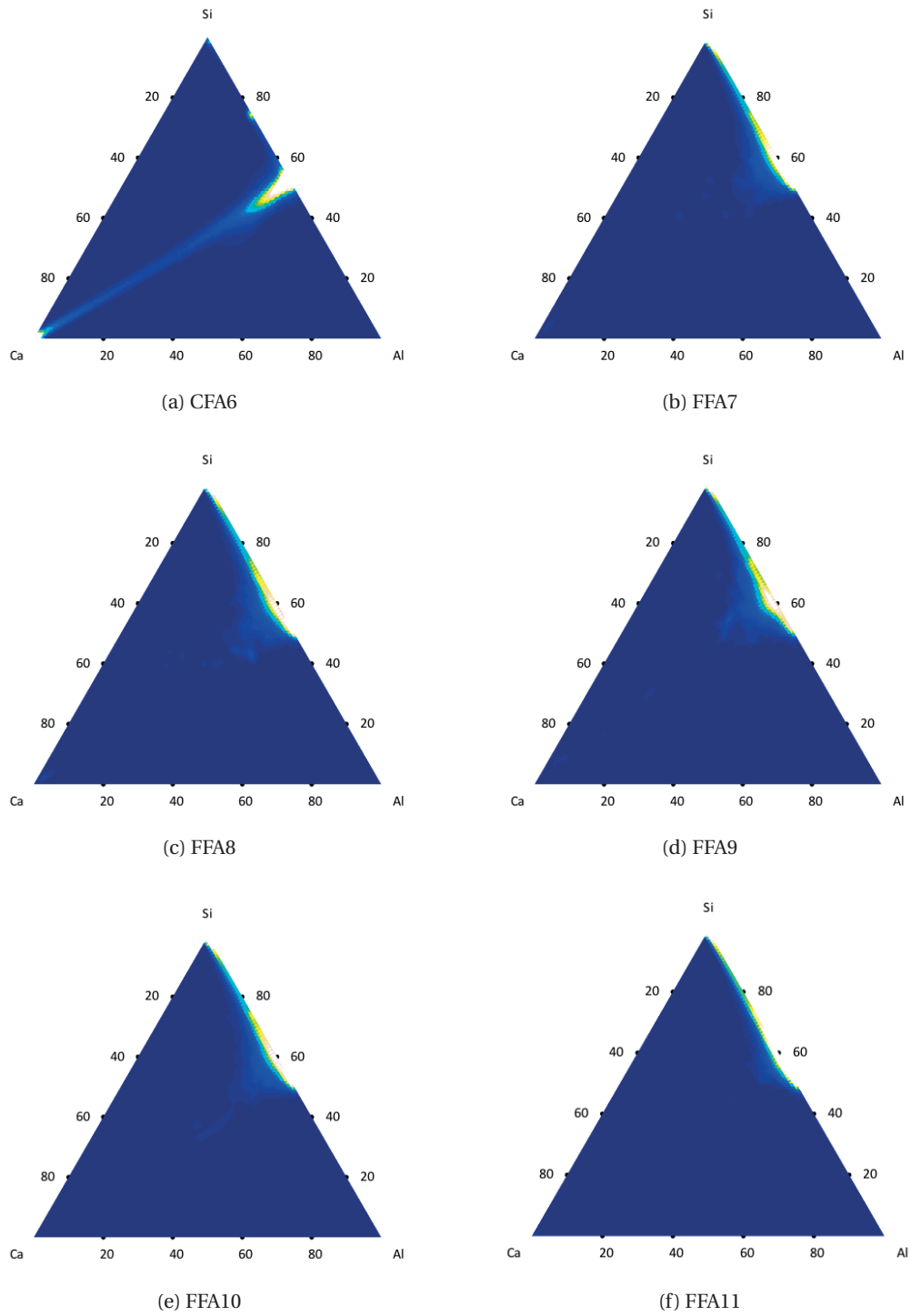


Figure 4.12: Al-Si-Ca atomic-% ternary frequency plots of the fly ashes 6-11.

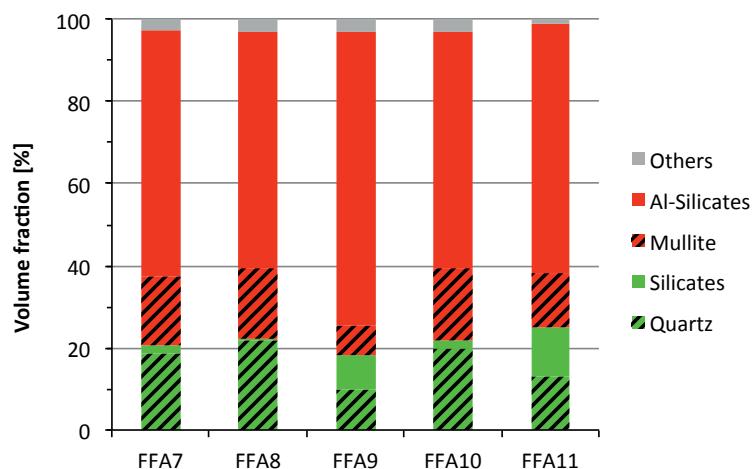


Figure 4.13: Quantitative comparison of the populations illustrated in Figure 4.9 obtained by SEM-EDS image analysis for the siliceous fly ashes. Hatched areas correspond to nonreactive crystalline phases such as quartz and mullite (XRD).

FFA9 70 vol.% of the aluminosilicate glass. This means that the reactive part is even smaller than suggested by the Rietveld refinement.

Figure 4.14 shows that for the calcareous fly ashes the situation is completely different. The presence of calcium clearly adds to the complexity of these ashes. In addition to predominantly silicate and aluminosilicate phases known from the siliceous ashes, we can also identify calcium-silicates with low to moderate Al as well as Ca-rich aluminosilicates. The actual type and proportion of the populations quantified can vary substantially depending on the ash. The predominantly silicate nonreactive fraction can make from almost none up to around 35 vol.% of calcareous ash. In many cases part of the silicate population is crystalline quartz (hatched areas in Figure 4.14). Calcium-silicates with low to moderate Al may appear in calcareous fly ashes and in most of the ashes studied here this population accounted for around 10-20 vol.%. We did not identify any crystalline phases belonging to this population. Aluminosilicates may account for 10 up to 70 vol.% of the ash. This population may contain nonreactive crystalline phases such as mullite and anorthite. The Ca-rich aluminosilicates constitute from around 10 to 50 vol.% of the calcareous ashes. This population may include nonreactive crystalline gehlenite but also the reactive clinker phases such as C_3A and C_4AF (the reactive crystalline part is not hatched in Figure 4.14). It is expected that the Ca-rich aluminosilicate glass will react the fastest and the most due to high amount of calcium. Other phases present in these ashes include predominantly anhydrite, lime and C_2S . The total content of reactive phases in the studied calcareous fly ashes ranges from 98 vol.% for CFA1 to 57 vol.% for CFA5.

An interesting question is the distribution of calcium in the calcareous ashes. According to the bulk chemical analysis (Table 4.2) the CaO content in is similar for CFA1 (20.7 wt.%) and CFA5 (21.3 wt.%) as well as between CFA2, CFA3, CFA4-1 and CFA4-2: 26.5, 27.5, 25.3 and 25.5 wt.% respectively. However, in CFA1 calcium is mostly present in the large fraction of

4.8. Comparison of aluminosilicate glasses among the fly ashes

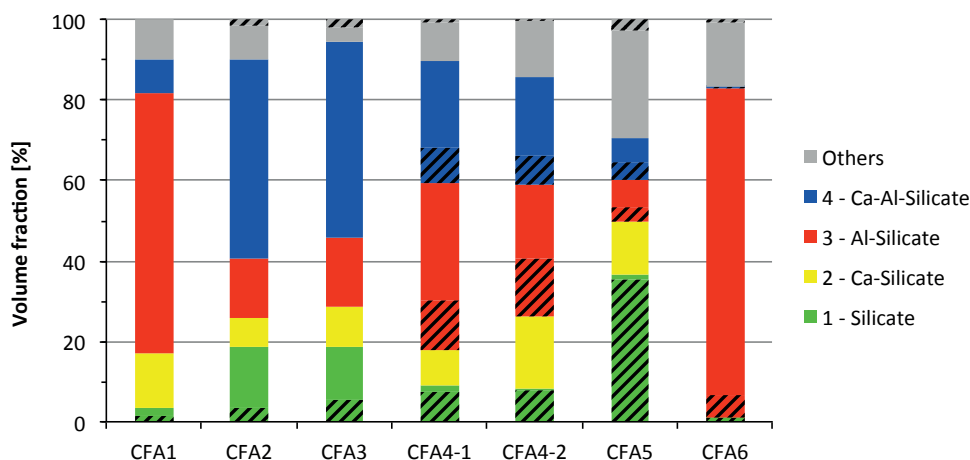


Figure 4.14: Quantitative comparison of the populations illustrated in Figure 4.9 obtained by SEM-EDS image analysis for the calcareous fly ashes. Hatched areas correspond to nonreactive crystalline phases such as quartz, mullite, anorthite, gehlenite, periclase and hematite as determined by XRD.

aluminosilicates with low to moderate-calcium. In CFA5 most Ca is found in anhydrite and lime. For the latter four ashes, in CFA2 and CFA3 most of Ca is located in the large amount of Ca-rich aluminosilicates. In CFA4-1 and CFA4-2, Ca is distributed more evenly between the aluminosilicates, Ca-rich aluminosilicates and anhydrite.

4.8 Comparison of aluminosilicate glasses among the fly ashes

The composition of the aluminosilicate populations measured by SEM-EDS (Figure 4.15) was found to be very similar among the siliceous fly ashes and slightly more variable but still very comparable among the calcareous ones. The main difference lies between the two fly ash groups. There is more Ca (around 10 wt.% CaO) and less Fe in the aluminosilicates in calcareous ashes compared to the siliceous ones. This may be expected to improve their reactivity compared to those in the siliceous ashes (around 2 wt.% CaO).

The chemical composition of the Ca-rich aluminosilicates from the different calcareous fly ashes is compared in Figure 4.16. The differences in CaO, Al₂O₃ and SiO₂ content range from none to 10 wt.%. The 10 wt.% CaO difference may have some effect on the reactivity of the populations in question. However, in the light of the strong variability of the bulk chemical composition between the calcareous fly ashes, this result actually demonstrates that the Ca-rich aluminosilicates are quite similar. Similarities between the corresponding populations in different ashes support the correctness and wide applicability of the chosen selection thresholds.

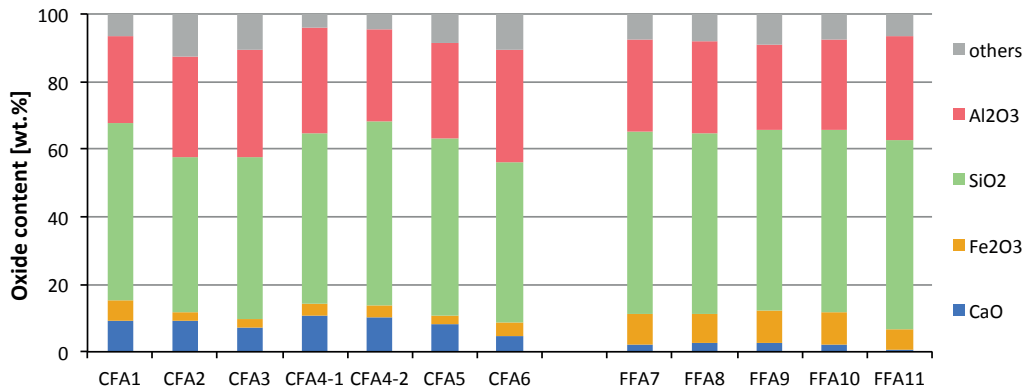


Figure 4.15: Comparison of the EDS chemical composition of the aluminosilicate population among the fly ashes studied.

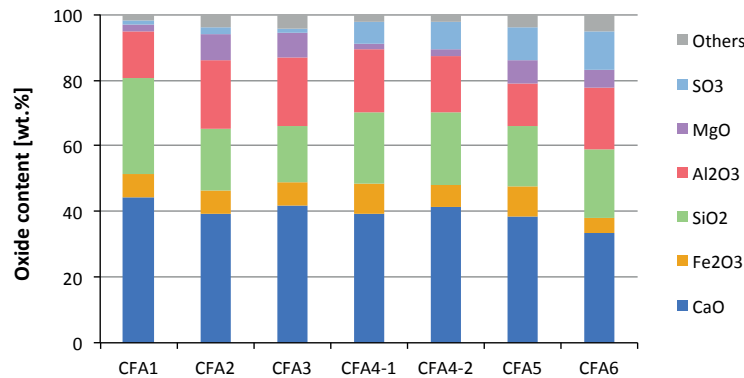


Figure 4.16: Comparison of the EDS chemical composition of the Ca-rich aluminosilicate population among the calcareous fly ashes.

4.9 Summary of fly ash characterization

Fly ash is an extremely complex and heterogeneous material and advanced techniques are needed to be able to characterize it meticulously.

- A fully-controllable EDS data treatment protocol and a ternary frequency plot were introduced, that allow a quick and intuitive identification and evaluation of chemically different fly ash components, notably amorphous.
- Four populations of predominantly silicate, Ca-silicate, aluminosilicate and Ca-rich aluminosilicate composition were identified in the studied ashes. The new method was used to quantify their proportions, determine the full chemical composition, assess the particle sizes and display their location in fly ash microstructure.
- The siliceous ashes contained only the silicate and the aluminosilicate glass. Calcareous fly ashes contained all four populations and it was found that despite similarities in bulk

4.9. Summary of fly ash characterization

chemistry the amount of each of these populations may vary significantly. This may have an important impact on the reactivity of these ashes.

As current standards neglect the inherent chemical and microstructural heterogeneity of fly ashes, many are needlessly discarded. An improved classification is needed that could be based on the content of the different populations and that would lead to an improved classification and use of calcareous fly ashes in concrete.

In a wider perspective, the presented method opens new possibilities to study supplementary cementitious materials in detail. With small adjustments it could be extended to other types of SEM-EDS data.

5 Degree of reaction of fly ash and slag in cement

Contents

5.1 Introduction	63
5.2 Adaptation of the SEM-EDS technique to measure fly ash reaction	64
5.3 Study on synthetic glasses	68
5.3.1 Glass synthesis and processing	68
5.3.2 Dissolution experiment	71
5.3.3 Hydration study of glass-portland composite cements	73
5.4 Quantitative analysis of glass reactivity in paste	78
5.5 The influence of chemical composition of glass	80
5.6 Summary on glass reactivity by SEM-EDS	84
5.7 Advances in XRD analysis - Practical implementation in HighScore Plus	85
5.7.1 PONKCS	86
5.7.2 Full Structure Method	88
5.7.3 Summary on PONKCS and FSM	91

Part of this work on the reaction of the fly ash glasses has been published in *A new quantification method based on SEM-EDS to assess fly ash composition and study the reaction of its individual components in hydrating cement paste* [84].

The study of synthetic glasses and the quantitative analysis of reaction have been published in *Fly ash as an assemblage of model Ca-Mg-Na-aluminosilicate glasses* [94].

5.1 Introduction

The main reactive component of fly ash is glass. It was shown in the previous chapter that this glass can be made up of several populations of different compositions and sizes. Since glass populations of differing chemical composition are expected to react at different rates or not react at all, the fly ash reaction should not be characterized by a unique degree of

reaction. To understand the reactivity of fly ash, it is essential to track the reaction of each of the glass populations separately. In the previous chapter a new SEM-EDS technique was used to segment fly ashes into glass populations. In this chapter the same technique is used to extract and quantify the amount of each of these populations individually in a hydrating fly ash-cement paste. To study the reaction of fly ash-type glasses in more detail, model glasses were synthesised. Batch dissolution experiment gave an insight into the dissolution potential of these glasses. The SEM-EDS technique was used to track the consumption of these glasses in paste, which was compared to the consumption of glasses in real fly ash. Quantitative analysis of the reaction decoupled the effect of particle size and showed a clear trend to higher intrinsic reactivity with increasing disorder of the glass structure. Advanced XRD refinement was developed in attempt to track the glassy part of fly ash and compare with the SEM-EDS results.

5.2 Adaptation of the SEM-EDS technique to measure fly ash reaction

The same SEM-EDS technique that was used to segment unreacted fly ash into glass populations was adapted to quantify the reaction of these populations in hydrating cement paste. The main modification was a supplementary filter to mask out the hydrated phases that overlap in the Al-Si-Ca ternary density plot with the anhydrous populations of interest. Assuming that all the elements are present as oxides, the stoichiometric oxygen is calculated and summed up for each pixel separately. Because hydrates contain water and hydrogen is not detected by EDS, the total amount of the quantified elements as well as the total respective oxygen is lower in hydrates compared to anhydrous phases. The difference in total stoichiometric oxygen between hydrates and anhydrous phases can be seen in the B' histogram in Figure 5.1. In practice, pixels with less than 55 atomic-% of the total oxygen were assigned to hydrates and removed from further analysis. This threshold value was determined empirically and worked best for all the investigated mixes. Slight variations most likely due to a bias in calibration of the microscope are possible and can be corrected by modifying of the threshold. This process was not automated because in some of the samples there was no clear minimum between the hydrates and anhydrous contributions. In some cases it was necessary to test several thresholds and verify the obtained segmentations to chose the one with the least hydrates and the least pixels removed from the anhydrous particles. Slight shifts in the threshold value in the range of several % were observed, most likely related to variation in the calibration of the microscope and the quantification of element contents from the spectra.

The previously defined thresholds (Table 4.7) were used to assign pixels of the EDS maps to the four main fly ash populations, as before: (1) silicate, (2) Ca-silicate, (3) aluminosilicate, and (4) Ca-rich aluminosilicate. Noise filtering was carried out using an open (erode-dilate) morphological operation with a diamond shaped structuring element of 3-pixel distance from the structuring element origin to the points of the diamond. For each of the populations, the number of segmented pixels was divided by the total number of pixels in the frame to give an

5.2. Adaptation of the SEM-EDS technique to measure fly ash reaction

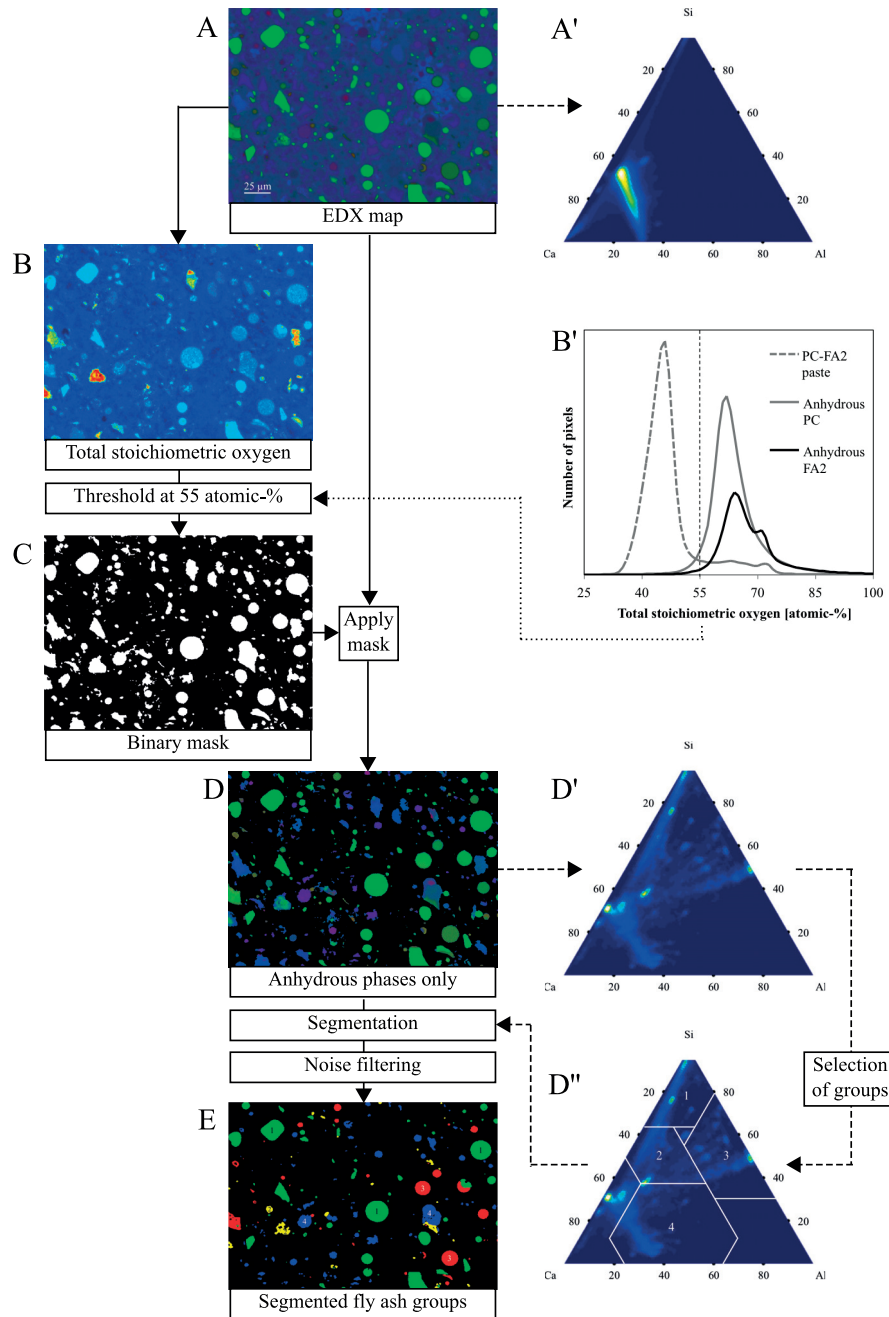


Figure 5.1: The amounts of elements in each pixel of an EDS map (A) are used to calculate total stoichiometric oxygen (B). Thresholding at 55 atomic-% of oxygen (B') provides a mask (C) to remove the hydrates from the initial EDS map (A) leaving only the anhydrous phases (D). Selection thresholds (D'') are used to extract the four main fly ash populations (E).

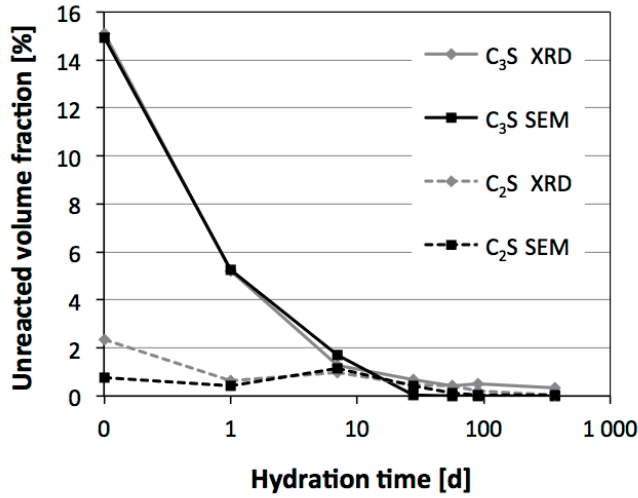


Figure 5.2: Quantification of C₃S and C₂S by SEM-EDS and XRD in PC-CFA2 showing a close correlation of the two techniques. Typical uncertainty ± 0.5 wt. %.

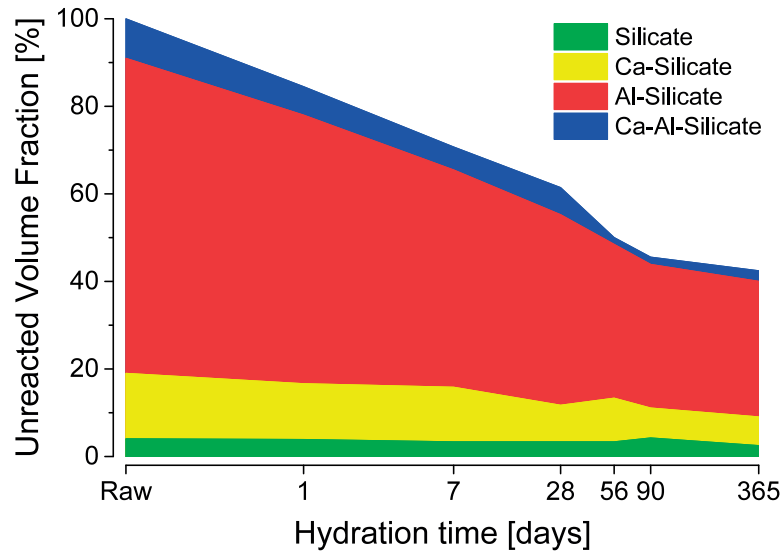
area fraction (equivalent to volume fraction). The values at time zero were calculated from the mass proportions of portland clinker, calcareous fly ash and water in the mix and their densities ρ :

$$vol_{FA} = \frac{\frac{m_{FA}}{\rho_{FA}}}{\frac{m_{PC}}{\rho_{PC}} + \frac{m_{FA}}{\rho_{FA}} + \frac{m_{H_2O}}{\rho_{H_2O}}} \quad (5.1)$$

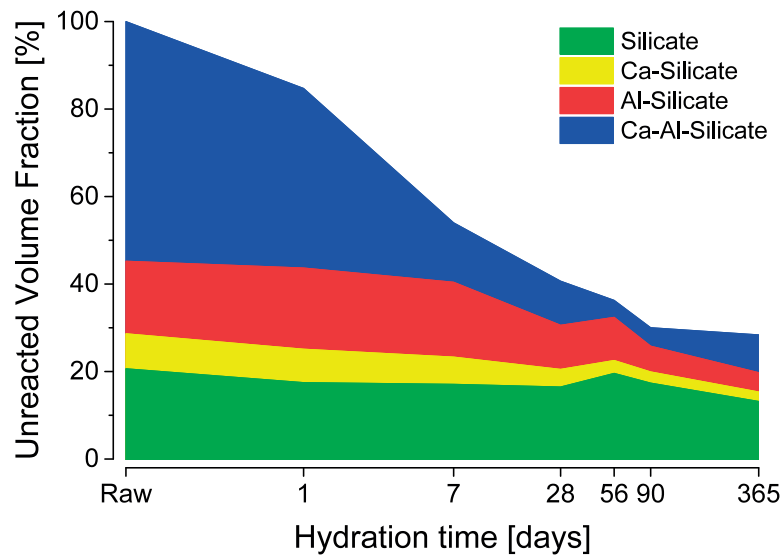
In the case of population 4 (Ca-rich aluminosilicate), it was necessary to account for its overlap with the anhydrous C₃A and C₄AF phases from portland clinker. The volume fractions of C₃A and C₄AF, unreacted at each time and including those from CFA, were computed from XRD-Rietveld quantification results and subtracted from the volume fractions of the population 4. To verify that such operation did not carry a significant error, a comparison between SEM-EDS and XRD was made. Quantification of C₃S and C₂S in PC-CFA2 showed only minor differences between the two techniques (Figure 5.2).

The reaction of fly ash was studied on paste samples PC-CFA1 and PC-CFA2 which contained 55 wt.% PC and 45 wt.% FA. Preparation of these samples is described in the section 3.2.1 of the Materials and Methods. The individual unreacted volume fractions of each of the four fly ash populations in PC-CFA1 and PC-CFA2 pastes were obtained after 1, 7, 28, 56, 90 and 365 days of hydration (Figure 5.3). The points were joined with lines to guide the reader's eye and facilitate visual assessment of the results. The overall trends are quite smooth as local fluctuations tend to cancel out, which raises confidence in the results and suggests that the observations made using this method are quite robust.

5.2. Adaptation of the SEM-EDS technique to measure fly ash reaction



(a) PC-CFA1



(b) PC-CFA2

Figure 5.3: Consumption of the anhydrous fly ash populations in hydrating pastes. Clinker phases from fly ashes are excluded. Typical error of $\pm 5\%$ may be higher at 1 and 7 days of hydration due to limited resolution of the finest particles by electron microscope.

Figure 5.3 shows that the CFA1 and CFA2 investigated here contain significantly different proportions of the four main populations at different hydration times. These populations clearly contribute differently to the reaction of fly ash. The silicate phases hardly react at all, which has little importance for the reactivity of CFA1 (around 5 wt.% silicates) but for CFA2 (around 20 wt.% silicates) means that one fifth of this fly ash will never react. CFA1 is mainly composed of aluminosilicates with low to moderate calcium (70 vol.%) and calcium-silicates with low to moderate aluminum (15 vol.%), while in CFA2 these two phases account together

for only around 20 vol.%. These two populations react at a moderate pace and reach around 60 % degree of reaction after one year of hydration. CFA2 contains a significant amount of around 55 vol.% of Ca-rich aluminosilicate phases, which in CFA1 are only present in a small quantity, below 10 vol.-%. These calcium-rich aluminosilicates are by far the most reactive, exceeding 80 % degree of reaction at 28 days (PC-CFA2) and 56 days (PC-CFA1) of hydration and contribute the most to the overall reaction of CFA2. Clinker phases from the fly ashes are not included in Figure 5.3 and were quantified by XRD together with those from the portland clinker.

Ca-rich glasses tend to be more reactive than those with moderate and low Ca contents [95]. Calcium acts as a modifier in the glass structure; breaking up Si-O bonds. It creates a network that is less connected and thus easier to break apart upon contact with solvents. However, Ca is only one of many elements that can impact the structure and reactivity of glass. The issue of whether, how and to which extent the chemical composition affects the glass reactivity in cement remains poorly understood.

5.3 Study on synthetic glasses

To study the reactivity of the different fly ash-type glasses in detail, these were separately synthesised. Their chemical composition was chosen to match the chemical composition of glasses identified in a calcareous fly ash (CFA2). Batch dissolution experiment provided an insight into the initial dissolution rates of these synthetic glasses in an alkaline environment. The new SEM-EDS technique was used to track the consumption of the synthetic glasses in hydrating cement paste, which was then compared to the consumption of the real glasses in a fly ash. Slag glass (S1) of a chemical composition close to that of one of the investigated glasses was also included in the study. The SEM-EDS data was used to examine how the glass reaction in cement paste depends on the glass chemical composition and fineness.

5.3.1 Glass synthesis and processing

Four dominant compositions identified as the centres of the blobs in the ternary plot of CFA2 (Figure 5.4) were selected as marked (A) silicate, (B) Ca-silicate, (C) aluminosilicate and (D) Ca-rich aluminosilicate. Their full chemical composition was determined by EDS, simplified to a Ca-Mg-Na-Al-Si system and used as a target for the model glasses (Table 5.1). The minor components left out were the K, Fe, S, Ti, P oxides: their mass totalled 6.7 wt.% for A, 8.8 wt.% for B, 4.8 wt.% for C and 11.2 wt.% for D.

The model glasses were synthesised from mixes of reagent-grade Al_2O_3 , SiO_2 , CaCO_3 , Na_2CO_3 and MgO. The powders were mixed in an ethanol suspension for 4 h in an alumina ball mill. The dried mixes were pelletized (Figure 5.5a) and melted at 1600 °C in Pt crucibles in a high-temperature chamber furnace (Borel MO 1700). An additional Pt crucible was used as a cover to minimize the volatilization of alkalis. The samples were heated at a slow rate of

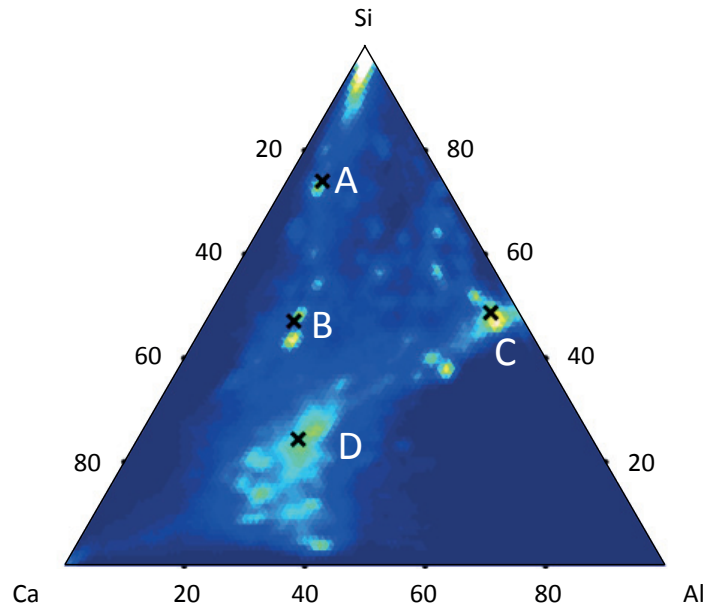


Figure 5.4: Al-Si-Ca ternary frequency plot of CFA2 shows blobs corresponding to the glass groups in the fly ash and the compositions selected for glass synthesis.

5 °C/min up to 950 °C to allow for a complete decarbonation of the carbonates. Above 950 °C the heating rate was increased to 10 °C/min until 1600 °C. The samples were kept at the target temperature for 4 h to complete the melting and the homogenization. The glasses were then quenched in deionized water (Figure 5.5b). Glass pieces were rinsed with isopropanol, dried and stored in a vacuum desiccator over silica gel until further use. The glass chemical composition was measured by XRF (Table 5.1), which revealed only minor deviation from the targeted compositions. The presence of any crystalline phases was checked by X-ray powder diffraction (XRD).

The synthesised glasses A, B and D were transparent, homogeneous and entirely amorphous with no Bragg peaks in their XRD scans (Figure 5.6). Glass C was opaque and an XRD-Rietveld

Table 5.1: The targeted and obtained (XRF) chemical composition of the model glasses.

wt.%	Al ₂ O ₃		SiO ₂		CaO		Na ₂ O		MgO	
	Target	XRF	Target	XRF	Target	XRF	Target	XRF	Target	XRF
A Silicate	4.8	5.3	70.5	69.7	17.9	17.6	2.9	2.7	3.8	3.6
B Ca-silicate	11.9	12.4	45.1	44.6	34.1	33.4	1.7	1.6	7.2	7.2
C Aluminosilicate	38.5	39.1	47.6	47.3	4.2	4.5	8.2	7.9	1.5	1.7
D Ca-rich aluminosilicate	21.8	23.5	23.4	24.8	43.8	41.1	1.2	1.2	9.8	9.9



(a) Homogenized powder pellets in Pt crucibles before firing



(b) Quenching

Figure 5.5: Glass synthesis.

quantification found 2.2 wt.% corundum, which remained from the C raw mix despite high amounts of alkalis and the 4-hour treatment at 1600 °C. Glass C was therefore slightly poorer in alumina than the target composition, but neither this, nor the presence of corundum, were expected to affect the reactivity of glass C significantly.

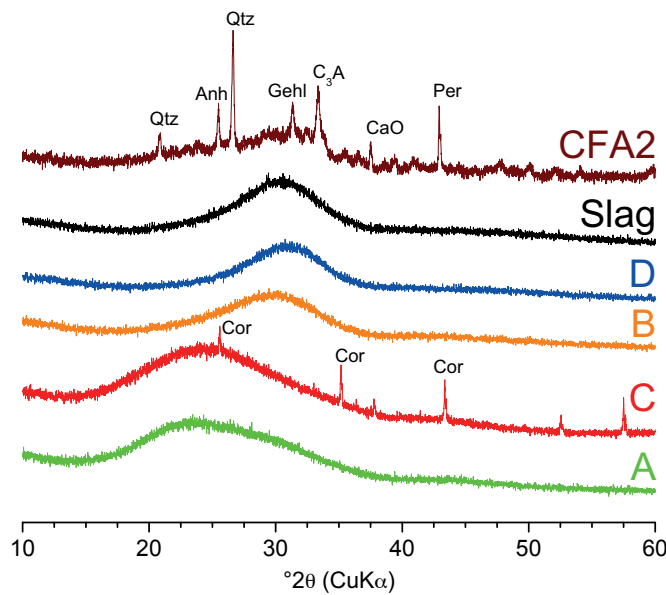


Figure 5.6: Comparison of the XRD scans of the synthetic glasses, slag and CFA2.

The position of the X-ray diffuse scattering maximum (the 'hump') is related to the degree of polymerization of glass, more depolymerized glasses having humps at higher diffraction angles [87, 88, 96, 97]. From Figure 5.6 glasses A and C are more polymerised than B and D. The XRD scan of the CFA2 shows a wide 'hump' indicating the presence of a combination of glasses of various compositions but does not give more detail about the individual glasses.

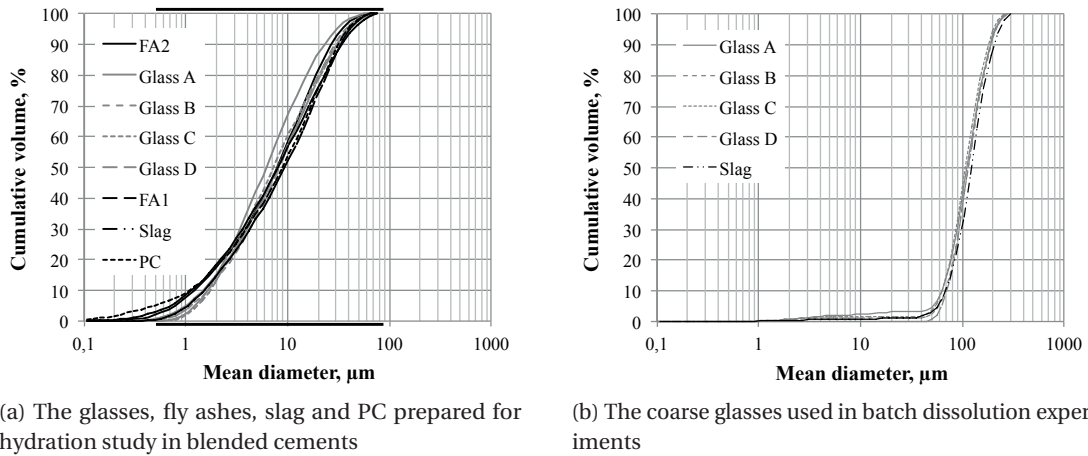
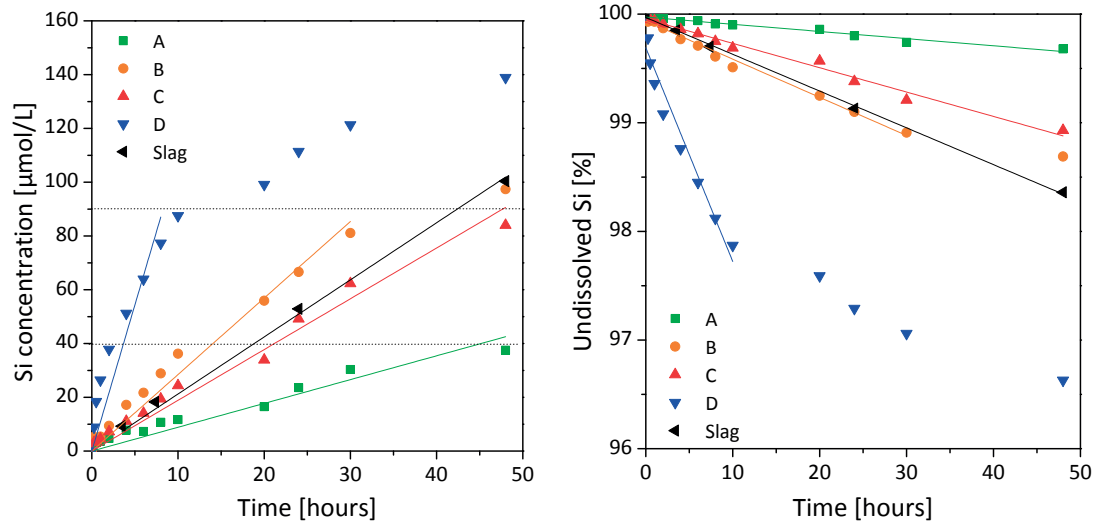


Figure 5.7: Particle size distributions. In (a), the part of the x-axis in bold shows the range of particle sizes that are correctly accounted for by image analysis in this study.

The model glasses and the slag were processed in two ways for two separate experiments: batch dissolution and hydration in a blended cement paste. The dissolution experiment followed a protocol established by Snellings to study the dissolution rates of slags and synthetic glasses [96, 97]. In this protocol large glass particles, around $100\ \mu\text{m}$, are selected, so the dissolution is not too fast and can be measured more accurately. The glasses were hand ground and dry-sieved to obtain the $50\text{-}125\ \mu\text{m}$ fraction. Tiny particles adsorbed on surfaces were removed by cleaning of the glass in an ultrasonic bath with isopropanol in cycles of around 5 min. The isopropanol was replaced between the cycles and the washing continued until the supernatant was clear (usually after 3-5 cycles). The hydration study required glasses of fineness similar to the fly ash. The samples were dry-ground in a disc mill. The particle size distributions of fine and coarse glasses were measured by laser diffraction in isopropanol dispersions using Malvern MasterSizer S (Figure 5.7).

5.3.2 Dissolution experiment

Initial dissolution rates were measured in batch dissolution in a NaOH solution of pH 13.2, which corresponds to that of hydrated portland cement pore solution. The NaOH solution was prepared with 5.6 g of analytical-grade NaOH per 1000 g of ultrapure water that was decarbonated by boiling. The concentration of the NaOH solution was 0.14 M. The experiment was carried out in 250 mL polypropylene bottles at $20 \pm 1^\circ\text{C}$. The bottles were cleaned with nitric acid and ultrapure water. To ensure far-from-equilibrium conditions for the measurement of the 'initial rates' of dissolution and to avoid precipitation of hydrates, the solution to glass weight ratio was 1000. To avoid abrasion, solutions were not stirred. During the experiment, the solution was sampled at 1/4, 1/2, 1, 2, 4, 6, 8, 10, 20, 24, 30 and 48 hours. Portions of 5 mL were taken, filtered ($0.4\ \mu\text{m}$) and stored at 4°C . After each sampling, 5 mL of the NaOH solution was added to keep the volume in the reactor constant. Doing so causes dilution,



(a) Silicon concentrations measured in solution in batch dissolution reactors

(b) The data from (a) normalized by the Si content of the unit mass of glass

Figure 5.8: Results of the dissolution experiment.

which was accounted for during data analysis. Silicon, aluminium and calcium aqueous concentrations were measured by ICP-OES with matrix-matched standards. Slag dissolution data was provided by R. Snellings.

The elemental release of Si measured in the batch dissolution study (Figure 5.8a) provided an indication of the initial dissolution kinetics of the glasses under alkaline conditions. Although the setup does not guarantee pure dissolution it still provides a good approximation of dissolution conditions in a cement paste. Glass D did not show linear dissolution, although it could be argued that the dissolution was linear within certain ranges, i.e. 0-40, 40-90 and 90-140 $\mu\text{mol}(\text{Si})/\text{L}$. Similarly glass B showed some variation between the ranges 0-40 and 40-90 $\mu\text{mol}(\text{Si})/\text{L}$. We fitted the linear slope in the range corresponding to 0-90 $\mu\text{mol}(\text{Si})/\text{L}$ as a compromise between the number of data points and the goodness of fit. The observed deceleration of the initial dissolution is likely caused by ions accumulating in solution, which lowers the undersaturation degree, i.e. the driving force for dissolution. It is also possible that, despite high dilution, precipitation may remove Si from solution. An assessment of this effect by thermodynamic modelling is difficult, due to lack of suitable thermodynamic data for high Al-Si systems. A significant reduction in dissolution speed above 90 $\mu\text{mol}(\text{Si})/\text{L}$ might indeed be associated with precipitation. Other factors behind the non-linear trends may include incongruent glass dissolution and protective layer formation, but these have been shown to be uncommon under alkaline conditions [98].

The initial dissolution rates were calculated as a slope of a linear fit to the dissolution data normalized to Si content of a unit of glass (Figure 5.8b) and the geometric specific surface area derived from a PSD measurement by laser diffraction. The results are presented in (Table 5.2)

Table 5.2: Initial dissolution rates calculated from the batch dissolution experiment.

Log dissolution rate [mol/m ² /s]	A	B	C	D	Slag
Si-based	-8.17	-7.45	-7.57	-6.22	-7.25
Al-based	-8.22	-7.53	-7.63	-6.28	-7.37

together with the dissolution rates based on Al release, which were calculated in the same way. The Al-based dissolution rates were almost identical to those based on Si. Slightly lower values for Al compared to Si are due to hydrotalcite precipitation, which removes Al from the solution. The rates of the different glasses studied varied considerably, which indicates that the chemical composition is an important factor. The rate increased in the order $A < C < \text{Slag} \approx B < D$ with a 25-fold difference between the slowest and the fastest dissolving glass. This is critical, as illustrates that glasses in fly ash may react at very different rates. Among the fly ash glasses, those with the highest silicate contents (A) dissolved the slowest, followed by the Al-silicate (C) and Ca-silicate (B) compositions that dissolved at moderate rates. The Ca-rich Al-silicate (D) was by far the fastest dissolving one. The slag dissolution speed was almost identical to that of the compositionally very similar glass B.

5.3.3 Hydration study of glass-portland composite cements

The hydration study was carried out on 55 wt.% PC - 45 wt.% glass systems. The replacement was chosen to match the replacement level in the fly ash composite cements, PC-CFA1 and PC-CFA2. The reaction of individual synthetic glasses was investigated in systems: PC-A, PC-B, PC-C, PC-D.

A mix of all four glasses, ABCD, was prepared to simulate the CFA2 ash. Such simulated ash is composed of single-phase particles while real ashes contain both single- and multi-phase particles. Nevertheless, most of the phases in real ashes are randomly distributed and of enough abundance that even if a part of them is trapped inside multi-phase grains this should not affect their reactivity significantly. The simulated ash does not contain crystalline phases, but as the reactive crystalline phases in fly ashes form preferably within the glass grains, where the cooling is slower, most of them are expected to be unavailable for direct dissolution anyway.

Slag was used in a mix with portland cement, PC-S, and in a ternary blend also containing calcareous fly ash, PC-CFA2-S. The mix proportions are detailed in Table 5.3. The paste samples were prepared according to the protocol in section 3.2.1 of the Materials and Methods.

In all mixes, gypsum was added so that the overall SO₃ content of the blend was 3.25 wt.% despite the potentially different sulfate requirement of the systems, which was unknown prior to the experiments. Isothermal calorimetry showed an intense heat release in under two hours of hydration in PC-D and PC-ABCD systems (Figure 5.9a). This heat release was attributed to an early depletion of sulfate and a rapid uncontrolled reaction of aluminates. In well-sulfated

Table 5.3: Mix proportions of glass-portland composite cements [wt.%].

Mix	PC	A	B	C	D	S	FA
PC	100	-	-	-	-	-	-
PC-ABCD (simulated CFA2)	55	9.9	5.4	9.0	20.7	-	-
PC-A	55	45	-	-	-	-	-
PC-B	55	-	45	-	-	-	-
PC-C	55	-	-	45	-	-	-
PC-D	55	-	-	-	45	-	-
PC-S (as in 6.1)	55	-	-	-	-	45	-
PC-CFA2-S (as in 6.1)	55	-	-	-	-	20	25
PC-CFA2 (as in 6.1)	55	-	-	-	-	-	45
PC-CFA1 (as in 6.1)	55	-	-	-	-	-	45

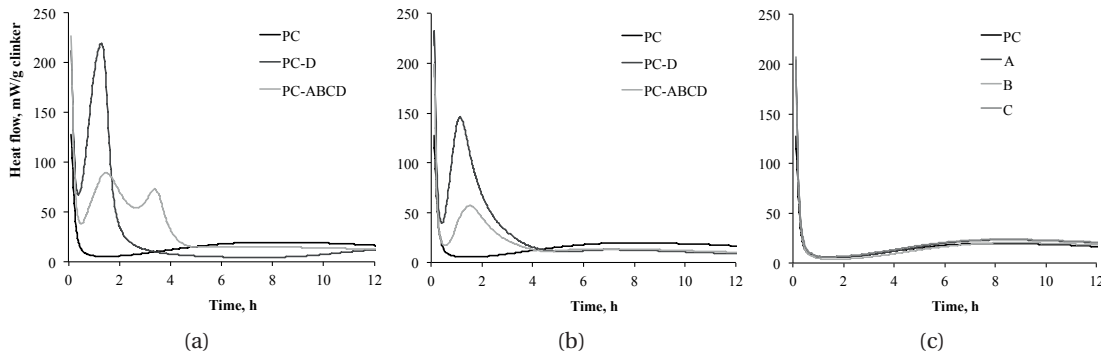


Figure 5.9: Isothermal calorimetry curves show undersulfation of PC-D and PC-ABCD systems both at (a) a moderate and (b) an increased SO₃ content. Intense heat release from rapid aluminate reaction occurs before silicates start to react and is only slightly affected by higher sulfate addition. No undersulfation was observed in the other PC-glass systems (c).

systems the aluminates react after the main silicate reaction (Figure 5.9c). In undersulfated systems, the silicate reaction is significantly inhibited.

New PC-D (7.78 wt.% SO₃) and PC-ABCD (4.91% SO₃) were prepared with more sulfate so that the ratio SO₃/Al₂O₃ would be 0.69, as in the neat PC. This ratio included alumina brought to these systems by the glass D. This glass contains 23.5 wt.% alumina and reacts very fast thus contributing with high amounts of alumina at early stages of reaction. Isothermal calorimetry of the new PC-D and PC-ABCD mixes (Figure 5.9b) showed that high sulfate content reduced the early aluminate reaction to some extent, but not enough to let the silicates react first. Limited supplies of glass D prevented further investigation on how to control the reaction of glass D.

SEM-EDS image analysis was used to track the consumption of individual glasses directly in the hydrating cement pastes. The investigations of the polished sections were carried out according to procedures described in 5.2 and in [84]. The segmentation of the synthetic glasses

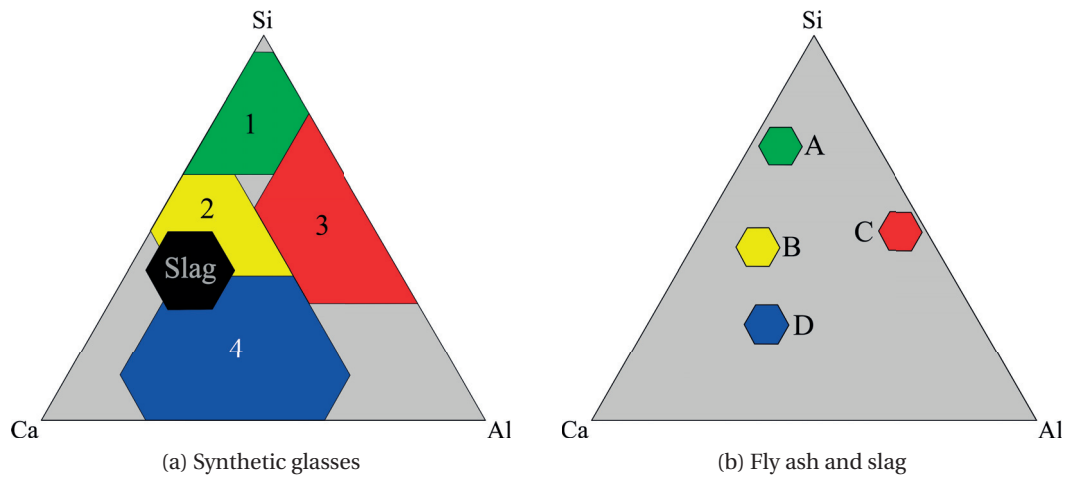


Figure 5.10: Illustration of the segmentation thresholds for image analysis.

Table 5.4: Segmentation thresholds used in image analysis to extract the glasses according to their chemical composition. Coordinates of the centre point and the spread [atomic-%].

	Al	Si	Ca	Spread (\pm)
A	7	71	22	5
B	15	45	40	5
C	45	49	6	5
D	27	25	48	5
Slag	14	39	47	10
1	-5	89	16	24
2	11	51	38	13
3	44	56	0	24
4	38	12	50	25

and the slag was carried out using thresholds on the amounts of Al, Si and Ca as shown in Table 5.4 and Figure 5.10. The identified amounts of slag in PC-CFA2-S sample were corrected for the overlap with the Ca-silicates and Ca-rich aluminosilicates from CFA2 by thresholding of the Fe content. Slag contained less Fe than the two glass populations from CFA2. The results of the SEM-EDS analysis are presented in Figure 5.11. Measured points follow smooth trends that indicate good precision of this new method. The scatter (and relative error) of the results is larger if the amount of the quantified phase in cement paste is low.

In this study we aimed at reproducing the fly ash glass populations of often broad and sometimes multi-modal chemical composition by synthetic glasses of precise stoichiometry. Comparing image analysis results for the CFA 2 in PC-CFA2, the simulated fly ash assembled from glass A, B, C and D in PC-ABCD as well as for these glasses hydrated in individual systems (PC-A, PC-B, PC-C, PC-D) in Figure 5.11 we can see that the order in which the glasses react is largely conserved. This points to the chemical composition as being the main determinant of

Chapter 5. Degree of reaction of fly ash and slag in cement

reactivity of glasses, as already observed in the batch dissolution experiments. The total degree of reaction of fly ash in PC-CFA2 at 90 days was 75% while that of the ensemble of glasses in PC-ABCD was 71%. Notably, glass D was by far the most reactive and almost completely consumed over a timespan of less than 28 days in both single (PC-D) and mixed (PC-ABCD) systems. The glass A is more reactive than its counterpart, the population 1 in CFA2, this is probably because A corresponds to the Ca- and Al-rich end of the population 1 (cf. Figure 5.4 and Figure 5.10). Minor elements, which are present in a real fly ash but not in the synthetic glasses, may have an effect on reactivity but given the limited resolution of the image analysis technique, this effect was not assessed. The similarities in reaction measured for glasses A, B, C individually and in PC-ABCD are even closer than the reaction of their corresponding populations 1, 2, 3 in PC-CFA2. At the same time, the synthetic glasses were ground to similar particle size distributions, while the fineness of the populations in CFA2 was more diverse (Figure 5.12). Indeed, fineness is not taken into account in the results presented in Figure 5.11. Because finer materials react faster, for a more detailed analysis of glass reaction requires the effects of fineness and chemical composition to be decoupled as described below.

The reaction of slag was investigated in portland-slag PC-S and in portland-fly ash-slag PC-CFA2-S systems. The slag reacted at a rate comparable to the rate of the Ca-silicate glass in CFA2. This is not surprising as these two components have very similar chemical compositions and dissolution rates measured in the batch reactor (Table 5.2). However, it may seem odd that a glass present in fly ash can react as fast as slag. Further, the Ca-rich aluminosilicate glass reacted much faster than the slag. The typical degrees of reaction measured for slags reach around 50 - 60 % at 90 days [77] compared to 75 % for the calcareous fly ash CFA2. For siliceous fly ashes, which do not contain Ca-silicate and Ca-aluminosilicate glasses but only the silicate and aluminosilicate ones [84], the reported degrees of reaction are around 30 % [42, 35]. The data for populations 1 and 3 in Figure 5.11 shows that a mix of these two populations would react in 35-40 % after 90 days.

The reaction of slag in the PC-CFA2-S blend did not seem to be affected by the presence of fly ash and reached around 40 % reaction after 7 days and around 65 % at 90 days. In contrast, the reactivity of fly ash glasses seemed to be slightly reduced in the presence of slag. The trends were the same as in PC-CFA2 system: silicates < aluminosilicates < calcium silicates < Ca-rich aluminosilicates. This reduction is likely due to a fairly rapid reaction of large amounts of slag present and thus less space available for hydration of the fly ash glasses. It is expected that the reaction of clinker, especially the slower reacting C_2S and C_4AF may be affected in a similar manner, which will be investigated in Chapter 6.2. It may not be surprising to see a reduction in the degree of reaction of fly ash and slag if a more reactive component is present in significant amounts in the system, such as a reactive calcined clay, for example.

5.3. Study on synthetic glasses

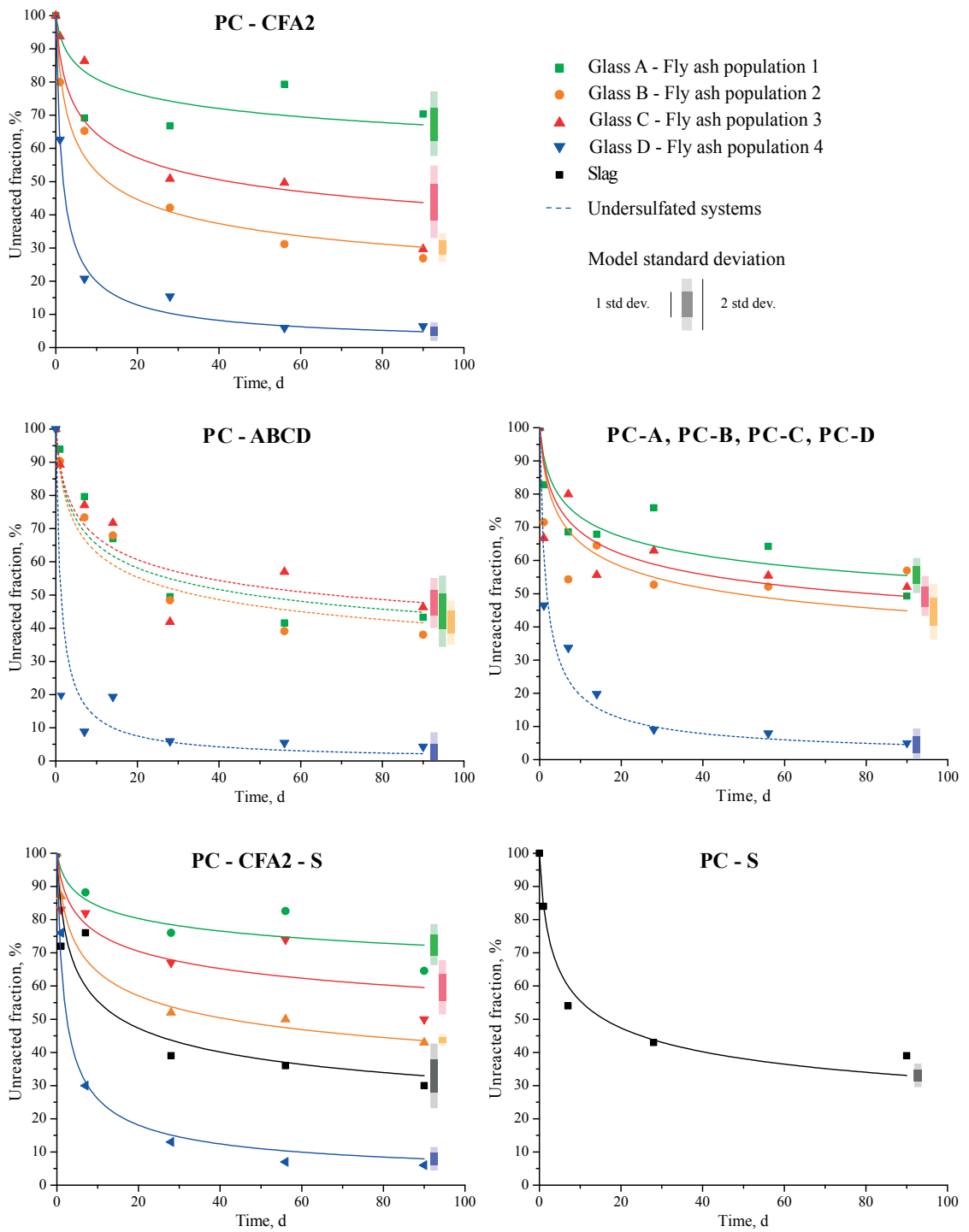


Figure 5.11: Fitted kinetics of glass reaction in composite cements containing fly ash CFA2, synthetic glass A, B, C, D and slag S. Points represent experimental measures.

5.4 Quantitative analysis of glass reactivity in paste

To quantify the reactivity of glasses in cement paste we first have to decouple the influence of particle sizes. By image analysis we can calculate a ratio of a collective perimeter to a collective area of the particle sections in the image. This ratio is proportional to a collective ratio of surface to volume of the real particles $\frac{S}{V}$ [μm^{-1}]. By taking the $\frac{S}{V}$ collectively we simplify the analysis and treat a range of particle sizes as a single "averaged" or equivalent spherical particle. The $\frac{S}{V}$ ratio is certainly not a sufficient description of a PSD in general. Within the context of this analysis, which concerns itself with the links between the volume, the surface and the intrinsic reactivity of glass, it is the most immediate descriptor of these powders.

To correctly use the $\frac{S}{V}$, it has to be measured at each of the studied hydration ages. We observed that it decreased for slag and C_3S but not for fly ash glasses (Figure 5.12). Slag and C_3S initially spanned a wide range of sizes and contained a considerable amount of fines, below $2 \mu\text{m}$. The 3 vol.% below $0.5 \mu\text{m}$ is not detected by image analysis. Nonetheless, the 15 vol.% of particles between $0.5 \mu\text{m}$ and $2 \mu\text{m}$ contributes to around 50 % of the total surface area. These fine particles are first to react completely and $\frac{S}{V}$ decreases. The lack of a clear decrease in $\frac{S}{V}$ of fly ash and synthetic glasses may have been due to low reactivity or narrow particle size distribution. To use the $\frac{S}{V}$ data in further calculations the evolution of $\frac{S}{V}$ was fitted with:

$$\frac{S}{V} = m \ln(t) + n \quad (5.2)$$

The $\frac{S}{V}$ of C_2S , C_3A and C_4AF were obtained as a single value from the examination of raw portland clinker. A collective $\frac{S}{V}$ was taken for C_3A and C_4AF ; due to intermixing it was impossible to differentiate between them under SEM. Indeed, due to microscopy limitations the finest grain fraction may not be resolved correctly and clusters of fine particles may appear as larger ones while fine and isolated particles may be filtered out as noise.

The rate of reaction of a single spherical glass particle can be described by the rate of decrease of the radius thereof (Eq. 5.3). This rate is constant if the external factors, such as temperature and pore solution composition, do not change significantly in the course of reaction and thus have a uniform effect on the rate:

$$\frac{d}{dt}r = \text{const.} \quad (5.3)$$

Here the experimental data of volume fraction $\frac{V}{V_0}$ measured at time t (Figure 5.11) was fitted with a generic power law function:

$$\frac{V}{V_0} = (1 + t)^{-\kappa \frac{S}{V}} \quad (5.4)$$

which can be approximated to:

$$\frac{V}{V_0} \approx e^{-\kappa \frac{S}{V} t} \quad (5.5)$$

5.4. Quantitative analysis of glass reactivity in paste

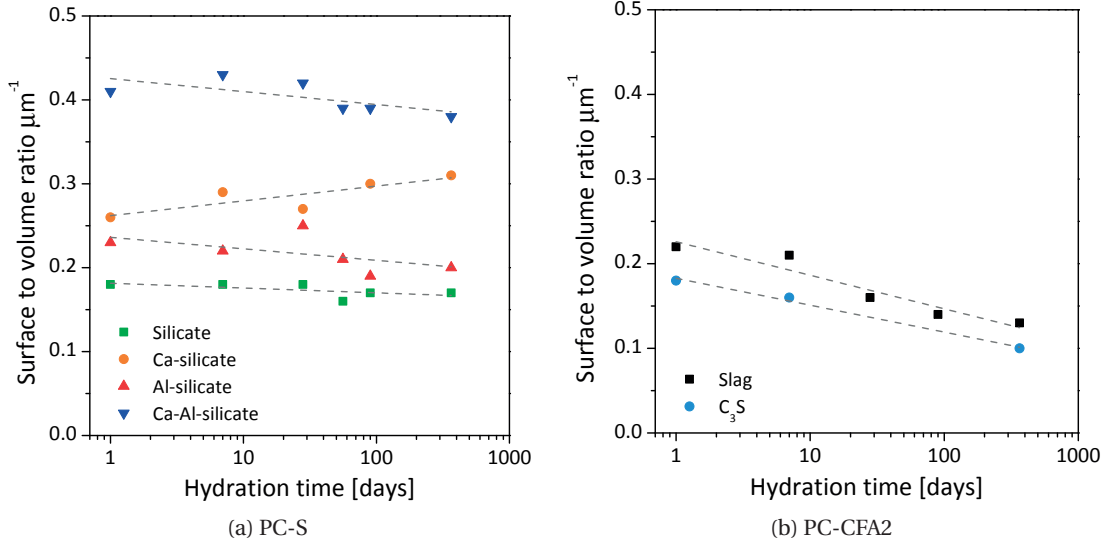


Figure 5.12: The surface to volume ratios of slag and C_3S measured by image analysis decrease over the reaction time. The ratios of the CFA2 glass populations, shown here as an example, are largely constant. A logarithmic trend was fitted to the data.

where $\kappa \frac{S}{V}$ is a measure of the rate of reaction. This was done by transforming

$$\frac{V}{V_0} = (1 + t)^{-\kappa \frac{S}{V}} = e^{-\ln(1+t) \cdot \kappa \frac{S}{V}} \approx e^{-[t - \frac{t^2}{2!} + \frac{t^3}{3!} - \dots] \cdot \kappa \frac{S}{V}} \approx e^{-t \kappa \frac{S}{V}} \quad (5.6)$$

where the last expression is a first order approximation from a Taylor series expansion.

Since $\frac{S}{V}$ takes into account the PSD of the considered phase, κ is independent of the particle morphology and can be used as a relative measure of the intrinsic reactivity of the different phases, introduced here as an intrinsic reactivity index (Figure 5.13). This index has a unit of $[\mu\text{m}/\text{day}]$ as it is related to the rate of consumption of the particle radius. The κ indices of C_3S , C_2S , C_3A and C_4AF were calculated from XRD-Rietveld quantification of hydration of these phases and are enclosed here for comparison.

The effect of fly ash on the cement reaction can be observed in an enhanced hydration of C_3S and C_2S and an unchanged reaction of C_3A and C_4AF . The reaction of C_2S in PC-CFA1 however did not seem to be enhanced. Further, the reaction of C_3A in PC-CFA2 was decreased. A possible explanation for these two observations may be linked to the fact that CFA1 contains around 2.5 wt.% C_2S and CFA2 contains around 4 wt.% C_3A , which may have crystallized inside of the glassy particles and were thus not directly available for the reaction. However, if these phases were detected and quantified by the XRD-Rietveld along with their counterparts from portland cement this would result in lower apparent rate of their reaction. Trapped inside glass, the clinker phases present in fly ashes may react more slowly or with a considerable delay compared to the same phases from the portland clinker.

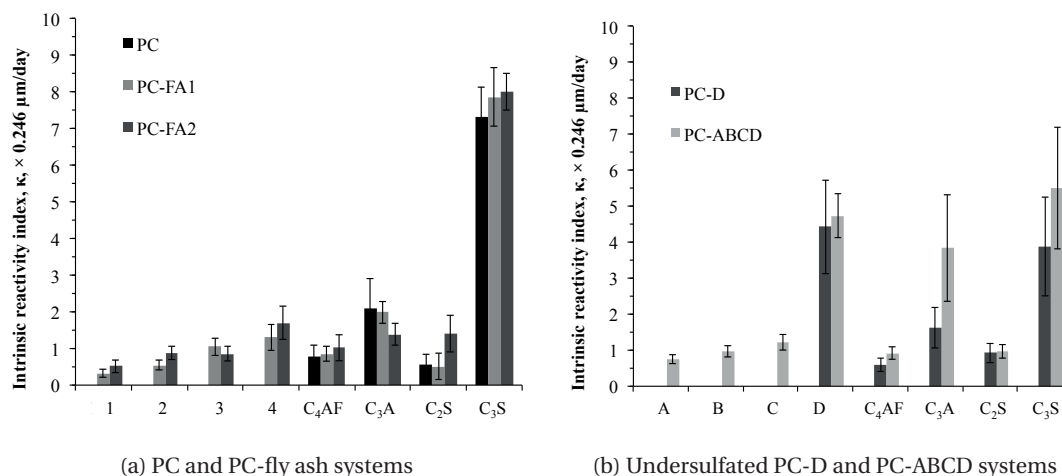


Figure 5.13: Intrinsic reactivity of fly ash populations and cement phases. The value 0.246 μm is the pixel size.

The κ values obtained for the analogous glasses in two different calcareous fly ashes CFA1 and CFA2 as well as the synthetic ones, except glass D, were largely similar (Figure 5.13). This indicates that the approach used may be universal enough to be applied or adapted for analysis of any glassy phases. An exceptionally high reactivity of glass D in PC-D and PC-ABCD systems, a much decreased C₃S reactivity and a simultaneous increase in C₃A reactivity in PC-ABCD suggested that these systems were indeed undersulfated as shown earlier by the isothermal calorimetry (Figure 5.9). Glass D contained 23.5 wt.% of Al₂O₃ and it seems that a fast reaction of this glass rapidly releases the Al into the system, which could then lead to premature sulfate depletion and thus trigger C₃A reaction. In undersulfated systems, the rapid depletion of gypsum is expected to lead to higher Al concentrations during the main reaction of C₃S and Al has been shown to strongly reduce C₃S reactivity [99]. The very high reactivity of glass D compared to its analogue glass in fly ash may be due to its precise chemical composition in contrast to the large spread of chemical composition of glass 4. Rapid cooling of the synthetic glass could have too increased its reactivity. Further, once the C₃S reaction in pastes with glass D has been hindered at early age there must have been more space and water available for the glass reaction, which would further increase it.

5.5 The influence of chemical composition of glass

In principle, the reaction of fly ash in cement consists of the dissolution of glass and the precipitation of hydrates. We can assume that the overall reaction rate is limited by the dissolution and not precipitation as the reported dissolution rates of Ca-Al-Si glasses [96] are lower than typical growth rates of C-S-H [100]. The dissolution of glassy components in cementitious systems depends on their fineness and their intrinsic reactivity. The intrinsic reactivity of glass is linked to its structure [101, 102]. More depolymerised and disordered

5.5. The influence of chemical composition of glass

structures break up more easily upon contact with the solution. According to classical theory (Zachariasen model), glass structure is made of an anionic silicon-oxygen network, where $[\text{SiO}_4]^{4-}$ tetrahedra are joined through bridging oxygens. The degree of polymerisation of glass, depends on the chemical composition thereof [103]: the relative amounts of glass formers such as Si, Al and glass modifiers, e.g. Ca, Na, K, Mg [104]. These network-modifying cations (Ca^{2+} , Mg^{2+} , K^+ , Na^+) break the Si-O bonds and depolymerize the structure by creating non-bridging oxygens (NBO), e.g. $\text{Si-O}^- \text{Na}^+$. The degree of polymerisation of glass can be represented by NBO/T, the number of non-bridging oxygens (NBO) per tetrahedral network-forming ion (T) [103, 105]. Higher NBO/T values correspond to more depolymerised glass structures. NBO/T = 0 refers to a fully interconnected network, NBO/T = 1 to sheets, NBO/T = 2 to a chains or rings, NBO/T = 3 to dimers, and the maximum value of NBO/T = 4 to monomers. A structure with an NBO/T = 4 is fully depolymerised.

In the studied glasses the T ion can be Si^{4+} or Al^{3+} , but Al can exist both as a network former and as a modifier. As a network former, Al^{3+} substitutes for Si^{4+} . The substitution produces a negative charge that has to be balanced by a cation sitting near the Al instead of modifying the network. Since Al-O-Al bonds are unstable, the amount of Al in glass is limited by the Si to Al ratio and the cations available for charge compensation. However, Al can also act as a network modifier, with no need for charge compensation, even if cations are still present. The actual proportion between network forming and modifying Al could potentially be estimated by Raman spectroscopy, ^{27}Al NMR or ^{17}O NMR. But, it may be difficult to extract individual glasses from fly ash to be able to test them.

Here Equation 5.7 [103] was used to calculate the theoretical NBO/T ratio from the chemical composition of glass. It is based on the EDS mean chemical composition of the glasses in the fly ash and the XRF analysis of the synthetic glasses. The used formula assumes all Al acts as a glass former. This simplification is acceptable for glasses of high Si/Al but is probably erroneous for Al-rich glasses with low amounts of silica and cations, in which considerable amount of network-modifying Al is expected.

$$\frac{\text{NBO}}{\text{T}} = \frac{2(x_{\text{CaO}} + x_{\text{MgO}} + x_{\text{Na}_2\text{O}} + x_{\text{K}_2\text{O}} + x_{\text{FeO}} + x_{\text{TiO}_2} - x_{\text{Al}_2\text{O}_3})}{x_{\text{SiO}_2} + 2x_{\text{Al}_2\text{O}_3}} \quad (5.7)$$

The results of this calculation for the synthetic glasses, slag, CFA1 and CFA2 are shown in Table 5.5. The calculated NBO/T values increase in the order of glass: $1 \approx 3 < A < 2 \approx B < \text{Slag} \approx 4 \approx D$, which corresponds to the trend in reactivity of these glasses measured by SEM-EDS image analysis. Glass C is excluded from this comparison due to the negative NBO/T (probably due to the high Al content), which is outside of the acceptable range $0 < \text{NBO/T} < 4$. The above equation could be easily modified to account for network-modifying Al if such is measured, for example, by one of the techniques mentioned before, Raman or NMR.

The NBO/T values obtained ranged from 0 to 2, which suggests that the dominant structural units are 3-D units, sheets, chains and rings. It has to be borne in mind that the NBO/T is a bulk measure and gives information only on the average speciation of the network forming

Chapter 5. Degree of reaction of fly ash and slag in cement

Table 5.5: NBO/T of the fly ash populations, the synthetic glasses and the slag.

	CFA1	CFA2	Synthetic glass	Slag
1/A - Silicate	0.07	0.16	0.65	
2/B - Ca-Silicate	0.86	1.45	1.42	2.01
3/C - Al-Silicate	0.14	0.16	-0.17	
4/D - Ca-Al-Silicate	1.91	2.35	2.02	

anions. Raman spectroscopy studies show that glasses may contain several types of anionic units at once [103, 106]. Depending on the type of the modifier cations and their relative proportions, the actual anionic species may vary. Large cations such as Na^+ and K^+ tend to promote sheets instead of chains and three-dimensional units [103]. Small, highly charged cations such as Ca^{2+} and Mg^{2+} lead more to monomers and dimers, which are balanced by chains and three-dimensional units. The cation type has an influence on the location of tetrahedral Al [107]; Ca^{2+} and Mg^{2+} promote Al in 3-D units; Na^+ and K^+ result in nearly random substitution of Al^{3+} for Si^{4+} .

Despite its limitations, NBO/T has been shown to correlate well with glass reactivity. The dissolution of ground slags in boiling distilled water clearly tended towards higher reactivity with higher NBO/T of the slag [101]. A study of Bumrongjaroen [108] has shown that the reactivity estimated from depth profiles of fly ash-type glasses leached in pH 12 LiOH largely corresponded to their NBO/T. Recently published results [109] on pastes prepared by alkali activation of siliceous fly ashes show a trend to higher compressive strength with increasing NBO/T of fly ash.

The results from this study, shown in Figure 5.14, present a clear almost linear trend towards higher reactivity in cement paste with increasing glass structure disorder.

The silicate populations present the lowest intrinsic reactivity and are highly polymerised. The intrinsic reactivity of glass A is greater than that of the silicate phases. A is more depolymerised and the composition of A was at the Ca-rich end of that of the population 1 (silicate). The aluminosilicate populations CFA1-3 and CFA2-3 seem to be off the main trend. Their intrinsic reactivity corresponds to that of the Ca-silicates but the calculated NBO/T values are much lower. The intrinsic reactivity of glass B was almost identical as that of the Ca-silicate population of CFA2. The slag, however, showed intrinsic reactivity similar not to glass B but to the Ca-rich aluminosilicate glass (population 4 in CFA1 and CFA2). This means that the actual reactivity of slag in cement paste is less than that of the Ca-rich aluminosilicates because slag is coarser. The outlier is the glass D. The higher than expected reactivity of glass D may be linked to its structure being different from the classic Zachariasen model. Goto *et al.* [88] have shown that some of the gehlenite type glasses of chemical composition similar to that of glass D studied in gypsum-lime systems reacted faster and produced more heat than other Ca-aluminosilicate glasses with lower Al content. A recent study by Akola *et al.* [110] investigated the structure of a C_{12}A_7 glass (mayenite-type) and a CA glass, which do not contain typical

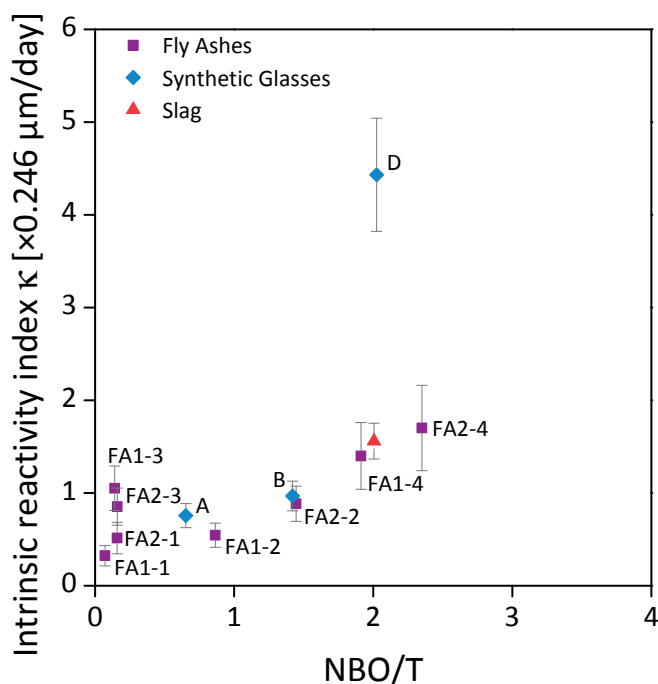


Figure 5.14: A comparison of the calculated intrinsic reactivity and the NBO/T. The value of $0.246 \mu\text{m}$ is the pixel size in image analysis.

glass formers such as Si. The study showed C_{12}A_7 glass had a greater topological disorder than the CA glass. Glass D contains a similar proportion of Ca to Al as C_{12}A_7 and relatively little Si compared to other glasses, this could explain its higher reactivity and the difficulty to control the reaction by calcium sulfate addition.

The correlation presented in Figure 5.14 is preliminary and needs further verification for a broader range of compositions. If confirmed, it could open a new possibility to assess fly ash reactivity in cement, not by trial and error testing, but based on raw fly ash characterization, notably the chemical composition and the proportions of its constituent glasses.

Future research should focus on the role of alumina in glass structure and notably the proportion of network forming and modifying Al. It would be useful to know the accurate NBO/T values not only for Al-rich glasses but for all glasses containing Al. The impact of Al content on NBO/T is seen in particular for the Al-rich glasses. The aluminosilicate glass C was excluded from the comparison due to negative NBO/T and for the aluminosilicate glass from fly ash the NBO/T were much less than expected. There are two main implications to this issue. First is that the NBO/T of all of the glasses studied here may be affected to some extent, which may have impact on the trend $\kappa=f(\text{NBO}/\text{T})$. The second is that the aluminosilicate glass is the most common and the most abundant reactive glass in fly ashes and it is essential to be able to evaluate its degree of polymerisation adequately. What is generally referred to in this study as the aluminosilicate glass may vary significantly in chemical composition, and thus reactivity, from one fly ash to another. Figure 5.15 shows that the reaction of the aluminosilicate glass

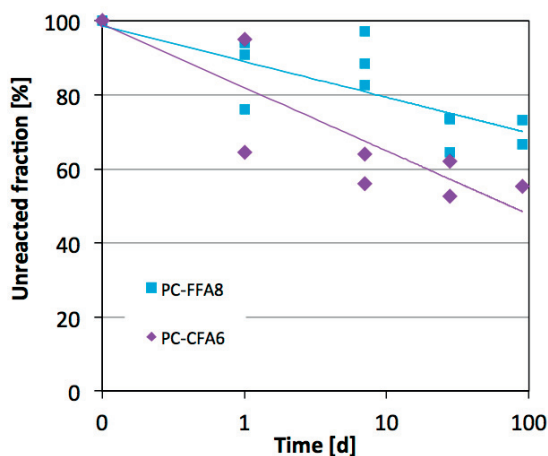


Figure 5.15: The aluminosilicate glasses from a siliceous (FFA8) and from a calcareous fly ash (CFA6) react in cement paste at clearly different rates.

from a calcareous fly ash can be around two times faster than that of the aluminosilicate glass from a siliceous fly ash. The data shown here was obtained by SEM-EDS and by XRD on PC-CFA6 and PC-FFA8. More details on how XRD can be used to quantify the reaction of amorphous components in cement are presented in the next section.

5.6 Summary on glass reactivity by SEM-EDS

A new SEM-EDS technique was used to analyse the individual reaction of four chemically different populations of glasses in portland-calcareous fly ash pastes. The results confirmed that each of these populations contributes differently to the overall fly ash reaction. The proportion of these populations therefore has a crucial impact on the reactivity of the fly ash.

Further investigation showed that simplified synthetic glasses can be used to study the reactivity of fly ashes containing several glass compositions.

- The rates of initial dissolution of the model glasses measured in batch reactors varied with the glass composition and decreased above certain Si concentrations in solution.
- This suggests that the maximum dissolution rate is related to the glass chemical composition but the actual rate will depend on other factors, notably the solution composition.
- The consumption of the model glasses in composite cements measured by SEM-EDS was similar to that of the glasses in the real fly ash and followed the trends found during the dissolution experiment.
- The effect of fineness and intrinsic reactivity of glass were separated and it was shown that the intrinsic reactivity increased with the degree of depolymerisation of glass expressed as the ratio of non-bridging oxygens per tetrahedral ion (NBO/T).

This study demonstrates that a systematic and generic understanding of the reactivity of fly ashes, slags and potentially other amorphous SCMs is possible if the problem is broken down to reactivity of their components, especially glasses.

5.7 Advances in XRD analysis - Practical implementation in HighScore Plus

The majority of XRD analysis techniques including Rietveld refinement fail to measure the reaction of fly ash in cement paste. In the standard addition approaches, the amorphous content is calculated as a difference between the total and the crystalline mass, the contributions from various amorphous components are treated collectively. The anhydrous fly ash glass and the amorphous hydration products C-(A)-S-H are thus not resolved. To do so a technique is required that would quantify each of these amorphous phases directly and individually. An overview of methodologies for determination of amorphous content by XRD has been published by Madsen *et al.* [111]. Among the presented methods two advanced XRD refinement techniques called PONKCS [112] and Full Structure Method (FSM) [111] appear the most promising. It seems that up to now FSM has not yet been applied to cement paste. A recent study by Snellings *et al.* [113] has shown that in a hydrating slag cement PONKCS can directly quantify the anhydrous slag glass despite the presence of amorphous hydrates. For an initial slag content of 60 wt.% it has been shown that PONKCS can be carried out with precision comparable to the Rietveld analysis of crystalline phases (2-3 wt.%). However, the precision is expected to scale down with decreasing amount of the quantified amorphous phase.

It has to be borne in mind that neither PONKCS nor FSM can identify the different amorphous phases in paste directly. These serve to quantify the amount of an amorphous phase which profile has been determined before. Such profile can be obtained from a sample, in which no other unknown amorphous phase is present. Only then such determined contributions can be quantified in a mixture of amorphous phases. For both PONKCS and FSM, we created a model profile to fit the diffuse scattering 'hump' of a raw slag or ash and then used this profile in hydrated samples. A second model is needed to fit the 'hump' of the C-(A)-S-H phase. These two methods follow largely the same routine as the external standard method (section 3.2.6), except that now the amorphous phase is included explicitly in the refinement. The actual difference between PONKCS and FSM lies in the fitting of the amorphous phase profile and the subsequent quantification as discussed below.

This section investigates the use of PONKCS and FSM to quantify the reaction of slag and fly ash in the cement pastes of this study. Of particular interest to this study are calcareous fly ashes that contain several amorphous glasses, which are the most difficult to quantify by any technique. Since it is not possible to determine the contribution of different glasses in fly ash by XRD we may, at most, be able to calculate only their total degree of reaction.

5.7.1 PONKCS

PONKCS stands for Partial Or No Known Crystal Structure. In this method the 'hump' can be fitted using peaks generated from the unit cell and space group information or peaks inserted in custom locations. No crystal structure is needed. A Le Bail fit redistributes the measured intensity among available peaks and refines the cell and profile parameters to minimize the differences. At this stage there is no scale factor. Since no crystal structure is defined for the amorphous phase (no atoms, density and volume), the obtained Le Bail fit is calibrated on a sample with known concentrations of all phases. This produces an HKL-file (amorphous phase model) with a calibrated 'phase constant', which can be used to represent the amorphous phase in future quantitative analyses. In a real sample, the amorphous content is calculated using the external standard method (Eq. 3.4) with the 'phase constant' from the prior calibration and the scale factor obtained by fitting the HKL-file model to the real sample.

As an example, PONKCS was used to quantify the reaction of slag in PC-S (55% PC + 45% S). Figure 5.16 demonstrates the fit to the raw slag pattern and its subsequent use in a hydrated sample. Any space group can be used that models the 'hump' correctly. Higher symmetry in principle means fewer peaks, which may be easier to fit. Since a more adequate space group may exist we searched for candidates among the space groups of minerals of chemical composition similar to the slag. Ultimately, the slag profile was derived from P-42m space group, which is that of gehlenite. The chemical composition of slag is close to the primary crystallization field of gehlenite (Figure 5.17) and the slag glass is of so-called gehlenite-type. The 'phase constant' for slag was calibrated on a slag-quartz 50-50 sample.

The C-S-H model was obtained by refining the cell ($\pm 1\%$) and profile ($W = 10$) parameters of a Tobermorite 14\AA crystal structure [114]. The refinement was carried out for the most hydrated PC-S sample (90 days). For the analysis of the remaining hydration times the cell and profile parameters were fixed and only the scale factor was refined.

Figure 5.18 shows the degree of reaction of slag measured in PC-S by PONKCS compared to results from electron microscopy techniques: SEM-EDS as described above in this chapter and SEM-BSE segmentation of grey levels combined with Mg EDS mapping as presented in Materials and Methods. The trends are smooth and there is close agreement between the techniques. This is likely related to the homogeneous nature of slag glass and to the large amount of this glass in the paste, which improve the precision of the quantification. The initial slag content was 45 wt.% of the anhydrous powders, equivalent to 32 wt.% of paste. The largest differences between PONKCS and SEM results are reported at 1 day hydration. However, electron microscopy techniques may overestimate the early reaction due to poor resolution of the finest particles. The results of the PONKCS analysis rely strongly on the choice of background. A polynomial background should be of the lowest order necessary for a correct fit. In the present analysis, the background was fitted with a first order Chebyshev polynomial and a $1/X$ parameter. A lot depends on the quality of the XRD data, especially the beam overflow at low angles should be limited by incident slits. The slit used was 0.5° . Significant overlap

5.7. Advances in XRD analysis - Practical implementation in HighScore Plus

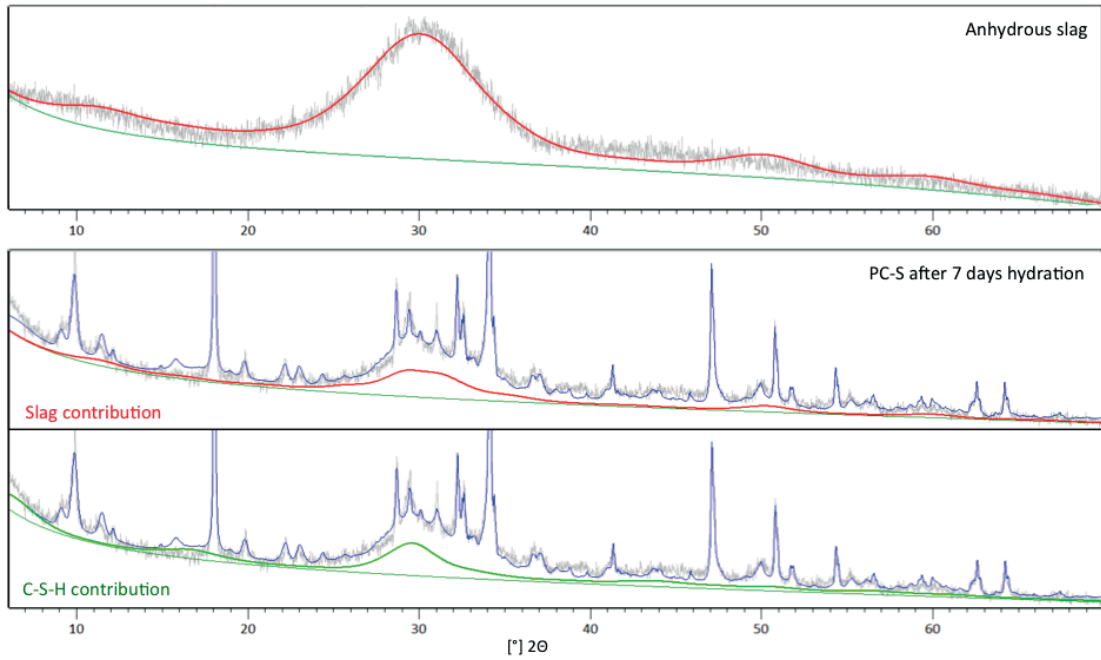


Figure 5.16: PONKCS analysis of slag cement. Top: anhydrous slag fitted with a PONKCS profile. Bottom: Slag and C-S-H contributions to the pattern of PC-S paste hydrated for 7 days.

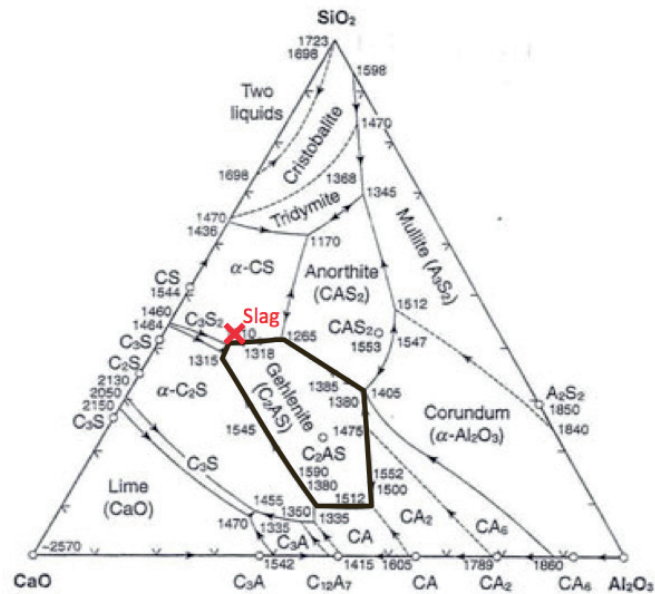


Figure 5.17: Phase diagram showing the primary crystallization field of gehlenite and the slag composition.

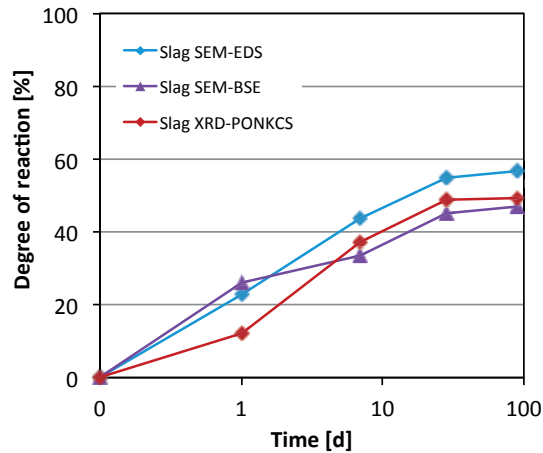


Figure 5.18: Quantification of the degree of reaction of slag in PC-S by three different techniques.

of the contributions from slag, C-S-H and amorphous AFm phases (including monosulfate, mono- and hemi-carbonate, hydrotalcite) can make the analysis more difficult and may affect the quantification results. To some extent, the C-S-H contribution was taken into account by the C-S-H model but that of the AFm phases was not yet accounted for due to increased complexity of fitting of multiple amorphous phases. The results presented in Figure 5.18 seem not to have suffered significantly from those simplifications and agree closely with the degree of reaction of a very similar slag reported by Kocaba [77], which she has quantified by SEM-BSE image analysis.

5.7.2 Full Structure Method

In FSM the amorphous 'hump' is modeled using a crystal structure. Refining of profile parameters to large values (W profile up to 100) transforms peaks into wide 'humps' that fit the amorphous signal. Since the crystal structure provides information on cell density and volume the quantification of mass is the same as for crystalline phases in the external standard method. The difficulty lies, however, in finding a structure that will adequately model the measured peak positions and intensities both in anhydrous material and in paste. The selected structure should also have a similar density to the modeled phase, or else the difference in densities should be accounted for in the quantification.

Similarly to finding a space group for the PONKCS analysis of slag, for a FSM analysis of fly ash we used phase diagrams to aid finding candidate crystal structures (Figure 5.19). We observed that several candidates may well fit the 'hump' of an anhydrous ash but only a few give consistent results in paste. Tridymite and anorthite were chosen. One may have expected mullite to provide the best match but it did not. In fact, as more crystalline mullite is present in the fly ash glass, the glass chemical composition shifts from aluminosilicate to

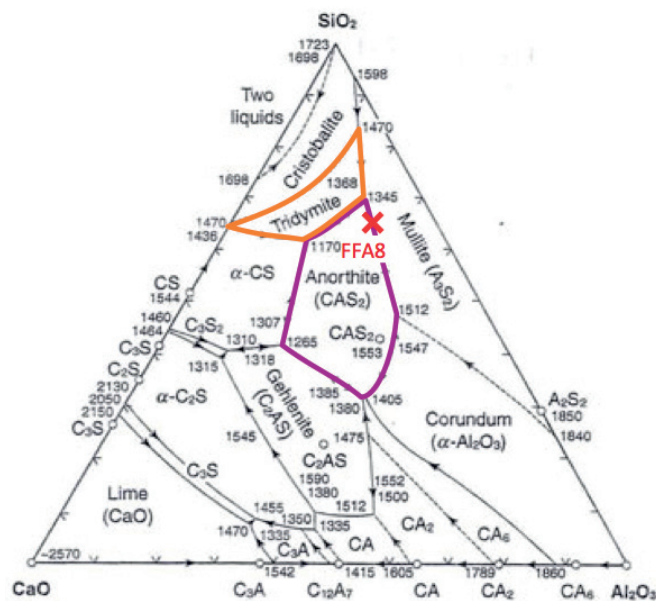


Figure 5.19: Phase diagram showing the composition of the amorphous part of fly ash FFA8 with respect to the primary crystallization fields of anorthite and tridymite.

Ca-aluminosilicate. A red cross in Figure 5.19 demonstrates the chemical composition of the glass in FFA8.

Figure 5.20 (top) shows the contributions of two crystal structures, tridymite [115] and anorthite [116], which were used to model the amorphous 'hump' of a siliceous fly ash FFA8. Figure 5.20 (bottom) shows the fit of these two structures and the contribution of C-S-H in PC-FFA8 paste hydrated for 7 days.

The results of the FSM quantification of the reaction of the amorphous part of FFA8 in PC-FFA8 are presented in Figure 5.21 along with the PONKCS and the SEM-EDS results. A good PONKCS fit was achieved using cubic F m-3m space group. Except for two outliers, the trends are very smooth and the three methods give very similar results. This may be because the amorphous part of the FFA8 is composed of only one aluminosilicate glass and no other type of glass (cf. Figure 4.12c). SEM-EDS can resolve reaction of different glasses individually which XRD cannot do. In more complex fly ashes, the agreement between SEM-EDS and XRD may be less.

An analysis of the reaction of a calcareous fly ash by PONKCS and FSM is more difficult due to the significantly more heterogeneous nature of its glass. The 'hump' from a calcareous ash may be broader or even multimodal due to contributions from various glasses. Complex contributions to the XRD pattern of CFA2 were shown already in Figure 5.6. Figure 5.22 (top) shows PONKCS profiles of the amorphous 'hump' in CFA1 and CFA2, which were derived from F m-3m space group. Figure 5.22 (bottom) shows patterns of the same two ashes fitted with crystal structures - that of anorthite [116] for CFA1 and that of C₂S [117] for CFA2. These two

Chapter 5. Degree of reaction of fly ash and slag in cement

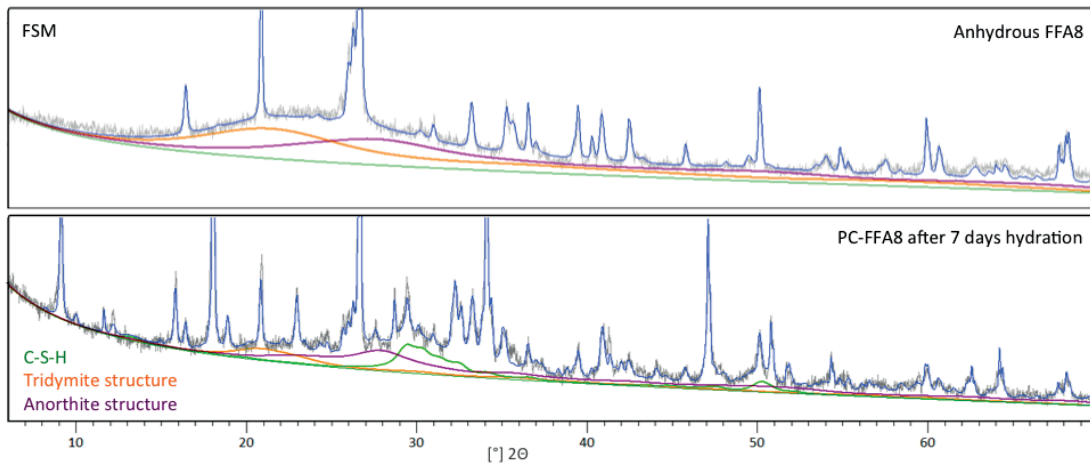


Figure 5.20: FSM analysis of siliceous fly ash FFA8 (top) and PC-FFA8 paste (bottom). FSM analysis of this fly ash uses two crystal structures to model the amorphous 'hump'.

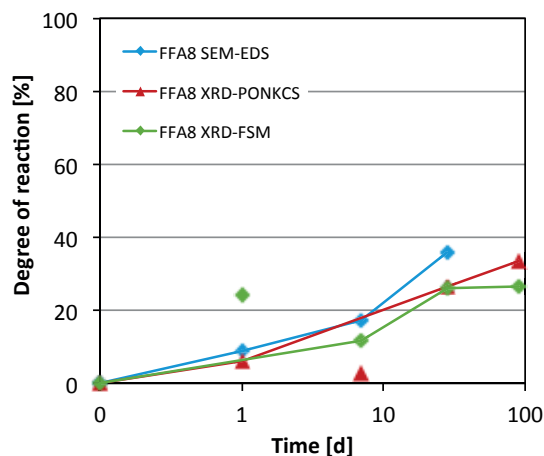


Figure 5.21: Quantification of the degree of reaction of the amorphous fraction from a siliceous fly ash FFA8 in PC-FFA8 by SEM and XRD techniques.

structures were chosen by trial and error as they offered the best fit among a large number of crystal structures tried.

We observed that a good fit of an anhydrous ash does not guarantee successful quantification in paste. The PONKCS analysis of these two fly ashes did not produce consistent results and neither did the FSM analysis of CFA2. The only successful quantification was obtained for the CFA1 reaction by FSM. It followed a trend very similar to that obtained for this fly ash by SEM-EDS (Figure 5.23a). The exact reason why the PONKCS and FSM analyses of calcareous fly ashes differ significantly from the SEM data like in Figure 5.23b is unknown. Among plausible causes are the difficulties in fitting the background and an excessive overlap with the contribution from C-S-H and amorphous AFm. Another source of potentially inconsistent

5.7. Advances in XRD analysis - Practical implementation in HighScore Plus

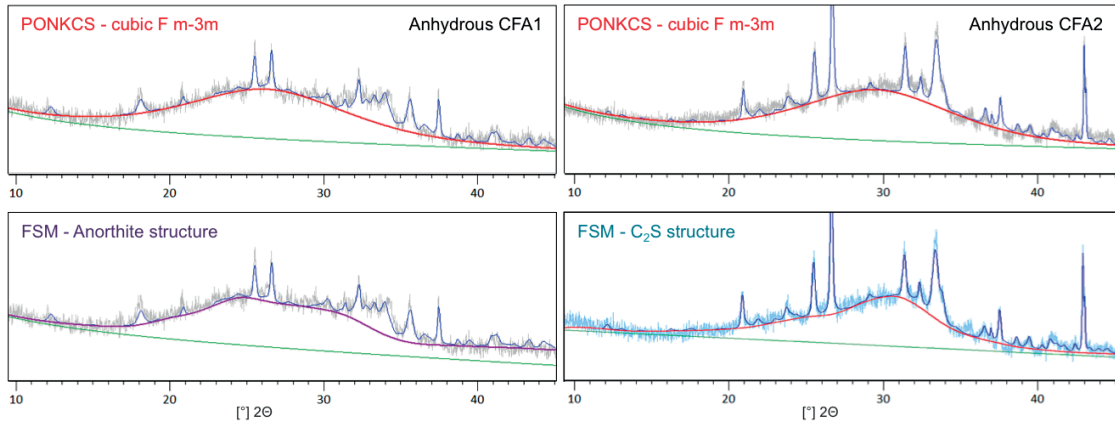


Figure 5.22: PONKCS and FSM models of the amorphous part of two calcareous fly ashes.

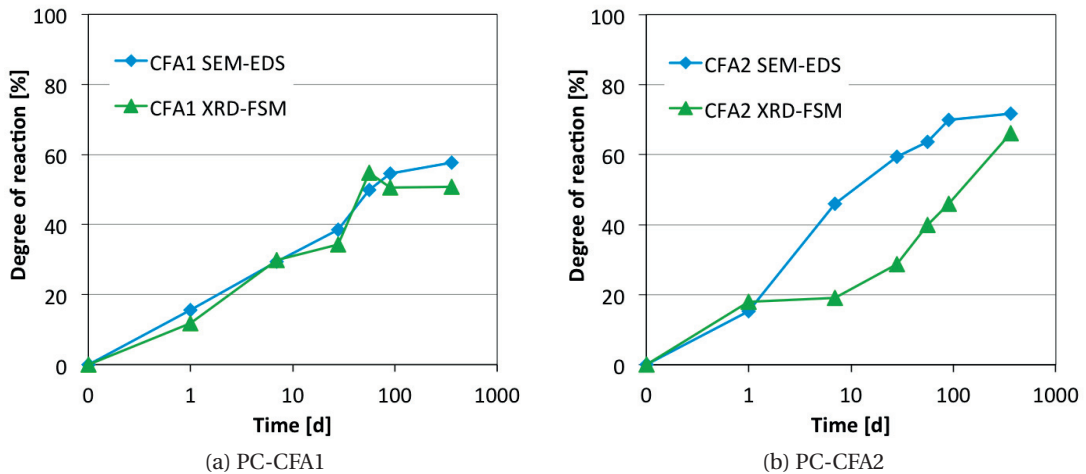


Figure 5.23: Quantification of the degree of reaction of calcareous fly ash. FSM failed to quantify the reaction of CFA2.

results is linked to the model phase, which is modeled as a whole. Even if more than one profiles are used to fit the background these do not necessarily correspond to the contributions from the different glasses present in fly ash. During reaction, the glasses react at different rates and the proportions of unreacted glasses change. So do their contributions to the amorphous 'hump'. As the PONKCS or FSM curve is defined for a raw ash it is not supposed to change shape, it is only rescaled.

5.7.3 Summary on PONKCS and FSM

This study showed the potential of two advanced XRD refinement techniques PONKCS and FSM to track the consumption of fly ash glassy components in cement paste.

Chapter 5. Degree of reaction of fly ash and slag in cement

- The results obtained by PONKCS and by FSM for a siliceous fly ash showed promise.
- For a more complex calcareous fly ash the analysis presented difficulties. Promising results in close agreement to those by SEM-EDS were obtained by FSM for one of the calcareous fly ashes. This fly ash composition was dominated by aluminosilicate glass with low to moderate Ca content.
- For complex calcareous fly ashes an improvement in XRD quantification may be difficult or even impossible.

FSM does not require calibration, and thus seems easier and faster to use than PONKCS. In both approaches strict and careful refinement should be followed to minimize the errors. It is advised to test the results against other techniques unless reliable and robust methodologies are established and verified for the investigated SCMs. Future work should focus on establishing ways to accurately model the background and to take into account the presence of amorphous AFm phases.

The development of the XRD techniques to quantify the reaction of glassy components in paste is an important issue. Using these techniques, a total degree of reaction of fly ash could be obtained simultaneously with the analysis of crystalline phases in pastes. This may offer a convenient and quicker alternative to the time-consuming SEM-EDS image analysis, for example in less demanding investigations or when access to electron microscopy is limited.

6 Phase assemblage and microstructure development

Contents

6.1 Introduction	93
6.2 Degree of reaction of clinker	95
6.2.1 Hypothesis 1: Decreased reaction due to change in pore solution	98
6.2.2 Hypothesis 2: Decreased reaction due to refinement of the pore structure	98
6.2.3 Microstructure development	101
6.3 Phase assemblage of the composite pastes	107
6.3.1 Experimental evidence from TGA and XRD	107
6.3.2 C-S-H composition by SEM-EDS	110
6.3.3 Complete phase assemblage calculated by mass-balance and thermo-dynamic simulations	110
6.4 Potential for reaction with limestone	114
6.5 Microstructure property comparison	115
6.5.1 Compressive strength	115
6.5.2 Water absorption	117
6.5.3 Migration of ions through the matrix	118
6.6 Summary of hydration study and microstructure development	121

6.1 Introduction

In the previous chapters it was shown that calcareous fly ashes may contain significantly different proportions of four main glassy populations: silicate, Ca-silicate, Al-silicate, and Ca-rich Al-silicate. Glass in the slag investigated was predominantly Ca-silicate. A detailed study of reaction in cement showed that the reactivity of these glasses depends on their chemical composition and fineness.

The consumption of the glasses from fly ash CFA1 and CFA2 in cement paste are recalled in Figure 6.1 a and b. CFA1 was mainly composed of Al-silicates and of some Ca-silicates, both

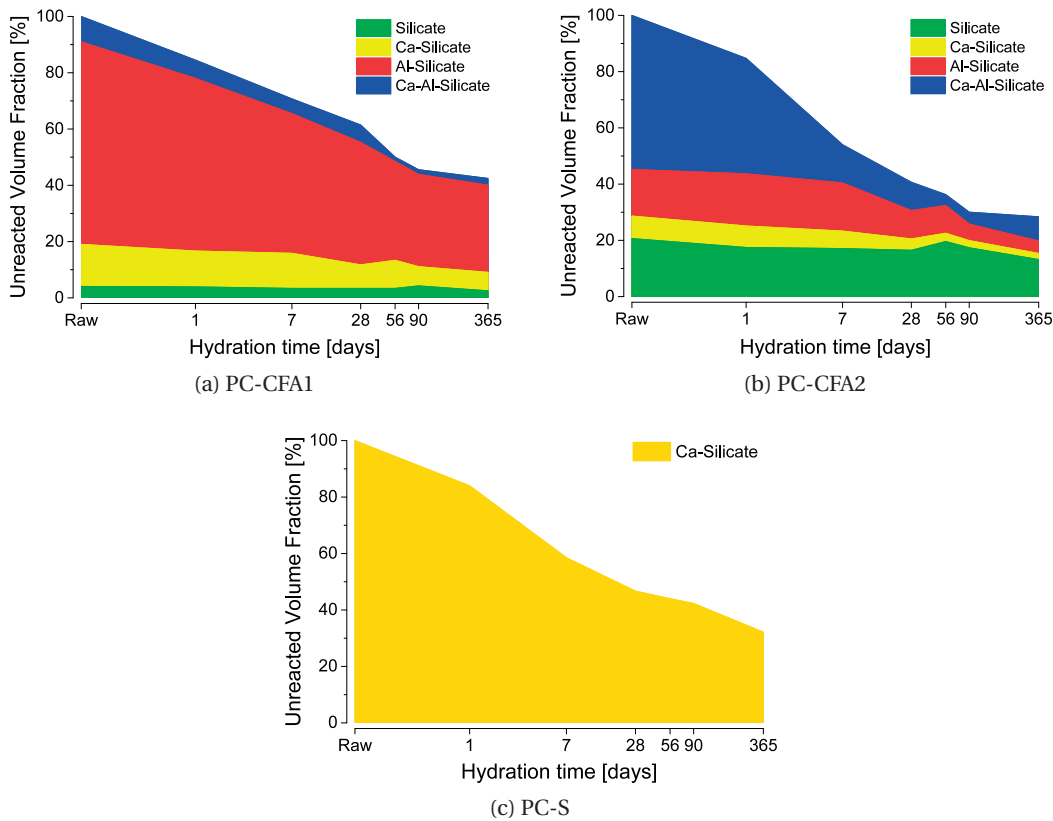


Figure 6.1: SEM-EDS image analysis data from Figure 5.3 showing that the two fly ashes studied contain significantly different proportions of the four main glass populations and that these populations react at considerably different rates. Data showing slag consumption was taken from Figure 5.11.

of which reacted at a moderate rate. After one year of hydration considerable amounts of Al-silicates remained unreacted. CFA2 contained around 50 vol.% of highly reactive Ca-rich Al-silicates that reacted almost completely within 28 days of hydration. The Al-silicates and Ca-silicates in this ash totaled around 20 vol.% and contributed to its reaction more slowly. One fifth of CFA2 were non-reactive silicates. After around 90 days of hydration the reactive part of CFA2 was almost entirely consumed. The consumption of slag glass is shown in Figure 6.1 c.

This chapter looks at how the chemical composition and the reaction kinetics of these glasses affect the hydration of multi-component cements, in particular:

- the reaction of cement clinker,
- the microstructure of hydrated paste, including the densification of pore structure and the types and amounts of hydrates formed (phase assemblage),
- the relation between microstructure and properties such as strength, water absorption and permeability.

Table 6.1: Mix formulations of the hydration study [wt.%].

	PC	L	CFA	Slag	Quartz
PC	100	-	-	-	-
PC-Q	55				45
PC-CFA1	55	-	45	-	-
PC-CFA1-S	55	-	25	20	-
PC-S	55	-	-	45	-
PC-CFA2-S	55	-	25	20	-
PC-CFA2	55	-	45	-	-
PC-L	90	10	-	-	-
PC-L-Q	49.5	5.5	-	-	45
PC-L-CFA1	49.5	5.5	45	-	-
PC-L-CFA1-S	49.5	5.5	25	20	-
PC-L-S	49.5	5.5	-	45	-
PC-L-CFA2-S	49.5	5.5	25	20	-
PC-L-CFA2	49.5	5.5	45	-	-

The above aspects were studied on pastes and mortars containing Portland clinker, CFA1, CFA2, Slag and limestone, for which the mix formulation chart is given in Table 6.1. The same portland cement was used for all the mixes and two series were prepared, one without and one with limestone substituting 10 wt.% of the portland cement. In each series the amount of portland cement substituted by CFA and slag was 45 wt.% of the total binder and the replacement was done with both a single SCM and with a mix of 25-20 wt.% CFA-slag. In each series two references were prepared, one without fly ash/slag and one with the same 45 wt.% amount of inert quartz filler to decouple the physical and chemical effects of adding CFA/slag. Gypsum was added to each system to adjust the SO₃ content to 3.25 wt.%. Paste and mortar samples were prepared according to procedures described in 3.2.1 and 3.2.12 respectively. These mix formulations were chosen from a wider range of mixes tested for compressive strength during a preliminary study. The results of that study together with heat of hydration of selected mixes measured by isothermal calorimetry are shown in Appendix B.

6.2 Degree of reaction of clinker

The amounts of C₃S, C₂S, C₃A and C₄AF in raw cement and in pastes after 1, 7, 28, 56, 90 and 365 days of hydration were quantified by XRD-Rietveld refinement. From this data the degree of reaction of clinker was calculated using equation 3.7.

Quantification of the clinker phases in composite pastes is significantly more difficult than in a PC paste. The diffraction peaks due to clinker phases often overlap with the broad 'humps' from fly ash, slag and C-S-H. This makes the refinement more difficult and requires accurate PONKCS/FSM models of the amorphous components to be fitted. The models for SCMs are prepared using scans of raw materials, as demonstrated in Chapter 5.7. Finding of an

Chapter 6. Phase assemblage and microstructure development

appropriate model may require several trials as the precise methodologies are only being developed. A model for the C-S-H contribution can be adapted by refining it on the most hydrated sample and excellent fitting results have been reported for blends of raw slag with C-S-H taken from a hydrated cement [113]. However, in real composite cements the structure of the C-S-H is likely to change with the progress of the SCM reaction, which may affect the shape of the C-S-H 'hump' and thus the quality of the refinement. In composite cements, typically there is also more AFm phases formed, part of which may be crystalline but part may remain semi- or non-crystalline. The contribution of these phases to the amorphous background was not investigated but may have an effect on the precision of the refinement.

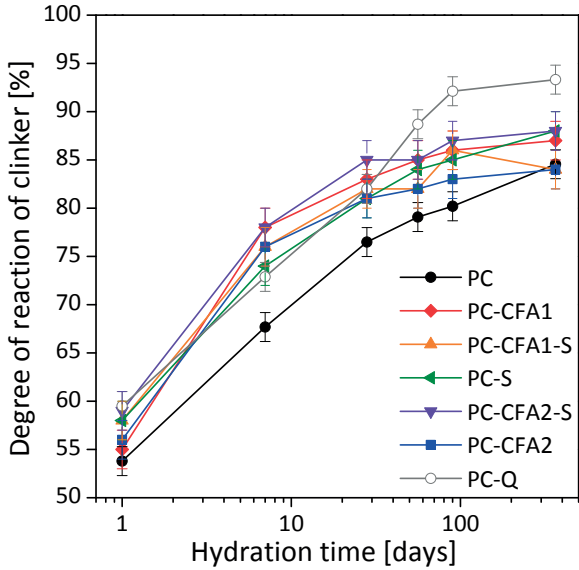
A strict refinement procedure was followed, with 14-70 °2 θ refined scan range and a background modeled by a first order Chebyshev polynomial and a flat background term. The clinker phases had their cell and peak shape parameters refined ($\pm 1\%$) on a scan of the anhydrous cement and fixed for refinement in paste. Only the scale factor of these phases was refined. Hydrates had all of the above-mentioned parameters refined. The C-S-H and the SCMs were refined as described in 5.7. More details on the XRD-Rietveld refinement are given in 3.2.6.

The results of the XRD-Rietveld quantification are shown in Figure 6.2. The degree of reaction of clinker in the PC-SCM systems studied is compared to that in the unsubstituted cement (PC) and in the presence of an inner quartz filler (PC-Q). The quantification error was estimated as $\pm 1.5\%$ for PC and $\pm 2\%$ for the blends.

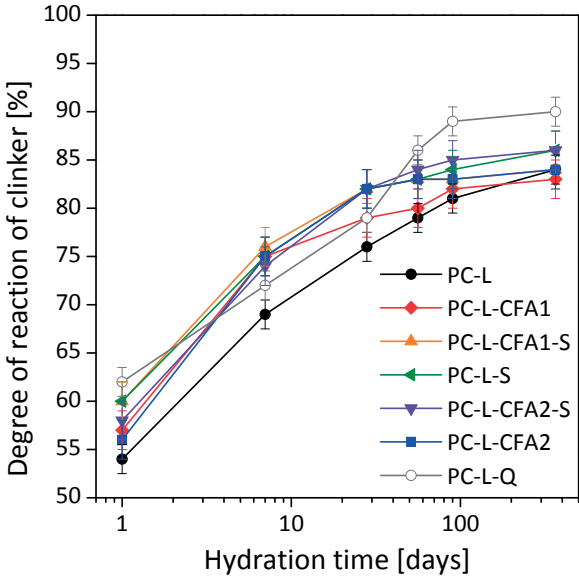
The effect of the SCMs on the degree of reaction of clinker is twofold and can be split into an early and a late regime at around 28 days of hydration. In the early regime, the relative proportion of clinker reacted in the presence of the SCMs studied was similar to that reacted in the presence of the inert quartz filler. Those degrees were higher than in the unsubstituted cement. As the reaction of SCMs is slower than that of clinker there is more space and water available for its early hydration, known also as the "filler effect".

Exceptionally, the degree of hydration of clinker in PC-CFA1 and PC-CFA2 at 1 day was lower than expected due to clinker phases from the two fly ashes. It is common for calcareous fly ashes to contain clinker phases and CFA1 and CFA2 both totaled around 6 wt.%, as shown before in Table 3.1. In composite cements, it is impossible for the XRD to distinguish between clinker phases of different origins and the degree of reaction is reported collectively. As the clinker phases in fly ash may be located within glass particles they may not be readily available for reaction. The measured degree of reaction of clinker in PC-CFA pastes can be lower than expected, in fact, even at later ages although this is less likely.

From 28 days the degree of reaction of clinker in the presence of SCMs was somewhat lower than in presence of the inert filler. The decrease of clinker reaction was more noticeable for the fly ashes than for the slag and in the presence of limestone than when the limestone was not added. In parallel to the clinker reaction, also the SCMs reacted the most in the early regime and significantly less in the late regime, as shown before in Figure 6.1. Two potential



(a) Systems without limestone addition



(b) Systems with limestone addition

Figure 6.2: Degree of hydration of clinker in composite pastes.

reasons are investigated, which may be responsible for the somewhat decreased reaction of the composite cement at later hydration ages. The first hypothesis, studied in Section 6.2.1, is the change in pore solution composition, which could decrease dissolution of the anhydrous phases directly. The second is linked to the physical constraints hindering the formation of hydrates and will be studied in more detail in Section 6.2.2.

6.2.1 Hypothesis 1: Decreased reaction due to change in pore solution

To investigate the first hypothesis the pore solution composition was measured by ICP on liquid samples extracted from pastes by high-pressure mechanical squeezing, as detailed in 3.2.10. The results are shown in Appendix H. Among the ion concentrations measured those of Al were of particular interest as Al has been reported to slow down the dissolution of silicates [96, 99]. The results presented in Figure 6.3a clearly demonstrate high and increasing Al concentrations in pastes containing CFA1 and CFA2 from 28 days of hydration. Replacing part of the fly ash with slag decreased the Al concentrations. In PC and in PC-S the Al level was almost undetectable. Figure 6.3b shows the combined degree of reaction of clinker silicates (C_3S and C_2S) measured by XRD-Rietveld. The reaction of these phases should be the most affected by high Al concentrations in pore solution. However, based on data presented there seems to be no observable influence of Al concentration in pore solution on the reaction of clinker silicates.

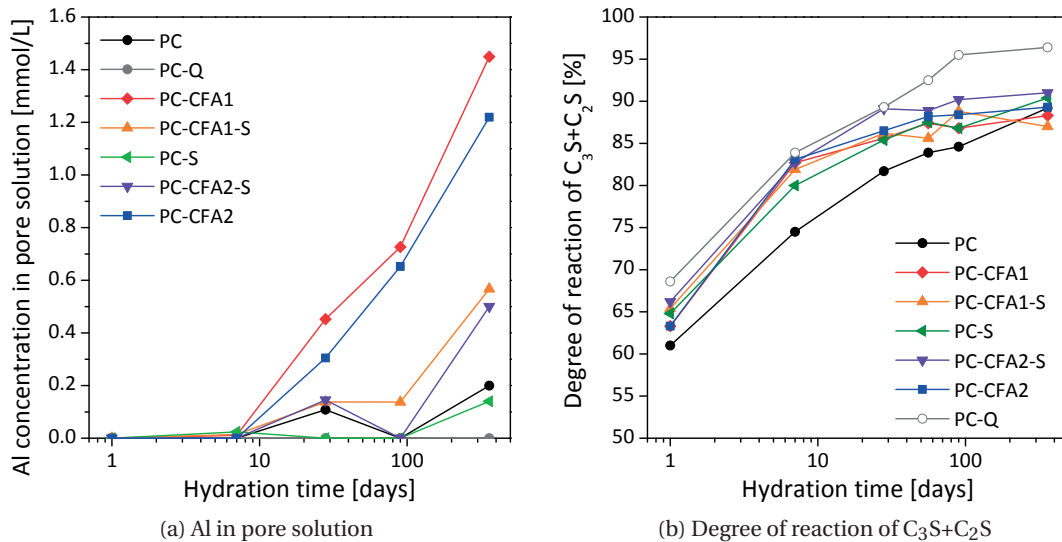


Figure 6.3: Comparison of the Al concentration in pore solution and the degree of reaction of clinker silicates (C_3S+C_2S).

6.2.2 Hypothesis 2: Decreased reaction due to refinement of the pore structure

The second hypothesis is that the reaction in PC-SCM composite pastes is less due to physical constraints from a more refined pore structure than in portland cement. The pore structure was investigated using mercury intrusion porosimetry (MIP), as detailed in Section 3.2.11. The complete set of the MIP curves measured is presented in Appendix I. The precision of MIP measurements were estimated at $\pm 1.5\%$ porosity and the relative error of determination of threshold pore entry radius at $\pm 20\%$.

6.2. Degree of reaction of clinker

The evolution of the total porosity of pastes with time is presented in Figure 6.4. The total porosity of the composite cements studied was higher than that of the PC due to a lower total degree of reaction of these systems. The degrees of reaction of clinker+SCMs are shown in Figure 6.5 and show a clear correlation to the total porosity data. Similar trends have been reported for other slags and fly ashes [51]. In the limestone-containing series the measured total porosities of the composite cements were practically the same as without limestone. The total porosity of PC-L was higher than of PC due to a larger absolute amount of limestone than in blends.

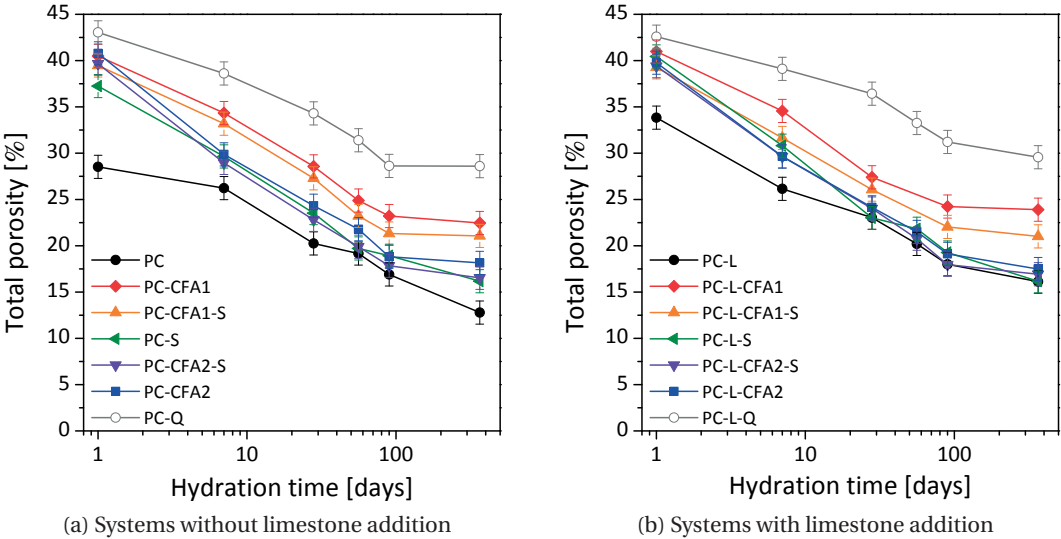


Figure 6.4: Total porosity: evolution in time measured by mercury intrusion porosimetry.

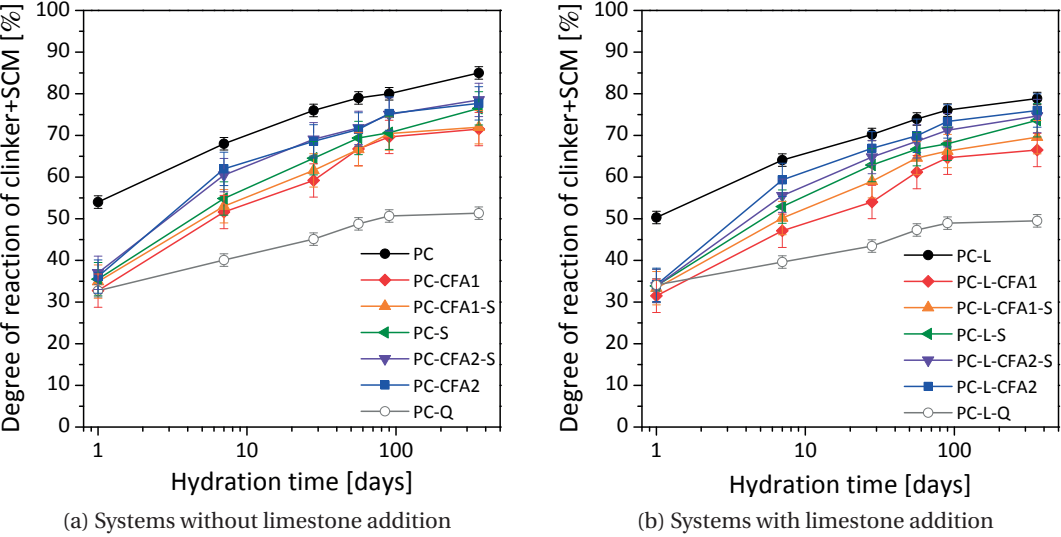


Figure 6.5: Total degree of reaction of clinker and SCMs.

Chapter 6. Phase assemblage and microstructure development

The trends in the total porosity do not explain the decrease in the rate of reaction at 28 days in PC-SCM systems observed in the previous section. The decrease in the reaction rate may thus be rather due to the refinement of pores, an important aspect of adding SCMs to cement [118]. Indeed, the crystallization in fine voids is more difficult than in the large ones due to a pressure build-up, which increases solubility [119]:

$$\Delta P v_m = RT \ln \left(\frac{c}{c_s} \right) \quad (6.1)$$

where P is the pressure, v_m is the molar volume of crystal, R the gas constant 8.314 J/molK, c the concentration and c_s the concentration when saturated. In a pore, the pressure is determined by the size of the pore entry radius r_p [120]:

$$\Delta P v_m = \gamma_{cl} \frac{2}{r_p - \delta} \quad (6.2)$$

where γ_{cl} is the interfacial free energy between crystal and liquid and δ is the thickness of a thin film of solution between the crystal and the pore. Another limitation could be the volume of pores left available for precipitation. This and the pore size entry were assessed based on MIP data. Threshold pore entry radius (Figure 6.6) was used as an indication of the refinement of pore entries. Capillary porosity (Figure 6.7) was calculated as the volume of pores with entry radius greater than 8.5 nm and was used as an indication of the volume of pores available for precipitation.

The initial, 1 day, pore structure in the composite cements was coarser than in PC but varied between the SCMs used. In the presence of CFA1 the pore entry radius was similar to that with inert filler. In the presence of CFA2 and slag the pore structure was finer than with CFA1, which is likely due to more reaction in these systems. As the reaction progressed both the threshold pore diameter and the volume of capillary porosity of the composite cements decreased significantly. Beside a bias in the XRD measurement due to clinker phases from the fly ashes, the microstructure refinement seems to be the major cause for the decreased degree of reaction of clinker in composite cements compared to PC. One implication of the much refined porosity is that it restricts the transport of ions in the matrix. As a result, more pronounced local inhomogeneities of solid and liquid phase composition are expected, which may also affect the degree of reaction of the composite cements.

The porosity data shows also that the densification does not progress the same way in the presence of the different SCMs studied. In particular, the CFA1 blends had initially the coarsest pore structure, but then showed the greatest refinement in time as evidenced by the significant drop of the threshold pore entry radius. Such a tendency was not observed in the other systems and is expected to be related to an increased formation of C-S-H and ettringite, which bind relatively more water than Portlandite and AFm phases and thus are able to better fill the space. The types and amounts of phases formed in the composite cements studied are investigated in

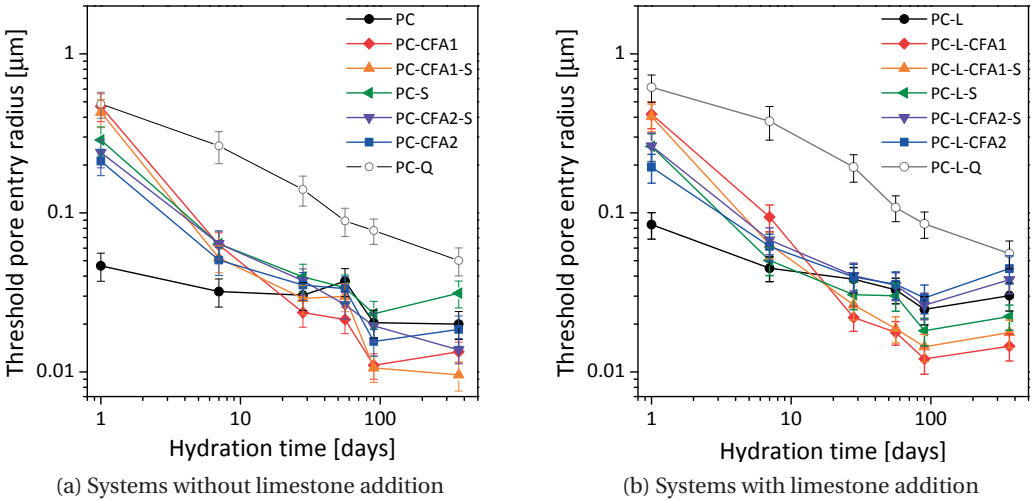


Figure 6.6: Threshold pore entry radius from MIP.

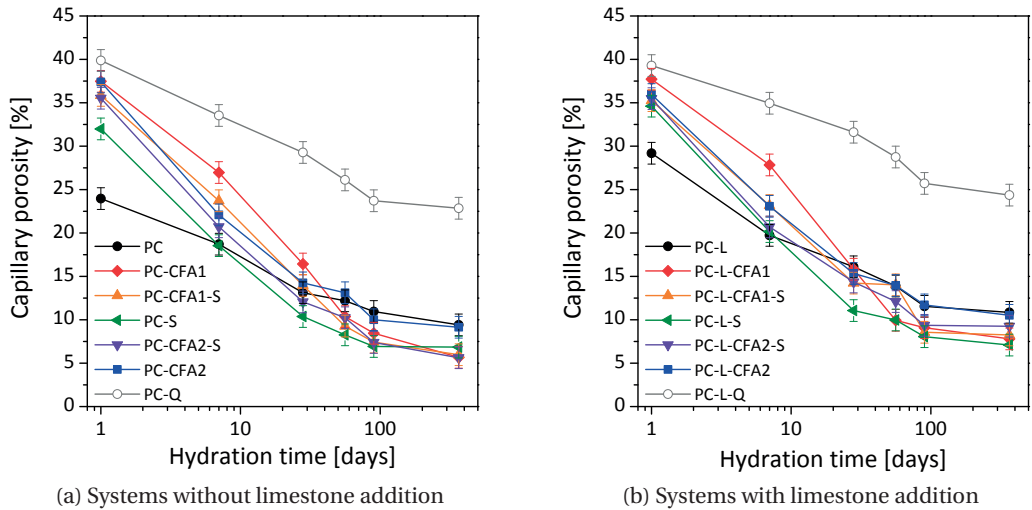


Figure 6.7: Capillary porosity by MIP.

Section 6.3. The following section gives a qualitative insight into the microstructure by means of backscatter electron micrographs.

6.2.3 Microstructure development

Backscatter-electron imaging was used to qualitatively assess the matrix development in pastes at 7, 28 and 90 days of hydration. The results presented in this section come from the PC and its binary mixes with slag, CFA1 and CFA2. The images were collected at 1000x and 4000x magnifications, with the field of view 256×192 μm and 64×48 μm respectively.

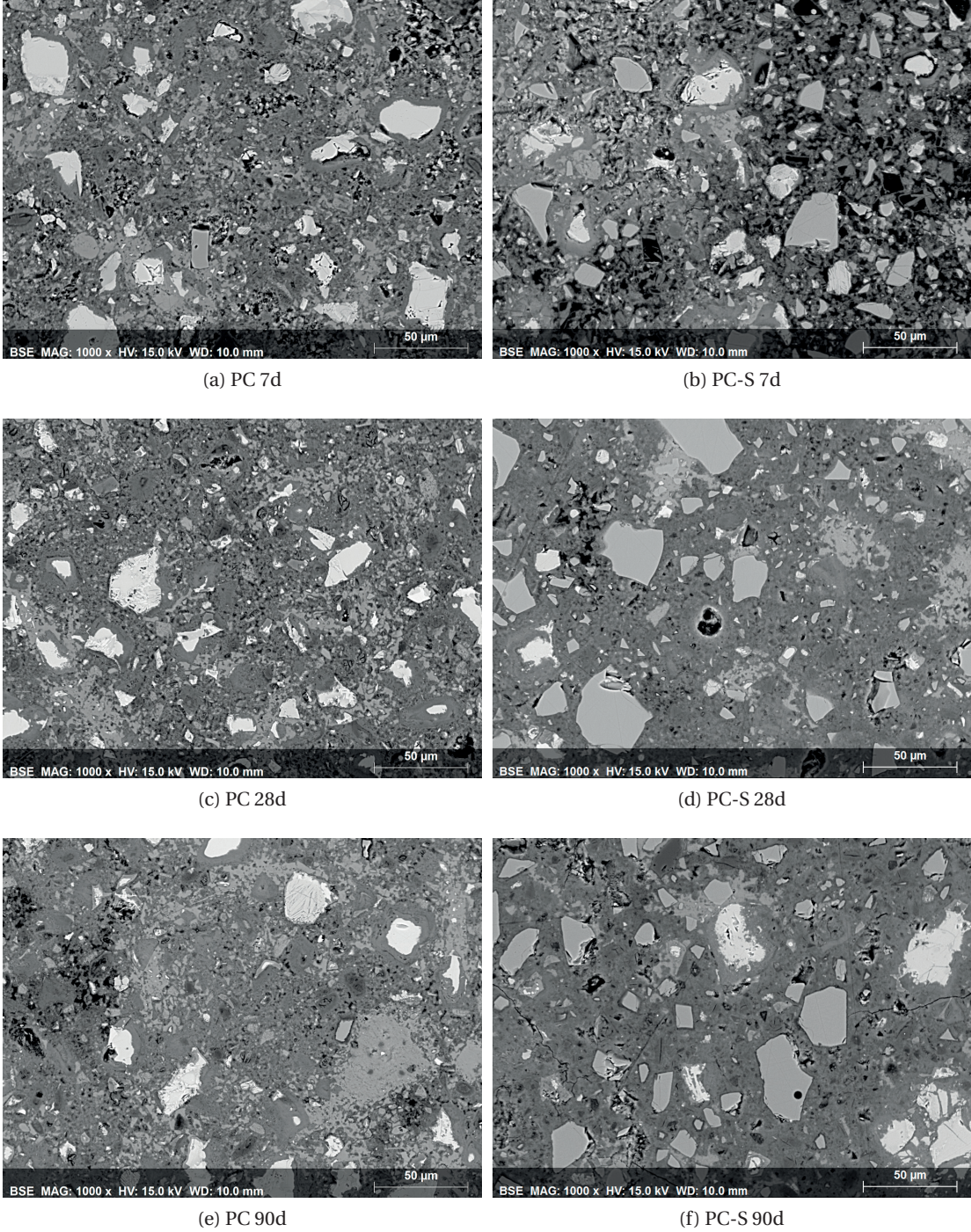


Figure 6.8: BSE images of the development of the microstructure of hydrated pastes - 1000x.

6.2. Degree of reaction of clinker

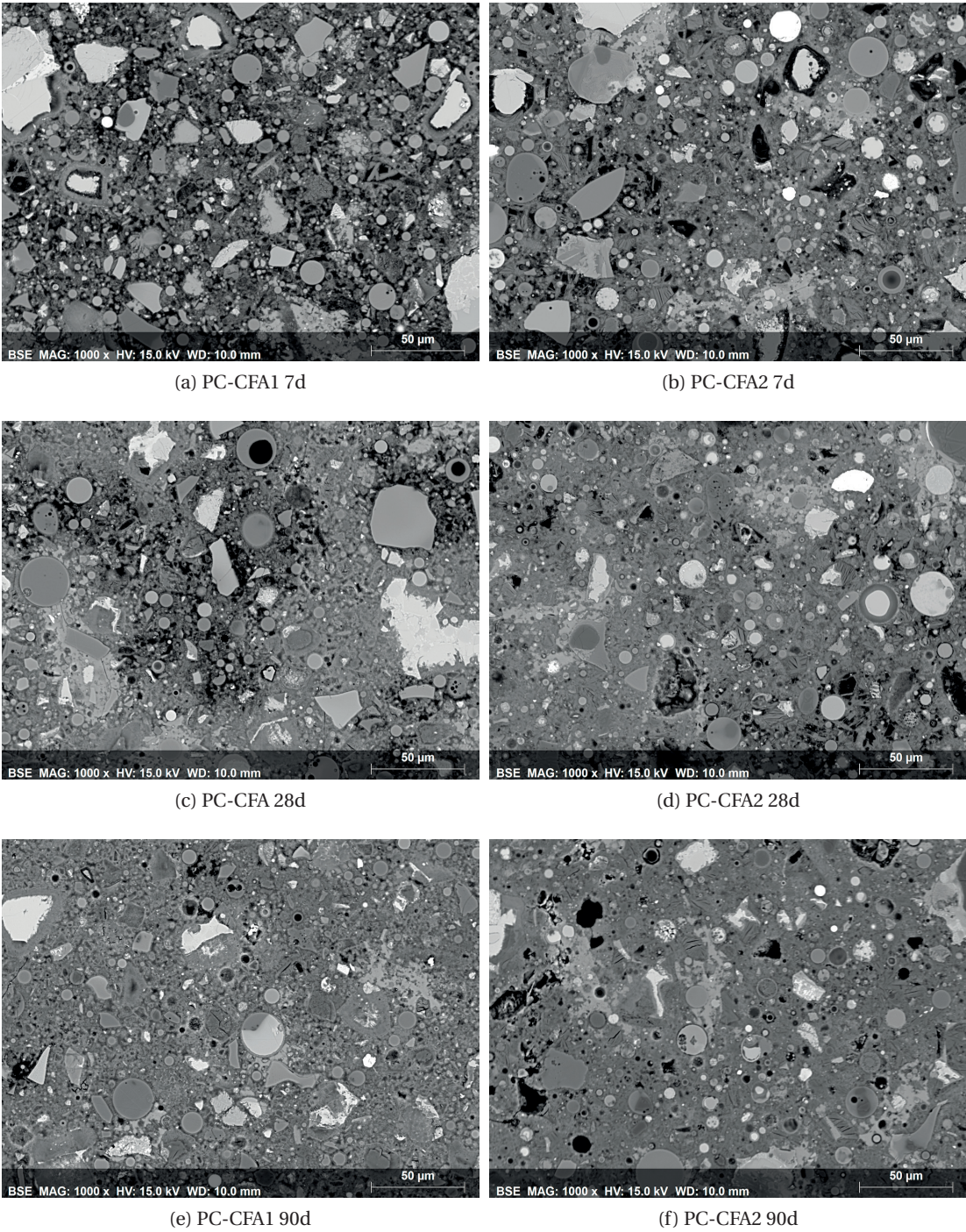
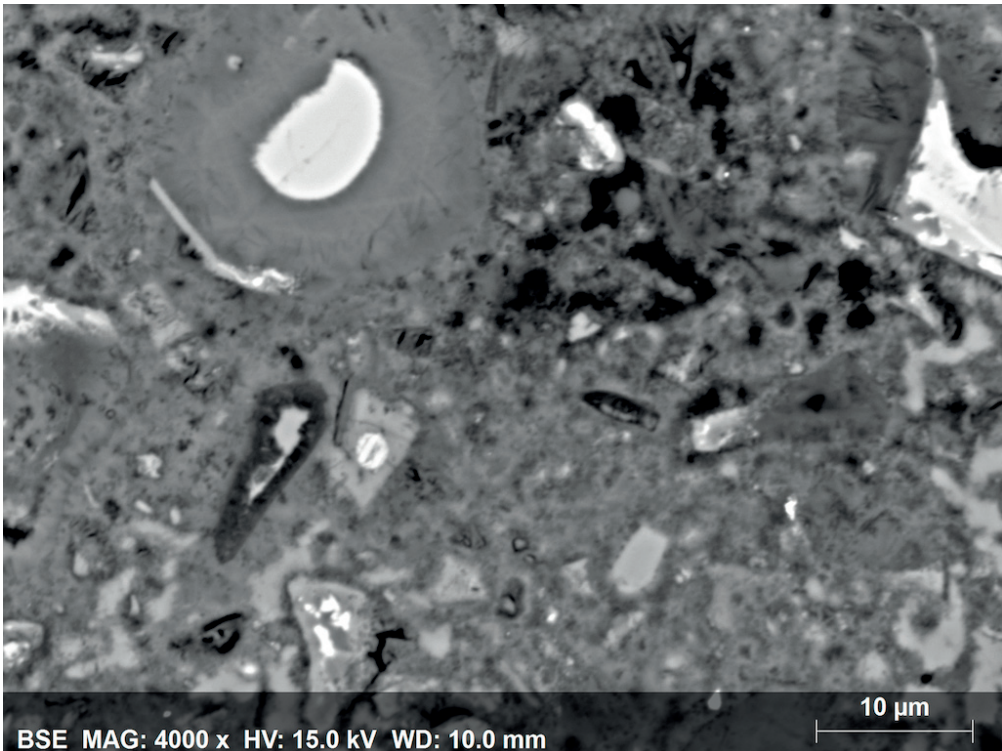
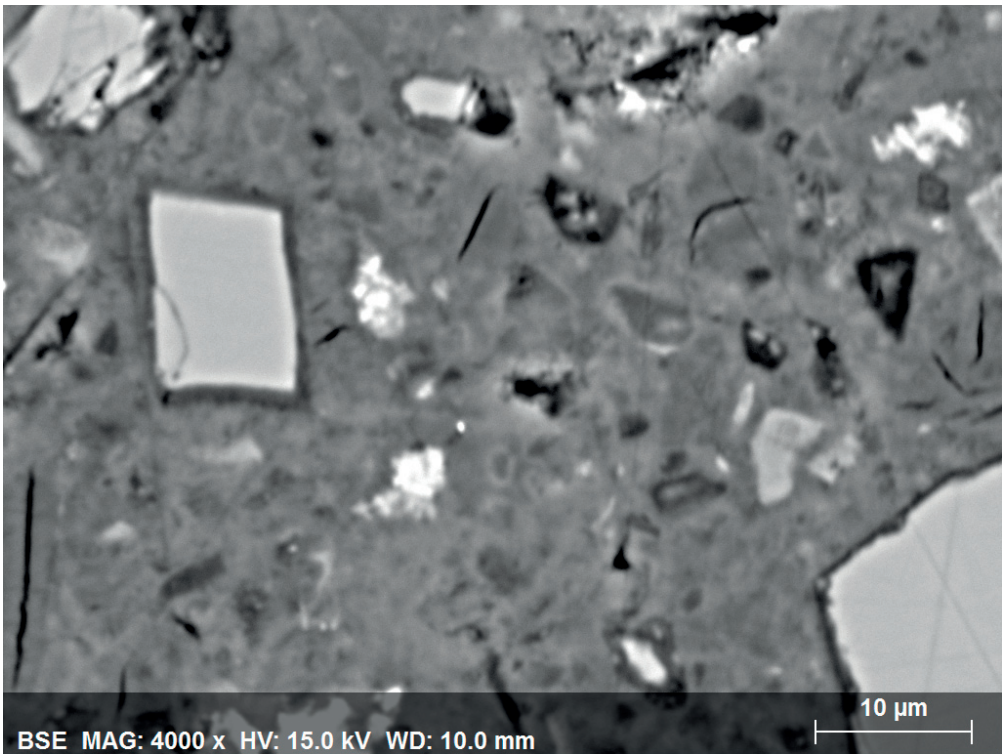


Figure 6.9: BSE images of the development of the microstructure of hydrated pastes - 1000x.

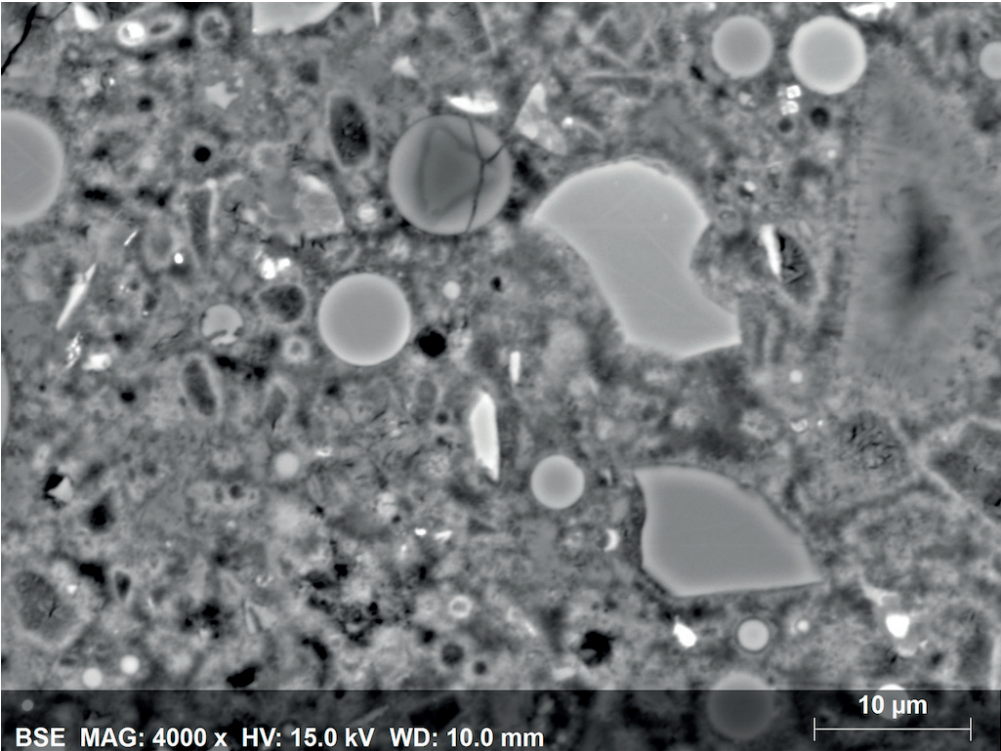


(a) PC 90d

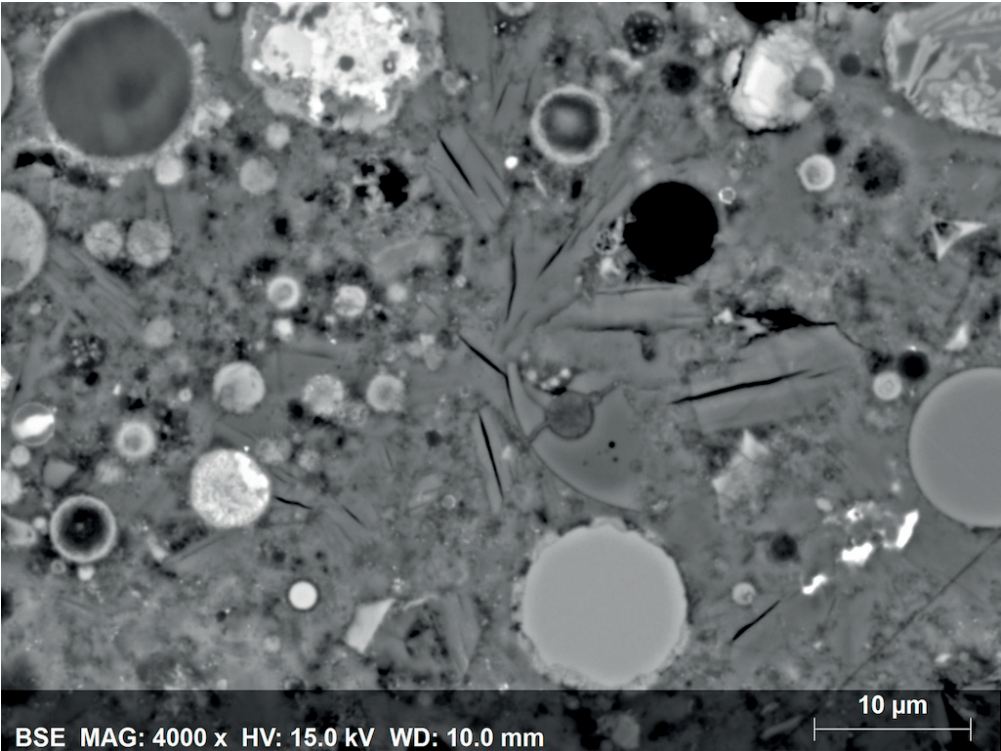


(b) PC-S 90d

Figure 6.10: BSE images of the microstructure of hydrated pastes - 4000x.



(a) PC-CFA1 90d



(b) PC-CFA2 90d

Figure 6.11: BSE images of the microstructure of hydrated pastes - 4000x.

Chapter 6. Phase assemblage and microstructure development

The 1000x magnification was used to assess the microstructure and space filling and the micrographs are presented in Figure 6.8 and Figure 6.9. These images demonstrate that the densification of the cementitious matrix not only progresses differently in PC and in PC with the SCMs but also differs between these different SCMs. After 7 days of hydration the main difference is the overall amount of space filled: PC > CFA2 > S > CFA1, which increased with higher degree of reaction (cf. Figure 6.5a).

At later ages system-specific microstructures develop, but some general similarities can still be observed. These include (1) the presence of inner C-S-H product around alite grains, which product seems rather similar between the different mixes, (2) the presence of outer C-S-H product in the matrix, and (3) portlandite clusters. The portlandite clusters are the main inhomogeneity observed in pastes, which could limit the accessibility of Ca for reaction at later ages if these clusters are spread, scarce and disconnected by a C-S-H matrix.

The main differences between the microstructures studied in Figure 6.9 are observed in the amount and the morphology of the outer C-S-H, AFm phases and portlandite. Portlandite is abundant in PC and clusters from small to large can be observed. There is significantly less portlandite in the composite cements with rather large clusters forming. There too seems to be less C-S-H in PC than in PC-SCM. As for the outer product itself, the microstructure of PC paste contains what seems to be a rather compact outer product, which does not fill the space as well as the one in the composites systems. In those systems the compactness of the outer product seems to further vary as a function of the SCM, with a less compact for CFA1 and a more compact for CFA2 and slag. Similar conclusions were drawn comparing these systems at 4000x magnification ($64 \times 48 \mu\text{m}$) in Figures 6.10 and 6.11. This qualitative assessment only suggests that the compactness of the C-S-H may differ between composite cements but further investigation is necessary to prove whether such difference really exists and to investigate what the cause could be. One hypothesis is that this C-S-H may have differently ordered globules leading to a larger amount of pores between the particle flocs in the size range of $1\text{--}12 \text{ nm}$ [121], and thus lower compactness. At the increased magnification we also observed significant amounts of AFm phases in PC-S and PC-CFA2, which precipitated in small clusters. These clusters were very abundant in PC-CFA2. No clusters of AFm were observed in PC-CFA1. The amounts of C-S-H, AFm and portlandite in the systems studied are investigated in Section 6.3.

The microscopic observations presented provide a potential explanation to the trends observed in MIP curves. Low threshold pore radius in PC-CFA1 in Figure 6.6 could be due to most of capillaries being filled by a less-compact product, which could too explain low measured capillary porosity of this system in Figure 6.7. This problem is better seen by comparing derivative MIP curves after 90 days of hydration in Figure 6.12. In such curves, a peak due to capillary porosity appears around tens of nanometers and that of C-S-H at the limit of MIP resolution, around 2 nm. For a denser C-S-H the latter peak may not be resolved. PC-CFA1 has only one peak, which appears between the expected ranges of the two mentioned peaks, possibly due to the less-compact product filling capillaries. This is not observed for PC-CFA2 and PC-S.

In PC-CFA2 a more compact product leaving more capillaries open would explain the two peaks observed in Figure 6.7 as well as the higher values of the threshold pore radius and the capillary porosity in Figures 6.6 and 6.7. In PC-S a rather compact product filling significant amount of capillaries could explain the presence of the two linked peaks in Figure 6.12.

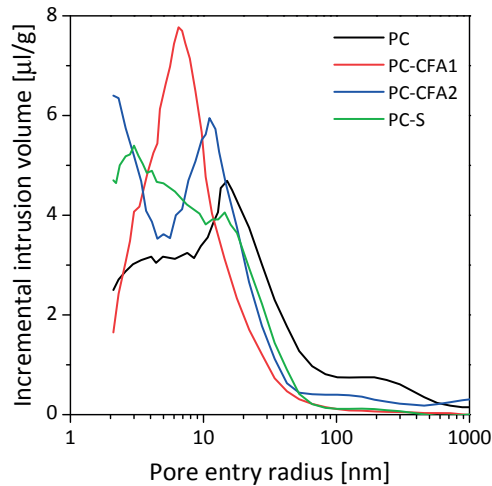


Figure 6.12: Comparison of derivative MIP curves for PC-CFA1 and PC-CFA2 after 90 days of hydration.

6.3 Phase assemblage of the composite pastes

A quantitative determination of a phase assemblage of a composite cement paste is difficult. Experimental techniques such as TGA and XRD provided important information on the types of hydrates present and XRD was used to quantify those that are crystalline. The composition of the C-S-H was determined experimentally by SEM-EDS. The results of TGA and XRD analysis of paste samples hydrated for 90 days are presented and discussed in Section 6.3.1 and the composition of the C-S-H formed in the different systems in Section 6.3.2. Based on this experimental data, we calculated a complete phase assemblage using two techniques: (1) mass-balance and (2) thermodynamic simulations. The results are investigated and compared to the experiments in Section 6.3.3.

6.3.1 Experimental evidence from TGA and XRD

A first indication of the phases formed in the different composite pastes was obtained from the TGA and the XRD data, which are shown in Figure 6.13 and Figure 6.14 respectively.

The assignment of the different peaks observed in differential TG curves is explained in Chapter 3.2.5. The thermo-gravimetric data in Figure 6.13a shows that after 90 days hydration the main hydrates in PC system were C-S-H, ettringite and portlandite, identified by the peaks at around 100-200 °C, 100 °C and 450 °C respectively. A shoulder on the right-hand side of the

peak at 100 °C suggests presence of AFm phases. The peak at around 650 °C may be related to artifacts of isopropanol treatment and to poorly crystalline carbonates due to carbonation of the samples during preparation or due to CO₂-AFm (monocarbonate, hemicarbonate) formed from the calcite present in clinker.

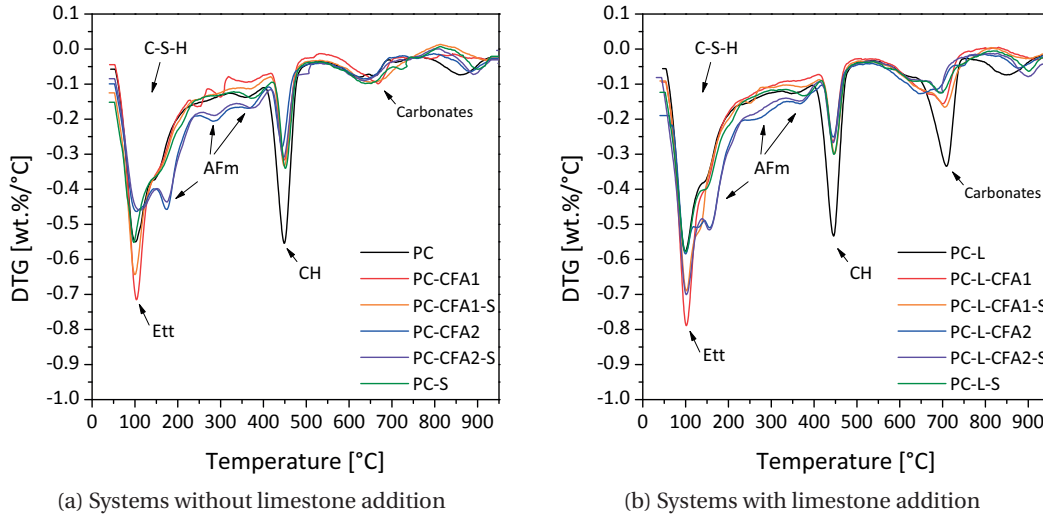


Figure 6.13: Differential thermo-gravimetric curves of the pastes studied hydrated for 90 days.

Systems without limestone addition

The main difference between the PC and the composite cements observed in the TGA data is in clearly lower amounts of portlandite present in the latter. XRD shows that the amount of portlandite indicated by the height of the peak around 18 ° [2θ] decreases in order of mixes containing: PC » Slag ≈ CFA1 > CFA2. Differences in the other TG peaks are specific to the SCM used. Comparing the TGA peak at 100 °C (1) PC-CFA1 and PC-CFA1-S seem to have produced more C-S-H and ettringite than PC, (2) PC-S a similar amount, while (3) PC-CFA2 and PC-CFA2-S produced less. Because it is difficult to separate the contributions of the C-S-H and the ettringite in TGA it is desirable to compare it with the XRD data. Figure 6.14a shows that compared to PC more ettringite was formed in the presence of CFA1 and less in the presence of CFA2 and S.

In TGA, due to overlap of peaks it is difficult to identify which AFm phases are present in the different pastes studied. It can only be observed that the mixes with CFA2 produce significantly more AFm compared to the others, as indicated by the peaks at around 160 °C, 260 °C and 360 °C. XRD may be used to identify the AFm phases, provided they are crystalline enough to appear in the diffractograms. The main AFm phase in PC was monocarbonate. The presence of monocarbonate and not monosulfate is most probably due to 1.8 wt.% calcite in clinker. By far the most AFm was produced in mixes with CFA2: monosulfate, hemicarbonate and monocarbonate. CFA2 contained 55 vol.% of Ca-rich aluminosilicates which provide significant amounts of Ca and Al to form AFm phases. In the diffractograms of PC-CFA2 and

6.3. Phase assemblage of the composite pastes

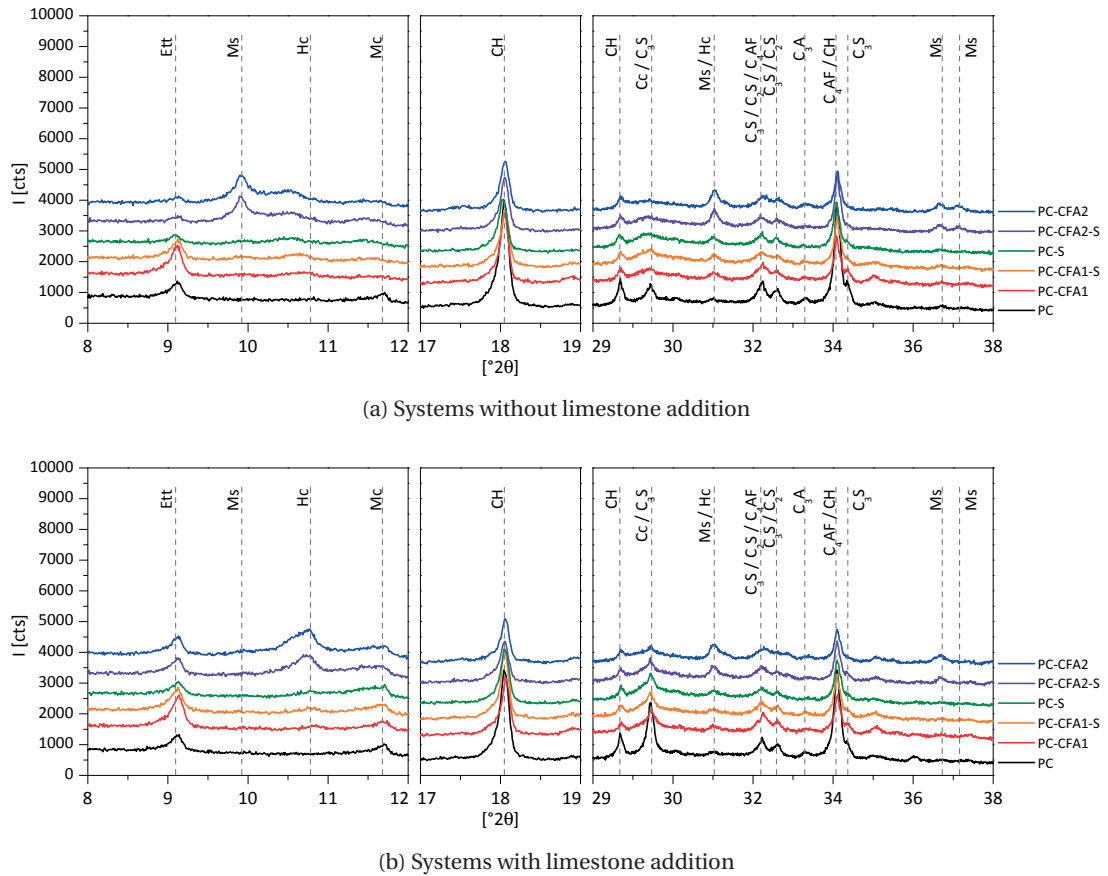


Figure 6.14: XRD patterns of the pastes studied hydrated for 90 days.

PC-CFA2-S an additional peak is observed between those of monosulfate and hemicarbonate, which is most likely due to solid solution between these two end-members [60].

Systems with limestone addition

The presence of limestone is clearly seen in the TG data in Figure 6.13b, in which an increased peak appears at 700 °C, corresponding to decarbonization of CaCO_3 . This peak is smaller in the composite cements due to the lower absolute amount of limestone added but may also be due to calcite consumption in these systems. The smallest calcite peak is observed in mixes containing CFA2, which suggests increased limestone consumption by CFA2 reaction. This correlates with the significantly increased compressive strength seen in combination of limestone and CFA2, shown in Appendix B.2.

Adding limestone to the composite cements changed their phase assemblages. The extent of the change depended on the phases present without the limestone addition. The carbonate from limestone essentially replaces monosulfate with hemicarbonate and then with monocarbonate, while the sulfate not used to form monosulfate is then available to form more ettringite. Therefore the addition of limestone had the most significant effect on the systems containing CFA2 and Slag, in which part or all monosulfate is replaced by hemicarbonate,

Chapter 6. Phase assemblage and microstructure development

monocarbonate and ettringite. The effect on the systems containing CFA1 was much less. Clear evidence of these changes can be seen in the XRD data in Figure 6.14b. A slight decrease in portlandite content is most likely due to the dilution of the clinker by the limestone addition.

XRD offered a more detailed resolution of the phases than TGA and the quantification of the identified phases by XRD-Rietveld refinement will be shown in Section 6.3.3.

6.3.2 C-S-H composition by SEM-EDS

The composition of the C-S-H was measured using SEM-EDS on around 100 carefully selected points per sample and analyzed as described in 3.2.7. The inner C-S-H composition was taken on the product formed around alite grains and the outer C-S-H in the space between the amorphous particles. The results presented in this section refer to the inner product, which is more homogeneous. On average, the difference between inner and outer product is little. The complete EDS point analysis data can be found in Appendix G.

Figure 6.15 compares the composition of the C-S-H in the different pastes after 90 days of hydration with the total amount of Al, Si and Ca dissolved from the clinker and the SCMs up to that moment. These amounts were calculated knowing the composition of the clinker and the reactive parts of the SCMs and their respective degrees of reaction.

Figure 6.15a shows a clear trend towards higher Al/Ca in the C-S-H with the increasing Al/Ca available in the systems. The latter ratio mainly depends on the Al and the Ca supplied to the reaction by the SCMs. The total amount of Al supplied, which increases with the order: Slag < CFA1 < CFA2, is not the only factor. Due to the significant amounts of Ca from the CFA2 glass the trend in Al/Ca is: Slag < CFA2 < CFA1.

Unlike the Al/Ca, the trend to higher Ca/(Si+Al) of the C-S-H with more Ca/(Si+Al) available is more a step function with a steep slope at around $\text{Ca}/(\text{Si}+\text{Al}) = 2.0$. In Figure 6.15b six mixes provide almost identical Ca/Si to the reaction but the Ca/(Si+Al) in the C-S-H varies from 1.25 (PC-L-CFA2) to 1.60 (PC-L-S). This demonstrates that Ca content of the C-S-H depends not on the Ca availability but on the Al and Si content in that phase. This is in agreement with Richardson and Groves [52] who have shown that the amount of cations such as Ca^{2+} in the C-S-H decreases with increasing Al, which substitutes the Si. To accommodate more Al in C-S-H more Si is required, which is confirmed by a clear trend in Figure 6.15c. These changes are accompanied by increasing polymerization of the aluminosilicate chains and charge balancing by additional interlayer Ca^{2+} .

6.3.3 Complete phase assemblage calculated by mass-balance and thermodynamic simulations

Mass-balance calculations (MB) and GEMS thermodynamic simulations (TS) were carried out in attempt to study the phase assemblages including phases that are difficult or impos-

6.3. Phase assemblage of the composite pastes

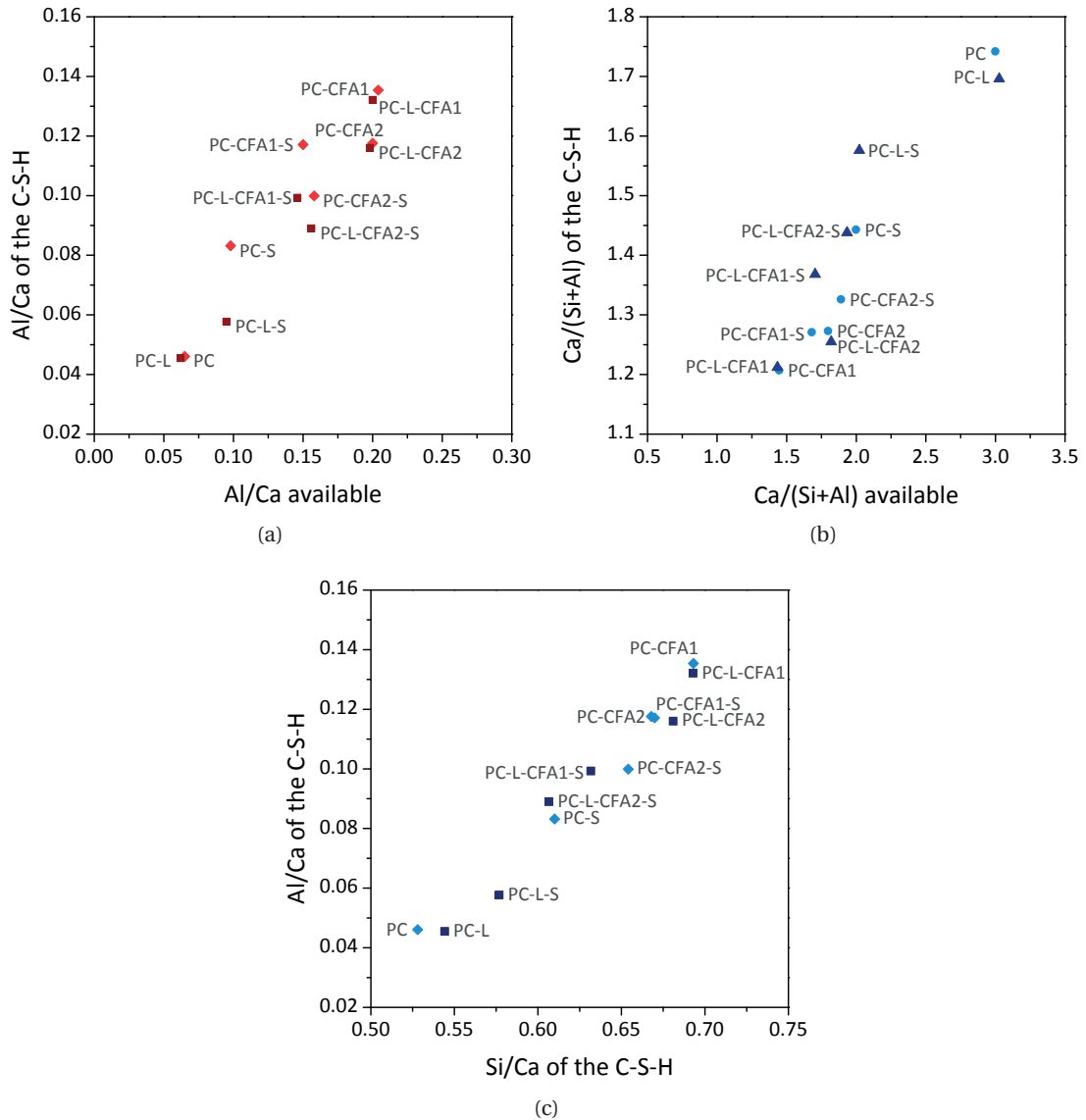


Figure 6.15: Comparison (a, b) of the C-S-H composition measured by SEM-EDS point analysis with the amount of Al, Ca and Si available for the reaction and (c) the relation between the experimental Al/Ca and Si/Ca of the C-S-H.

sible to quantify by XRD, notably C-S-H and the AFm phases (monosulfate, hemicarbonate, monocarbonate, hydrotalcite, strätlingite). MB distributes known amounts of reacted elements and water among user-specified phases expected to form in the analyzed system. TS calculates a stable phase assemblage by minimization of Gibbs free energy from among the phases included in the thermodynamic database used. Detailed information and a sensitivity analysis of MB and TS are given in Section 3.2.8 and 3.2.9 respectively. The uncertainty in $\text{cm}^3/100 \text{ cm}^3$ of hardened paste was estimated around 3.0 for C-S-H and monosulfate, around 2.0 for portlandite and monocarbonate and 1.0 for the other phases.

Chapter 6. Phase assemblage and microstructure development

For the two techniques the main input is the same, which is composed of the total amount of the elements available for the reaction at the studied hydration time. These amounts are known from the degree of reaction of the clinker phases quantified by XRD-Rietveld refinement in Section 6.2 and the degree of reaction and the chemical composition of Slag and of each of the glasses in CFA1 and CFA2 obtained by SEM-EDS in Chapter 5. Table 6.2 shows the amounts of Al, Si, Ca and Mg used for the calculations. Both MB and TS require additional input on the amount of Al and S in the C-S-H, which was taken from Section 6.3.2. Additionally in TS, the alkali concentration was adjusted. We observed that high alkali concentrations found in the initial input were the reason for unreasonable phase assemblages calculated by TS. To ensure modeling of conditions close to the experimental ones, the amounts of K_2O and Na_2O in the input were adjusted so that the output K^+ and Na^+ concentrations in the pore solution would match the experimental values measured by ICP on real pore solutions.

Table 6.2: Amounts of main oxides reacted after 90 days of hydration in the pastes studied.

	PC	PC-CFA1	PC-CFA1-S	PC-S	PC-CFA2-S	PC-CFA2
CaO	52.1	36.4	38.3	40.0	42.1	41.6
SiO ₂	15.0	19.0	18.3	17.2	16.7	15.9
Al ₂ O ₃	3.1	7.6	6.2	4.8	7.2	8.7

	PC-L	PC-L-CFA1	PC-L-CFA1-S	PC-L-S	PC-L-CFA2-S	PC-L-CFA2
CaO	48.1	34.2	36.7	38.9	40.6	40.4
SiO ₂	13.8	18.2	17.3	16.7	15.7	15.2
Al ₂ O ₃	2.7	7.1	5.9	4.5	6.9	8.4

The results presented in Figure 6.16 show the phase assemblages after 90 days of hydration calculated by MB and TS and compared to the experimental data by XRD-Rietveld. C-S-H was the main hydration product in all the pastes studied. The amounts of C-S-H calculated by TS were slightly lower than by MB but the differences lie within the error of 3 cm^3 . The amount of the C-S-H formed in the different systems is shown better in Figure 6.17. It depended on the amount of Si reacted (cf. Table 6.2) and increased in the order: CFA2 < Slag < CFA1. The composition of the C-S-H in the different pastes was not the same, which has been shown before in Section 6.3.2.

The ettringite content reported in the mass-balance is taken directly from the XRD-Rietveld refinement and for many systems TS produced similar results. The largest discrepancies were observed for PC-CFA1. Much higher ettringite content in the real system could be due to early availability of sulfate but limited accessibility of Ca and Al at later stages of the reaction, which are necessary to react with ettringite to monosulfate. TS and MB assume perfect homogenization of matrix components, which is not the case in real systems, as shown in BSE images in Section 6.2.3. Probably portlandite is the most restricted phase and since the glass of CFA1 cannot provide as much Ca locally as that of slag and CFA2 the major differences in ettringite content are observed in PC-CFA1. In the presence of limestone, ettringite is not predicted to react to monosulfate anyway thanks to the presence of carbonate, which

6.3. Phase assemblage of the composite pastes

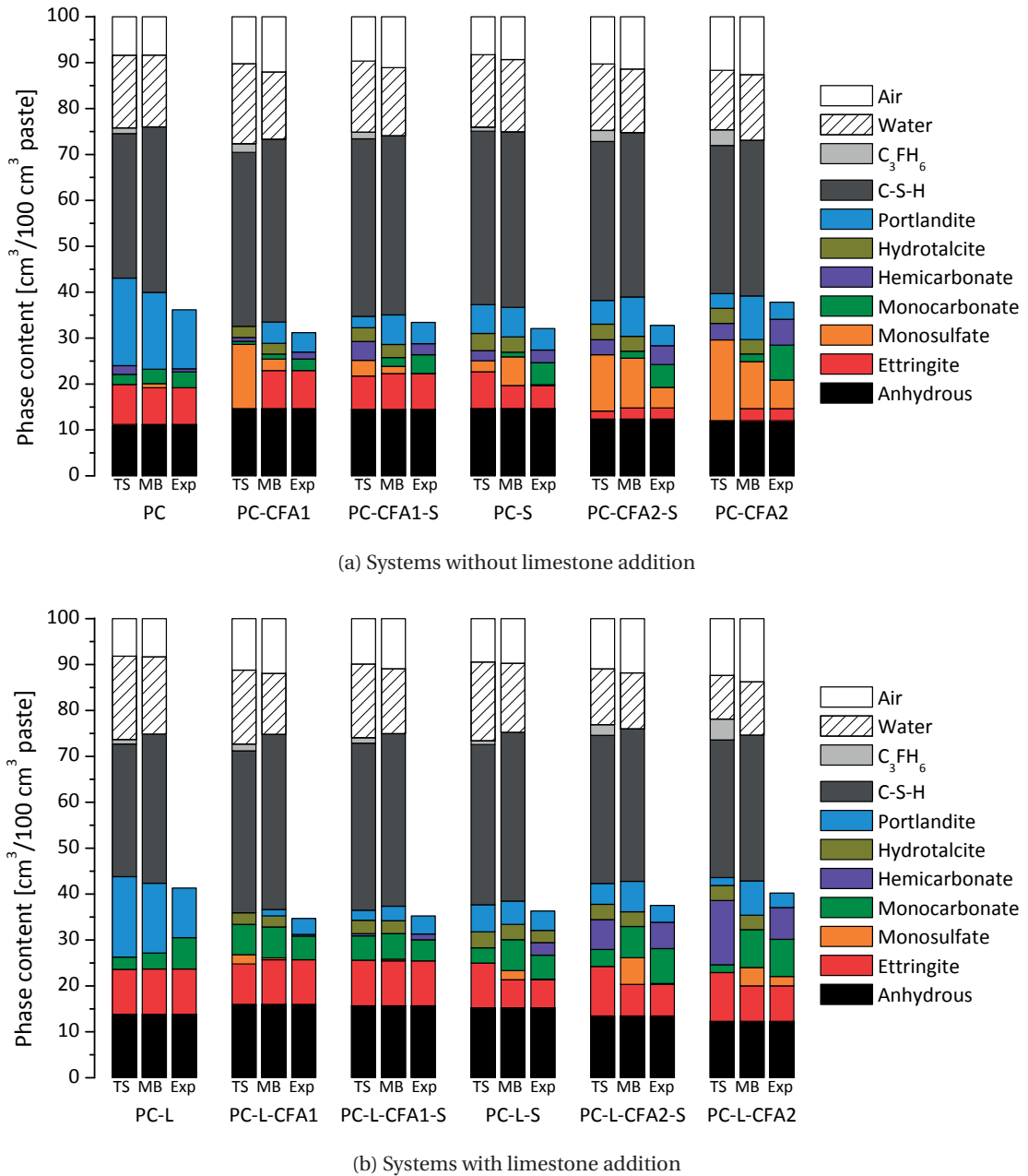


Figure 6.16: Comparison of the phase assemblages determined by mass-balance (MB) and thermodynamic modeling (TS) with experimental data (Exp).

decreases the problem of homogenization and thus the discrepancies between TS and MB. The most significant differences in portlandite content are observed for CFA1. TS shows that the portlandite could react, however it is still detected by XRD. This suggests there is a factor limiting its reaction, most probably the limited transport within a compact matrix.

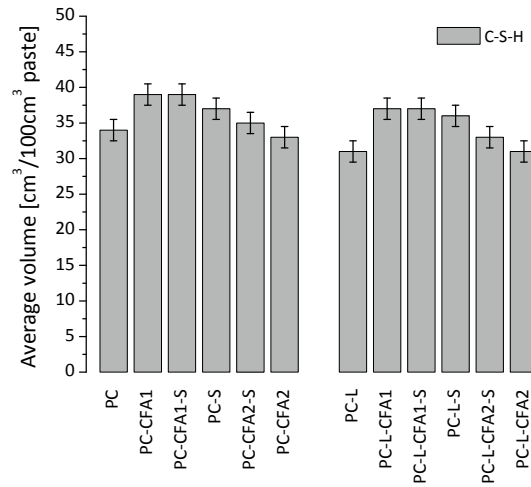


Figure 6.17: Volume of C-S-H in pastes after 90 days of hydration. Averaged results of MB and TS.

The calculated phase assemblages improve our assessment of the AFm phases formed, still these phases and portlandite is where most differences between the different techniques appear. There seems to be a large variation in the predicted and measured content of monosulfate and monocarbonate. More monocarbonate in experimental results could be due to carbonation of samples during handling. Hemcarbonate and C_3FH_6 were not calculated in the MB protocol used. The trends in amounts of hemcarbonate quantified by XRD corresponded quite well to those predicted by TS, except PC-L-CFA2, in which somewhat more monocarbonate was found by XRD. Hydrotalcite was predicted by TS and included in MB in all the systems to accommodate Mg. The presence of hydrotalcite could be found in TGA curves but was not clearly manifested in the experimental XRD data due to a significant overlap with most of the peaks of monocarbonate. The differences between the volume of AFm + ettringite quantified by XRD and that calculated by MB and TS did not exceed $5 \text{ cm}^3/100\text{cm}^3$ paste.

6.4 Potential for reaction with limestone

Limestone, if available and of acceptable quality, offers potential for a low-cost partial replacement of cement clinker. Further, carbonate-AFm phases are more stable than the sulfate-AFm and prevent the decomposition of ettringite to monosulfate after sulfate has been consumed. As a result, it is generally desirable to increase the content of limestone in composite cements. The amount of limestone that can react in a given mix is primarily determined by the availability of Al and Ca. In the view of the previous sections showing that some multi-component cement matrices may pose significant limitations on the transport of ions, here Al and Ca, the consumption of limestone may in fact be more limited locally.

The consumption of calcite in the different systems was quantified by XRD-Rietveld and is shown in Figure 6.18. By far the most calcite was consumed in PC-L-CFA2 and the possibility

of increasing the limestone content in mixes with CFA2 is explored in Appendix C. In the other systems, the calcite consumption in Figure 6.18 tends to plateau around 28 days of reaction. This should not be the case, as portlandite is still present in those systems (Figure 6.16) and pore solution analysis in Figure 6.3a has shown that Al is available. The trends in capillary porosity in Figure 6.7 show that the capillary porosity of PC-L-CFA2 was on the high side compared to the other systems, which would support the theory of limited limestone reaction due to limited transport. In the presence of CFA1 the capillary porosity was high at 1 and 7 days but the limestone itself reacts slowly, so the transport at later ages seems to be of more importance. Further, CFA2 and slag glass are richer in Ca than CFA1 and can provide more Ca locally.

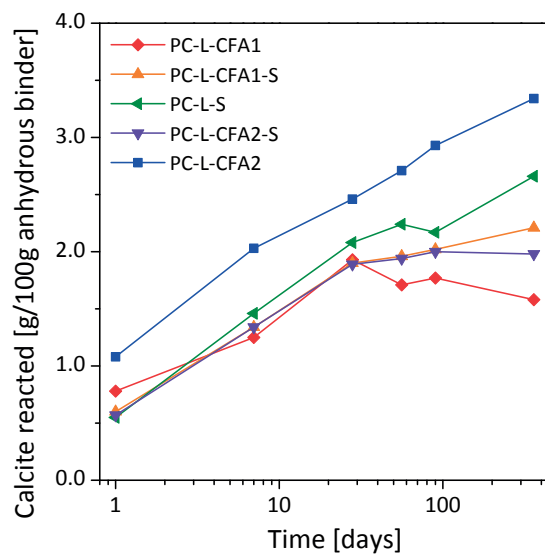


Figure 6.18: Calcite consumed in systems with the different SCMs studied.

6.5 Microstructure property comparison

In this section the microstructure of the pastes is compared to the performance of mortars in terms of compressive strength, water absorption and migration of ions through the matrix.

6.5.1 Compressive strength

Compressive strength of mortars depends on many factors, among which the amount of hydration products formed per unit of volume available, the so called gel-space ratio, is one of the most important [122]. To verify whether the strength could be related to the gel-space ratios these were calculated based on the results from GEMS thermodynamic modeling and the mass-balance calculations. The total amount of hydration products was divided by the total volume of fresh paste equal to the sum of clinker, SCM and water mass divided by their

Chapter 6. Phase assemblage and microstructure development

respective densities. Clinker density was 3.10 g/cm^3 , that of fly ash 2.73 g/cm^3 , that of slag 2.91 g/cm^3 , that of limestone 2.70 g/cm^3 and water 1.00 g/cm^3 .

The gel-space ratios are compared to the compressive strength in Figure 6.19a. Despite a general trend to higher strength with the increasing gel-space ratio the scatter in the data is considerable. However, looking closer at the strength vs. gel-space ratio of three selected mixes in Figure 6.19b there seems to be little scatter in the compressive strength results and the trends obtained are for each of the mixes are cleaner. These three mixes had different phase assemblages, as shown before in Figure 6.16, still the trends of strength vs. gel-space for two of them, PC-CFA2 and PC-S were almost the same. It therefore seems unlikely that different phases would contribute with significant difference to the compressive strength. The remaining possible causes of the spread between the different systems are (i) the effect of arrangement, which we don't know how to quantify at the moment and (ii) the discrepancy between the real and the calculated amount of gel, which estimation is represented by an error bar in Figures 6.19a and b. The size of this error bar represents the change of gel-space ratio if the total volume of hydrates varies by 4 cm^3 , which has been the estimate of error of this determination. Most of the scatter in the strength vs. gel-space ratio seems to be within this error. However, the consistently lower than expected gel-space of PC-CFA1 in Figure 6.19b suggests that there may be another factor. In the mass-balance used to calculate the gel-space ratios the density and the water content of the C-S-H was the same for all systems. If indeed the C-S-H in PC-CFA1 was less compact, as suggested by the BSE images in section 6.2.3, it would occupy more volume and the gel-space ratios for this mix would be higher.

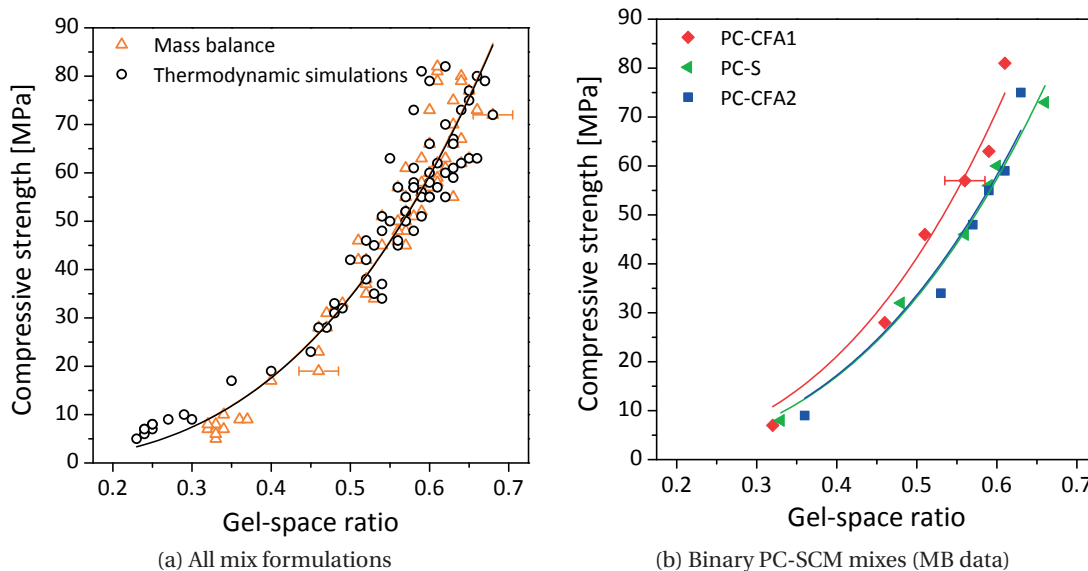


Figure 6.19: Compressive strength of mortars vs. gel-space ratio in pastes determined based on GEMS thermodynamic simulations and mass-balance calculations.

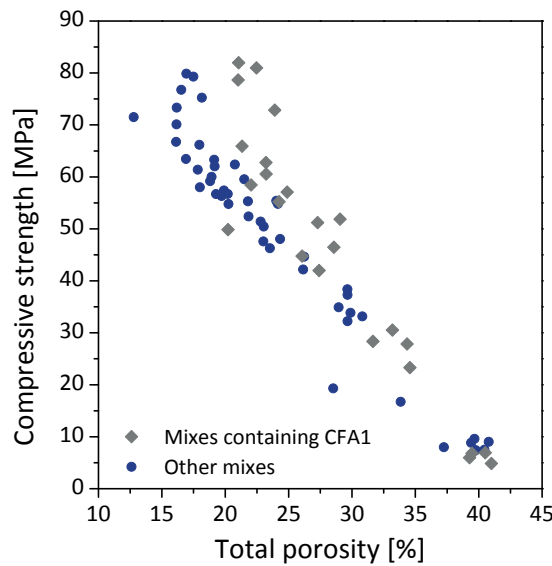


Figure 6.20: Compressive strength of mortars vs. total porosity measured by MIP.

The strength was also compared to the total porosity measured by mercury intrusion porosimetry, which comparison is presented in Figure 6.20. In this figure almost a linear trend to higher compressive strength is observed with decreasing total porosity. Mixes containing CFA1 tend to diverge from the main trend and were thus plotted using a different colour. The difference in the slope becomes evident when the total porosity decreases below 30%, i.e. from around 28 days of hydration. This discrepancy between the total measured porosity and the compressive strength may be due to different parts of porosity affecting the strength differently. Evidence of significant refinement of the pore structure in the presence of CFA1 at around 28 days of reaction, indicated by a significant decrease of the threshold pore entry radius, has been shown before in Figure 6.6.

6.5.2 Water absorption

The water absorption test was carried out to assess the permeability of mortars after 90 days of hydration. The procedure is explained in 3.2.14. The results presented in Figure 6.21 show linear relationship of the absorbed mass with square root of time for the first 4 hours of experiment. Afterwards, a decrease in the rate is observed, which is due to the contribution of smaller pores than the capillary. Therefore, only the linear part was considered in the further analysis.

Figure 6.21 demonstrates a clear decrease of water absorption due to incorporation of CFA1 and Slag. The decrease is less for CFA2, which could be related to a rather compact product of its reaction, which does not fill the space equally well as the less compact product from CFA1. The water absorption is expected to depend on the amount of open capillary porosity. The latter was determined from the MIP curves and is compared to the slope of absorption

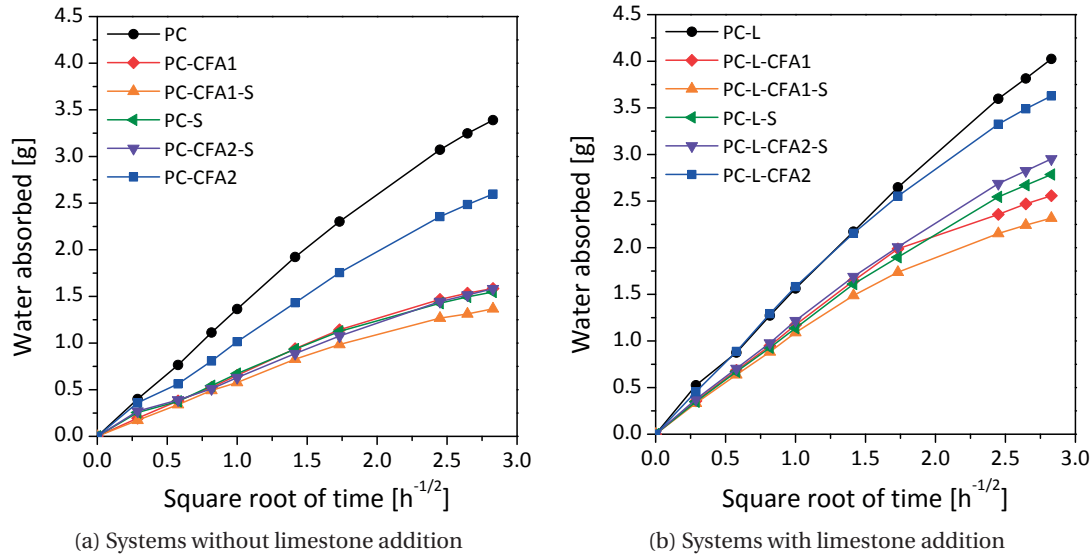


Figure 6.21: Water absorption of dried mortar cubes.

in Figure 6.22. It shows a trend towards a higher rate of water absorption with an increasing volume of capillaries. The SCMs studied lowered the rate of capillary absorption compared to PC. In general the largest reduction could be observed due to CFA1 and Slag, except PC-CFA2-S which was the least absorbing. Limestone addition increased the capillary porosity in all of the systems studied, which led to higher measured rates of water absorption.

6.5.3 Migration of ions through the matrix

The migration of ions through the matrix was assessed in a chloride migration experiment. A full description of this method can be found in section 3.2.15 of the Materials and Methods. The voltage applied was 30V except the PC and PC-L which were tested at 3V due to their much higher conductivity. These values were multiplied by 10 to compare with the remaining data. The evolution in time of the current measured is presented in Figure 6.23.

All fly ash/slag cements except PC-CFA2 showed lower current than the PC and PC-L references. Among the composite systems without limestone addition PC-CFA2 was the most permeable as evidenced by the highest current measured and the current reached its minimum the earliest, which is when chloride has penetrated through the sample to the downstream cell. Replacing part of CFA2 by Slag clearly decreases the current measured. The same is seen for CFA1, which showed much lower current than CFA2 and the partial replacement of CFA1 by Slag further decreased its permeability and thus the current. The PC-S mix showed the lowest current in this series.

In the series with limestone added, the current values measured were significantly less than in the limestone-free systems except the PC-L-S which was only slightly reduced. The trends

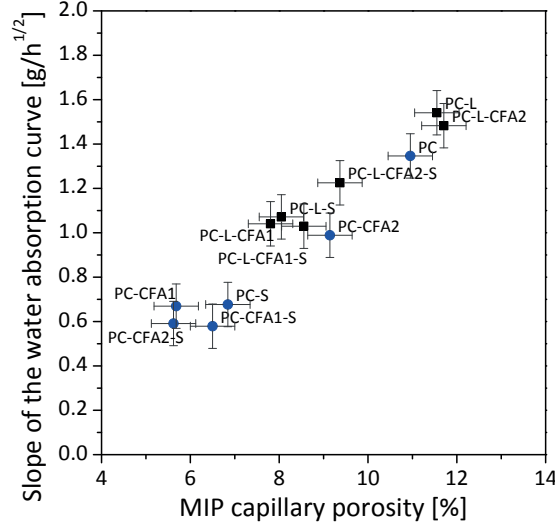


Figure 6.22: Dependence of the rate of water absorption on the volume of capillaries.

observed were similar too. PC-L-CFA2 showed the highest current which decreased with the partial Slag replacement in PC-L-CFA2-S. The current in PC-L-CFA1 was much less and decreased slightly with the partial Slag replacement in PC-L-CFA1-S. The lowest current was measured for PC-L-S.

The current measured is a function of the composition of the pore solution and of the porosity, the tortuosity and the constrictivity of the pore structure. To decouple the effect of the pore solution composition the so called formation factor was calculated. The formation factor Y is defined as a ratio between the conductivity of an electrolyte σ_e to the conductivity of the same electrolyte when physically constrained, inside a porous matrix σ_m [123]:

$$Y = \frac{\sigma_e}{\sigma_m} \quad (6.3)$$

The conductivity of cement pore solutions σ_e was calculated from concentrations of Na^+ , K^+ and OH^- according to the approach presented in [124]. The concentration of Na^+ and K^+ were measured by ICP on pore solutions obtained from paste samples after 90 days of hydration by high-pressure squeezing. The OH^- concentration was calculated from those of Na^+ and K^+ . The conductivity of a pore solution was calculated as a weighted sum of the equivalent conductivity λ_i of each ion, with valence z_i and molar concentration c_i as weighs:

$$\sigma_e = \sum z_i c_i \lambda_i \quad (6.4)$$

The equivalent conductivity depends on the solution concentration and was calculated using a single-parameter model proposed by Snyder *et al.* [124]:

$$\lambda_i = \frac{\lambda_i^0}{1 + G_i \sqrt{I_M}} \quad (6.5)$$

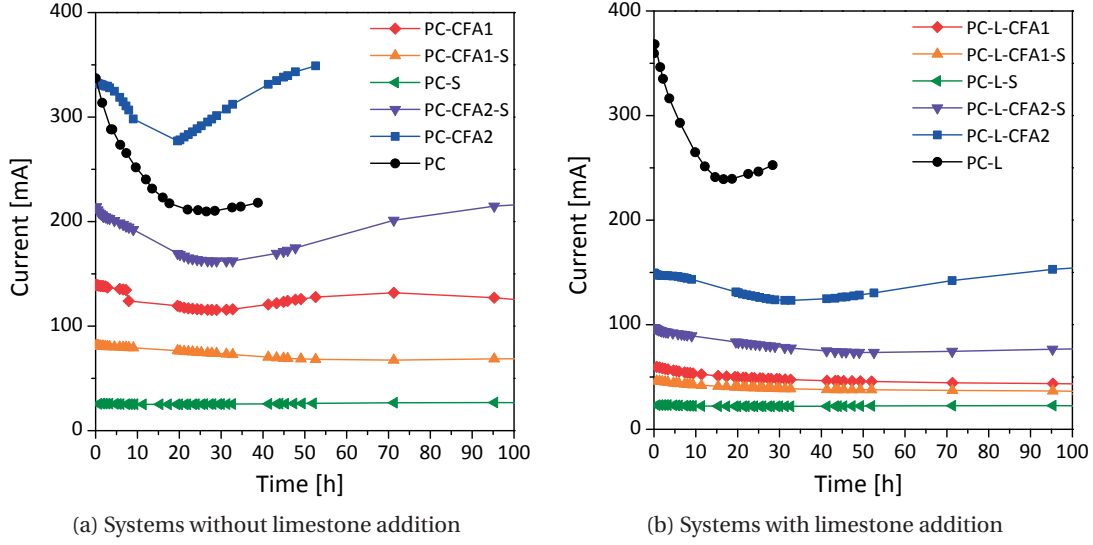


Figure 6.23: Current vs. time during the migration experiment.

Table 6.3: Equivalent conductivity λ_i^0 and coefficient G_i used for the calculation of the conductivity of the pore solutions.

	λ_i^0 [cm ² S/mol]	G_i [(mol/L) ^{-1/2}]
Na ⁺	50.1	0.733
K ⁺	73.5	0.548
OH ⁻	198.0	0.353

where λ_i^0 is the equivalent conductivity at infinite dilution, I_M is the ionic strength defined as:

$$I_M = \frac{1}{2} \sum z_i^2 c_i \quad (6.6)$$

and the empirical coefficients G_i proposed by [124] to best agree with published data. Table 6.3 shows λ_i^0 and G_i for Na⁺, K⁺ and OH⁻.

The conductivity of the electrolyte constrained by a cement matrix σ_m is defined as:

$$\sigma_m = \frac{Id}{US} \quad (6.7)$$

where I is the current, U the voltage, d the sample thickness and S the area exposed. Because the calculated conductivity was based on the pore solution from an unexposed sample the formation factor was calculated solely at the very onset of the migration experiment when the pore solution has not changed significantly. The calculated formation factors are presented in Figure 6.24. The formation factor is a complex function of porosity, tortuosity and constrictivity and mixed contributions of these three are assessed together.

6.6. Summary of hydration study and microstructure development

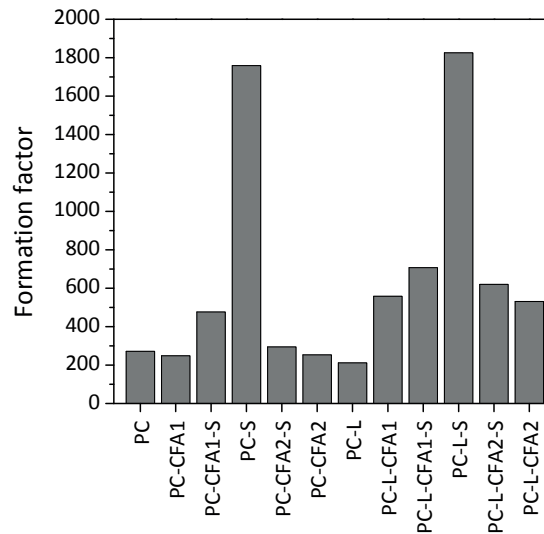


Figure 6.24: Formation factors calculated from the migration experiment and experimental Na^+ and K^+ concentrations in the pore solution.

Larger formation factor indicates a matrix more difficult for ions to penetrate and the results in Figure 6.24 show a particularly significant improvement due to Slag. However, no similar improvement was observed for the other composite cements whose water absorption was as low as for PC-S, for example. This may be due to the C-S-H limiting water absorption by depercolating capillaries but participating in the transport of ions, in which case it would be necessary to study the transport of ions through the C-S-H formed in the different systems.

It was also observed that the addition of limestone decreased the migration current (and increased the formation factors) of the composite cements studied, but increased the water absorption.

6.6 Summary of hydration study and microstructure development

SCMs impact the reaction in composite cements:

- < 28 days: an enhanced degree of reaction of clinker was observed due to dilution, so called "filler effect".
- > 28 days: the reaction of clinker slowed down due to refinement of the pore structure. The reaction of SCMs seems to have been affected in the same way.
- The slowing of the reaction was the most evident after the threshold pore entry radius decreased to around 15-20 nm. This radius was reached after different time of hydration in the different mixes.

Chapter 6. Phase assemblage and microstructure development

- The filling of the matrix did not progress the same way in the different systems studied. It is suspected that these differences are due to the differences in compactness of the C-S-H and thus its ability to fill the matrix voids.

The phase assemblage in composite cement pastes was found to depend on the Al, Si and Ca available for the reaction.

- Increasing Al/Ca available for the reaction impacts the composition of the C-S-H, in which more Al is incorporated. With increasing Al/Ca in the C-S-H the Si/Ca increases, which is necessary to accommodate more Al.
- Supply of Al promotes the formation of AFm instead of AFt. However, it seems that due to the densification of the matrix the transport of Ca from portlandite clusters to near fly ash grains where Al is available, and *vice versa*, can be severely restricted. Because of that the amounts of AFt and AFm in the real system may differ from the theoretical ones predicted by thermodynamic simulations. Since ettringite forms in the first place, the restriction of transport would preserve its transformation to monosulfate.

If calcite is added to the mix formulation, it favors the formation of hemicarbonate or monocarbonate rather than monosulfate. The remaining sulfate is bound in ettringite. The amount of calcite that can react is determined by the amount and ratio of Al and Ca, but again can be limited by the restricted transport of ions through the dense cementitious matrix formed in the presence of some SCMs.

The most reliable way to determine the phase assemblage seems to be a combination of experimental and modeling techniques, as none of them alone is free of limitations:

- Due to the potential variations in the input and due to the dependance of some calculations on the result of preceding ones, the precision of mass balance calculations is fairly low. Sensitivity analysis has indicated that the uncertainty of determination of phase volume in $\text{cm}^3/100 \text{ cm}^3$ of hardened paste was around 3.0 for C-S-H and monosulfate, around 2.0 for portlandite and monocarbonate and 1.0 for the other phases.
- The main limitation of the thermodynamic modeling using GEMS is the unknown C-S-H composition, which requires the operator to specify the Al and S content based on experimental values. The modeling assumes perfect homogenization, which is likely not the case in the real systems. A comparison of modeling and experiment allowed to hypothesize that the limited transport is the cause for a different than predicted phase assemblage, in particular AFt/AFm proportion and the amount of limestone reacted.

Macroscopic properties of mortars were compared to the paste microstructures:

- The compressive strength increased to the third power of the amount of hydrates formed but the trend had significant scatter, most of which but not all could be related to the

6.6. Summary of hydration study and microstructure development

precision of calculation of the amount of hydrates. We don't exclude the possibility of an impact of the type of C-S-H on the calculation of the gel-space ratio or else on the compressive strength.

- Comparison of the compressive strength with the total porosity showed that some systems diverge from the main trend obtained. This could be due to the different contribution to strength from different parts of porosity.
- A trend to a higher rate of water absorption was found with an increasing capillary porosity determined by MIP as the volume of pores with entry radius larger than 8.5 nm.
- Differences in current measured in a migration experiment showed a decrease in the transport of ions in the order of: PC \approx CFA2 > CFA1 » Slag. Adding limestone seems to bring further improvement in the fly ash systems.

7 Conclusions and Perspectives

The work presented in this thesis was developed in several directions to improve the understanding of calcareous fly ashes in multi-component cements. In this respect, the main contribution was the improvement of the techniques for fly ash characterization and measurement of the reaction of its individual components.

7.1 Conclusions

7.1.1 Fly ash characterization

A new procedure based on SEM-EDS full element mapping was developed. It allowed first the identification of the glasses constituting fly ashes, and then the quantification of their amount, and the assessment of their chemical composition, fineness and location in the microstructure. Four chemically distinct populations were identified in the studied ashes: predominantly (i) silicate, (ii) Ca-silicate, (iii) Al-silicate, and (iv) Ca-rich Al-silicate. Siliceous fly ashes contained only the silicate and the Al-silicate glass. Calcareous fly ashes generally contained all four populations. The proportions of these populations varied despite similarities in the bulk chemical composition.

7.1.2 Reactivity of amorphous SCMs

Once the calcareous fly ashes were characterized the same SEM-EDS technique was further developed to track the reaction of the individual fly ash glasses in hydrating cement paste. It was found that the glass populations reacted at different rates due to the differences in chemical composition and fineness. The reactivity of these glasses was investigated in more detail using model glasses, synthesised to match the composition of the real glasses in the fly ash. Dissolution experiments were carried out on these model glasses in 0.14 M NaOH solution at high dilution. The results suggested that the maximum dissolution rate per unit surface is related to the glass chemical composition but the actual rate depends on other factors, notably the solution composition. The hydration of the model glasses in cement

paste was investigated using the SEM-EDS technique. The consumption of these glasses was similar to that of the glasses in the real fly ash and followed the trends found during the dissolution experiments. The effect of fineness was decoupled from the intrinsic reactivity for more detailed analysis. The intrinsic reactivity increased with the degree of depolymerisation of glass evaluated from its chemical composition and expressed as the ratio of non-bridging oxygens per tetrahedral ion (NBO/T).

7.1.3 Impact of calcareous fly ash and slag on reaction in composite cements

The SCMs were found to increase the degree of reaction of clinker up to 28 days of hydration due to the so-called filler effect, i.e. more space and water available per gram of clinker due to a part of it being replaced by a material that reacts more slowly. After 28 days the reaction of clinker slowed down due to the refinement of the pore structure, as indicated by a decrease in the threshold pore entry radius below 15-20 nm.

It seems that the reaction kinetics have an influence on the morphology of the C-S-H. It seems that in the presence of a slower-reacting CFA1 a less compact C-S-H was formed compared to other systems, which could be related to the amount of water in the pores between the C-S-H flocs, in the size range <1-12 nm. The large amount of such nanometric pores matches with the mercury intrusion porosimetry data showing large difference between the total and the capillary porosity of CFA1-containing mixes.

7.1.4 Phase assemblage in composite cements

Thanks to the detailed characterization and measurement of the degree of reaction of fly ash and slag in hydrating composite cement pastes coupled to the measurement of the degree of reaction of clinker phases by XRD-Rietveld refinement we could calculate the amounts of Al, Si, Ca and other elements reacted at increasing times.

The phase assemblage in composite cements was found to depend mainly on the amounts of Al, Si and Ca available for the reaction. The composition of the C-S-H was principally affected by the ratio between Al and Ca available. The Al/Ca content of the C-S-H increased linearly with Al/Ca supplied to the reaction. With increasing Al/Ca of the C-S-H its Si/Ca increased. The supply of Al also had an impact on the amount of AFm phases.

Mass-balance and thermodynamic modeling were used to calculate the amounts of phases that cannot be measured experimentally, notably the poorly-crystalline C-S-H and AFm phases. Despite the overall agreement, some discrepancies in ettringite content were found between the thermodynamic results and experiment. These discrepancies suggested a physical rather than chemical effect on the phase assemblage. In particular, the transport of Ca away from portlandite clusters and the transport of Al away from fly ash grains may be affected. As a result, more ettringite than monosulfate was observed, as ettringite is formed early during the reaction and the limited transport of Ca and Al to it hinders its transformation to monosulfate.

The addition of limestone favored the formation of hemicarbonates or monocarbonates rather than monosulfates. The remaining sulfate is incorporated in ettringite. The amount of calcite that can react in a given system is determined by the amount and ratio of Al and Ca. Again, the limited transport of ions through the matrix plus the slow reaction and imperfect distribution of limestone grains may be the cause for lower than maximum reaction of this component.

7.1.5 Microstructure-property comparison

The compressive strength increased exponentially with the amount of hydrates calculated by the mass-balance and the thermodynamic simulations but the trend had significant scatter, not all of which could be explained by the precision of the calculation. The extreme refinement of the porosity and a more uniform space filling are among possible reasons that explain higher than expected strength of CFA1 mixes at later ages.

The rate of water absorption correlated linearly to the volume of capillary pores determined by mercury intrusion porosimetry. Generally a significant decrease in capillary absorption rate due to CFA1 and Slag was observed and somewhat less due to CFA2. Limestone addition increased the capillary porosity and thus the water absorption rate. The results of the ion migration test show a different picture, with a decrease of permeability due to limestone and a significant decrease due to Slag. The reasons for this discrepancy remain unclear and some of the results may need to be verified.

7.2 Perspectives

7.2.1 Studies on multi-component cements

There exist many possibilities to replace clinker by a combination of SCMs, including calcareous fly ashes and slag. This thesis illustrates that the choice of the SCM affects the properties on both micro- and macro- scale. Some aspects can be explained by the fundamental reactivity of the SCMs and the amounts of the elements they supply to the reaction. Some aspects remain unclear, such as:

- The exact reason for the different C-S-H morphologies observed.
- The role of different components (phases, links, fine and coarse porosity) of composite cement paste on the strength development.
- The role of the different pore sizes and the tortuosity in the transport of ions through the cementitious matrix.

The reactivity of amorphous SCMs is an important question in these studies. While alternative techniques based on the XRD data analysis, such as PONKCS and FSM, show promise, the SEM-EDS technique developed in this thesis brings a new perspective to the studies on complex mixes of amorphous phases. It is a robust and easy to use tool, which could be commonly

Chapter 7. Conclusions and Perspectives

employed and tailored to the specific case investigated. This technique could turn out very useful to analyze other types of SEM/TEM data including SCMs other than calcareous fly ash, hydration and corrosion products in cements, radioactive waste immobilization, etc. The specific case tackled in this thesis was calcareous fly ash, for which the use of this technique allowed great advance in understanding of the material and its reactivity.

A link between glass structure disorder, expressed as NBO/T and intrinsic reactivity was presented. The NBO/T is only a bulk description of the degree of glass depolymerisation and does not account for the different species possible. Further NBO/T is calculated assuming all Al as network former, and the presence of modifier Al leads to biased and sometimes nonsensical NBO/T values. The future work could focus on developing the techniques to determine the ratio between glass-forming and glass-modifying Al in the fly ash glasses. Alternative way of expressing the glass structure could be also of interest.

7.2.2 Use of calcareous fly ash

In a wider perspective of the use of fly ashes in cement and concrete, it would be of high interest to try to establish a generic link between the chemical composition of any glass and its reactivity in hydrating cement. Such knowledge, or a database, would allow to make predictions of the reactivity of any unknown fly ash simply based on the type and amount of its glasses determined by the SEM-EDS technique.

The necessary steps would be to characterize a large number of fly ashes and link this information to their mechanical performance in different systems and later also other properties such as durability. The ternary frequency plots of chemical composition could then be used as a basis for specification of desired composition of fly ash for a given application or to decide whether a locally available fly ash could be used in concrete or not. If such knowledge is gained, further steps would be to collaborate with the power plants and try to link the composition of coal and the burning and processing conditions to the characteristics of the output fly ash. Ultimately, it could be discussed whether the power plants could take actions to provide the cement producers with such specified fly ash and establish longer term contracts for its supplies. The quality control would then be based on comparing plots of composition of the resulting fly ash with that specified.

It is difficult to estimate the magnitude of potential gains from such collaboration. Besides more fly ash being used in concrete, it may turn out that less processing is necessary if certain adjustments are made at the power plants. Such modifications could also affect local availability of fly ash and improve its use in places where so far the fly ash had to be discarded. Also, if the quality of ashes is known and assured, the substitution limits imposed by international and local standards could be raised in to allow more fly ash replace cement clinker, to further decrease the cost and the environmental impact of concrete production.

A New image analysis technique of EDS full element maps

A.1 Model sample

The data treatment and analysis are shown for a model sample. The model sample was prepared with equal wt. proportion of three homogeneous and amorphous materials of known chemical composition (Figure A.1) - two slags: S1, S2 and a synthetic glass G. The materials were mixed, compacted into a pellet and embedded in epoxy resin. Their volume fractions were calculated using densities obtained according to [125] and are included in Table 10.

A.2 Microscope setup

The system was configured to take a backscatter electron image (BSE) and to carry out EDS element mapping. To analyse and interpret the element maps in detail, the acquisition of high quality spectra is essential. A large spot size was used to obtain high EDS count rate of 100 000 - 150 000 counts per second. Due to fast detector and signal processing the dead time remained between 0 and 5%. A dwell time of 256 μs was chosen to keep the scanning speed at a moderate rate. It provided balance between poorer measurement statistics at high speeds and larger sample damage at lower speeds. The field of view at 1000x magnification was $252 \times 189 \mu\text{m}$, the image resolution was 1024×768 and the pixel size $0.246 \times 0.246 \mu\text{m}$. An automated routine analysed eight frames per sample, which corresponds to approximately 20 000 particles. The total acquisition time was around 4.5 h per sample. Eight frames per sample per testing age were considered a good compromise between the size of the analysed area and the measurement time. Compared to other studies using SEM, eight frames may seem very few but the information carried in a precise EDS map allows a more accurate analysis and therefore less frames need to be measured. Samples made of compacted powder contain more particles per unit surface of the polished section compared to paste samples: a paste of 70 % Portland clinker and 30 % fly ash at 0.4 water/binder ratio contains around four times less fly ash. Eight frames measured on raw compacted powder are thus equivalent to

Appendix A. New image analysis technique of EDS full element maps

Table A.1: XRF analysis [wt.-%] of the materials used for the model sample for SEM-EDS analysis. * indicates exact values for a synthetic material.

	S1	S2	G*
Al ₂ O ₃	11.6	16.5	37
SiO ₂	36.7	31.9	43
CaO	38.9	35.8	20
Na ₂ O	0.2	0.6	-
K ₂ O	0.7	-	-
MgO	7.8	10.8	-
Fe ₂ O ₃	0.5	0.9	-
SO ₃	2.8	-	-
TiO ₂	0.9	-	-
P ₂ O ₅	-	-	-
Sum	100.0	96.4	100.0

32 on paste, which is typical of the numbers of images often used in paste studies. A detailed error analysis is presented in Appendix A.5.

A.3 Data treatment

The following elements were quantified from the spectra: Al, Si, Ca, Na, K, Mg, Fe, Ti and P. Oxygen was calculated by stoichiometry if needed. Quantification of oxygen by EDS is not reliable as its emitted X-rays have low energy and can be easily absorbed by the specimen or the detector window. The quantification of elements was carried out in microscope's software (Bruker Esprit[®]) using a profile fit with standards and PhiRhoZ matrix corrections. The calculations are automated and require around 1 hour per frame.

Custom MATLAB[®] software was used to treat the data. For the anhydrous particulate specimens, background pixels are removed using a mask from a thresholded BSE image. The threshold value was found using the grey level histogram of the image. The remaining data is smoothed (see Appendix A.4) and plotted in a ternary diagram for further analysis. Any of the quantified elements or their combinations can be used for the ternary plot, but in case of fly ashes the Al-Si-Ca system is typically of main interest. For each pixel the values of atomic-% of Al, Si and Ca are normalized to 100%, transformed to barycentric coordinates and plotted in a ternary diagram. As most of the compounds analysed were glasses it was preferred to plot the elements at the apexes rather than oxides, although all the elements are oxidised, using the formula Al₂O₃ can be confusing when subsequently considering ratios of Al to Si, for example. If all the data points are plotted individually the ternary plot is saturated with millions of points and cannot be interpreted (Figure A.1a). Our solution is to re-plot it as a ternary frequency plot. The area of the ternary plot is split into smaller triangular areas (bins). The size was set so that one bin would span 1 atomic-% on each of the three axes. Each axis is therefore divided into 100 equal sections and the resulting total number of bins is 10 000. The

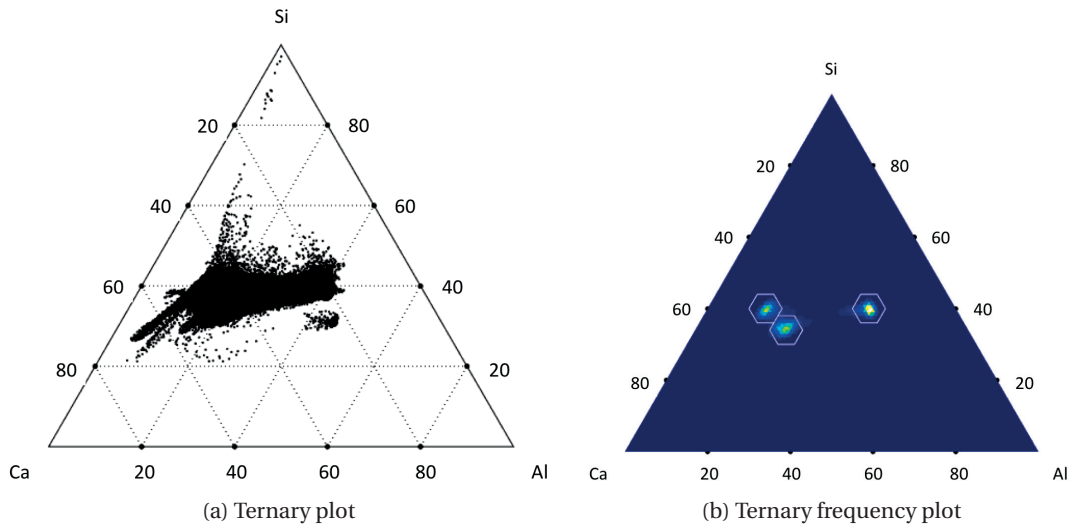


Figure A.1: Al, Si and Ca atomic-% ternary plots obtained from the EDS data from the model sample. Many of the points appearing in (a) are actually due to noise and do not appear in (b).

Table A.2: Quantification of the volume fractions in the model sample.

Component	Density [g/cm ³]	Volume fraction [%]				
		Expected	4 frames	Δ	8 frames	Δ
S1	2.9	33	26	7	33	0
S2	3.0	32	38	6	37	5
G	2.7	35	36	1	30	5
		Average		4.7		3.3

number of points that fall into each bin creates a height vector for it. The height vectors of all bins are presented in form of a ternary frequency plot with linear colour intensity scaled to the maximum value of the height vector (Figure A.1b). Figure A.1 illustrates the two versions for the model sample containing two slags and one synthetic glass. The plot of all points (Figure A.1a) is not very informative, whereas the frequency plot (Figure A.1b) clearly shows the chemical compositions of the three constituents.

Coordinates of points and areas in the ternary plot represent the proportions of Al, Si and Ca in atomic-%. Groups of similar chemical compositions appear as blobs in the graph. Separation of phases of very close chemical compositions is possible. The compositions identified in the ternary plots can then be mapped back onto the original image, from which the amount of each phase in vol.% is calculated from its area fraction (Figure A.2c), according to fundamental stereology (Delesse's principle). The accuracy of such quantification was assessed for the model sample by comparing with the known volume fractions of the materials used to prepare this specimen (Table A.2). The maximum absolute differences between the expected and the calculated values were around 5 vol.% for four frames analysed and around 3 vol.% for eight frames analysed.

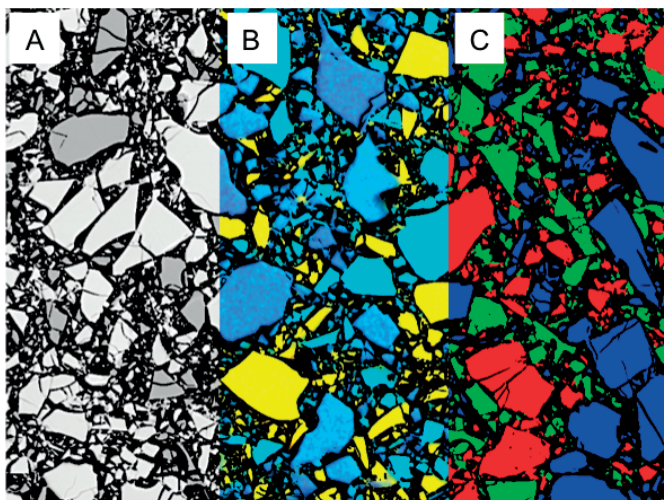


Figure A.2: Model sample: (A) BSE image, (B) EDS map with false-colours attributed to elements: red - Al, green - Si, blue - Ca, (C) the final segmentation of EDS data using compositional ranges determined before in the corresponding ternary frequency plot (Figure A.1b).

A.4 Quality of the EDS data

A reliable set of chemical composition data is a key for a precise and accurate image analysis. As the chemical composition is quantified for each pixel of the frame, the quality of the quantification depends primarily on the quality of the individual spectra. The quality of the individual spectra depends on the measurement conditions and can be evaluated by comparing the SEM-EDS results to bulk chemical composition by XRF. This was done for CFA2 (Figure A.3). The EDS data was treated in two ways. Quantification of a spectrum taken

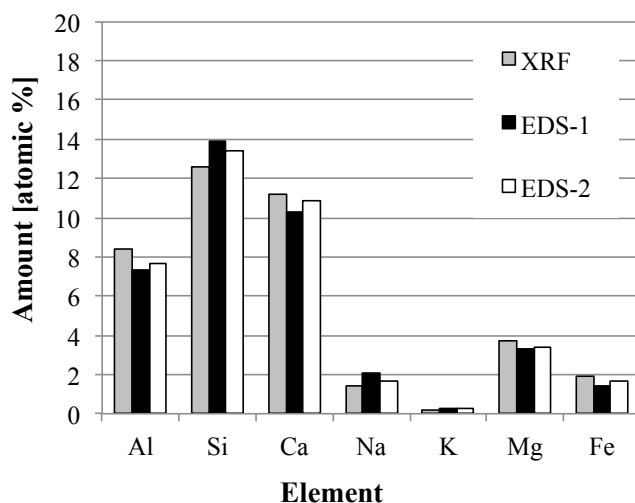


Figure A.3: A comparison of the bulk chemical composition quantification by XRF and EDS for CFA2.

collectively from the entire frame (EDS-1) showed that up to around 1.5 atomic-% difference is related to the quality of standards, the way the spectrum is treated in the software and the errors involved, all of which are largely independent of the user. When individual spectra were quantified and the results averaged (EDS-2) the differences did not change. This suggests satisfactory quality of the individual spectra.

It is difficult to evaluate all sources of errors of an EDS analysis and quantification. Due to sample-, microscope-, EDS detector- and data processing-related errors the combined uncertainty of quantification can be estimated around ± 1.5 atomic-%. In practice, the chemical composition is represented by bin coordinates and each of the data points adds to a single bin. To account for the uncertainty of quantification an individual data point adds to multiple bins. The value of the increment varies as a function of the distance from the data point coordinates according to a specified distribution. In this study, the uncertainty of quantification was assumed to follow Gaussian distribution with $2\sigma = 1.5$ %. This operation adds spread to the frequency plots but the results more truly reflect the meaning of the data.

Chemical resolution is limited by several factors. The uncertainty of quantification ($\pm 1.5\%$) sets the lowest limit. An important drawback of EDS is that the signal is collected from a volume of sample, several microns in size, called an interaction volume. Particle edges and finely intermixed fractions, below the pixel size, share contributions to the measured chemical composition with their surroundings. Mixed contributions are plotted in the frequency plots between the original areas reducing precision of the separation and quantification. To account for this effect the raw data was smoothed with a Hamming window (Figure A.5). This window belongs to a family of windows that reduce high frequency noise, but do not change the size and shape of the input. The size of the window was chosen to match the size of the interaction volume. The interaction volume was modelled using Monte Carlo simulation in Casino v2.41 software (www.gel.usherbrooke.ca/casino/index.html, accessed October 2015) for a bulk composition of CFA2 and the parameters the microscope was operated at (Figure A.4).

Despite data smoothing, mixed contributions can still be seen in the ternary frequency plots. In Figure A.6 we can identify a cloud of points between the two main components of CFA6, the aluminosilicate glass on one side and the anhydrite and lime at the other, Ca-rich side. By selecting only the points in between the two components, we can locate them back in the image. The majority of these points constitute particle edges, a clear sign that the proximity of the two very different compositions affects the EDS signal. During the analysis of this fly ash we split the intermediate points between the two dominant components.

Fly ashes can have a very wide range of chemical compositions that add spread to the groups seen in ternary frequency plots. The extent of this effect depends on the heterogeneity of the investigated material. With no clear borders between the groups, segmentation may be impossible or may require arbitrary decisions of a skilled operator. Some issues may be resolved using additional refinements and adjustments, depending on the case.

Appendix A. New image analysis technique of EDS full element maps

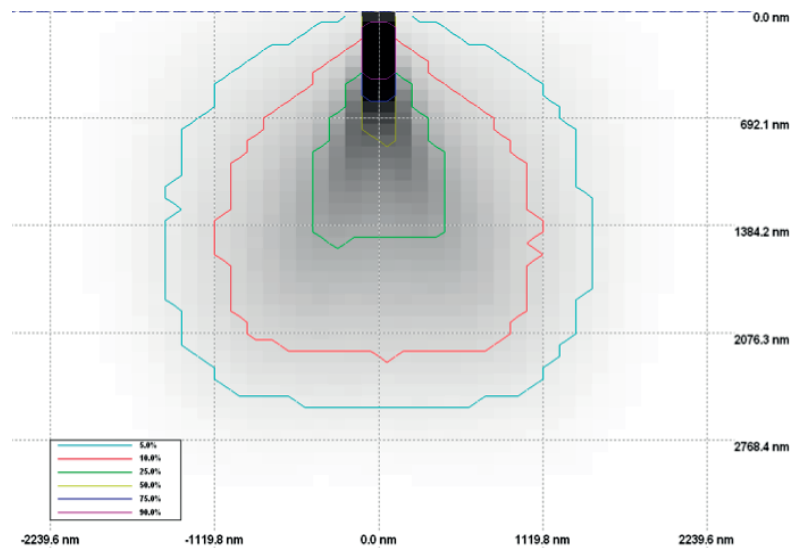


Figure A.4: SEM-EDS: The distribution of the X-ray density in the CFA2 sample modelled using Casino software.

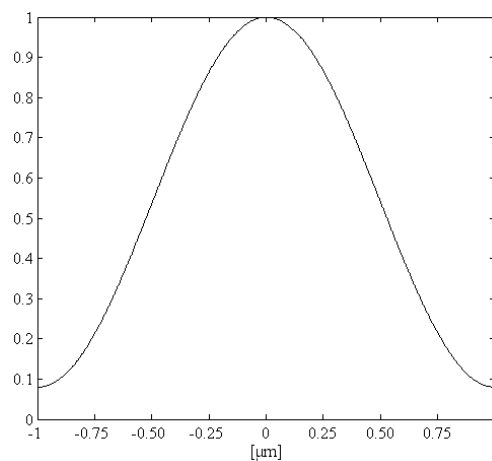


Figure A.5: The Hamming window used to smooth the EDS data.

A.5 Error assessment in image analysis

There exists no absolute measure of the error in general. Using a model system, the error for eight analysed frames was determined to be around 3 vol.-% (Figure A.7). In most cases the absolute values are unknown and a relative error analysis is carried out instead. For a certain quantity being assessed (e.g. volume fraction of a phase), one should prepare a log-log convergence plot of the relative differences of the amount quantified in different frames against the number of frames, which is the usual way to assess convergence. One can then fit a trend line to the calculated points and use it to determine the number of frames required to reach a certain relative error.

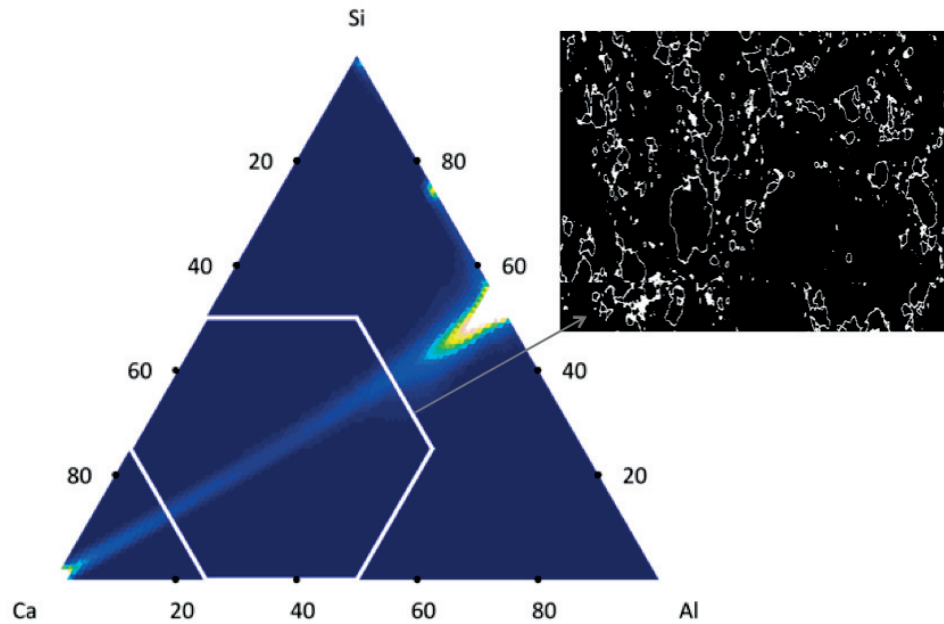


Figure A.6: The effect of the interaction volume on the SEM-EDS data presented in a ternary frequency plot. A cloud of intermediate compositions is due to the mixed contribution of two phases in a close proximity in the sample's microstructure.

The size of the particles may influence the uncertainty. Fine or finely intermixed phases below the size of the interaction volume or the size of the minimum recognizable grain may be inseparable and thus not correctly qualified. In image analysis, a particle is reliably identified as such if its diameter is at least the size of two pixels and at most half the size of the field of view. Resolution and frame field of view in this study result in a pixel size of $0.246 \times 0.246 \mu\text{m}$. Particles of a mean diameter smaller than 2 pixels ($0.5 \mu\text{m}$) or larger than 1/4 of the frame ($90 \mu\text{m}$) are thus not adequately identified. An independent measure of the particle size distribution (Figure A.8) can be used to assess the correctness of the chosen frame size (magnification). If the fractions below $0.5 \mu\text{m}$ and above $90 \mu\text{m}$ account for less than 2-3 vol.-% each, as it is for most of the studied ashes, the resulting error is not expected to influence the results much. However, larger errors should be expected for materials of broad particle size distributions (e.g. a non-ground fly ash), which may require significantly more frames to reach similar levels of certainty. Shortening of the measurement by allowing less time per frame may jeopardize the reliability of the results and lead to false interpretations. Decreased magnification would lower the precision and the resolution.

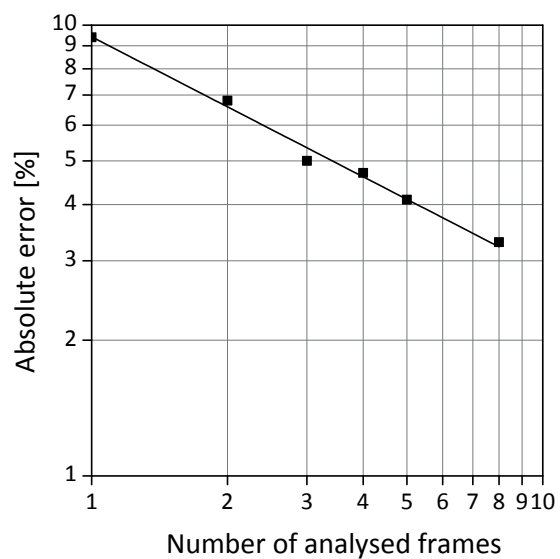
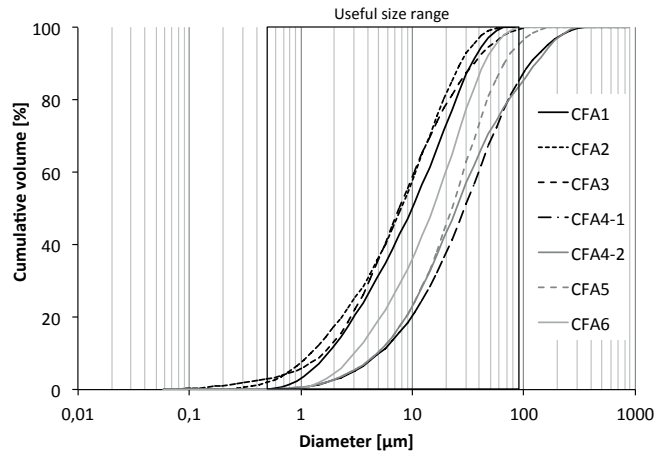
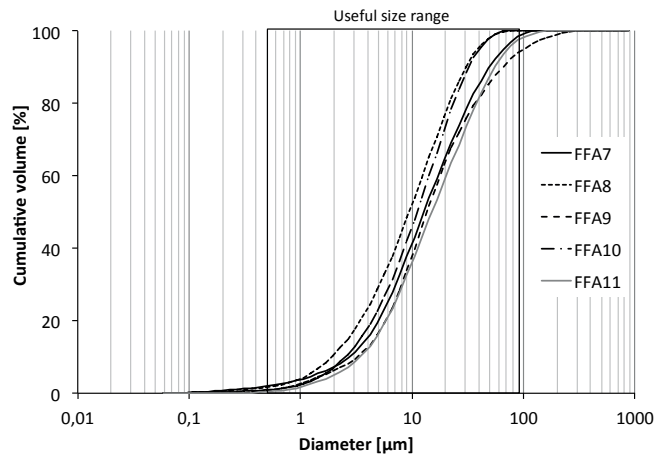


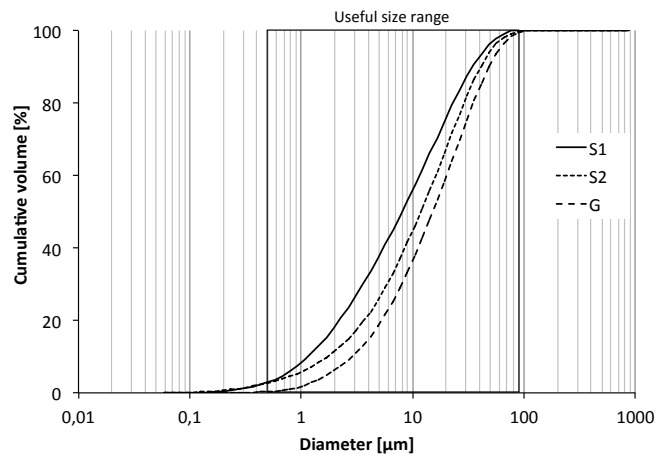
Figure A.7: An example convergence plot showing an absolute error of the quantification of a volume fraction of slag S1 in the model sample.



(a) Calcareous fly ashes



(b) Siliceous fly ashes



(c) Slags and glass G

Figure A.8: Particle size distributions by laser diffraction and the range of the particle sizes assessed by the presented technique with the parameters used in this study.

A.6 MATLAB[®] code used to plot the ternary frequency plot

```

%written by Cyrille F. Dunant and Pawel T. Durdzinski. 2013-2014.
function [fA, fB, fC, Z, coords, tri] =          end
ternDPlot(bins, A, B, C, bse, mincontent, X)    end

ticks = 5; %select how you want the numbers at %create input for trisurf function
the axes, default is 5, so (0, 20, 40, 60, 80) %tri - list of triple combinations of
                                                coordinates that are used to create each of
                                                the triangles
%get data as vectors for simplification
A = A(:); %xcoords, ycoords - lists of coordinates that
B = B(:); 'tri' can choose from
C = C(:); %zcoords - same size as xcoords but zeros
bse = bse(:); since we're interested in 2D plot
                                                tri = zeros(iterator-1,3);
                                                xcoords = zeros(3*(iterator-1),1);
                                                ycoords = xcoords;
                                                zcoords = xcoords*0;

%calculate normalized fractions, exclude %instead of struggling to get proper 'tri'
points where sum is zero list we create a simple one like
Total = (A+B+C); %tri=[1 2 3
fA=zeros(length(A),1); % 4 5 6
fB=zeros(length(B),1); % 7 8 9 etc] and create a set of
fC=zeros(length(C),1); coordinates for each of the rows
for i=1:length(A) %for the upright triangles
    if Total(i)<10E-4 for i = 1:iterator-iterator2-1
        fA(i) = 0; if tri(i,1)<1
        fB(i) = 0; %make 'tri'
        fC(i) = 0; tri(i,:)=[(i-1)*3+1,(i-1)*3+2,(i-
    else 1)*3+3];
        fA(i) = A(i)./Total(i); %change barycentric coordinates of
        fB(i) = B(i)./Total(i); the centers into cartesian
        fC(i) = C(i)./Total(i); ycenter =
    end coords(i,2)*sin(60/180*pi);
end xcenter = coords(i,1) +
mask = find(bse(:)>0); ycenter*cot(60/180*pi);
fA = fA(mask); %create coordinates for the
fB = fB(mask); vertices
fC = fC(mask); xcoords((i-1)*3+1)= xcenter-
%create the list of coordinates for centers of 1/(2*bins);
the triangles that we're about to create; xcoords((i-1)*3+2)= xcenter;
first the centers for upright triangles xcoords((i-1)*3+3)=
iterator = 1; xcenter+1/(2*bins);
coords = [0 0 0] ; ycoords((i-1)*3+1)= ycenter-
for i = 1/(3*bins):1/(1*bins):1-1/(3*bins) cos(30/180*pi)/(3*bins);
    for j = 1/(3*bins):1/(1*bins):1-1/(3*bins) ycoords((i-1)*3+2)=
        for k = 1/(3*bins):1/(1*bins):1- ycenter+2*cos(30/180*pi)/(3*bins);
            1/(3*bins) ycoords((i-1)*3+3)= ycenter-
                if abs(i+j+k-1) < .000001 cos(30/180*pi)/(3*bins);
                    coords(iterator,:) = [i j k] ; end
                    iterator = iterator+1; end
                end end
            end
        end
    end
end
%centers for upside-down ones
iterator2 = 0;
for i = 2/(3*bins):1/(1*bins):1-1/(3*bins)
    for j = 2/(3*bins):1/(1*bins):1-1/(3*bins)
        for k = 2/(3*bins):1/(1*bins):1-
            1/(3*bins)
                if abs(i+j+k-1) < .000001
                    coords(iterator,:) = [i j k] ;
                    iterator = iterator+1 ;
                    iterator2 = iterator2+1;
                end
            end
        end
    end
end

```

A.6. MATLAB® code used to plot the ternary frequency plot

```

ycoords((i-1)*3+1)=
ycenter+cos(30/180*pi)/(3*bins);
    ycoords((i-1)*3+2)= ycenter-
2*cos(30/180*pi)/(3*bins);
    ycoords((i-1)*3+3)=
ycenter+cos(30/180*pi)/(3*bins);
    end
end

%create height vector Z that will be filled in
a loop by assigning fractions to bins
Z = zeros(iterator-1,1);

sigma = 7.5e-3; %sigma of gaussian
distribution. 95.6% of points should be within
range of 2sigma, 99.8% within 3sigma
%for an area to be hit on of
radius=2sigma=1.5%, sigma is 7.5e-3

for j = 1:length(fA)
    index = []; %added for 'spreading' of
intensity if a point hits
    indexiterator = 1; % more than one bin at
a time - edge or vertex
    coef = []; %Gaussian distribution for the
error so it is not a box anymore
    for i = 1:iterator-iterator2-1
        if (bse(j)>0 &&...
            fB(j)<X && A(j)+B(j)+C(j) >
mincontent &&...
            fA(j)+fB(j)+fC(j) > 1e-4 &&...
            -1/(3*bins)-3*sigma<=fA(j)-
coords(i,1) && fA(j)-
coords(i,1)<=2/(3*bins)+3*sigma &&...
            -1/(3*bins)-3*sigma<=fB(j)-
coords(i,2) && fB(j)-
coords(i,2)<=2/(3*bins)+3*sigma &&... %we used
1e-2 as 1% error
            -1/(3*bins)-3*sigma<=fC(j)-
coords(i,3) && fC(j)-
coords(i,3)<=2/(3*bins)+3*sigma) %

            distanceSquared = (fA(j)-
coords(i,1))^2+(fB(j)-coords(i,2))^2+(fC(j)-
coords(i,3))^2;
            index(indexiterator)=i;
            coef(indexiterator)=exp(-
distanceSquared/(2*sigma*sigma)); %gaussian
distribution is exp(-dist^2/2sigma^2)
            indexiterator=indexiterator+1;
        end
    end
    for i = iterator-iterator2:iterator-1
        if (bse(j)>0 &&...
            fB(j)<X &&...
            A(j)+B(j)+C(j) > mincontent &&...
            fA(j)+fB(j)+fC(j) > 1e-4 &&...
            -2/(3*bins)-3*sigma<=fA(j)-
coords(i,1) && fA(j)-
coords(i,1)<=1/(3*bins)+3*sigma &&...
            -2/(3*bins)-3*sigma<=fB(j)-
coords(i,2) && fB(j)-
coords(i,2)<=1/(3*bins)+3*sigma &&... %we used
1e-2 as 1% error
            -2/(3*bins)-3*sigma<=fC(j)-
coords(i,3) && fC(j)-
coords(i,3)<=1/(3*bins)+3*sigma) %

            distanceSquared = (fA(j)-
coords(i,1))^2+(fB(j)-coords(i,2))^2+(fC(j)-
coords(i,3))^2;
            index(indexiterator) = i;
            coef(indexiterator) = exp(-
distanceSquared/(2*sigma*sigma));
            indexiterator = indexiterator
1;
        end
    end
    if ~isempty(index)
        for i = 1:indexiterator-1
            Z(index(i))=Z(index(i)) +
coef(i)/sum(coef); % we always want to ad a
total of 1 so need to divide by sum of coef
        end
    end
end

figure;
hold on;
set(gca,'dataaspectratio',[1 1 1]), axis off;

majorticks = linspace(0, 1, ticks + 1);
majorticks = majorticks(2:end-1);
labels = num2str(majorticks'*100);

lya = (1-majorticks)*sin(60/180*pi);
lyb = 0*lya;
lyc = majorticks*sin(60/180*pi);

lxa = lya*cot(60/180*pi);
lxb = majorticks + lyb*cot(60/180*pi);
lxc = 1-majorticks + lyc*cot(60/180*pi);

xoffset = 0.04;
yoffset = 0.04;

text(lxc+xoffset, lyc, labels);
text(lxb-0.25*xoffset, lyb-1.25*yoffset,
labels);
text(lxa-2*xoffset, lya, labels);

plot(lxc, lyc, '.', 'MarkerSize',15,
'MarkerEdgeColor','k');
plot(lxb, lyb, '.', 'MarkerSize',15,
'MarkerEdgeColor','k');
plot(lxa, lya, '.', 'MarkerSize',15,
'MarkerEdgeColor','k');

trisurf(tri,xcoords, ycoords, zcoords, Z);

text(1.05,-0.05,'Al','horizontalalignment',
'center');
text(0.5,0.93,'Si','horizontalalignment',
'center');
text(-0.05,-0.05,'Ca','horizontalalignment',
'center');
view(0, 90);
shading flat

```


B Preliminary study on a wide range of mix formulations

B.1 Mix formulations

At the beginning of the study a wide range of compositions was tested for compressive strength, which served to identify interesting formulations to be selected for further study. The mix formulations are presented in Table B.1.

Table B.1: Mix formulations of the preliminary study [wt.%].

	PC	L	CFA	Slag	Selected
Portland cement	100	-	-	-	x
inert filler	55	-	45% Quartz	-	x
CFA1	55	-	45	-	x
	55	-	35	10	
CFA1 + Slag	55	-	25	20	x
	55	-	15	30	
Slag	55	-	-	45	x
	55	-	15	30	
CFA2 + Slag	55	-	25	20	x
	55	-	35	10	
CFA2	55	-	45	-	x
Portland limestone cement	90	10	-	-	x
L + inert filler	49.5	5.5	45% Quartz	-	x
L + CFA1	49.5	5.5	45	-	x
	49.5	5.5	35	10	
L + CFA1 + Slag	49.5	5.5	25	20	x
	49.5	5.5	-	45	x
L + Slag	49.5	5.5	-	45	x
	49.5	5.5	15	30	
L + CFA2 + Slag	49.5	5.5	25	20	x
	49.5	5.5	25	20	x
L + CFA2	49.5	5.5	45	-	x

The combined amount of fly ash and slag was fixed at 45 wt.% with varying proportions of CFA1, CFA2 and Slag. Part of the samples contained no limestone and the other part contained

Appendix B. Preliminary study on a wide range of mix formulations

limestone in the amount of 10 % of the mass of clinker. To separate the physical effect of introducing a secondary material to cement from the contribution of this material to the reaction a reference containing 45 wt.% inert filler (quartz) was prepared. Another reference was a non-substituted portland cement for the limestone-free series and a portland cement with 10 wt.% of limestone for the limestone-containing series. To have better control over studied parameters, gypsum was added to each mix to adjust the SO₃ content to an arbitrary value of 3.25 wt.%.

B.2 Compressive strength of mortars

Figure B.1 presents the compressive strength results of (a) the binary PC-SCM and (b) ternary PC-L-SCM systems. The compressive strength of the neat cement increased rapidly in first 7-28 days after which the increase slowed down. A mix containing 45 wt.% inert filler (quartz) developed much lower strengths and the strength increased at much slower rate. The effect of replacing 45 wt.% PC with fly ash or slag on the development of compressive strength of composite binders is clearly seen comparing the composite curves and those of the two references. At one day the strength of the composite binders was practically the same as that of the inert filler system. At seven days the strength of composite cements increased 2-3 times compared to that of the inert filler. The strength of the composite cements continued to increase at a rate faster than that of non-substituted PC and of the PC-10 wt.% limestone, exceeding these two at around 200 days of hydration.

The difference in strength development between CFA1, CFA2 and Slag systems in the limestone-free series were rather small. Higher strengths by around 5 MPa were found for CFA2 at early ages, and from 56 days on by CFA1. Slag blends produced intermediate strengths at all ages.

Limestone addition caused dilution and decreased the strength of the cement reference, the quartz reference and the PC-L-CFA1 mix. However, no major decrease was observed for PC-L-Slag and a significant increase was observed for PC-L-CFA2. The strength of the PC-L-CFA2 increased much faster than any other composite system and exceeded the strength of PC-L reference at 28 days. The effect of adding limestone to particular systems as well as the specific positive interaction of CFA2 and limestone is presented in more detail in Figure B.3 and Appendix C respectively.

Figure B.2 shows how strength is affected if the clinker replacement is done with combination of fly ash and slag in different proportions. Using a combined addition of fly ash and slag, strength gains from none to approximately 5 MPa can be observed depending on curing time and mix formulation compared to non-combined replacement. Neither of the tested CFA-Slag proportions 35-10, 25-20 and 15-30 produced clearly identifiable higher strengths, with CFA1 or CFA2, with or without limestone.

B.2. Compressive strength of mortars

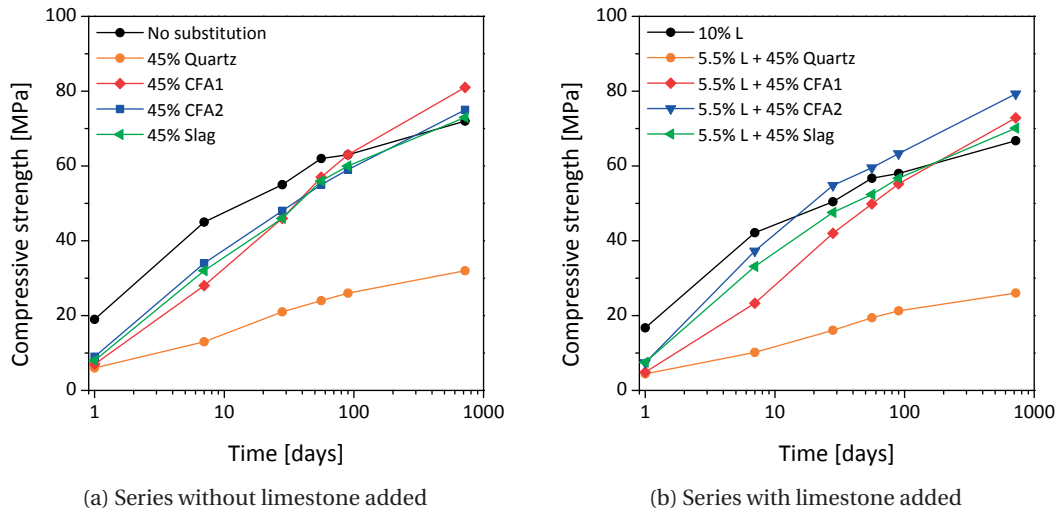


Figure B.1: Compressive strength of binary and ternary composite cement mortars.

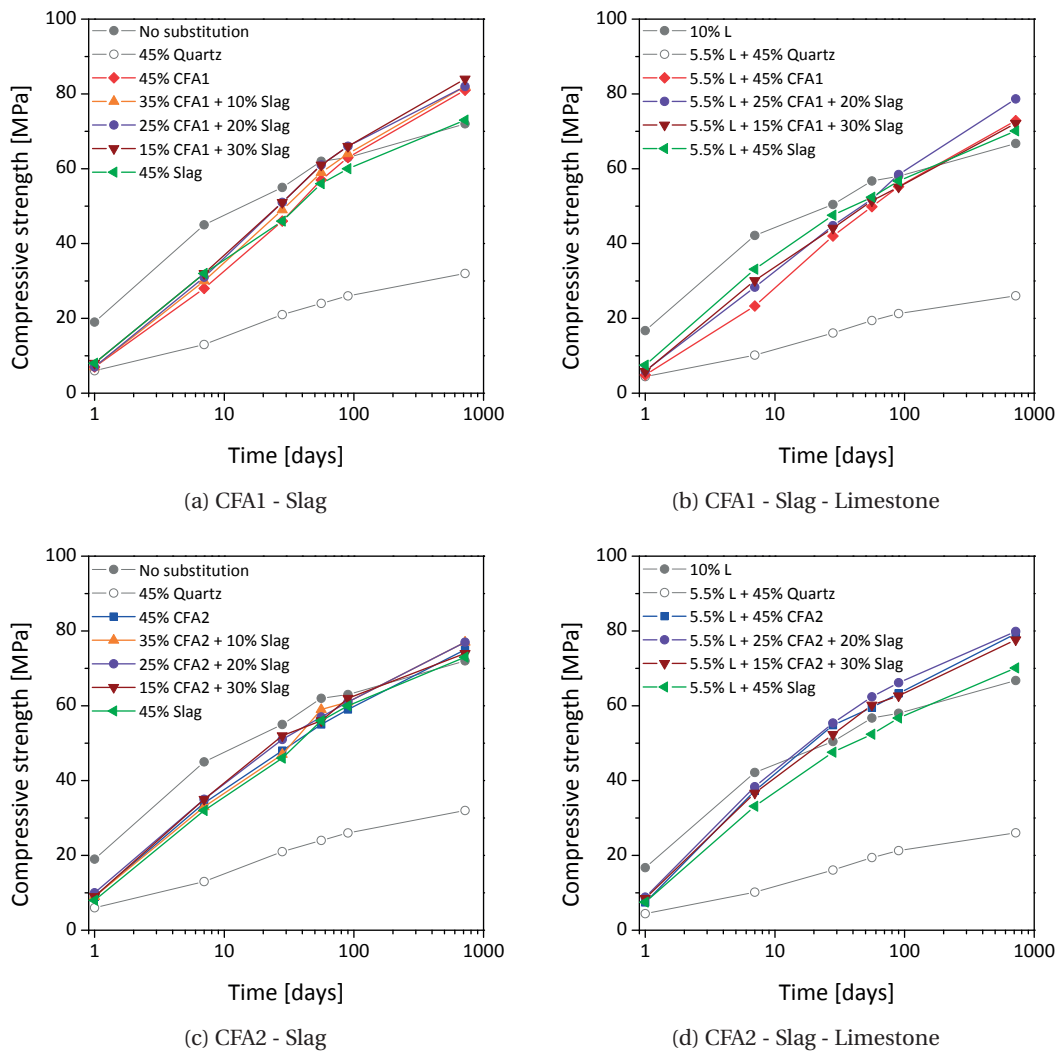


Figure B.2: Compressive strength of ternary and quaternary composite cement mortars.

Appendix B. Preliminary study on a wide range of mix formulations

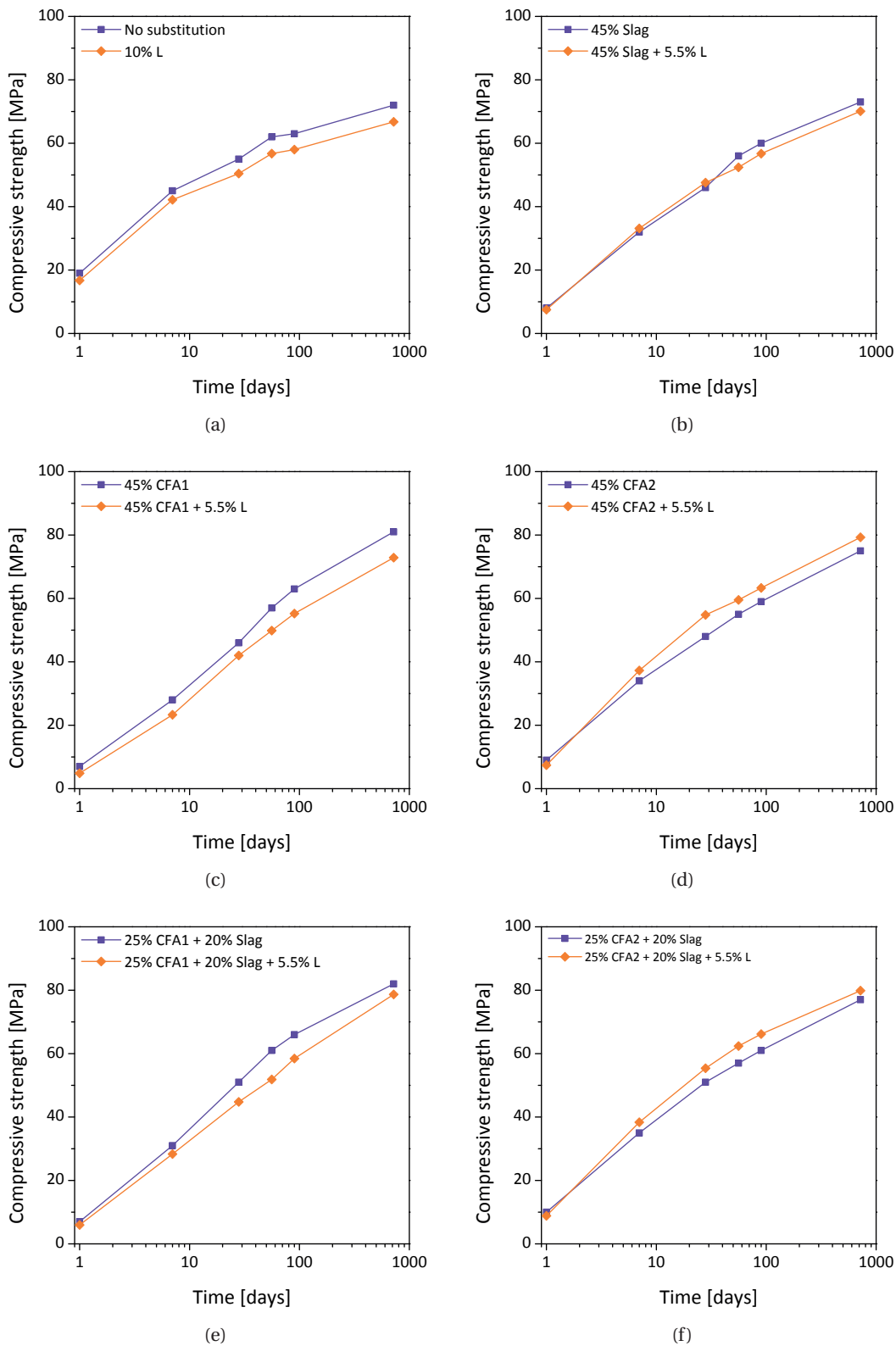


Figure B.3: The effect of substituting 10 wt.% of the clinker amount by limestone on the compressive strength of mortars

B.3 Hydration kinetics

Cement hydration is an exothermic reaction, which allows the hydration to be followed by means of isothermal calorimetry. The kinetics of the first 7 days of hydration of the screened systems were investigated on paste specimens. Comparing the calorimetry curves in Figure B.4a it can be seen that the shape of the first peak related to the silicate reaction of CFA1 and Slag does not differ a lot from the quartz reference. A second peak related to the aluminate reaction is clearly present in the curves of CFA1 (at 100 h) and Slag (at 35 h) but not observed in that of quartz. The heat release of the slow continued reaction, after the first major exothermic effects, is higher in CFA1 and Slag mixes than in the quartz reference and even higher in the CFA2 mix. The CFA2 curve has a very different shape from those of the other SCMs. Initial retardation of about four hours and less steep slope of the first peak are followed by an important heat release from the aluminate reaction.

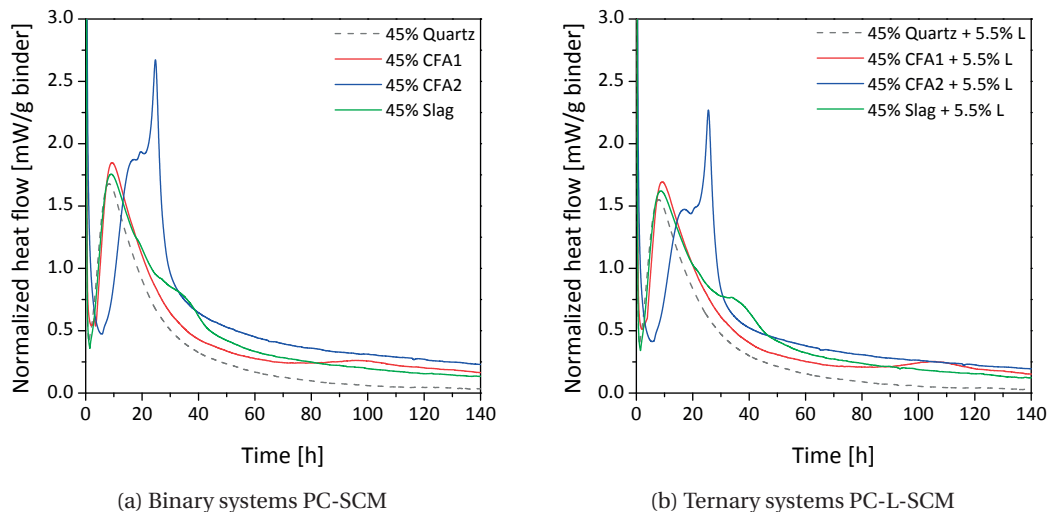


Figure B.4: Derivative calorimetry curves show different heat evolution during hydration of different SCMs.

Adding limestone (Figure B.4b) causes dilution of the systems and leads to slightly decreased heat evolution but does not affect the shape of the calorimetry curves. When fly ash and slag are intermixed, the curve of the new blend is a combination of fly ash and slag respective curves (Figure B.5).

The cumulative heat release measured in isothermal calorimetry can be used to assess the SCM contribution to the reaction of the composite cement. A comparison of quartz and clinker reference curves in Figure B.6 shows that introduction of quartz filler enhances early clinker hydration as more heat is generated per gram of cement (filler effect). A similar behaviour can be observed for the SCMs until around one day of hydration. Then the SCM reaction begins to contribute to the heat production.

Appendix B. Preliminary study on a wide range of mix formulations

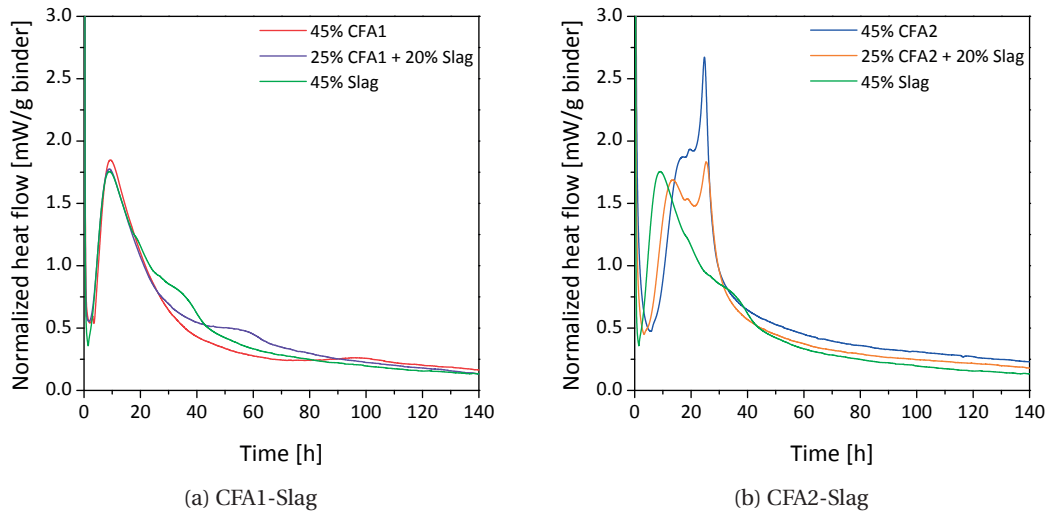


Figure B.5: Comparison of calorimetry curves of single and combined fly ash and slag systems.

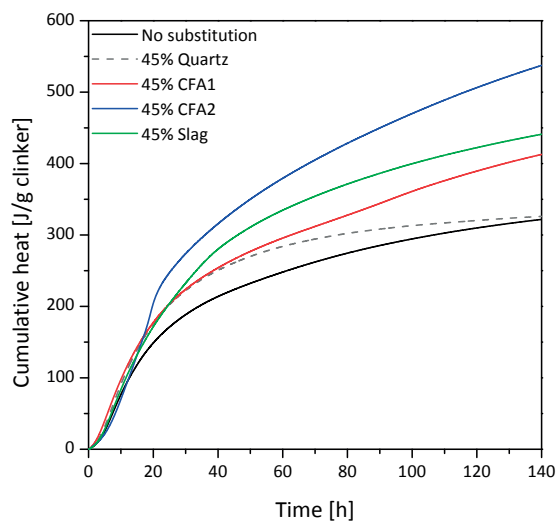


Figure B.6: Cumulative calorimetry curves showing filler effect and contribution of the reaction of the SCMs.

Among the tested SCMs and within the test period CFA2 produces the most heat and CFA1 the least, while the values for Slag were intermediate. The heat generated per gram of reacted component depends on the enthalpy of reaction of this component. Enthalpies of the reaction of clinker phases found in the book of Taylor [44] vary from -517 kJ/kg for C_3S , -262 kJ/kg for C_2S to -1672 kJ/kg for C_3A and -418 kJ/kg for C_4AF . Similarly, the enthalpy of reaction of crystalline and glassy components may vary. Despite those differences, higher generated heat basically means higher reactivity.

B.4 Comparison of strength evolution and heat release

Comparison between cumulative heat and compressive strength is plotted in Figure B.7. The correlation between these two measures is very weak and the same heat can be produced by systems whose compressive strength differs by 10 MPa. This comparison shows, however, how the SCMs begin to contribute to the reaction and strength. After one day of hydration the values corresponding to composite cements are comparable to quartz filler reference. At this time the contribution of SCM reaction seems minimal. At seven days, however, a shift is observed towards the values of PC and PC-L references. The contribution of the SCM reaction has evidently begun.

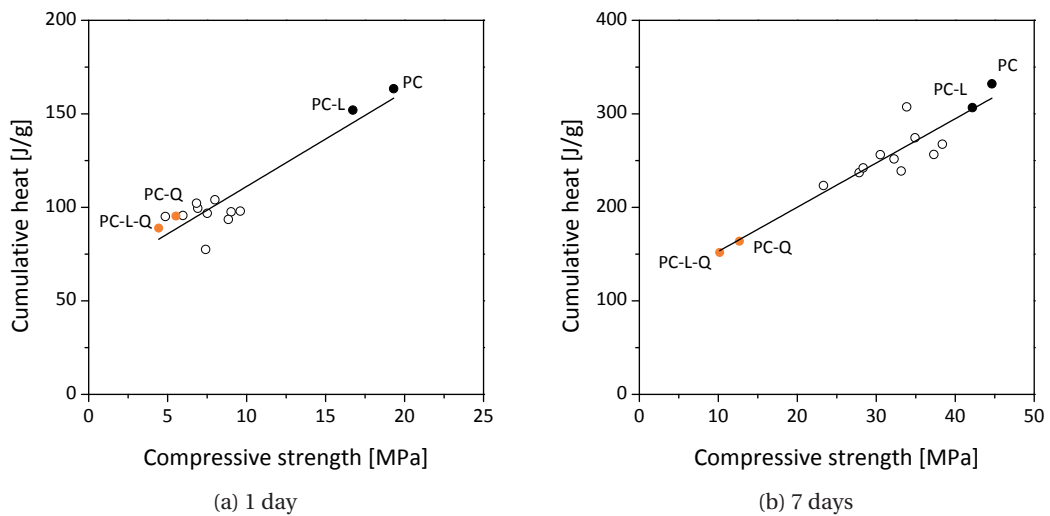


Figure B.7: Comparison between cumulative heat and compressive strength for tested mix compositions at one and seven days of curing.

B.5 Selection of mix formulations for the main study of hydration

The main initial scope of this thesis was to study multi-component cements, which is why for the preliminary study of compressive strength several combined additions of CFA-slag were prepared (35-10, 25-20, 15-10). The binary PC-CFA and PC-S were essentially added for comparison. However, the compressive strength results in Section B.2 above have shown that the differences in the compressive strength between the mixes containing different proportions of CFA-slag were not as significant as those between the binary systems, and ternary if limestone was added. In particular, the positive interaction between CFA2 and limestone, which was clearly more pronounced for this fly ash and not the other led to a decision to study the simpler systems in more detail and to keep only the 25-20 CFA-slag formulation to represent the more complex ones.

Appendix B. Preliminary study on a wide range of mix formulations

As a result the screening did not eliminate many samples but clearly pointed out the need to understand the nature of calcareous fly ash and its reaction first before moving on to study the hydration products and macroscopic properties of many different CFA-slag formulations. The screened samples are marked with an x in the last column of Table B.1.

C Interaction CFA2 - Limestone

C.1 Introduction

It was shown in B.2 that combining CFA2 and limestone produced higher compressive strengths. It was then demonstrated in Figure 6 that in the presence of CFA2 more calcite was consumed than in the other mixes studied. This effect has been attributed to the Ca-rich aluminosilicate glasses from CFA2. They provided significant and balanced amounts of Al and Ca to bind calcite into hemihydrate and monohydrate and sulfate into monosulfate and ettringite. With more calcite consumed, ettringite was produced instead of the monosulfate and monohydrate instead of the hemihydrate. Evidence of monosulfate in PC-L-CFA2 suggests that more calcite could be added in the presence of CFA2.

The PC-L-CFA2 contained 49.5 wt.% clinker, 45 wt.% CFA2 and 5.5 wt.% limestone. The target of this section was to explore whether, thanks to the interaction CFA2 and limestone, more clinker could be replaced by limestone without strength loss. The mixes studied were:

- PC-8L-CFA2: 47 wt.% PC + 45 wt.% CFA2 + 8 wt.% limestone,
- PC-10L-CFA2: 45 wt.% PC + 45 wt.% CFA2 + 10 wt.% limestone.

C.2 Compressive strength

The compressive strength of mortars containing 45 wt.% CFA2 and increasing amounts of limestone are presented in Figure C.1. All of the formulations tested which contained CFA2 and limestone produced higher strengths than those with the CFA2 alone, despite less clinker present. The strength development of the PC-L-CFA2, PC-8L-CFA2 and PC-10L-CFA2 was very similar. This means that additional 4.5 wt.% of clinker can be replaced by limestone without strength loss compared to the PC-L-CFA2. An optimum limestone amount seems to be 8 wt.% which is investigated in the following sections.

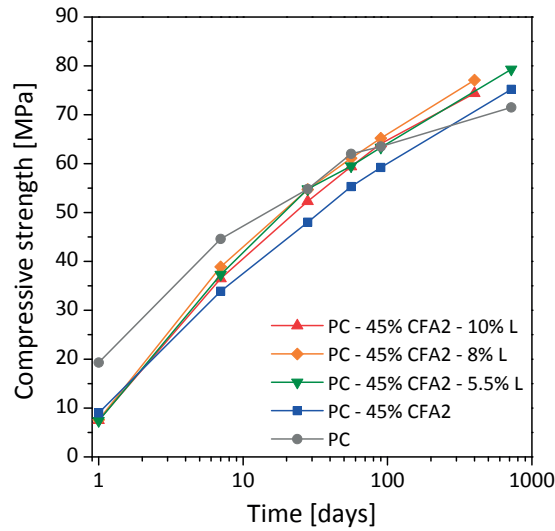


Figure C.1: Compressive strength of mortars with 45 wt.% CFA2 and increasing limestone content.

C.3 Theoretical optimal substitution

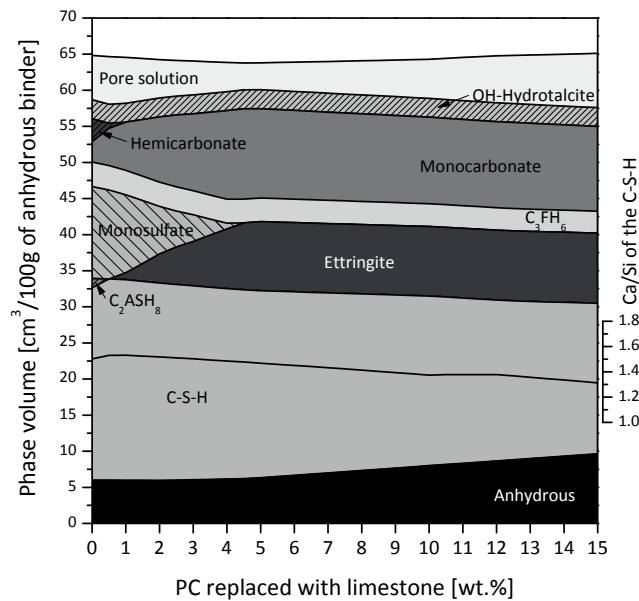


Figure C.2: Thermodynamic modeling of the effect of replacing clinker with limestone in mixes with 45 wt.% CFA2.

The theoretical optimal amount of limestone for a system with 45 wt.% CFA2 was investigated by GEMS thermodynamic modeling. Figure C.2 shows the modeled phase volumes with increasing amount of limestone substituting the clinker. Due to limestone added less Hemicarbonate and Monosulfate is produced and more Ettringite and Monocarbonate. The optimum limestone content corresponds to the formulation with around 4.5 wt.% limestone,

in which all limestone is consumed and no more Monosulfate is left but no excess limestone remains. This formulation should produce the highest strength as the volume of hydrates formed is the largest. The maximum strength measured on mortars however, corresponded to 8 wt.% of limestone.

C.4 Real systems

To clarify the discrepancies between the modeling and the experimental strength the phase evolution was investigated and quantified. The TGA data in Figure C.3 confirms the consumption of limestone seen in the decrease of the peak at 700 °C and the formation of significant amounts of AFm phases (150-350 °C).

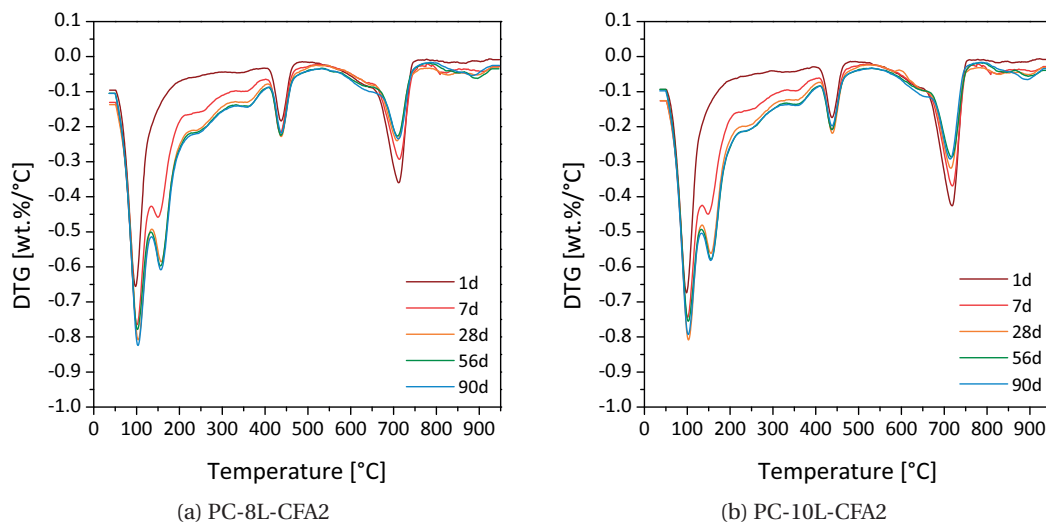


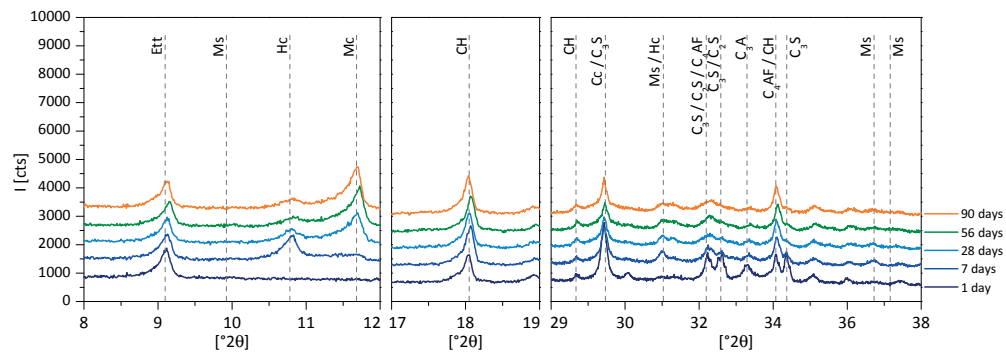
Figure C.3: Thermo-gravimetric curves showing calcite consumption and formation of significant amounts of AFm phases.

Similar observations can be made based on the diffractograms in Figure C.4. Consumption of calcite is accompanied by the formation of ettringite and hemicarbonate, which then reacts to monocarbonate.

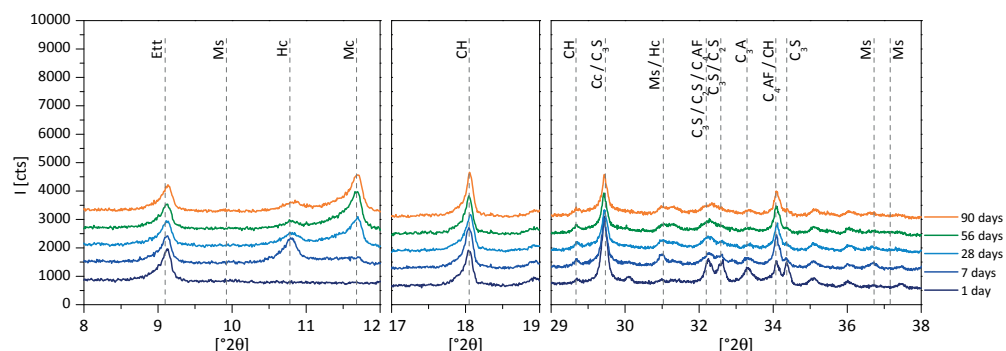
To express these changes quantitatively and to account for the formation of the C-S-H, mass-balance calculations were carried out, which are presented in Figure 6.5. In these calculations the amount of hemicarbonate, monocarbonate, ettringite and portlandite was taken from the XRD-Rietveld analysis of pastes not treated in isopropanol. The large amounts of hemicarbonate formed in both systems presented in the Figure C.5 suggest that the reaction of calcite is the limiting factor.

The calcite consumption quantified by XRD-Rietveld refinement is shown in Figure C.6. The calcite consumption plateaus around 28 day of reaction. The maximum amount of calcite consumed is around 5 g per 100 g of the anhydrous binder, which agrees with the thermo-

Appendix C. Interaction CFA2 - Limestone

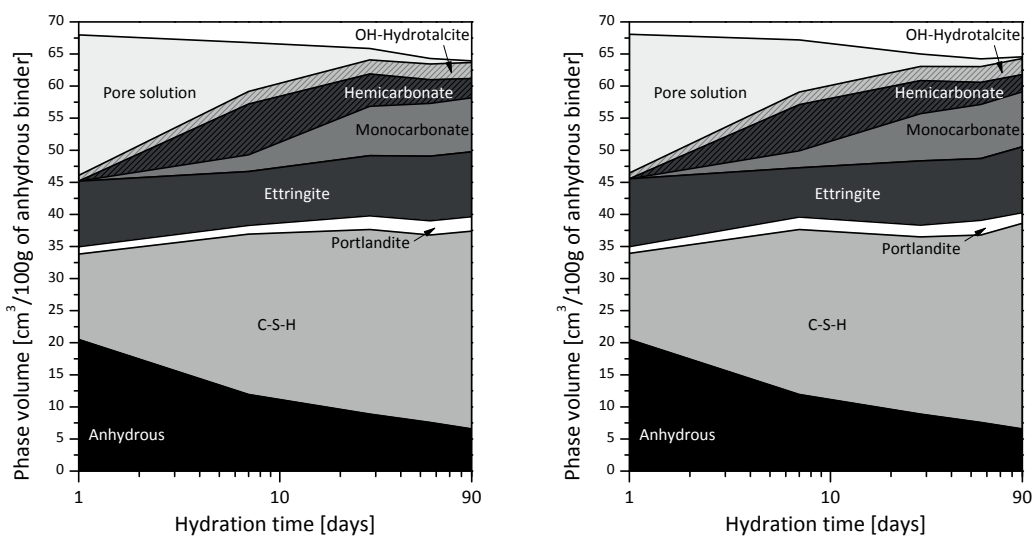


(a) PC-8L-CFA2



(b) PC-10L-CFA2

Figure C.4: X-ray diffractograms.



(a) PC-8L-CFA2

(b) PC-10L-CFA2

Figure C.5: Mass-balance analysis.

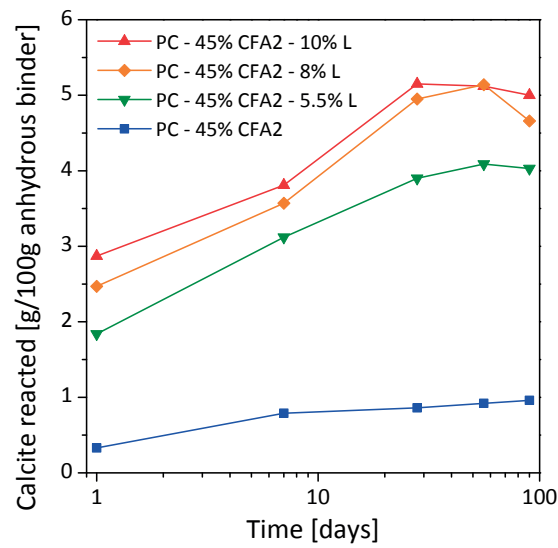


Figure C.6: Calcite consumption quantified by XRD-Rietveld refinement.

dynamically modelled maximum calcite consumption. This consumption was observed in systems with 8 wt.% and 10 wt.% of limestone. In the system with 5.5 wt.% limestone this amount of limestone consumed is not achieved. It seems that due to low reactivity less carbonate is available than could react until 28 days in this system. However, it seems that when higher amounts of limestone are present there is more reaction at early ages.

Less reaction of calcite may too be linked to its poor dispersion. An aggregate of limestone particles can be seen in top right part of Figure C.7 and aggregated particles may be less accessible for the reaction.

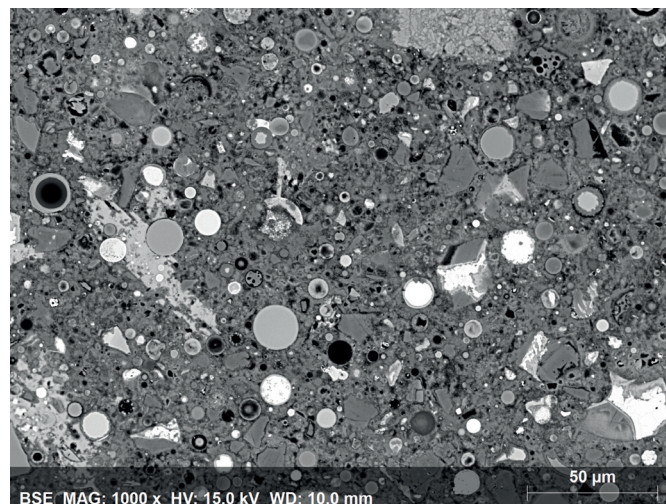


Figure C.7: BSE micrograph of PC-8L-CFA2 after 90 days of hydration.

In terms of the amount of limestone reacted the real system with 8 wt.% limestone corresponds to the modelled system with 5 wt.%.

C.5 Summary

Interaction between a calcareous fly ash and limestone was investigated:

- The fly ash used contained reactive Ca-rich aluminosilicate glass, which provided significant amounts of Al and Ca for the reaction with calcite.
- According to the thermodynamic modelling the maximum amount of limestone consumed was around 4.5 wt.%, which agrees with the maximum experimental consumption of 5 wt.%.
- This maximum consumption was only achieved in systems with excess limestone (8 and 10 wt.%), which may be related to low calcite reactivity and limited dispersion.
- Thanks to the large availability of Al and Ca the amount of limestone that substituted clinker could be raised from 5.5 wt.% to 10 wt.% without significant strength loss.

D Durability

D.1 Introduction

The effect of SCMs on the durability of composite cements is both physical and chemical. Due to a decreased permeability the ingress of aggressive media is reduced. SCMs also modify the phase assemblage and therefore affect the chemical mechanisms of interaction between cement paste and aggressive ions (e.g. chloride binding).

In Chapter 6 it was shown that the presence of glasses of different chemical composition and reactivity impacts the phase assemblage and the permeability of composite cements. This part looks at the durability of the composite cements studied in various aggressive environments:

- Chloride ingress,
- Sulfate attack.

The mortar samples used for the testing were conditioned for 90 days prior to exposure to allow sufficient time for the SCMs to react. The details of the experimental procedures are given in Materials and Methods, sections D.2 and D.3.

This chapter presents the results of the tests and only a limited analysis. Due to many samples made and large amount of work done in a relatively short time it has been impossible to analyse the results in detail at this stage.

D.2 Chloride ponding

Chloride-induced corrosion of reinforced concrete is governed by the transport of chloride ions through the cementitious matrix to the steel rebars. It depends on the porosity and the tortuosity of the matrix and is often assessed using a macroscopic chloride diffusion coefficient. The refinement of pore structure by SCMs has an important impact on reducing chloride penetration. From a chemical point of view, chloride can be bound to hydration products by physical adsorption on C-S-H, AFm and AFt phases and by chemical reaction of

Appendix D. Durability

monosulfate and other AFm phases to Friedel's salt. Adding SCMs, in particular fly ash, can significantly increase the aluminate content and thus increase chloride binding [126, 127].

A ponding experiment was set up to assess the susceptibility of mortars to ingress of chloride. The protocol was based on NordTest standard NT BUILD 443 (www.nordtest.org). The $4 \times 4 \times 16$ cm mortar bars were cut into cubes of around $3 \times 4 \times 4$ cm. Five faces of each cube were sealed with a double aluminium tape leaving the cut face exposed to solution. The cubes were immersed in 0.5 M NaCl solution at room temperature. The solution was renewed every 5 weeks during 6 months. To obtain the chloride penetration profile, the cubes were gradually ground at 2.5 mm intervals perpendicular to the direction of chloride ingress, using automated grinding equipment. The powdered material obtained was analysed by XRD, then dried to constant mass in an oven at 110 °C, weighed and leached with 6 M HNO₃ for at least 12 hours. An extracted sample of the supernatant liquid was analysed by chromatography for Cl⁻ concentration.

The obtained chloride concentrations in the acid solution were expressed as a wt.% of dry sample and plotted versus the depths below sample surface in Figure D.1. The effective chloride transport coefficient D_e [m²/s] is obtained by fitting this data with a least squares fit of a function based on the error function *erf* :

$$C(x, t) = C_S - (C_S - C_j) \cdot \text{erf} \left(\frac{x}{\sqrt{4D_e t}} \right) \quad (\text{D.1})$$

where $C(x, t)$ is the chloride concentration at depth x [m] after exposure time t [s], C_S is the boundary condition at the exposed surface, which is calculated in this regression analysis, and C_j is the initial chloride concentration, here assumed zero. The first point of the profile from the most outer layer is omitted in the regression analysis. In Figure D.1, points represent the experimental data and the profiles show the result of the regression analysis. The calculated effective diffusion coefficients D_e are presented in Table D.1.

Blending of PC with CFA1 and Slag significantly decreased the chloride penetration into the mortars. This effect can be attributed to a more compact and refined microstructure and thus lower permeability in addition to binding of chloride. The improvement due to CFA2 was less, which agrees with the trends in the results in the section 6.5 showing that among the composite cements studied the mixes containing CFA2 had generally higher water absorption rate and migration current. The ingress of chloride was related to the amount of capillary porosity in Figure D.2 in which the effective diffusion coefficients are plotted against the volume of pores whose entry radius is larger than 8.5 nm. In this figure, a tendency towards higher diffusion coefficient with higher volume of capillary porosity can be observed, but there is no clear relationship. Since MIP measures the accessible porosity only, this should already account for the effect of percolation on chloride diffusion. The reason for discrepancies may rather lie in depercolation during the test. The capillary porosity was determined on pastes after 90 days of hydration but the chloride penetration took additional 6 months, during which the matrix may have further densified.

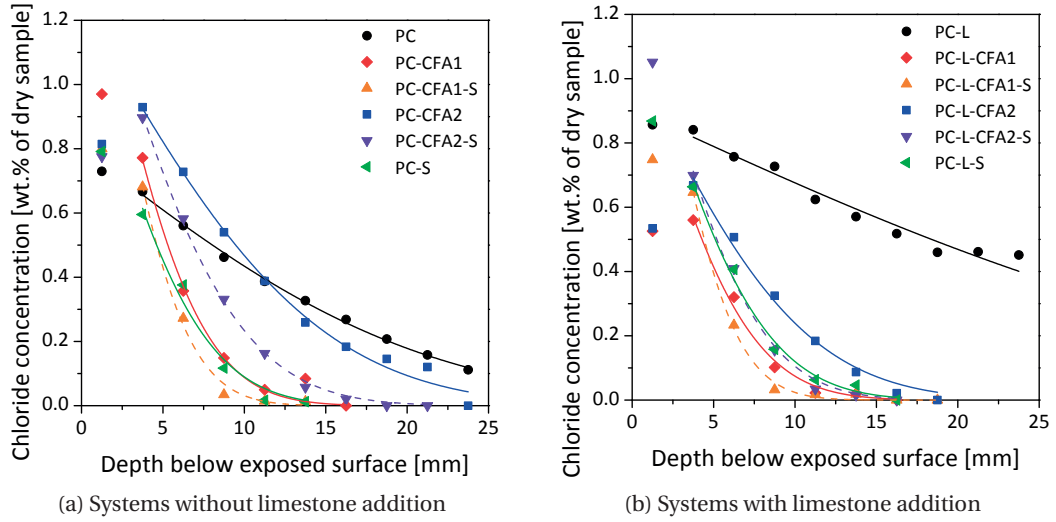


Figure D.1: Chloride ponding experiment results: measured total chloride and fitted profiles.

Another reason for scatter in Figure D.2 may be the chloride binding by the hydration products. The actual amount of chloride bound cannot be derived from the ponding experiment and would require additional testing to obtain so called chloride binding isotherms, which relate the concentration of chloride in the pore solution and the bound chloride. Even if such isotherms are obtained it may be difficult precisely relate the bound chloride to the amounts of specific hydration products. This is because most of the hydration products can bind chloride, either chemically by reaction or physically by adsorption. C-S-H [128] and the AFm phases [129] are known to be able to bind chloride ions and the product of the reaction of chloride with the AFm phases, Friedel's salt, may further bind chloride by physical adsorption

Table D.1: Effective diffusion coefficients D_e determined by a regression analysis of the chloride ponding experiment.

	D_e [$\text{m}^2/\text{s}\cdot 10^{-13}$]
PC	86
PC-CFA1	9
PC-CFA1-S	6
PC-CFA2	40
PC-CFA2-S	16
PC-S	10
PC-L	307
PC-L-CFA1	9
PC-L-CFA1-S	5
PC-L-CFA2	22
PC-L-CFA2-S	10
PC-L-S	21

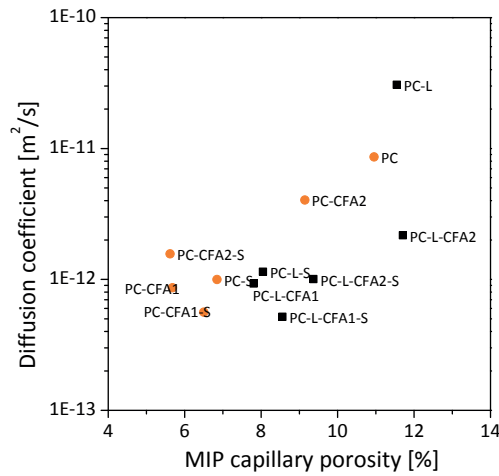


Figure D.2: Effective diffusion coefficient from ponding vs. capillary porosity from MIP.

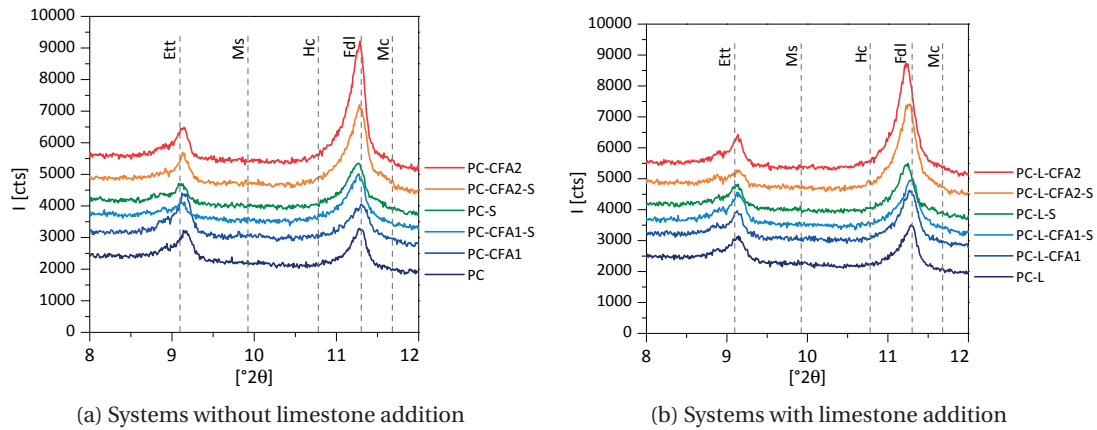


Figure D.3: XRD data collected on the second slice of mortars exposed to chloride solution for 6 months showing the presence of Friedel's salt.

[130]. The evidence of chloride binding by AFm phases into Friedel's salt in the mixes studied is shown in XRD diffractograms Figure D.3. The amount of Friedel's salt is by far the largest in mixes containing CFA2, which initially contained large amounts of AFm phases. However, as mentioned above, the binding of chloride by AFm phases is only a part the overall binding.

D.3 Sulfate attack

According to recent findings [131, 132, 133], the sulfate-induced deterioration of concrete is primarily due to the chemical interaction of the sulfate ions with AFm crystals finely intermixed with the C-S-H. This reaction mainly concerns monosulfate but monocarbonate, hemihydrate and hydrotalcite can also react with sulfate ions to ettringite [134]). There is a competition between the growth of ettringite in large and in small (nano-metric) pores,

which depends on the location of the mentioned AFm phases in the matrix prior to sulfate exposure. Crystallization pressure exerted on the matrix by the reaction in the nano-metric pores causes expansion and cracking [133, 135]. The transport of sulfate ions into the matrix is generally regarded as a secondary factor, but it has been shown for slag mixes [133] that due to a very impermeable matrix and thus reduced transport of sulfate ions, the mode of deterioration may change from general expansion to surface spalling. Therefore the important factors influencing sulfate attack are: (i) from the chemical point of view, the amount of AFm in nanometric pores available to react with the sulfate ions and (ii) from the physical point of view, the permeability of the cement matrix [136].

The impact of limestone addition is mainly physical. Up to 5 wt.-% reduces porosity [132]. However, larger amounts (>10 wt.-%) increase porosity and lower the sulfate resistance [132, 136, 137]. The initial compressive strength is decreased and subsequent decrease of compressive strength under sulfate attack is larger [137]. Using 40-50 wt.-% replacement of PC by slag ($\text{Al}_2\text{O}_3 < 11$ wt.-%) was found effective in increasing sulfate resistance [138]. This was explained by lower binder permeability and lower portlandite content.

Compared to siliceous fly ashes the calcareous ones have been reported to be less efficient in reducing sulfate attack [139]. Attempts were made to find out whether there is a relationship between calcium content, chemical and mineralogical composition of the fly ash and the sulfate resistance [18, 140]. In general, fly ashes containing glass of mullite or anorthite type tend to have a beneficial effect on sulfate resistance, those of gehlenite type were more likely to be susceptible to sulfate attack. The calcium-aluminosilicate glass (gehlenite type) was found to be more reactive and supply more alumina for the formation of monosulfate. For the same reason C_3A and C_4AF in calcareous fly ashes are believed to decrease sulfate resistance [140]. A possibility to increase the sulfate resistance of PC-calcareous fly ash mixes by adding slag has been reported [141].

In this thesis, sulfate attack was investigated similarly to [142] by measuring linear expansion of a series of three $2 \times 2 \times 16$ cm mortar bars immersed in 3 g/L Na_2SO_4 solution at room temperature. The mortar bars were obtained by removing 1 cm from each of the four longer walls of the $4 \times 4 \times 16$ cm bars. Each set of samples was stored separately in a sealed plastic box keeping a constant ratio of 25 between the volume of the sulfate solution and the total volume of the mortar bars. The measurement of linear expansion and renewal of sulfate solution was carried out every 2 weeks for a period of 80 weeks. The linear expansion vs. time is shown in Figure D.4. Most of the composite cements did not display significant expansion (values below 0.025 %) and are not presented in this figure. PC expanded significantly until breaking at 3.5 % expansion after around 70 weeks exposure. Substitution of 10 wt.% of PC by limestone resulted in an earlier and faster expansion and the damage occurred at lower expansion, which was expected based on the observations in [132]. Among the composite cements linear expansion was only recorded for PC-CFA2 and PC-CFA2-S.

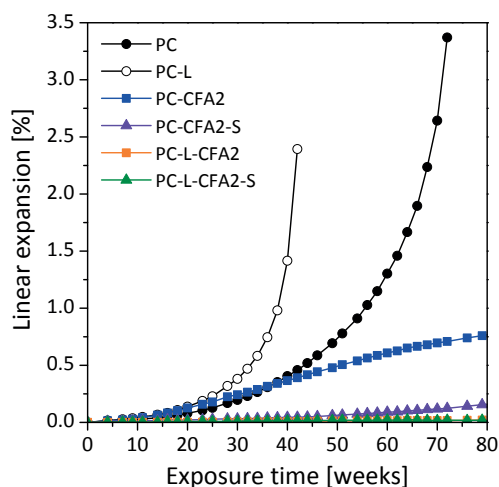


Figure D.4: Linear expansion of mortars immersed in 3 g/L calcium sulfate solution.

An important drawback of the linear expansion test is that it looks only at the expansion part of the sulfate-induced damage and does not assess the surface spalling. Significant surface spalling was generally not observed but softening and slight material loss on the edges was seen in mortars containing CFA2 and Slag. The PC-S did not show linear expansion during the experiment, which does not necessarily mean that this formulation is sulfate-resistant. Due to the refinement of porosity in composite cements, the ingress of ions may be significantly limited.

The ingress of sulfate into the mortars was investigated by SEM-EDS measurement of the sulfur content in the hydrated matrix. Every 120 days of sulfate ponding three 5 mm-thick slices of a companion bar in the sulfate solution were cut for microstructural analysis. The slices were soaked in isopropanol for 7 days, dried, kept in vacuum desiccator for another 7 days. One of the slices was prepared for electron microscopy by impregnation in an epoxy resin, gradual polishing and coating with conductive carbon. The first step of the SEM investigation was to obtain a sulfate penetration profile. An area was carefully selected near the sample surface where two frames of 2.5×1.9 mm were analysed with BSE and EDS. Sulfate profile going 5 mm into the sample was obtained with a MATLAB code written to treat the data. The code first finds the aggregates by thresholding low intensity signal in a Ca map and excludes them from further analysis. In each line of the image perpendicular to sample depth the sulfur atomic-% is summed up, converted to sulfate wt.% and divided by the number of pixels not containing the aggregates.

The sulfur content was then expressed in terms of SO_3 wt.% and the results are presented in Figure D.5. Among the composite cements tested, PC-CFA2 was the most penetrated by the sulfate ions. In PC-CFA2-S the penetration was slightly reduced and only the limestone addition to these systems seems to have decreased the penetration significantly. The mixes containing CFA1 and Slag were much less penetrated and the limestone addition had little

influence on their penetration profiles. A surprisingly low penetration observed in PC-CFA1-S was probably due to a measurement error as such low penetration would seem odd and this profile should be verified.

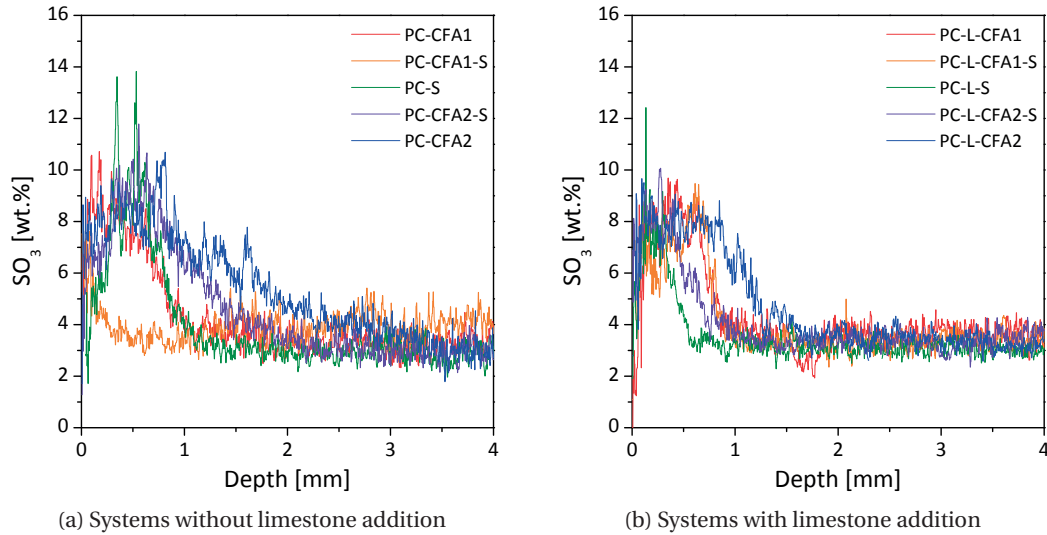


Figure D.5: Sulfate penetration profiles measured by SEM-EDS.

A detailed analysis of sulfate resistance of the mixes studied remains incomplete. Clearly the permeability of the matrix plays an important role and the mixes containing CFA1 and Slag could be sensitive to sulfate but may have not been expanding due to limited penetration of the sulfate into their microstructures. Another aspect that still needs to be evaluated is the location of the AFm phases in the microstructure of the mortars studied. In Chapter 6 it was shown that AFm phases were present in all of the pastes studied but the sulfate-induced damage will only be caused by the expansion in nanometric pores. The amount of AFm phases finely intermixed with the C-S-H should be assessed and the technique recommended is SEM-EDS point analysis.

E Thermo-gravimetric curves

Appendix E. Thermo-gravimetric curves

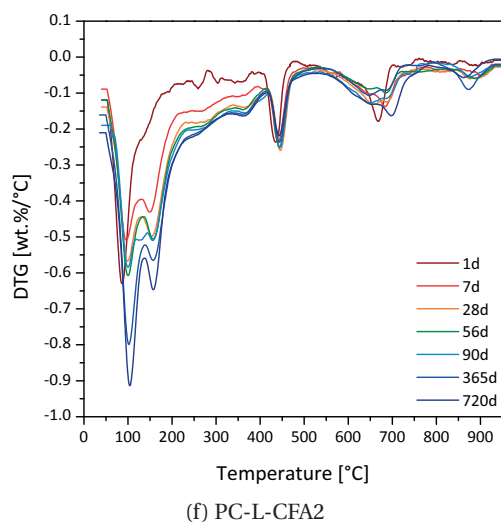
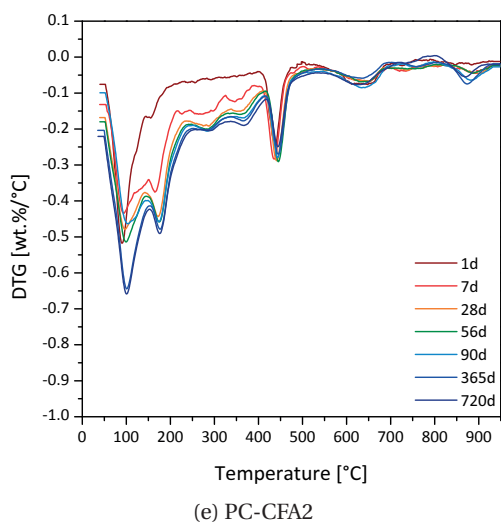
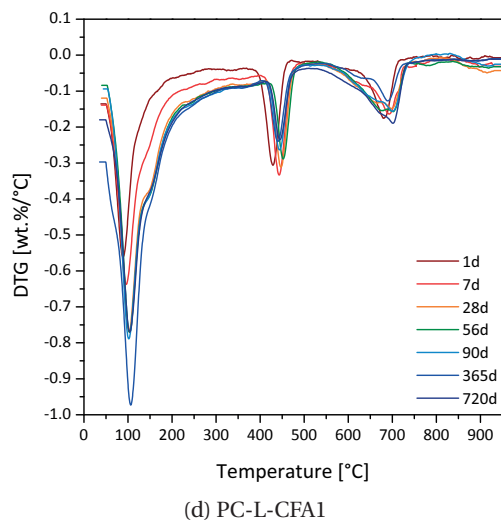
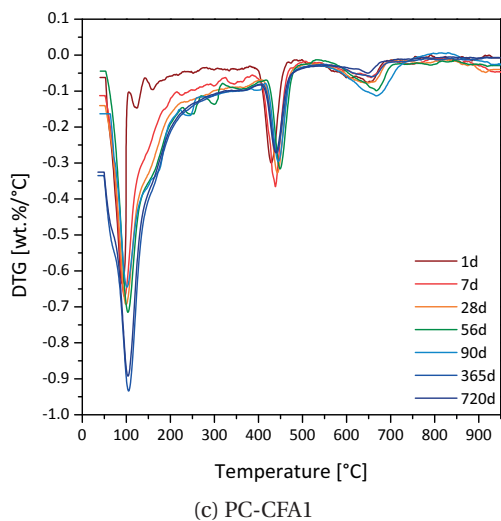
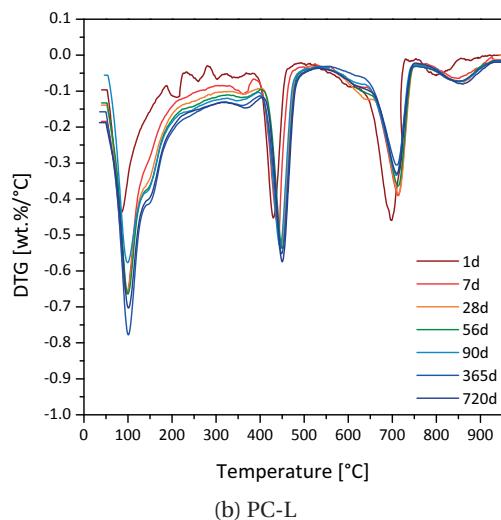
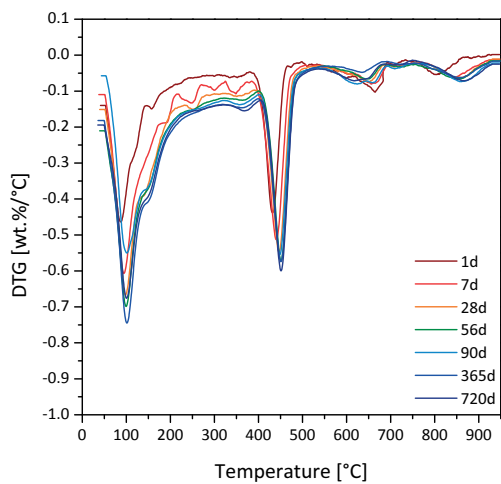
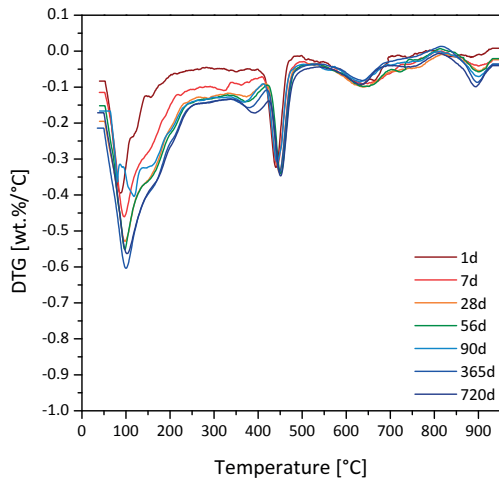
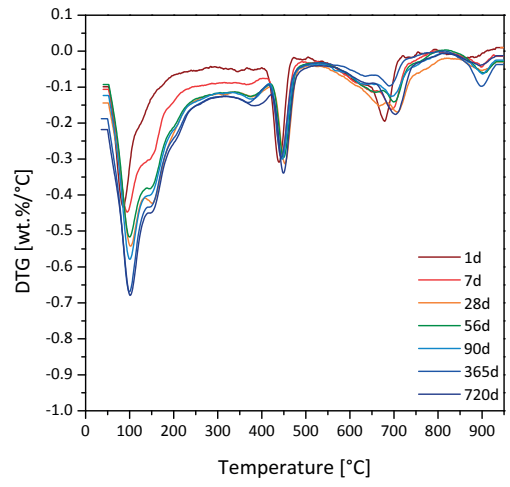


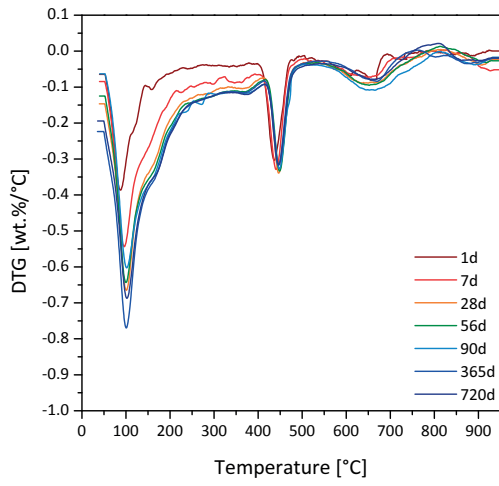
Figure E.1: Differential thermo-gravimetric curves - 1/2.



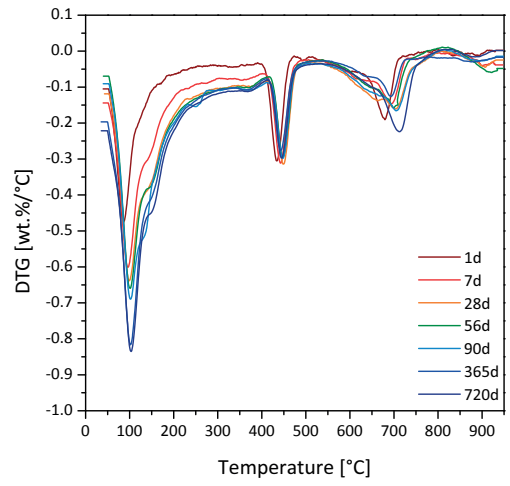
(a) PC-S



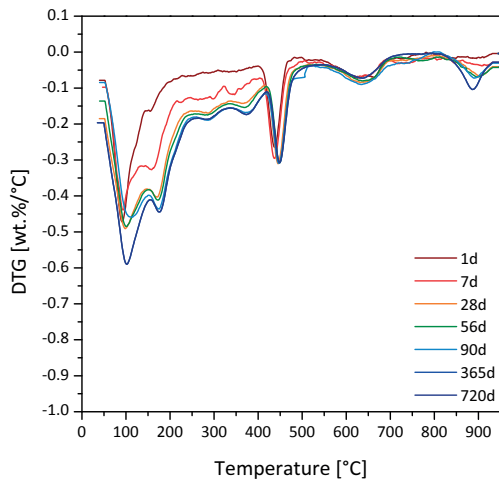
(b) PC-L-S



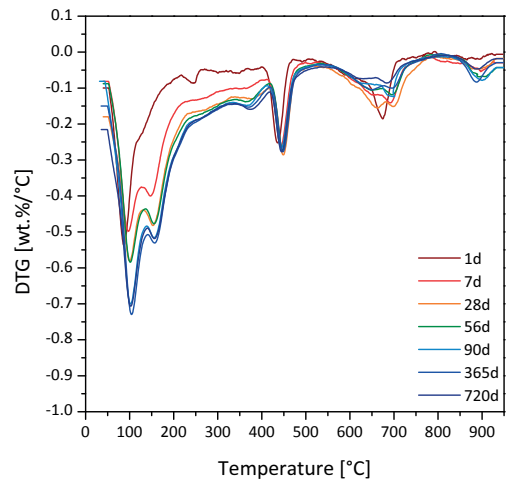
(c) PC-CFA1-S



(d) PC-L-CFA1-S



(e) PC-CFA2-S



(f) PC-L-CFA2-S

Figure E.2: Differential thermo-gravimetric curves - 2/2.

F X-ray diffractograms

Appendix F. X-ray diffractograms

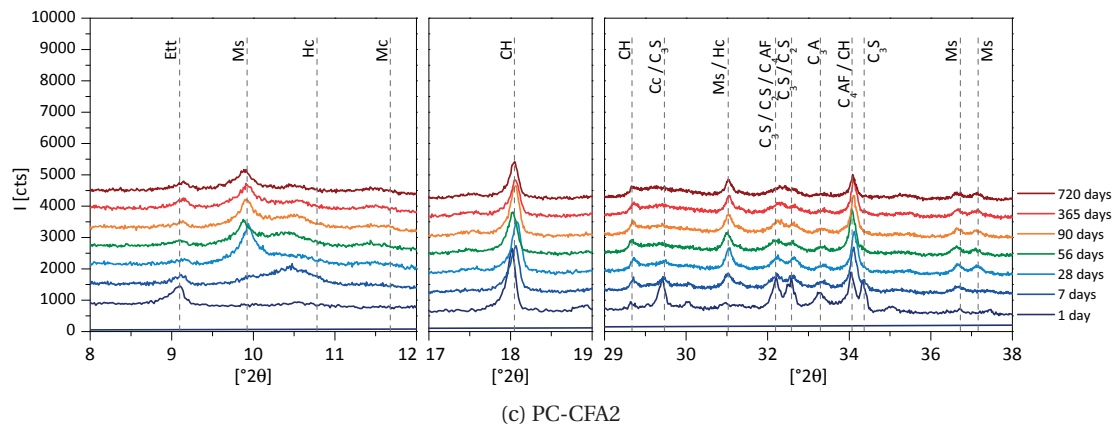
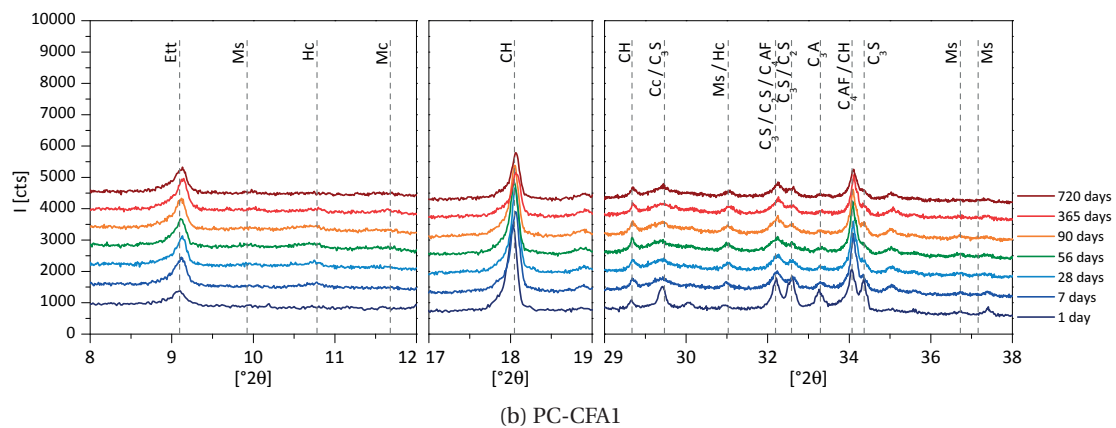
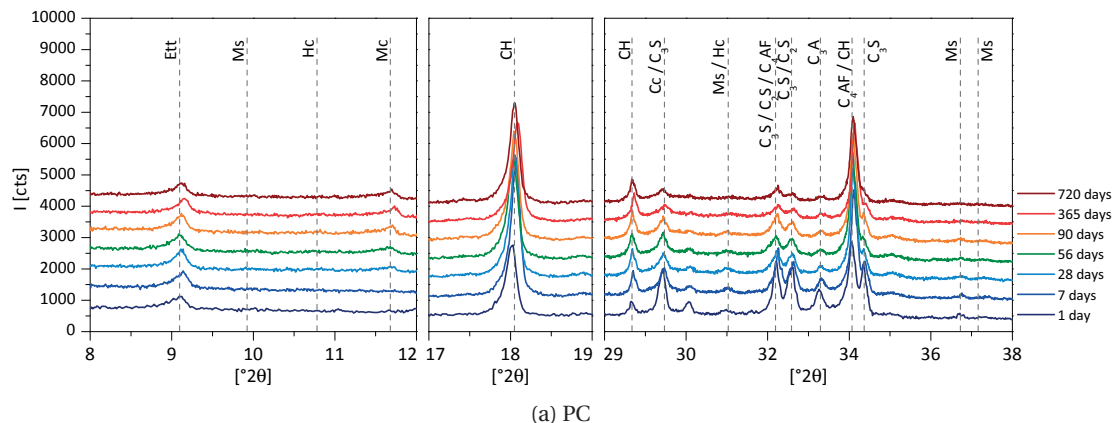


Figure F.1: X-ray diffractograms - 1/4.

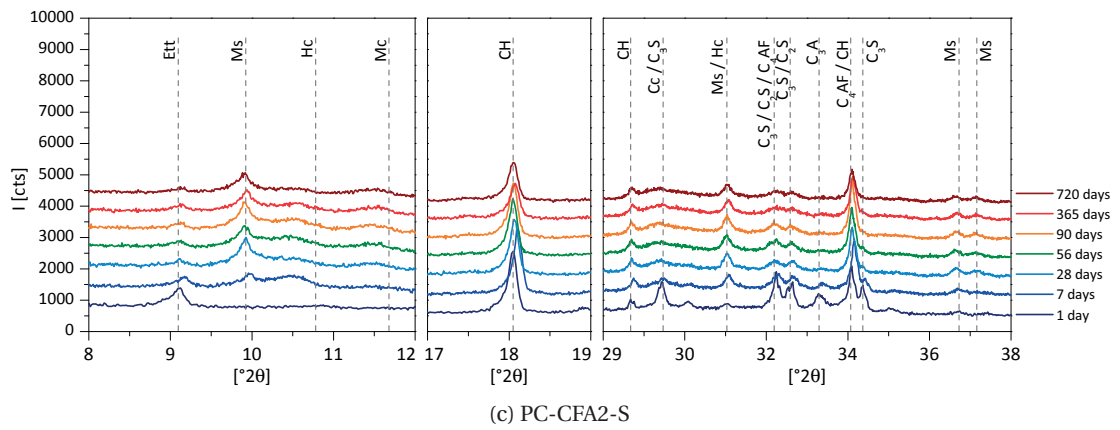
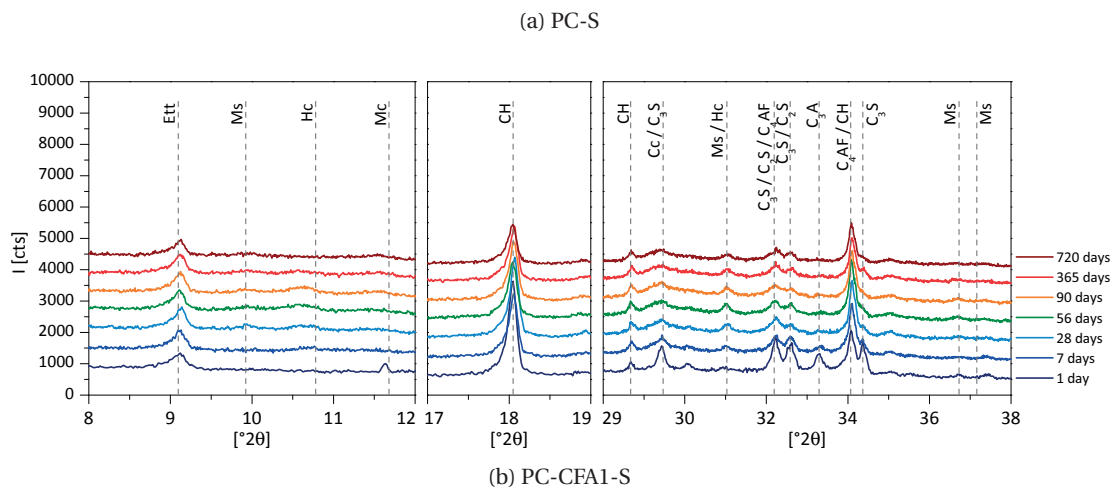
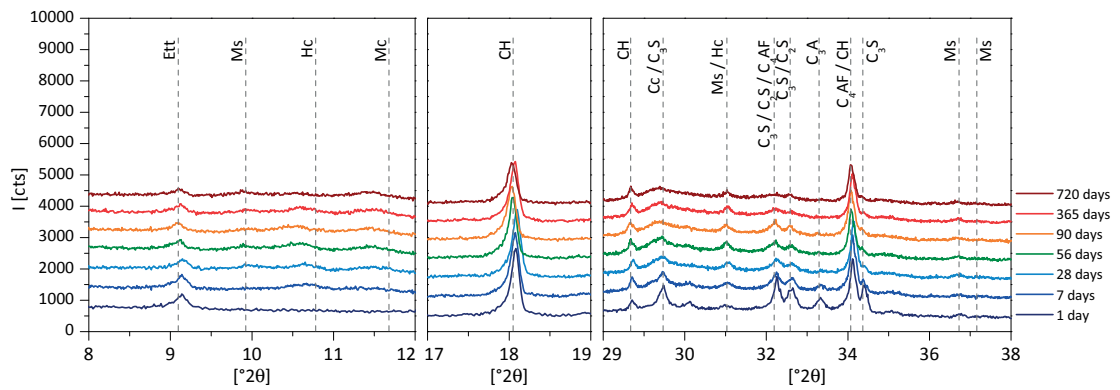


Figure F.2: X-ray diffractograms - 2/4.

Appendix F. X-ray diffractograms

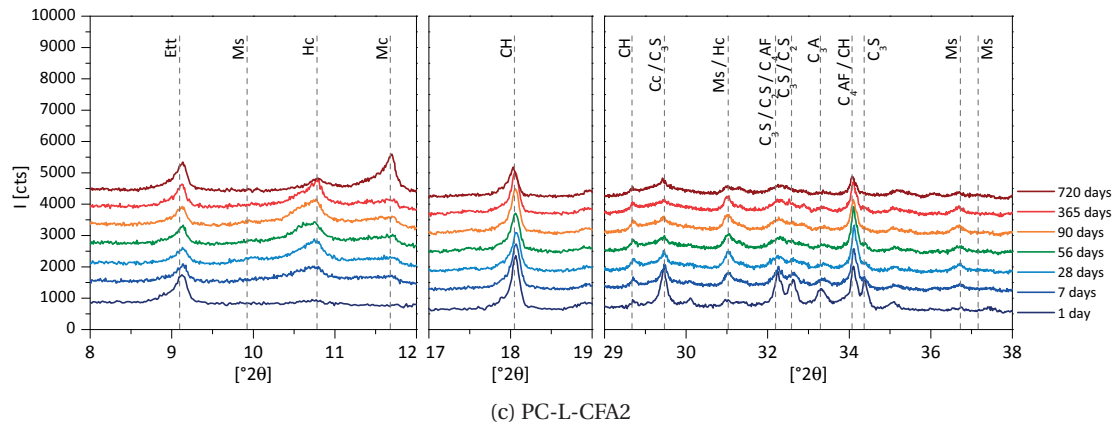
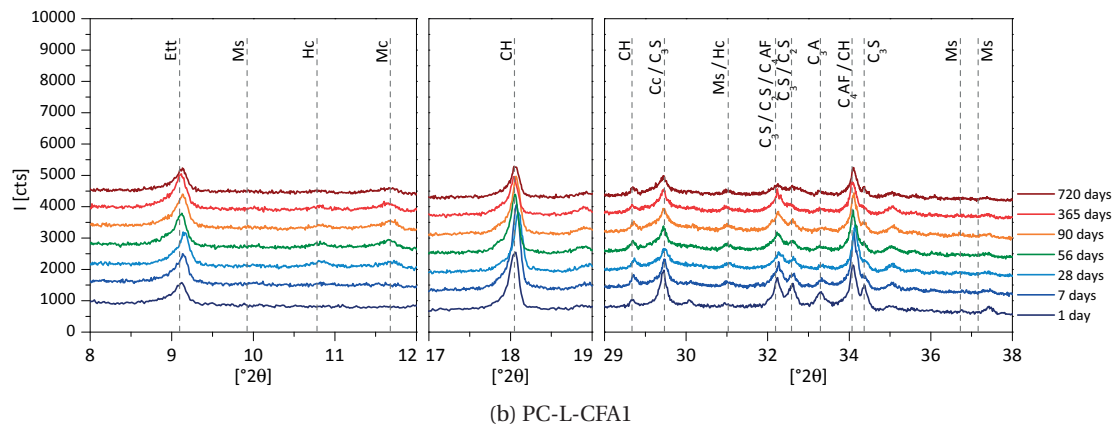
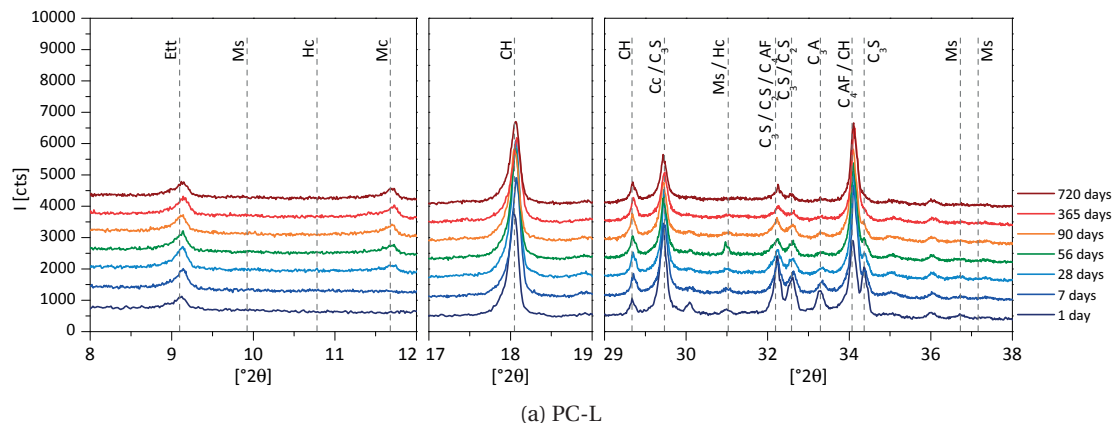
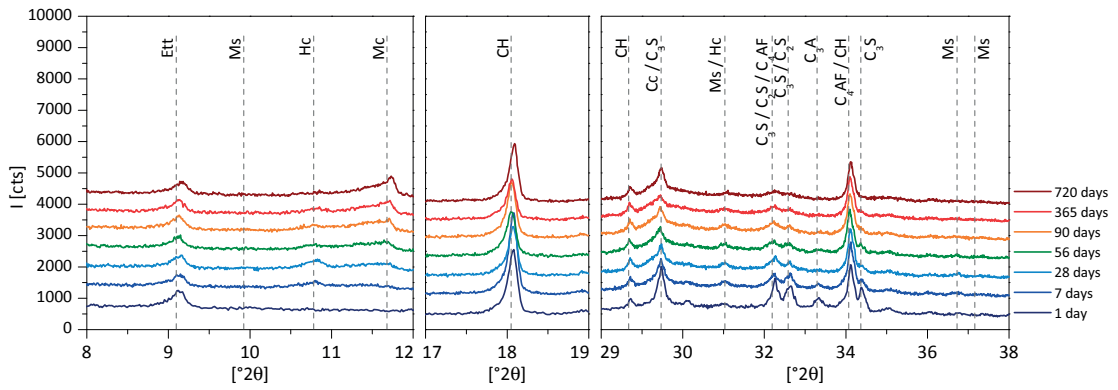
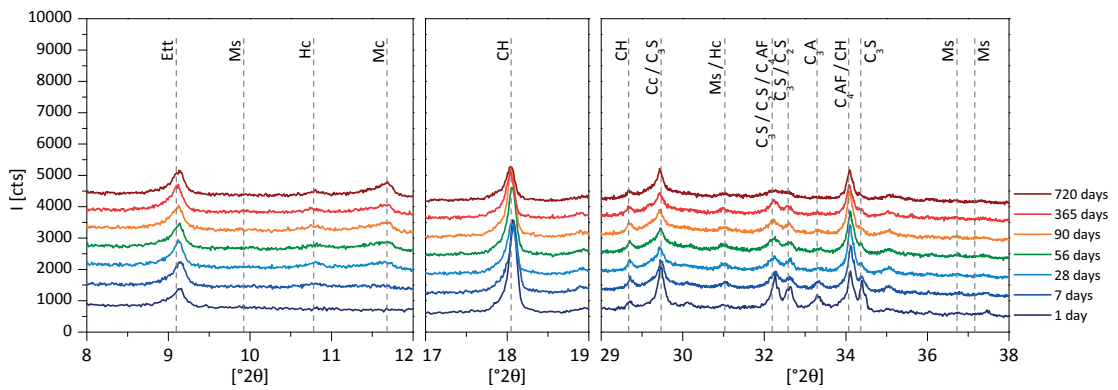


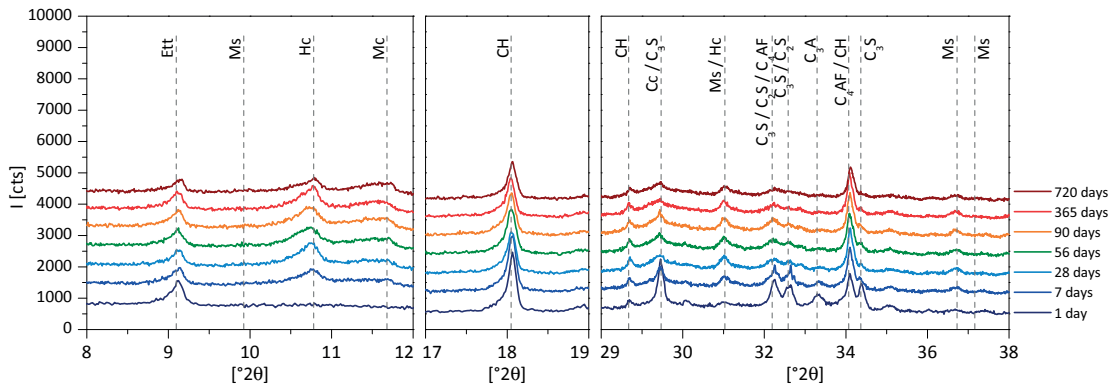
Figure E3: X-ray diffractograms - 3/4.



(a) PC-L-S



(b) PC-L-CFA1-S



(c) PC-L-CFA2-S

Figure F4: X-ray diffractograms - 4/4.

G SEM-EDS point analysis of C-S-H data

Appendix G. SEM-EDS point analysis of C-S-H data

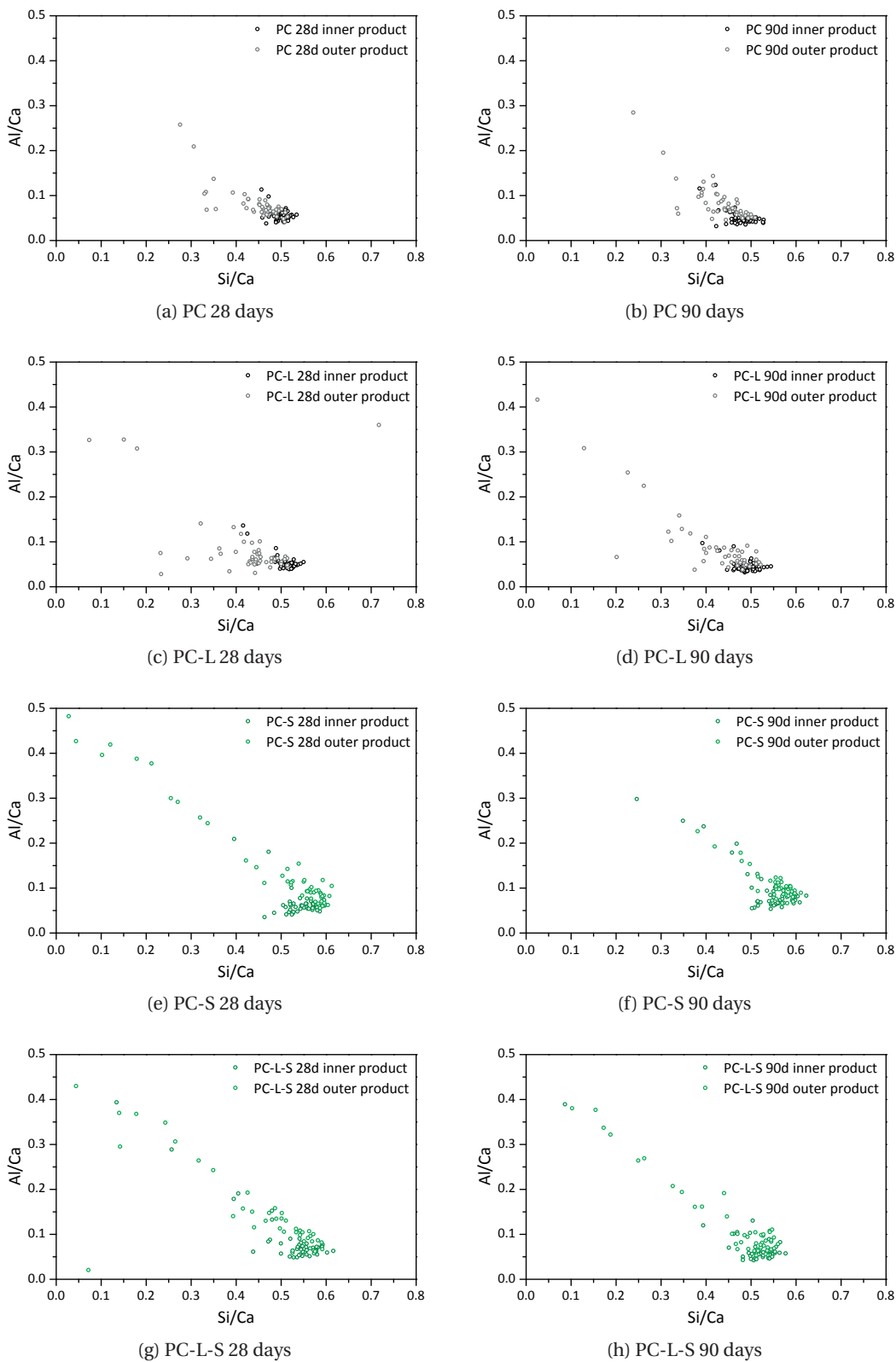


Figure G.1: EDS point analysis data - 1/3.

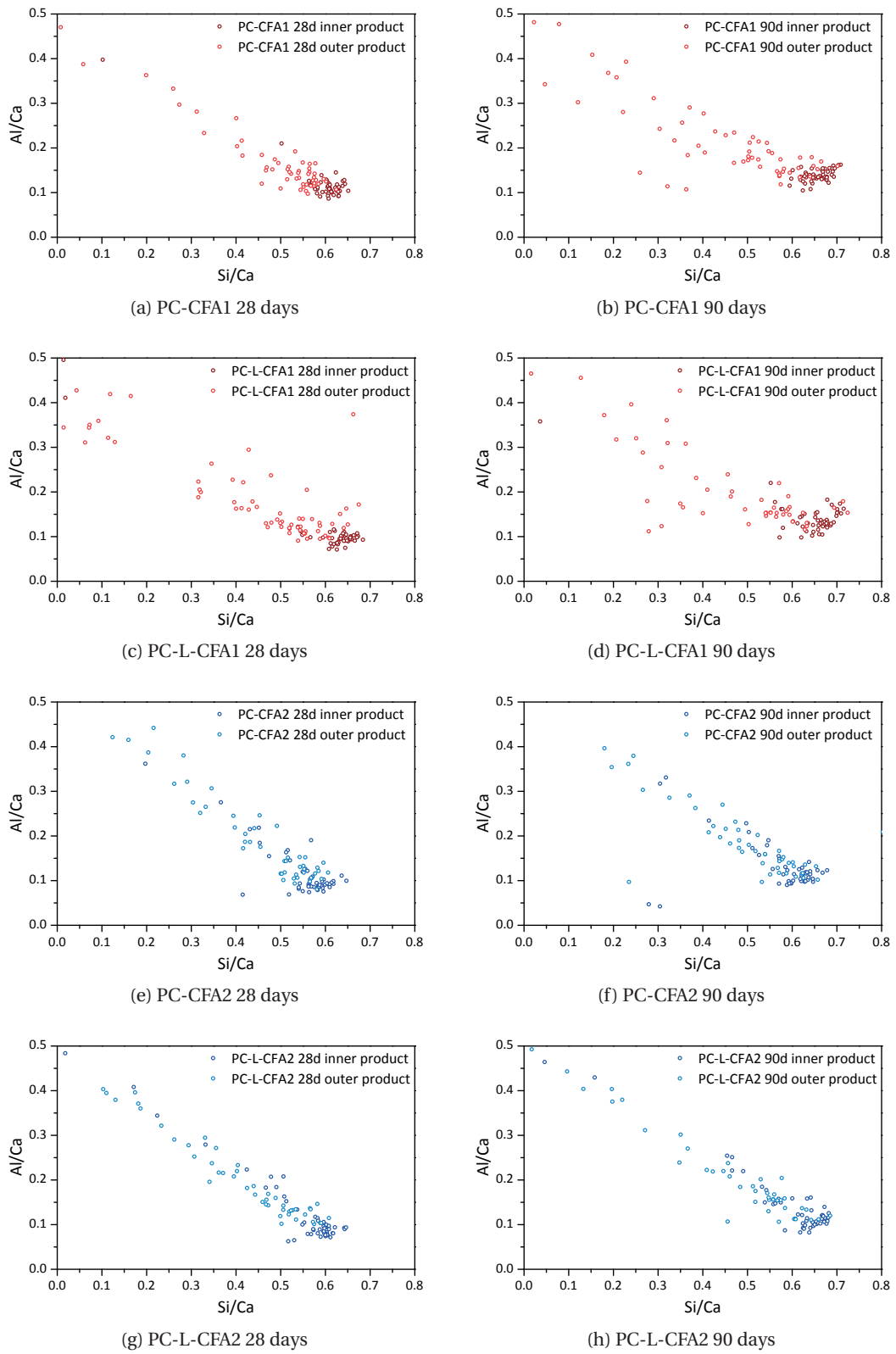
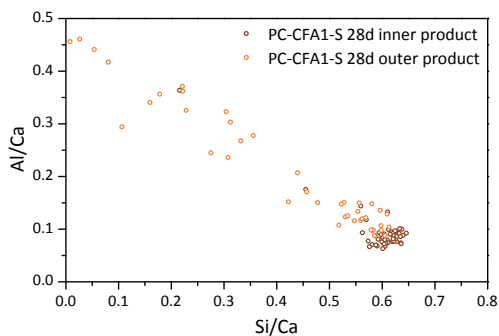
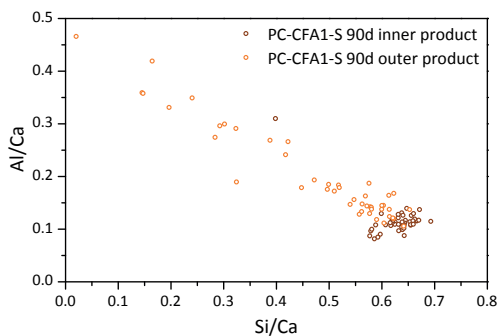


Figure G.2: EDS point analysis data - 2/3.

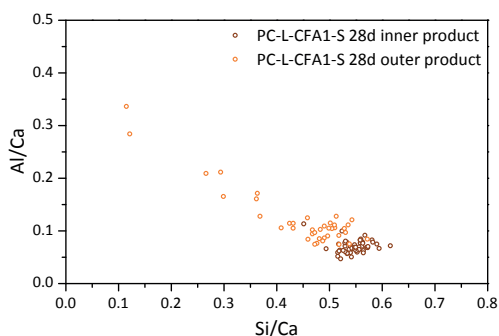
Appendix G. SEM-EDS point analysis of C-S-H data



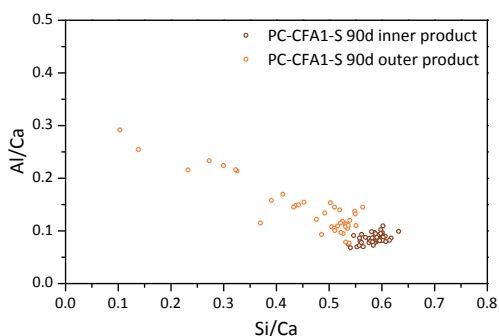
(a) PC-CFA1-S 28 days



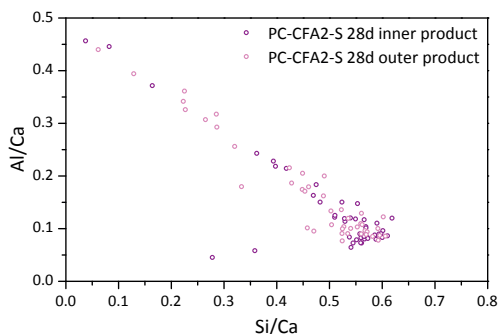
(b) PC-CFA1-S 90 days



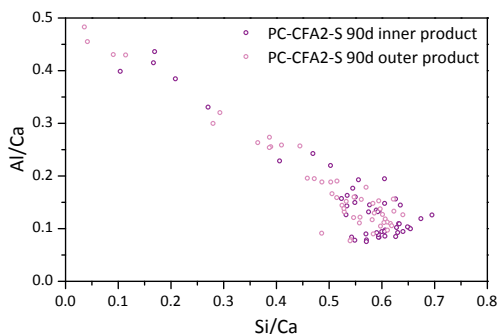
(c) PC-L-CFA1-S 28 days



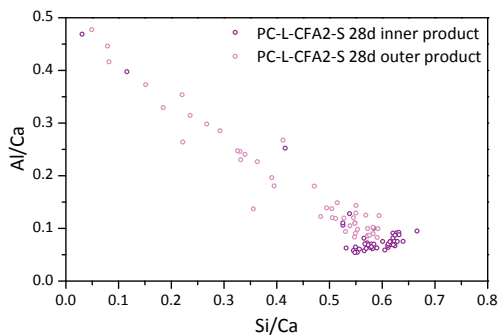
(d) PC-L-CFA1-S 90 days



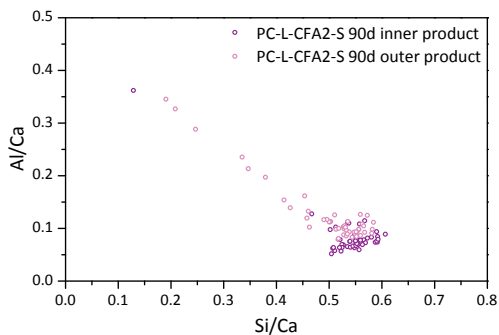
(e) PC-CFA2-S 28 days



(f) PC-CFA2-S 90 days



(g) PC-L-CFA2-S 28 days



(h) PC-L-CFA2-S 90 days

Figure G.3: EDS point analysis data - 3/3.

H Ion concentrations in pore solutions

Appendix H. Ion concentrations in pore solutions

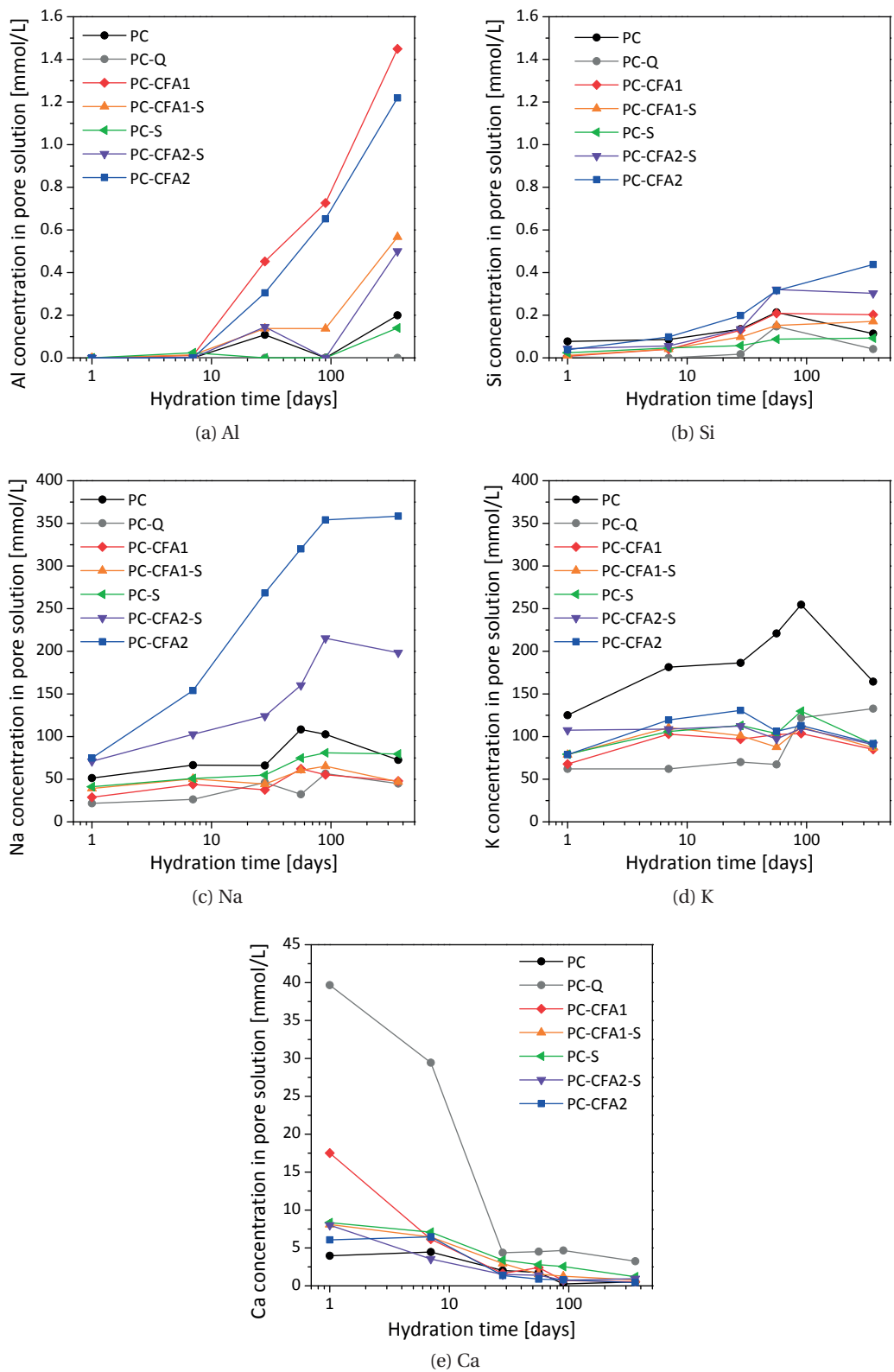


Figure H.1: Ion concentrations measured by ICP in the pore solutions obtained by high-pressure squeezing of pastes.

I Mercury Intusion Porosimetry curves

Appendix I. Mercury Intusion Porosimetry curves

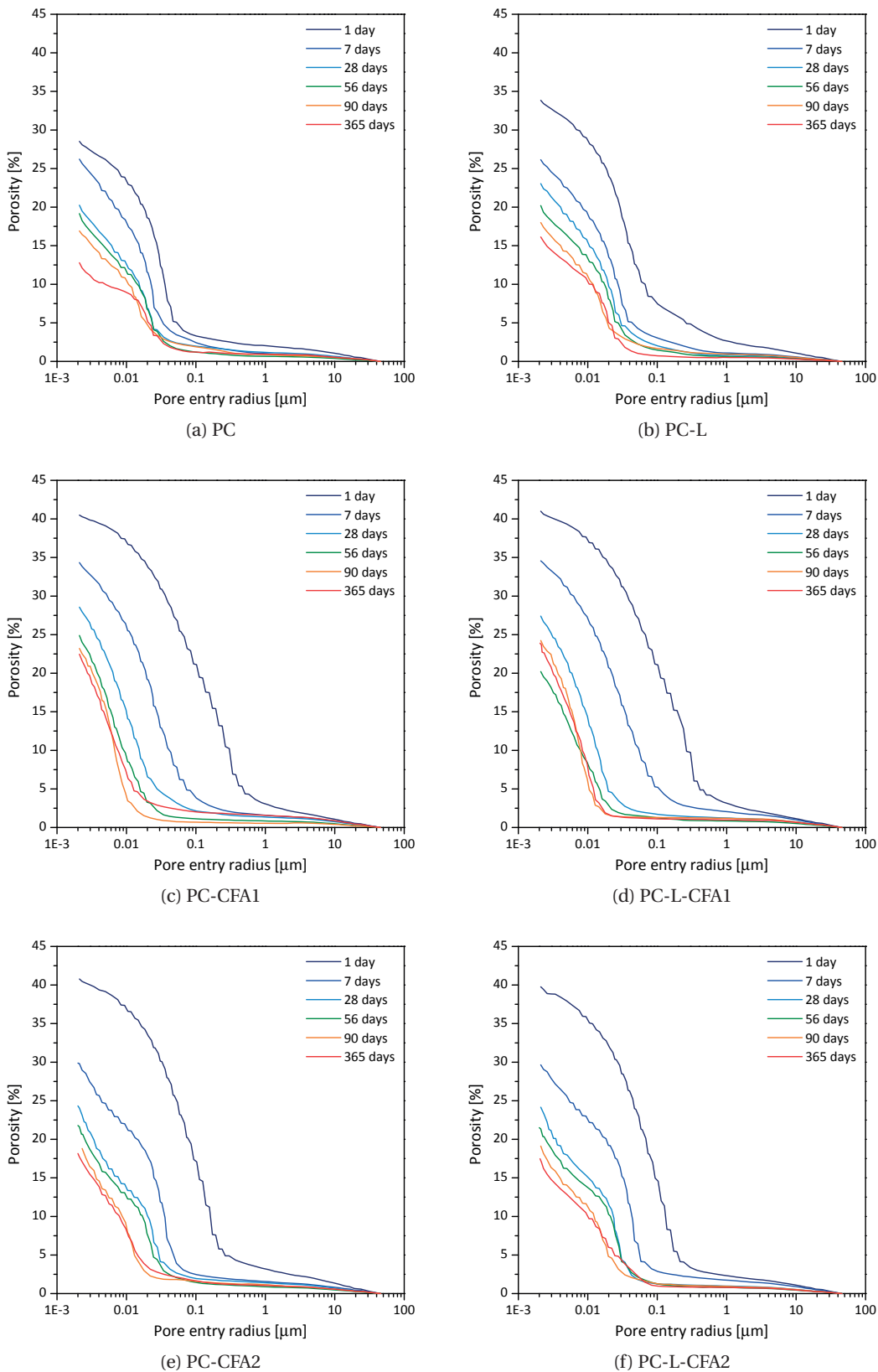


Figure I.1: Mercury intrusion porosimetry curves - 1/3.

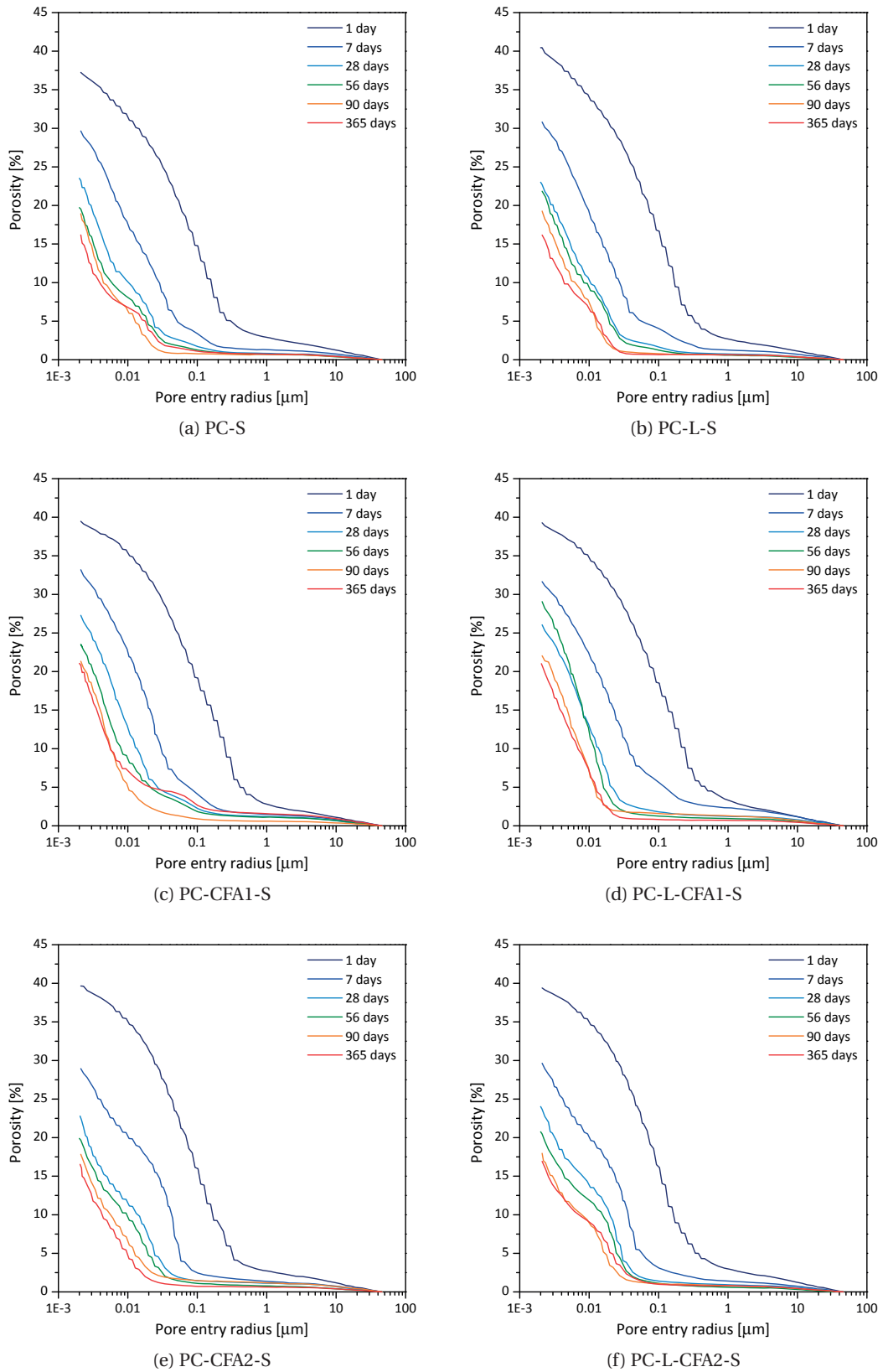


Figure I.2: Mercury intrusion porosimetry curves - 2/3.

Appendix I. Mercury Intusion Porosimetry curves

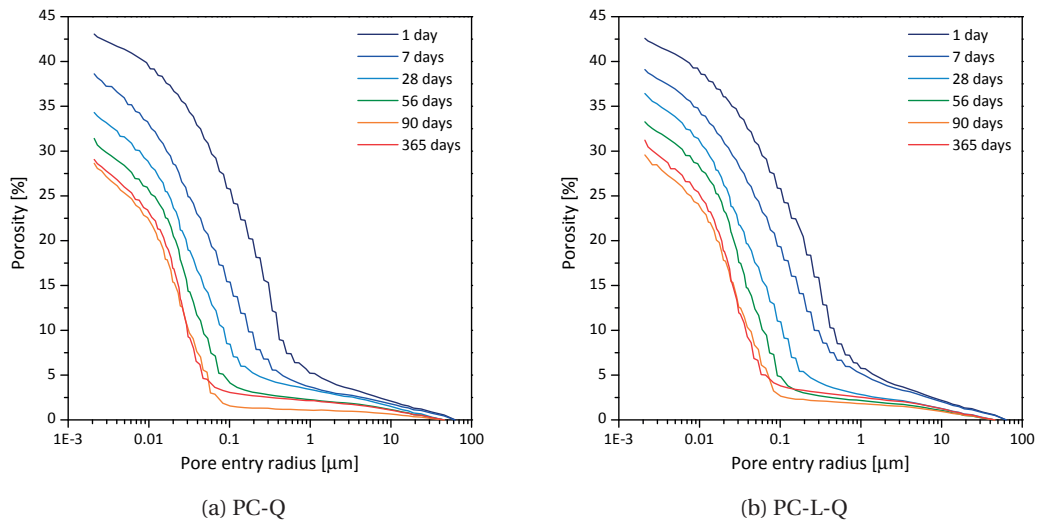


Figure I.3: Mercury intrusion porosimetry curves - 3/3.

Bibliography

- [1] U.S. Geological Survey, Mineral Commodity Summaries 2013, U.S. Geological Survey (2013) 38.
- [2] J. Damtoft, J. Lukasik, D. Herfort, D. Sorrentino, E. Gartner, Sustainable development and climate change initiatives, *Cement and Concrete Research* 38 (2) (2008) 115–127.
- [3] EN, EN 197-1:2011 - Cement - Part 1: Composition, specifications and conformity criteria for common cement, Tech. rep., CEN European Committee for Standardization (2011).
- [4] J. E. Anderson, Sustainable Cement Using Fly Ash: An Examination of The Net Role of High Volume Fly Ash cement on Carbon Dioxide Emissions, in: *Ecocity World Summit 2008 Proceedings*, 2008, pp. 1–12.
- [5] N. Koukoulas, J. Hämäläinen, D. Papanikolaou, A. Tourunen, T. Jäntti, Mineralogical and elemental composition of fly ash from pilot scale fluidised bed combustion of lignite, bituminous coal, wood chips and their blends, *Fuel* 86 (14) (2007) 2186–2193.
- [6] K. Erdoğdu, P. Türker, Effects of fly ash particle size on strength of portland cement fly ash mortars, *Cement and Concrete Research* 28 (9) (1998) 1217–1222.
- [7] S. V. Vassilev, R. Menendez, D. Alvarez, M. Diaz-Somoano, M. Martinez-Tarazona, Phase-mineral and chemical composition of coal fly ashes as a basis for their multicomponent utilization. 1. Characterization of feed coals and fly ashes, *Fuel* 82 (14) (2003) 1793–1811.
- [8] C. R. Ward, D. French, Determination of glass content and estimation of glass composition in fly ash using quantitative X-ray diffractometry, *Fuel* 85 (16) (2006) 2268–2277.
- [9] ASTM, ASTM Standard C618: Standard Specification for Coal Fly Ash and Raw or Calcined Natural Pozzolan for Use in Concrete, Tech. rep., ASTM International, West Conshohocken, PA (2012).
- [10] P. C. Hewlett, F. Massazza, *Lea's Chemistry of Cement and Concrete*, Butterworth-Heinemann, Elsevier Ltd., 2003.
- [11] S. Mindess, J. F. Young, D. Darwin, *Concrete*, Pearson Education, Inc., 2003.

Bibliography

- [12] P. Mehta, Pozzolanic and cementitious by-products in concrete—another look, ACI Special Publication (1989) 1–44.
- [13] Y. Nathan, M. Dvorachek, I. Pelly, U. Mimran, Characterization of coal fly ash from Israel, *Fuel* 78 (2) (1999) 205–213.
- [14] H. Pietersen, Reactivity of fly ash and slag in cement, Ph.D. thesis, TU Delft (1993).
- [15] S. Diamond, Particle morphologies in fly ash, *Cement and Concrete Research* 16 (4) (1986) 569–579.
- [16] R. S. Winburn, D. G. Grier, G. J. McCarthy, R. B. Peterson, Rietveld quantitative X-ray diffraction analysis of NIST fly ash standard reference materials, *Powder Diffraction* 15 (2000) 163–172.
- [17] R. J. Lauf, Application of materials characterization techniques to coal and coal wastes, Dept. of Energy, Oak Ridge National Laboratory, Oak Ridge, Tenn., 1981.
- [18] R. Dhole, M. D. A. Thomas, K. J. Folliard, T. Drimalas, Characterization of fly ashes for sulfate resistance, *ACI Materials Journal* 110 (2) (2013) 159–168.
- [19] A. Johnson, L. J. J. Catalan, S. D. Kinrade, Characterization and evaluation of fly-ash from co-combustion of lignite and wood pellets for use as cement admixture, *Fuel* 89 (10) (2010) 3042–3050.
- [20] B. G. Kutchko, A. G. Kim, Fly ash characterization by SEM–EDS, *Fuel* 85 (17–18) (2006) 2537–2544.
- [21] R. J. Stevenson, Mineralogical characterization of a lignite gasification ash from a low-BTU fixed-bed gasifier II. Scanning electron microscope phase analysis, *Cement and Concrete Research* 14 (4) (1984) 485–490.
- [22] R. J. Stevenson, J. C. Collier, J. J. Crashell, L. R. Quandt, Characterization of North American Lignite Fly Ashes I. Chemical Variation, *MRS Proceedings* 113 (2011) 87.
- [23] W. Bumrongjaroen, I. Muller, R. A. Livingston, J. Davis, A Performance-based Fly Ash Classification System Using Glassy Particle Chemical Composition Data, in: 2011 World of Coal Ash (WOCA) Conference Proceedings, 2011, p. www.flyash.info.
- [24] R. J. Stevenson, R. A. Larsen, Characterization of a Lignite Ash from the Metc Gasifier II. Scanning Electron Microscopy, *MRS Proceedings* 43 (1984) 177.
- [25] J. W. Lydon, The measurement of the modal mineralogy of rocks from SEM imagery: the use of Multispec© and ImageJ freeware, Geological Survey of Canada (4941).
- [26] R. T. Chancey, P. Stutzman, M. C. G. Juenger, D. W. Fowler, Comprehensive phase characterization of crystalline and amorphous phases of a Class F fly ash, *Cement and Concrete Research* 40 (2010) 146–156.

- [27] L. Biehl, D. Landgrebe, MultiSpec—a tool for multispectral–hyperspectral image data analysis, *Computers & Geosciences* 28 (2002) 1153–1159.
- [28] F. Deschner, F. Winnefeld, B. Lothenbach, S. Seufert, P. Schwesig, S. Dittrich, F. Goetz-Neunhoeffler, J. Neubauer, Hydration of Portland cement with high replacement by siliceous fly ash, *Cement and Concrete Research* 42 (10) (2012) 1389–1400.
- [29] G. Baert, S. Hoste, G. De Schutter, N. De Belie, Reactivity of fly ash in cement paste studied by means of thermogravimetry and isothermal calorimetry, *Journal of Thermal Analysis and Calorimetry* 94 (2008) 485–492.
- [30] L. Lam, Y. Wong, C. Poon, Degree of hydration and gel/space ratio of high-volume fly ash/cement systems, *Cement and Concrete Research* 30 (5) (2000) 747–756.
- [31] K. Luke, F. P. Glasser, Internal chemical evolution of the constitution of blended cements, *Cement and Concrete Research* 18 (4) (1988) 495–502.
- [32] E. Sakai, S. Miyahara, S. Ohsawa, S.-H. Lee, M. Daimon, Hydration of fly ash cement, *Cement and Concrete Research* 35 (6) (2005) 1135–1140.
- [33] S. Ohsawa, K. Asaga, S. Goto, M. Daimon, Quantitative determination of fly ash in the hydrated fly ash - $\text{CaSO}_4 \cdot 2\text{H}_2\text{O}$ - $\text{Ca}(\text{OH})_2$ system, *Cement and Concrete Research* 15 (2) (1985) 357–366.
- [34] B. Suprenant, G. Papadopoulos, Selective Dissolution of Portland-Fly-Ash Cements, *Journal of Materials in Civil Engineering* 3 (1) (1991) 48–59.
- [35] M. B. Haha, K. De Weerd, B. Lothenbach, Quantification of the degree of reaction of fly ash, *Cement and Concrete Research* 40 (11) (2010) 1620–1629.
- [36] K. L. Scrivener, H. H. Patel, P. L. Pratt, L. J. Parrott, Analysis of Phases in Cement Paste using Backscattered Electron Images, Methanol Adsorption and Thermogravimetric Analysis, *MRS Proceedings* 85.
- [37] K. O. Kjellsen, R. J. Detwiler, Reaction kinetics of portland cement mortars hydrated at different temperatures, *Cement and Concrete Research* 22 (1) (1992) 112–120.
- [38] J. Ash, M. Mellas, Application of backscattered electron imaging to concrete materials, *Cement and Concrete Research* 23 (3) (1993) 576–580.
- [39] M. Mouret, A. Bascoul, G. Escadeillas, Study of the degree of hydration of concrete by means of image analysis and chemically bound water, *Advanced Cement Based Materials* 6 (3–4) (1997) 109–115.
- [40] K. Scrivener, Backscattered electron imaging of cementitious microstructures: Understanding and quantification, *Cement and Concrete Composites* 26 (2004) 935–945.

Bibliography

- [41] X. Feng, E. Garboczi, D. Bentz, P. Stutzman, T. Mason, Estimation of the degree of hydration of blended cement pastes by a scanning electron microscope point-counting procedure, *Cement and Concrete Research* 34 (10) (2004) 1787–1793.
- [42] F. Deschner, B. Münch, F. Winnefeld, B. Lothenbach, Quantification of fly ash in hydrated, blended Portland cement pastes by backscattered electron imaging, *Journal of Microscopy* 251 (2013) 188–204.
- [43] A. C. A. Muller, K. L. Scrivener, A. M. Gajewicz, P. J. McDonald, Densification of C-S-H measured by ^1H NMR relaxometry, *Journal of Physical Chemistry C* 117 (1) (2013) 403–412.
- [44] H. F. W. Taylor, *Cement Chemistry*, Thomas Telford Publishing, 1997.
- [45] Y. Halse, P. L. Pratt, Development of Microstructure and other properties in fly ash OPC systems, *Area 14* (c) (1984) 491–498.
- [46] R. Taylor, I. Richardson, R. Brydson, Composition and microstructure of 20-year-old ordinary Portland cement–ground granulated blast-furnace slag blends containing 0 to 100% slag, *Cement and Concrete Research* 40 (7) (2010) 971–983.
- [47] J.-I. Escalante-Garcia, J. Sharp, The chemical composition and microstructure of hydration products in blended cements, *Cement and Concrete Composites* 26 (8) (2004) 967–976.
- [48] N. Bouzoubaâ, M. H. Zhang, V. M. Malhotra, Laboratory-produced high-volume fly ash blended cements: Compressive strength and resistance to the chloride-ion penetration of concrete, *Cement and Concrete Research* 30 (7) (2000) 1037–1046.
- [49] N. Bouzoubaâ, M. H. Zhang, V. M. Malhotra, Mechanical properties and durability of concrete made with high-volume fly ash blended cements using a coarse fly ash, *Cement and Concrete Research* 31 (10) (2001) 1393–1402.
- [50] V. Kocaba, Development and evaluation of methods to follow microstructural development of cementitious systems including slags, Ph.D. thesis, École polytechnique fédérale de Lausanne EPFL (2009).
- [51] B. Lothenbach, K. Scrivener, R. Hooton, Supplementary cementitious materials, *Cement and Concrete Research* 41 (12) (2011) 1244–1256.
- [52] I. Richardson, G. Groves, The incorporation of minor and trace elements into calcium silicate hydrate (C-S-H) gel in hardened cement pastes, *Cement and Concrete Research* 23 (1) (1993) 131–138.
- [53] T. Wagner, D. A. Kulik, F. F. Hingerl, S. V. Dmytrievava, Gem-selector geochemical modeling package: TSolMod library and data interface for multicomponent phase models, *Canadian Mineralogist* 50 (5) (2012) 1173–1195.

- [54] D. A. Kulik, T. Wagner, S. V. Dmytrieva, G. Kosakowski, F. F. Hingerl, K. V. Chudnenko, U. R. Berner, GEM-Selektor geochemical modeling package: Revised algorithm and GEMS3K numerical kernel for coupled simulation codes, *Computational Geosciences* 17 (1) (2013) 1–24.
- [55] W. Hummel, U. Berner, E. Curti, F. J. Pearson, T. Thoenen, Nagra/PSI chemical thermodynamic data base 01/01, in: *Radiochimica Acta*, Vol. 90, 2002, pp. 805–813.
- [56] T. Matschei, B. Lothenbach, F. P. Glasser, Thermodynamic properties of Portland cement hydrates in the system CaO-Al₂O₃-SiO₂-CaSO₄-CaCO₃-H₂O, *Cement and Concrete Research* 37 (10) (2007) 1379–1410.
- [57] B. Lothenbach, T. Matschei, G. Möschner, F. P. Glasser, Thermodynamic modelling of the effect of temperature on the hydration and porosity of Portland cement, *Cement and Concrete Research* 38 (1) (2008) 1–18.
- [58] A. Schöler, B. Lothenbach, F. Winnefeld, M. Zajac, Hydration of quaternary Portland cement blends containing blast-furnace slag, siliceous fly ash and limestone powder, *Cement and Concrete Composites* 55 (2015) 374–382.
- [59] G. Le Saoût, V. Kocaba, K. Scrivener, Application of the Rietveld method to the analysis of anhydrous cement, *Cement and Concrete Research* 41 (2) (2011) 133–148.
- [60] T. Matschei, B. Lothenbach, F. Glasser, The role of calcium carbonate in cement hydration, *Cement and Concrete Research* 37 (4) (2007) 551–558.
- [61] K. De Weerd, K. Kjellsen, E. Sellevold, H. Justnes, Synergy between fly ash and limestone powder in ternary cements, *Cement and Concrete Composites* 33 (1) (2011) 30–38.
- [62] W. P. Inskeep, P. R. Bloom, An evaluation of rate equations for calcite precipitation kinetics at less than 0.01 atm and pH greater than 8, *Geochimica et Cosmochimica Acta* 49 (10) (1985) 2165–2180.
- [63] B. Lothenbach, G. Le Saout, E. Gallucci, K. Scrivener, Influence of limestone on the hydration of Portland cements, *Cement and Concrete Research* 38 (6) (2008) 848–860.
- [64] K. D. Ingram, K. E. Daugherty, A review of limestone additions to Portland cement and concrete, *Cement and Concrete Composites* 13 (3) (1991) 165–170.
- [65] T. Vuk, V. Tinta, R. Gabrovšek, V. Kaučič, The effects of limestone addition, clinker type and fineness on properties of Portland cement, *Cement and Concrete Research* 31 (1) (2001) 135–139.
- [66] S. Tsvilis, G. Batis, E. Chaniotakis, G. Grigoriadis, D. Theodossis, Properties and behavior of limestone cement concrete and mortar, *Cement and Concrete Research* 30 (10) (2000) 1679–1683.

Bibliography

- [67] J. Dweck, P. M. Buchler, A. C. V. Coelho, F. K. Cartledge, Hydration of a Portland cement blended with calcium carbonate, *Thermochimica Acta* 346 (1-2) (2000) 105–113.
- [68] K. De Weerd, M. B. Haha, G. Le Saout, K. Kjellsen, H. Justnes, B. Lothenbach, Hydration mechanisms of ternary Portland cements containing limestone powder and fly ash, *Cement and Concrete Research* 41 (3) (2011) 279–291.
- [69] G. Menéndez, V. Bonavetti, E. F. Irassar, Strength development of ternary blended cement with limestone filler and blast-furnace slag, *Cement and Concrete Composites* 25 (1) (2003) 61–67.
- [70] I. Elkhadiri, A. Diouri, A. Boukhari, J. Aride, F. Puertas, Mechanical behaviour of various mortars made by combined fly ash and limestone in Moroccan Portland cement, *Cement and Concrete Research* 32 (10) (2002) 1597–1603.
- [71] P. Chindapasirt, C. Jaturapitakkul, T. Sinsiri, Effect of fly ash fineness on compressive strength and pore size of blended cement paste, *Cement and Concrete Composites* 27 (4) (2005) 425–428.
- [72] C. Poon, Y. Wong, L. Lam, The influence of different curing conditions on the pore structure and related properties of fly-ash cement pastes and mortars, *Construction and Building Materials* 11 (7-8) (1997) 383–393.
- [73] J. Zhang, G. W. Scherer, Comparison of methods for arresting hydration of cement, *Cement and Concrete Research* 41 (10) (2011) 1024–1036.
- [74] J. J. Beaudoin, P. Gu, J. Marchand, B. Tamtsia, R. E. Myers, Z. Liu, Solvent replacement studies of hydrated portland cement systems: The role of calcium hydroxide, *Advanced Cement Based Materials* 8 (2) (1998) 56–65.
- [75] A. Ipavec, R. Gabrovšek, T. Vuk, V. Kaučič, J. Maček, A. Meden, Carboaluminate Phases Formation During the Hydration of Calcite-Containing Portland Cement, *Journal of the American Ceramic Society* 94 (4) (2011) 1238–1242.
- [76] D. C. Creagh, J. H. Hubbell, X-ray absorption (or attenuation) coefficients, in: E. Prince (Ed.), *International Tables for Crystallography*, Vol. C Math. Phys. Chem. Tables, 6th Edition, International Union of Crystallography, 2006, Ch. 4.2, pp. 220 – 229.
- [77] V. Kocaba, E. Gallucci, K. L. Scrivener, Methods for determination of degree of reaction of slag in blended cement pastes, *Cement and Concrete Research* 42 (2012) 511–525.
- [78] A. M. Harrisson, N. B. Winter, H. F. W. Taylor, MICROSTRUCTURE AND MICROCHEMISTRY OF SLAG CEMENT PASTES, in: *Materials Research Society Symposia. Microstructural Development During Hydration of Cement*. Boston, Vol. 85, 1986, pp. 213–222.
- [79] D. A. Kulik, Improving the structural consistency of C-S-H solid solution thermodynamic models, *Cement and Concrete Research* 41 (5) (2011) 477–495.

- [80] R. Barneyback, S. Diamond, Expression and analysis of pore fluids from hardened cement pastes and mortars, *Cement and Concrete Research* 11 (2) (1981) 279–285.
- [81] R. A. Cook, K. C. Hover, Experiments on the contact angle between mercury and hardened cement paste, *Cement and Concrete Research* 21 (6) (1991) 1165–1175.
- [82] J. Bizzozero, Hydration and dimensional stability of calcium aluminate cement based systems, PhD Thesis, École Polytechnique Fédérale de Lausanne, <https://infoscience.epfl.ch/record/202031?ln=fr>.
- [83] A. C. A. Muller, Characterization of porosity & C-S-H in cement pastes by ¹H NMR, PhD Thesis, École Polytechnique Fédérale de Lausanne, <https://infoscience.epfl.ch/record/202011?ln=fr>.
- [84] P. T. Durdziński, C. F. Dunant, M. B. Haha, K. L. Scrivener, A new quantification method based on SEM-EDS to assess fly ash composition and study the reaction of its individual components in hydrating cement paste, *Cement and Concrete Research*.
- [85] G. Kalousek, J. Kopanda, Approach to fundamentals of concrete strength, *Cement and Concrete Research* 1 (1) (1971) 63–73.
- [86] R. Helmuth, *Fly Ash in Cement and Concrete*, Portland Cement Assn, 1987.
- [87] S. Diamond, On the glass present in low-calcium and in high-calcium flyashes, *Cement and Concrete Research* 13 (1983) 459–464.
- [88] S. Goto, H. Fujimori, A. Hidaka, K. Ioku, Effects of components on the rate of heat liberation of the hydration in the system of glass/gypsum/lime, *Journal of the European Ceramic Society* 26 (2006) 771–776.
- [89] W. Vogel, Phase separation in glass, *Journal of Non-Crystalline Solids* 25 (1-3) (1977) 170–214.
- [90] W. Kingery, P. Vandiver, I.-W. Huang, Y.-M. Chiang, Liquid-liquid immiscibility and phase separation in the quaternary systems K₂O-Al₂O₃-CaO-SiO₂ and Na₂O-Al₂O₃-CaO-SiO₂, *Journal of Non-Crystalline Solids* 54 (1-2) (1983) 163–171.
- [91] M. I. Wood, P. C. Hess, The structural role of Al₂O₃ and TiO₂ in immiscible silicate liquids in the system SiO₂-MgO-CaO-FeO-TiO₂-Al₂O₃, *Contributions to Mineralogy and Petrology* 72 (3) (1980) 319–328.
- [92] L.-n. Ngu, H. Wu, D.-k. Zhang, Characterization of Ash Cenospheres in Fly Ash from Australian Power Stations, *Energy & Fuels* 21 (6) (2007) 3437–3445.
- [93] D. Bibby, Composition and variation of pulverized fuel ash obtained from the combustion of sub-bituminous coals, New Zealand, *Fuel* 56 (4) (1977) 427–431.

Bibliography

- [94] P. T. Durdziński, R. Snellings, C. F. Dunant, M. B. Haha, K. L. Scrivener, Fly ash as an assemblage of model Ca–Mg–Na-aluminosilicate glasses, *Cement and Concrete Research* 78 (2015) 263–272.
- [95] K. L. Aughenbaugh, R. T. Chancey, P. Stutzman, M. C. Juenger, D. W. Fowler, An examination of the reactivity of fly ash in cementitious pore solutions, *Materials and Structures* 46 (5) (2013) 869–880.
- [96] R. Snellings, Solution-Controlled Dissolution of Supplementary Cementitious Material Glasses at pH 13: The Effect of Solution Composition on Glass Dissolution Rates, *Journal of the American Ceramic Society* 96 (8) (2013) 2467–2475.
- [97] R. Snellings, T. Paulhiac, K. Scrivener, The Effect of Mg on Slag Reactivity in Blended Cements, *Waste and Biomass Valorization* 5 (3) (2014) 369–383.
- [98] R. Snellings, Surface Chemistry of Calcium Aluminosilicate Glasses, *Journal of the American Ceramic Society* 98 (1) (2015) 303–314.
- [99] L. Nicoleau, E. Schreiner, A. Nonat, Ion-specific effects influencing the dissolution of tricalcium silicate, *Cement and Concrete Research* 59 (2014) 118–138.
- [100] S. Bishnoi, K. L. Scrivener, Studying nucleation and growth kinetics of alite hydration using μic , *Cement and Concrete Research* 39 (2009) 849–860.
- [101] E. Olbrich, G. H. Frischat, Corrosion of granulated glassy blast furnace slags in aqueous solutions, *Glass Science and Technology: Glastechnische Berichte* 74 (4) (2001) 86–96.
- [102] M. Moesgaard, D. Herfort, J. Skibsted, Y. Yue, Calcium aluminosilicate glasses as supplementary cementitious materials, *Glass Technology-European Journal of Glass Science and Technology Part A* 51 (5) (2010) 183–190.
- [103] B. r. O. Mysen, D. Virgo, F. A. Seifert, The structure of silicate melts: Implications for chemical and physical properties of natural magma, *Reviews of Geophysics* 20 (1982) 353.
- [104] W. H. Zachariasen, The Atomic Arrangement in Glass, *Journal of the American Chemical Society* 54 (10) (1932) 3841–3851.
- [105] I. Kushiro, On the nature of silicate melt and its significance in magma genesis; regularities in the shift of the liquidus boundaries involving olivine, pyroxene, and silica minerals, *American Journal of Science* 275 (4) (1975) 411–431.
- [106] T. Furukawa, K. E. Fox, W. B. White, Raman spectroscopic investigation of the structure of silicate glasses. III. Raman intensities and structural units in sodium silicate glasses, *The Journal of Chemical Physics* 75 (7) (1981) 3226.

- [107] F. A. Seifert, B. O. Mysen, D. Virgo, Three-dimensional network structure of quenched melts (glass) in the systems SiO_2 - NaAlO_2 , SiO_2 - CaAl_2O_4 and SiO_2 - MgAl_2O_4 , *American Mineralogist* 67 (7-8) (1982) 696–717.
- [108] W. Bumrongjaroen, R. Livingston, J. Schweitzer, S. Swatekititham, Synthetic Glass Models for Investigating Fly Ash Reactivity, in: *Proceedings of the 3rd International Conference on the Use of Fly Ash, Silica Fume, Slag, and Natural Pozzolans in Concrete*, Warsaw, 2007, pp. 227 – 242.
- [109] K. L. Aughenbaugh, T. Williamson, M. C. G. Juenger, Critical evaluation of strength prediction methods for alkali-activated fly ash, *Materials and Structures* 48 (3) (2015) 607–620.
- [110] J. Akola, S. Kohara, K. Ohara, A. Fujiwara, Y. Watanabe, A. Masuno, T. Usuki, T. Kubo, A. Nakahira, K. Nitta, T. Uruga, J. K. R. Weber, C. J. Benmore, Network topology for the formation of solvated electrons in binary $\text{CaO-Al}_2\text{O}_3$ composition glasses., *Proceedings of the National Academy of Sciences of the United States of America* 110 (25) (2013) 10129–34.
- [111] I. C. Madsen, N. V. Y. Scarlett, A. Kern, Description and survey of methodologies for the determination of amorphous content via X-ray powder diffraction, *Zeitschrift für Kristallographie* 226 (12) (2011) 944–955.
- [112] N. V. Y. Scarlett, I. C. Madsen, Quantification of phases with partial or no known crystal structures, *Powder Diffraction* 21 (04) (2006) 278–284.
- [113] R. Snellings, A. Salze, K. L. Scrivener, Use of X-ray diffraction to quantify amorphous supplementary cementitious materials in anhydrous and hydrated blended cements, *Cement and Concrete Research* 64 (2014) 89–98.
- [114] E. Bonaccorsi, S. Merlino, A. R. Kampf, The Crystal Structure of Tobermorite 14 A (Plombierite), a C-S-H Phase, *Journal of the American Ceramic Society* 88 (3) (2005) 505–512.
- [115] K. Kihara, T. Matsumoto, M. Imamura, Structural change of orthorhombic-I tridymite with temperature: A study based on second-order thermal-vibrational parameters, *Zeitschrift für Kristallographie - Crystalline Materials* 177 (1-4).
- [116] J. E. Wainwright, J. Starkey, A refinement of the structure of anorthite, *Zeitschrift für Kristallographie - Crystalline Materials* 133 (1-6).
- [117] W. G. Mumme, R. J. Hill, G. Bushnell-Wye, E. R. Segnit, Rietveld crystal structure refinements, crystal chemistry and calculated powder diffraction data for the polymorphs of dicalcium silicate and related phases, *Neues Jahrbuch fuer Mineralogie* 169 (1) (1995) 35–68.
- [118] S. Ouellet, B. Bussière, M. Aubertin, M. Benzaazoua, Microstructural evolution of cemented paste backfill: Mercury intrusion porosimetry test results, *Cement and Concrete Research* 37 (12) (2007) 1654–1665.

Bibliography

- [119] C. W. Correns, Growth and dissolution of crystals under linear pressure, *Discussions of the Faraday Society* 5 (1949) 267.
- [120] R. J. Flatt, Salt damage in porous materials: how high supersaturations are generated, *Journal of Crystal Growth* 242 (3-4) (2002) 435–454.
- [121] H. M. Jennings, Refinements to colloid model of C-S-H in cement: CM-II, *Cement and Concrete Research* 38 (3) (2008) 275–289.
- [122] T. C. Powers, Structure and Physical Properties of Hardened Portland Cement Paste, *Journal of the American Ceramic Society* 41 (1) (1958) 1–6.
- [123] R. E. Collins, *Flow of Fluids Through Porous Materials*, Reinhold Publishing Co., New York, 1961.
- [124] K. A. Snyder, X. Feng, B. D. Keen, T. O. Mason, Estimating the electrical conductivity of cement paste pore solutions from OH⁻, K⁺ and Na⁺ concentrations, *Cement and Concrete Research* 33 (6) (2003) 793–798.
- [125] A. Fluegel, Global Model for Calculating Room-Temperature Glass Density from the Composition, *Journal of the American Ceramic Society* 90 (8) (2007) 2622–2625.
- [126] T. Cheewaket, C. Jaturapitakkul, W. Chalee, Long term performance of chloride binding capacity in fly ash concrete in a marine environment, *Construction and Building Materials* 24 (8) (2010) 1352–1357.
- [127] R. Dhir, M. Jones, Development of chloride-resisting concrete using fly ash, *Fuel* 78 (2) (1999) 137–142.
- [128] T. Luping, L.-O. Nilsson, Chloride binding capacity and binding isotherms of OPC pastes and mortars, *Cement and Concrete Research* 23 (2) (1993) 247–253.
- [129] F. Glasser, A. Kindness, S. Stronach, Stability and solubility relationships in AFm phases, *Cement and Concrete Research* 29 (6) (1999) 861–866.
- [130] Y. Elakneswaran, T. Nawa, K. Kurumisawa, Electrokinetic potential of hydrated cement in relation to adsorption of chlorides, *Cement and Concrete Research* 39 (4) (2009) 340–344.
- [131] W. Kunther, B. Lothenbach, K. L. Scrivener, On the relevance of volume increase for the length changes of mortar bars in sulfate solutions, *Cement and Concrete Research* 46 (2013) 23–29.
- [132] T. Schmidt, B. Lothenbach, M. Romer, J. Neuenschwander, K. Scrivener, Physical and microstructural aspects of sulfate attack on ordinary and limestone blended Portland cements, *Cement and Concrete Research* 39 (12) (2009) 1111–1121.

- [133] C. Yu, W. Sun, K. Scrivener, Mechanism of expansion of mortars immersed in sodium sulfate solutions, *Cement and Concrete Research* 43 (1) (2013) 105–111.
- [134] P. Feng, E. J. Garboczi, C. Miao, J. W. Bullard, Microstructural origins of cement paste degradation by external sulfate attack, *Construction and Building Materials* 96 (2015) 391–403.
- [135] G. W. Scherer, Factors affecting crystallization pressure, in: *International RILEM Workshop on Internal Sulfate Attack and Delayed Ettringite Formation*, no. September, 2004, pp. 139–154.
- [136] K. Tosun-Felekoğlu, The effect of C3A content on sulfate durability of Portland limestone cement mortars, *Construction and Building Materials* 36 (2012) 437–447.
- [137] S. T. Lee, R. D. Hooton, H. S. Jung, D. H. Park, C. S. Choi, Effect of limestone filler on the deterioration of mortars and pastes exposed to sulfate solutions at ambient temperature, *Cement and Concrete Research* 38 (1) (2008) 68–76.
- [138] R. S. Gollop, H. F. W. Taylor, Microstructural and microanalytical studies of sulfate attack. IV. Reactions of a slag cement paste with sodium and magnesium sulfate solutions, *Cement and Concrete Research* 26 (7) (1996) 1013–1028.
- [139] P. J. Tikalsky, R. L. Carrasquillo, Fly ash evaluation and selection for use in sulfate-resistant concrete, *ACI Materials Journal* 90 (1993) 545–51.
- [140] E. R. Dunstan, A Possible Method for Identifying Fly Ashes That Will Improve the Sulfate Resistance of Concretes, *Cement, Concrete and Aggregates* 2 (1) (1980) 20–30.
- [141] S. Kandasamy, M. H. Shehata, Durability of ternary blends containing high calcium fly ash and slag against sodium sulphate attack, *Construction and Building Materials* 53 (2014) 267–272.
- [142] V. Fernández-Altable, C. Yu, G. L. Saout, K. Scrivener, Characterisation of slag blends and correlation with their sulphate resistance in static and semi-dynamic conditions, in: *13th International Congress on the Chemistry of Cement.*, 2011, pp. 1–7.

List of publications

Peer-reviewed journal publications

- P.T. Durdziński, R. Snellings, C.F. Dunant, M. Ben Haha and K.L. Scrivener. Fly ash as an assemblage of model Ca-Mg-Na-aluminosilicate glasses. *Cement and Concrete Research* 78 (2015) 263–272
- P.T. Durdziński, C.F. Dunant, M. Ben Haha and K.L. Scrivener. A new quantification method based on SEM-EDS to assess fly ash composition and study the reaction of its individual components in hydrating cement paste. *Cement and Concrete Research* 73 (2015) 111–122

Conference papers

- P.T. Durdziński, C.F. Dunant, M. Ben Haha and K.L. Scrivener. Understanding calcareous fly ashes: from characterization to reactivity and hydration products in composite cements. The 14th International Congress on the Chemistry of Cement, Beijing, China, October 2015.
- P.T. Durdziński, R. Snellings and K.L. Scrivener. Reactivity of fly ash and synthetic Ca-Mg-Na-aluminosilicate glasses in Portland cement and alkaline solutions. 25th Goldschmidt Geochemistry Conference, Prague, Czech Republic, August 2015.
- P.T. Durdziński, C.F. Dunant, M. Ben Haha and K.L. Scrivener. A new quantification method based on SEM-EDS to assess fly ash chemical composition and its reactivity in composite cements. 15th Euroseminar on Microscopy Applied to Building Materials, Delft, The Netherlands, June 2015.
- P.T. Durdziński, M. Ben Haha and K.L. Scrivener. Durability of quaternary cements containing calcareous fly ash, slag and limestone. XIII International Conference on Durability of Building Materials, Paper 96, São Paulo, Brasil, September 2014.
- P.T. Durdziński, M. Ben Haha and K.L. Scrivener. Characterization of calcareous fly ash. 33rd Cement and Concrete Science Conference, Portsmouth, United Kingdom, September 2013.

Paweł Tadeusz DURDZIŃSKI

Polish
03 May 1987

Contact

Av. Églantine 24
1006 Lausanne
Switzerland

CH: +41 77 494 23 92

PL/EU: +48 662 05 05 02

pawel.durdzinski@gmail.com

Languages

English: fluent
French: fluent
German: basic
Spanish: basic
Polish: mother tongue

Professional experience

2011 - 2015 **École Polytechnique Fédérale de Lausanne**

Laboratory of Construction Materials

Assistant researcher in construction materials

- Supervision and training of visiting PhD students
- Supervision of master semester projects
- Teaching practical works for material science and civil engineering students

Education and Training

2011 - 2015 **PhD in Materials Science** École Polytechnique Fédérale de Lausanne, Switzerland

Hydration of multi-component cements containing portland clinker, calcareous fly ash, slag and limestone.

2006 - 2011 **B.Sc and M.Sc in Chemical Technology** AGH, Cracow, Poland

Master thesis in Concrete Technology: Factors influencing the mechanical properties of Al-Si-gel based materials.

2011 **Research Internship** HeidelbergCement Technology Center, Germany
(1 month)

2010 **Exchange semester** Universidad Politècnica de València, Spain
School of Industrial Engineering

2009 **Research Internship** HeidelbergCement Technology Center, Germany
(1 month)

2003 - 2006 **Polish National Diploma** I Liceum Ogólnokształcące, Rybnik, Poland
specialized in Mathematics, Physics and Chemistry

Others

IT skills: Office, Origin, Matlab, GEMS, X'Pert High Score Plus (Rietveld analysis), LaTeX

Interests: Sports and outdoor activities, travelling, languages, cooking